Αριστοτέλειο Πανεπιστήμιο Θεσσαλονίκης
Τμήμα Φυσικής

Μελέτη των ιδιοτήτων του κουάρκ b με τα πρώτα δεδομένα του **ATLAS**

Ιωάννης Νομίδης

Διδακτορική διατριβή

Θεσσαλονίκη, Σεπτέμβριος 2013

Aristotle University of Thessaloniki
Department of Physics

Study of the *b*-quark properties with the first ATLAS data

Ioannis Nomidis

A thesis submitted for the degree of
Doctor of Philoshophy, Ph.D.

Thessaloniki, Greece
September 2013

This research has been co-financed by the European Union (European Social Fund - ESF) and Greek national funds through the Operational Program "Education and Lifelong Learning" of the National Strategic Reference Framework (NSRF) - Research Funding Program: Heracleitus II. Investing in knowledge society through the European Social Fund.

Η παρούσα έρευνα έχει συγχρηματοδοτηθεί από την Ευρωπαϊκή Ένωση (Ευρωπαϊκό Κοινωνικό Ταμείο - ΕΚΤ) και από εθνικούς πόρους μέσω του Επιχειρησιακού Προγράμματος "Εκπαίδευση και Δια Βίου Μάθηση" του Εθνικού Στρατηγικού Πλαισίου Αναφοράς (ΕΣΠΑ) - Ερευνητικό Χρηματοδοτούμενο Έργο: Ηράκλειτος ΙΙ. Επένδυση στην κοινωνία της γνώσης μέσω του Ευρωπαϊκού Κοινωνικού Ταμείου.

PhD. commitee:

Ch. Petridou (supervisor), Professor, Department of Physics, AU of Thessaloniki

Th. Alexopoulos, Professor, School of SAMS, NTU of Athens

M. Dris, Professor Emeritus, School of SAMS, NTU of Athens

S. Palestini, Dr, Researcher A', CERN, Switzerland

R. Nikolaidou, Dr, Researcher A', IRFU, CEA Saclay, France

D. Sampsonidis, Assistant Professor, Department of Physics, AU of Thessaloniki

K. Kordas, Lecturer, Department of Physics, AU of Thessaloniki

Day of the defense: 20/9/2013

Signature from head of PhD committee:

Dedicated to my parents,
for bringing me all the way here
& my friends,
for supporting me in times of need.

Περίληψη

Η παρούσα διδακτορική διατριβή εστιάζει στη μελέτη των ιδιοτήτων του μεσονίου B^+ μέσω της ανάλυσης των πρώτων δεδομένων του LHC στο CERN από συγκρούσεις πρωτονίων σε ενέργεια κέντρου μάζας $\sqrt{s} = 7$ TeV. Τα δεδομένα καταγράφηκαν από τον ανιχνευτή ATLAS την περίοδο 2010–2011 και προσφέρουν τη δυνατότητα για νέες μελέτες της φυσικής του κουάρκ b με δύο συγκεκριμένους στόχους: α) να επιβεβαιώσουν την καλή απόκριση του ανιχνευτή αναπαράγοντας τις γνωστές ιδιότητες των βαριών μεσονίων και β) να δώσουν τα πρώτα αποτελέσματα φυσικής στις ενέργειες του LHC. Καθώς το μεσόνιο B^+ αποτελείται από ένα αντι-κουάρκ b και ένα ελαφρύτερο κουάρκ, το u, συνιστά ιδανικό εργαλείο για να μελετήσουμε τις ιδιότητες του κουάρκ b, μέσω της διάσπασής του σε μεσόνια J/ψ και K^+, όπου τα J/ψ διασπώνται σε δύο μιόνια ($\mu^+\mu^-$). Η ανάλυση των δεδομένων που συλλέχθηκαν το 2010 (περίπου 40 pb^{-1} συνολικά) οδήγησε στην παρατήρηση της παραγωγής των μεσονίων $B^\pm$ αποδεικνύοντας την ικανότητα του ανιχνευτή ATLAS να ανακατασκευάζει διασπάσεις του τύπου $B \to J/\psi X$. Στη συνέχεια, παρουσιάζεται η μέτρηση της μάζας και του χρόνου ζωής του μεσονίου $B^\pm$ με τη μέθοδο του ταυτόχρονου προσδιορισμού. Αναπαράγοντας τις τιμές των ιδιοτήτων αυτών, γνωστές και καλά προσδιορισμένες από προηγούμενα πειράματα, αναδεικνύεται η εξαιρετική απόκριση και απόδοση του εσωτερικού ανιχνευτή και των αλγορίθμων ανακατασκευής. Ήδη με τα πρώτα δεδομένα πιστοποιείται η σωστή λειτουργία του ανιχνευτή ενόψει των μετρήσεων και ανακαλύψεων που ακολουθούν. Το κύριο αποτέλεσμα φυσικής της παρούσας διατριβής είναι η μέτρηση της ενεργού διατομής παραγωγής $B^\pm$ μεσονίων με δείγμα 2.4 fb^{-1} των δεδομένων που συλλέχθηκαν το 2011. Η ενεργός διατομή παραγωγής μετρήθηκε ως συνάρτηση της εγκάρσιας ορμής του μεσονίου $B^\pm$, εκτείνοντας αντίστοιχες μετρήσεις που έγιναν πρόσφατα από τα πειράματα CMS και LHCb στην ίδια ενέργεια των $\sqrt{s} = 7$ TeV σε μεγαλύτερες τιμές εγκάρσιας ορμής μέχρι περίπου τα 100 GeV. Για πρώτη φορά ήταν δυνατή η σύγκριση των αποτελεσμάτων με θεωρητικές προβλέψεις της Κβαντικής Χρωμοδυναμικής ώστε να διαπιστωθεί η ισχύς των θεωρητικών υπολογισμών στις ενέργειες του LHC, ειδικά μετά τις πρόσφατες βελτιώσεις στους θεωρητικούς υπολογισμούς που πραγματοποιήθηκαν με βάση προηγούμενα δεδομένα από το Tevatron. Επιπρόσθετα, ο έλεγχος των θεωρητικών υπολογισμών έγινε σε μεγαλύτερο εύρος ωκύτητας και εγκάρσιας ορμής από αυτό που είχε μελετηθεί στο παρελθόν, καθώς οι περιοχές αυτές έγιναν προσβάσι-

μες και πειραματικά μέσω των αποτελεσμάτων της παρούσας διατριβής. Οι μετρήσεις της ενεργού διατομής συγκρίνονται με προβλέψεις από διαφορετικά θεωρητικά πλαίσια, όπως το POWHEG και το MC@NLO αλλά και με προβλέψεις της μεθόδου FONLL, τα οποία λαμβάνουν υπόψη υπολογισμούς υψηλότερης τάξης σε διαγράμματα Feynman και προσεγγιστικές τεχνικές άθροισης λογαρίθμων. Σε όλες τις περιπτώσεις διαπιστώνεται καλή συμφωνία με τις θεωρητικές προβλέψεις, ιδιαίτερα στην περιοχή μεγάλων τιμών εγκάρσιας ορμής, όπου οι προσεγγίσεις των υπολογισμών από τα παραπάνω θεωρητικά πλαίσια είναι ιδιαίτερα ευαίσθητες. Οι μετρήσεις που παρουσιάζονται φέρουν συνολική αβεβαιότητα μικρότερη αυτής των θεωρητικών προβλέψεων, δίνοντας έτσι κίνητρο για την πραγματοποίηση νέων θεωρητικών υπολογισμών καλύτερης ακρίβειας.

Abstract

In this doctoral thesis a study of the properties of the B^+ meson is presented, analyzing the first pp collision data at $\sqrt{s} = 7$ TeV recorded with the ATLAS detector at the LHC at CERN in 2010–2011. The first data from the LHC provide an excellent opportunity for B-physics studies with two important goals: a) to validate the performance of the detector by reproducing well-known properties of heavy-flavor mesons and b) to provide the first physics results from the LHC. The B^+ meson consists of a b anti-quark and a u quark, with the b being much heavier than the light u quark. The decay of B^+ mesons to $J/\psi\, K^+$, with J/ψ mesons decaying to two muons, is an ideal testbed for extended studies on b-quark properties. This thesis presents an analysis of the data recorded in 2010 (about 40 pb^{-1} in total) that led to the observation of the production of $B^\pm$ mesons, demonstrating the ability of the ATLAS detector to reconstruct exclusive $B \to J/\psi X$ decays. Next, a simultaneous measurement of the mass and lifetime of $B^\pm$ mesons is presented, in good agreement with the world-average values. By reproducing these well-known properties, the excellent performance of the inner detector system and the vertex reconstruction algorithms is demonstrated already with the first ATLAS data and its proper functioning is validated in light of the physics measurements and discoveries that follow. The main physics result of this thesis is the measurement of the $B^\pm$ production cross-section with 2.4 fb^{-1} of data collected in 2011. The cross-section was measured as a function of transverse momentum and rapidity of $B^\pm$ mesons, extending recent measurements by the CMS and LHCb experiments at $\sqrt{s} = 7$ TeV to a higher transverse momentum region, up to about 100 GeV. The comparison of results with theoretical predictions of Quantum Chromodynamics is interesting in order to assess their validity at the new energy regime, especially after recent developments in the calculations that also showed good agreement with data from Tevatron. Moreover, comparisons are made in wider rapidity and transverse momentum ranges than what was previously studied. The measured cross-sections are compared with predictions obtained with the POWHEG and MC@NLO theoretical frameworks and with predictions of the FONLL approach, comprising next-to-leading-order calculations and resummation techniques. Good agreement is found with the measurements provided by this doctoral thesis, especially in the high-p_{T} region, where the approximations used in the calculations

within these frameworks are particularly sensitive. The measurements presented in this doctoral thesis provide points with total uncertainty smaller than that of the theory predictions, thus providing a motivation for theorists to improve the theoretical uncertainties.

Contents

Μελέτη των ιδιοτήτων του κουάρκ b με τα πρώτα δεδομένα του **ATLAS**

Αντικείμενο της διατριβής αποτελεί η μελέτη του κουάρκ b το οποίο παράγεται σε αφθονία στις συγκρούσεις πρωτονίων στο LHC, έτσι μας δίνεται η ευκαιρία να πραγματοποιήσουμε σημαντικές μελέτες με τα πρώτα δεδομένα που συλλέχθηκαν από τον ανιχνευτή ATLAS και τα οποία αφορούν την παραγωγή αυτού του σωματιδίου. Στόχος είναι να εξετάσουμε την απόδοση του ανιχνευτή αλλά και να εξάγουμε αποτελέσματα που είναι ενδιαφέροντα από θεωρητικής πλευράς κυρίως όσον αφορά τον έλεγχο της ισχύος των προβλέψεων του Καθιερωμένου Προτύπου.

Μετά από μια σύντομη περιγραφή του μηχανισμού παραγωγής μεσονίων B ακολουθούν τα δύο βασικά μέρη της διατριβής. Το πρώτο αφορά τις προετοιμασίες για την πραγματοποίηση μετρήσεων φυσικής, στα πλαίσια του οποίου αναπτύχθηκε λογισμικό εποπτείας της ποιότητας των δεδομένων και αναλύθηκαν δεδομένα από συγκρούσεις με σκοπό την επαλήθευση της σωστής ανακατασκευής μεσονίων B με τον ανιχνευτή ATLAS. Το δεύτερο μέρος αφορά τη μέτρηση της διαφορικής ενεργού διατομής παραγωγής μεσονίων B^+, που είναι και το κύριο αποτέλεσμα που παρουσιάζεται σε αυτή τη διατριβή. Η μέτρηση αυτή συγκρίνεται με θεωρητικές προβλέψεις, καθώς και με άλλες παρόμοιες μετρήσεις παραγωγής μεσονίων B, για την εξαγωγή συμπερασμάτων που αφορούν την ισχύ των θεωρητικών υπολογισμών.

Θεωρητικό υπόβαθρο

Η παραγωγή του κουάρκ b και η αδρονοποίησή του περιγράφεται, έως ένα συγκεκριμένο βαθμό, από το κομμάτι εκείνο του Καθιερωμένου Προτύπου που ονομάζεται Κβαντική Χρωμοδυναμική [1]. Για το τμήμα εκείνο της αδρονοποίησης που δεν μπορεί να περιγραφεί από την θεωρία χρησιμοποιούνται φαινομενολογικά μοντέλα περιγραφής.

Οι υπολογισμοί της Κβαντικής Χρωμοδυναμικής βασίζονται στη Θεωρία Διαταραχών, η οποία σε αυτή την περίπτωση μπορεί να εφαρμοστεί για την ανελαστική σκέδαση που οδηγεί στην παραγωγή του κουάρκ b και για το αρχικό κομμάτι της διαδικασίας της αδρονοποίησης. Το τελικό στάδιο της αδρονοποίησης είναι αυτό που δεν μπορεί να περιγραφεί στην Θεωρία Διαταραχών, αλλά δεν αποτελεί πρόβλημα για τους υπολογισμούς, γιατί μπορεί να παραμετροποιηθεί και να προσδιοριστεί πειραματικά με μεγάλη ακρίβεια. Πραγματοποιώντας όμως υπολογισμούς στην Θεωρία Διαταραχών για μηχανισμούς παραγωγής δεύτερης ή μεγαλύτερης τάξης, προκύπτουν όροι οι οποίοι στην περίπτωση εκπομπής γκλουονίων μικρής ενέργειας ή/και συγγραμμικών γκλουονίων απειρίζονται και έτσι οι υπολογισμοί της ενεργού διατομής αποκλίνουν σε μεγάλες ενέργειες. Για την επίλυση αυτών των προβλημάτων απαιτούνται ειδικές τεχνικές και προσεγγίσεις, η υλοποίηση των οποίων γίνεται σε διάφορα θεωρητικά πλαίσια, όπως αυτό της μεθόδου FONLL [2, 3], της μεθόδου POWHEG [4, 5] και της MC@NLO [6, 7]. Σκοπός της παρούσας διατριβής είναι η μελέτη της παραγωγής του κουάρκ b και η σύγκριση με τις προβλέψεις από υπολογισμούς αυτών των θεωρητικών πλαισίων, ώστε να αποφανθούμε για την ισχύ των μεθόδων αυτών και των προσεγγίσεων που υλοποιούν.

Για την μέτρηση της παραγωγής του κουάρκ b χρησιμοποιούνται τα B αδρόνια (μεσόνια και βαρυόνια) που είναι το αποτέλεσμα της αδρονοποίησης του κουάρκ b. Για τις μελέτες αυτής της διατριβής χρησιμοποιείται το μεσόνιο B^+ που αποτελείται από ένα κουάρκ b και ένα άλλο ελαφρύτερο κουάρκ, το u. Η διάσπαση των μεσονίων B^+ σε μεσόνια J/ψ και K^+ είναι από τις πιο πιθανές ανάμεσα στις υπόλοιπες διασπάσεις B μεσονίων. Επιπλέον, τα J/ψ διασπώνται σε δύο μιόνια ($\mu^+\mu^-$) με επίσης μεγάλη πιθανότητα και μάλιστα αρκετά γρήγορα, αφού η διάσπαση γίνεται μέσω της ηλεκτρομαγνητικής αλληλεπίδρασης. Συνεπώς, η διάσπαση αυτή έχει αρκετά απλή και καθαρή τελική κατάσταση που αποτελείται από τρία φορτισμένα σωματίδια με σχετικά μεγάλο χρόνο ζωής προερ-

χόμενα από τον ίδιο κόμβο αλληλεπίδρασης και είναι εύκολο να ανακατασκευαστεί στον ανιχνευτή ATLAS. Επιπλέον, η παρουσία μιονίων στην τελική κατάσταση προσφέρει μια ξεκάθαρη ένδειξη για τη γρήγορη και εύκολη επιλογή γεγονότων ανάμεσα σε πληθώρα άλλων γεγονότων υποβάθρου με τη βοήθεια του συστήματος σκανδαλισμού. Συμπεραίνουμε έτσι πως η επιλεγμένη διάσπαση είναι ένα ιδανικό εργαλείο για να μελετήσουμε τις ιδιότητες των μεσονίων B, και μάλιστα με τα πρώτα δεδομένα, δεδομένης της μεγάλης πιθανότητας παραγωγής κουάρκ b στο LHC.

Διασφάλιση της σωστής απόκρισης του ανιχνευτή ATLAS με τα πρώτα δεδομένα

Το πείραμα ATLAS [8] χρησιμοποιεί έναν ανιχνευτή γενικής σκοπιμότητας που αποτελείται από τον ανιχνευτή τροχιών, τα θερμιδόμετρα και το μιονικό φασματόμετρο. Ο ανιχνευτής τροχιών περικλείει το σημείο όπου συμβαίνουν οι συγκρούσεις και βρίσκεται μέσα σε μαγνητικό πεδίο 2 T. Ο ανιχνευτής αυτός περιβάλλεται από ένα θερμιδομετρικό σύστημα που αποτελείται από ένα ηλεκτρομαγνητικό και ένα αδρονικό υποσύστημα. Το θερμιδομετρικό σύστημα περιβάλλεται από ένα μεγάλο μιονικό φασματόμετρο που βρίσκεται μέσα σε ισχυρό τοροειδές μαγνητικό πεδίο. Μια πλήρης άποψη του ανιχνευτή ATLAS και των υποσυστημάτων που τον αποτελούν φαίνεται στο σχήμα 1.

Για την ανακατασκευή της διάσπασης του μεσονίου B^+ χρησιμοποιείται πληροφορία από τον ανιχνευτή τροχιών και το μιονικό φασματόμετρο. Ο ανιχνευτής τροχιών ανακατασκευάζει τις τροχιές των φορτισμένων σωματιδίων (μ και K) και μετράει την εγκάρσια ορμή τους με μεγάλη ακρίβεια. Επίσης, προσδιορίζει τη θέση της σύγκρουσης των πρωτονίων όπου παράγεται το B^+ μεσόνιο (πρωτογενής κόμβος αλληλεπίδρασης) και την θέση όπου το B^+ μεσόνιο διασπάται (δευτερογενής κόμβος διάσπασης). Το μιονικό φασματόμετρο βοηθάει στην ταυτοποίηση των μιονίων και τον διαχωρισμό τους από το υπόβαθρο.

Η διασφάλιση της ποιότητας των δεδομένων και της ανακατασκευής των σωματιδίων γίνεται με ένα ειδικό προγραμματιστικό πλαίσιο, η ανάπτυξη του οποίου προήλθε και μέσω της προσωπικής μου συμμετοχής. Ειδικότερα, η συνεισφορά μου συνίσταται στο κομμάτι που αφορά την ανακατασκευή των τροχιών μιονίων και των συντονισμών

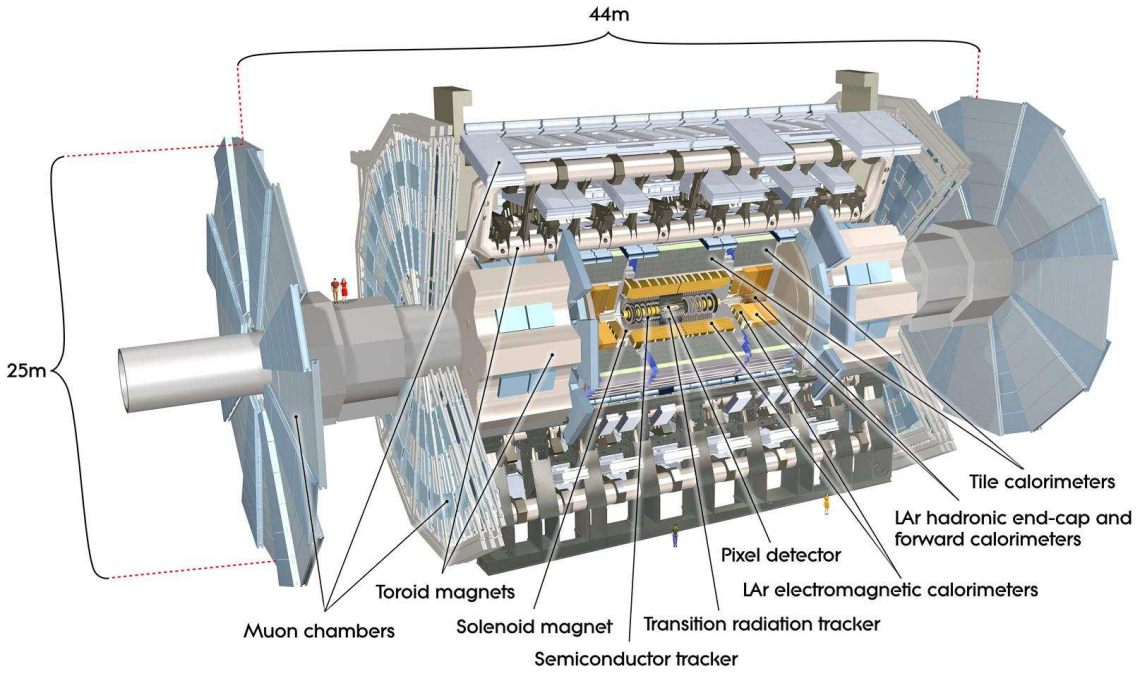

Σχήμα 1: Ο ανιχνευτής ATLAS και τα υποσυστήματα που τον αποτελούν.

που διασπώνται σε δύο μιόνια. Με αυτό το προγραμματιστικό πλαίσιο τα δεδομένα που καταγράφονται από το πείραμα ελέγχονται με έναν αυτοματοποιημένο τρόπο με προκαθορισμένους αλγόριθμους. Η διαδικασία αυτή είναι απαραίτητη ώστε να διασφαλίζεται η καλή λειτουργία του ανιχνευτή και η ικανότητα να εξάγουμε αξιόπιστα αποτελέσματα από τα δεδομένα. Στο σχήμα 2 δίνεται μια όψη του πλαισίου που πραγματοποιεί τους ελέγχους αυτούς και εμφανίζει τα αποτελέσματα για τη λειτουργία των μιονικών ανιχνευτών, των αλγόριθμων ανακατασκευής τροχιών και συντονισμών J/ψ και Z από τις τροχιές αυτές.

Στην συνέχεια, παρουσιάζεται μια ανάλυση των δεδομένων για μελέτες φυσικών διαδικασιών. Σε πρώτο στάδιο χρησιμοποιούνται τα πρώτα δεδομένα που καταγράφηκαν το 2010 και από την ανάλυση ενός δείγματος που αντιστοιχεί σε ολοκληρωμένη φωτεινότητα περίπου 3.4 pb^{-1} παρατηρήθηκε η παραγωγή B^+ μεσονίων (σχήμα 3), επιδεικνύοντας την ικανότητα του ανιχνευτή ATLAS να ανακατασκευάζει διασπάσεις B μεσονίων που περιέχουν J/ψ μεσόνια στην τελική κατάσταση. Με τη βοήθεια μεθόδου προσαρμογής

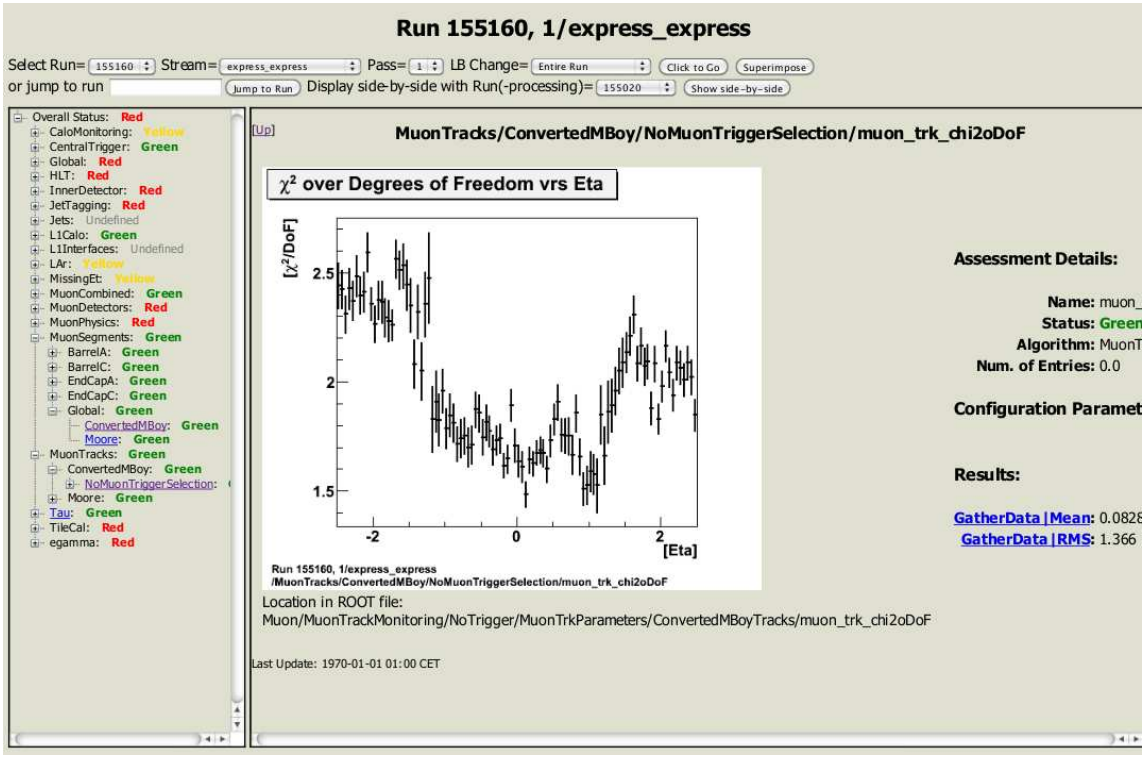

Σχήμα 2: Όψη του πλαισίου εποπτείας της ποιότητας δεδομένων.

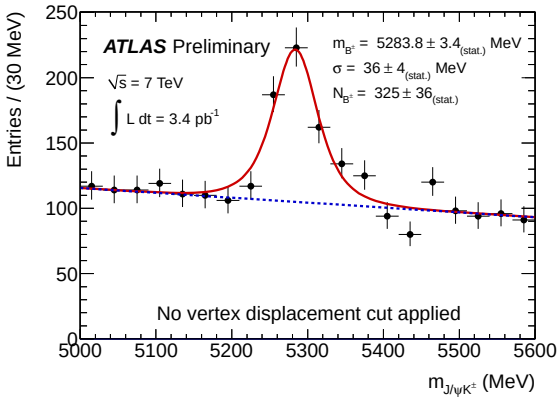

Σχήμα 3: Κατανομή της αναλλοίωτης μάζας του συστήματος J/ψ-K σε δείγμα ολοκληρωμένης φωτεινότητας 3.4 pb^{-1} που συλλέχθηκε κατά τη διάρκεια του 2010. Παρατηρείται καθαρά η ύπαρξη σήματος που ξεχωρίζει από το υπόβαθρο στην περιοχή της μάζας του μεσονίου B^+. Η συνεχής μπλε γραμμή δείχνει το αποτέλεσμα της προσαρμογής στα δεδομένα χρησιμοποιώντας κανονική κατανομή για την περιγραφή του σήματος και γραμμική συνάρτηση για το υπόβαθρο.

των δεδομένων εξάγουμε τις ιδιότητες του σήματος οι οποίες αναγράφονται στο σχήμα. Βρίσκουμε ότι η μάζα των ανακατασκευασμένων γεγονότων σήματος είναι συμβατή με τη γνωστή τιμή από προηγούμενα πειράματα [9] και ότι η διακριτική ικανότητα είναι συμβατή με την αναμενόμενη τιμή της, σύμφωνα με εκτιμήσεις από προσομοίωση. Στο δεδομένο δείγμα (3.4 pb^{-1}) μετρούμε περίπου 325 γεγονότα σήματος [10].

Χρησιμοποιώντας το συνολικό δείγμα δεδομένων που συλλέχθηκε το 2010 που αντιστοιχεί σε ολοκληρωμένη φωτεινότητα περίπου 40 pb^{-1}, μπορούμε να μετρήσουμε όχι μόνο τη μάζα αλλά και τον χρόνο ημίσειας ζωής του μεσονίου B^+. Η μάζα μπορεί να προσδιοριστεί, όπως και στην ανάλυση για την παρατήρηση της παραγωγής του μεσονίου, από την εύρεση της μέσης τιμής της κανονικής κατανομής της αναλλοίωτης μάζας των προϊόντων του σήματος, ενώ ο χρόνος ημίσειας ζωής προσδιορίζεται από την κλίση της εκθετικής κατανομής του χρόνου πτήσης του μεσονίου B^+ από τον πρωτογενή κόμβο αλληλεπίδρασης μέχρι τον κόμβο διάσπασης, ανηγμένο στο σύστημα αναφοράς του μεσονίου (ιδιο-χρόνος ζωής). Η μέθοδος που χρησιμοποιήθηκε προσφέρει ταυτόχρονη μέτρηση της μάζας και του χρόνου ζωής με την προσαρμογή των δεδομένων για την αναλλοίωτη μάζα και τον ιδιο-χρόνο ζωής των υποψήφιων γεγονότων B^+. Αφού επιλέχτηκαν τα κατάλληλα μοντέλα πυκνότητας πιθανότητας για την περιγραφή του σήματος

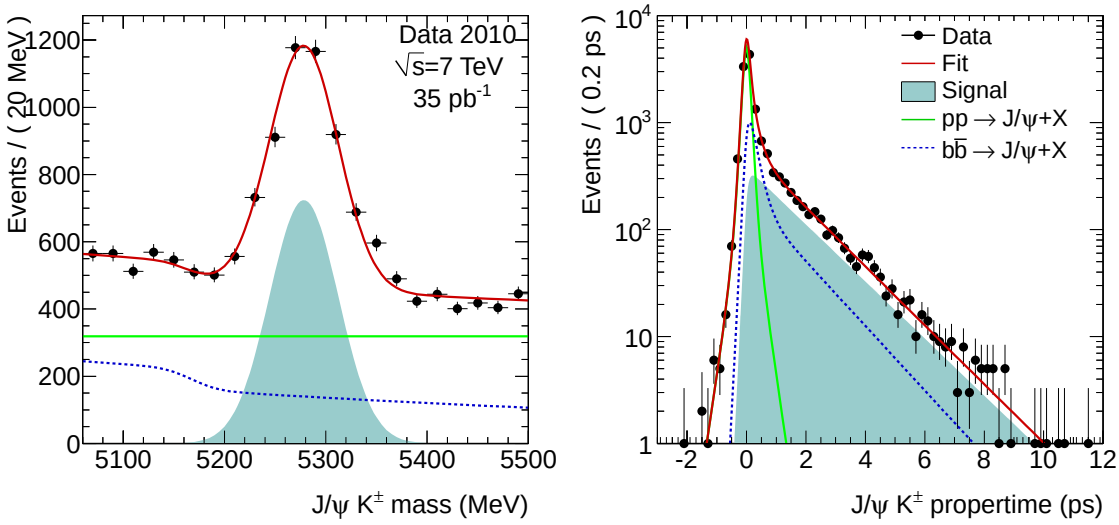

Σχήμα 4: Κατανομές της αναλλοίωτης μάζας (αριστερά) και του ιδιο-χρόνου ζωής (δεξιά) ανακατασκευασμένων B^+ μεσονίων που διασπώνται σε $J/\psi\, K^+$. Η κόκκινη συνεχής γραμμή είναι η προβολή της προσαρμοσμένης συνάρτησης πιθανοφάνειας στις δύο κατανομές. Η συνάρτηση προσαρμογής έχει ξεχωριστές συνιστώσες για την περιγραφή του σήματος και των διαφόρων πηγών υποβάθρου, οι οποίες φαίνονται στο σχήμα. Στο δείγμα που αναλύθηκε και αντιστοιχεί σε 35 pb^{-1} ολοκληρωμένης φωτεινότητας βρέθηκαν περίπου 3080 γεγονότα σήματος με μάζα 5278.4 ± 0.8 GeV και χρόνο ημίσειας ζωής 1.63 ± 0.04 ps.

και του υποβάθρου, η μέθοδος εφαρμόστηκε στα δεδομένα και οι τιμές που προκύπτουν για τη μάζα και τον χρόνο ημίσειας ζωής του B^+ μεσονίου είναι:

$$m_{B^\pm} = 5278.4 \pm 0.8 \text{ MeV} \ , \ \tau_{B^\pm} = 1.63 \pm 0.04 \text{ ps} \ .$$

Οι κατανομές της αναλλοίωτης μάζας και και ιδιο-χρόνου ζωής φαίνονται στο σχήμα 4 μαζί με το αποτελέσμα της προσαρμογής στα δεδομένα. Η μέτρηση αυτή είναι σε πολύ καλή συμφωνία με τις ήδη γνωστές τιμές της μάζας και του χρόνου ζωής [9] και αποτελεί σημαντική επιβεβαίωση της καλής λειτουργίας του εσωτερικού ανιχνευτή και του μιονικού φασματομέτρου αλλά και του λογισμικού ανακατασκευής τροχιών και κόμβων διάσπασης.

Μέτρηση της ενεργού διατομής παραγωγής του μεσονίου B^+

Έχοντας διασφαλίσει τη σωστή απόκριση του ανιχνευτή με τις παραπάνω μελέτες, το επόμενο βήμα είναι η μέτρηση της διαφορικής ενεργού διατομής παραγωγής του μεσονίου B^+, που είναι η ενδιαφέρουσα φυσική ποσότητα που σκοπεύουμε να μετρήσουμε στα πλαίσια αυτής της διατριβής. Για τη μέτρηση αυτή χρησιμοποιήθηκαν τα δεδομένα από τη λειτουργία του LHC το 2011 σε συνθήκες αυξημένης φωτεινότητας που προσέφεραν πολύ μεγαλύτερο δείγμα δεδομένων και μάλιστα σε πολύ μικρότερο χρονικό διάστημα σε σχέση με τη λειτουργία του το 2010. Το δείγμα που χρησιμοποιήθηκε αντιστοιχεί σε ολοκληρωμένη φωτεινότητα 2.4 fb^{-1}. Η διαφορική ενεργός διατομή παραγωγή μετρήθηκε ως συνάρτηση της εγκάρσιας ορμής και της ωκύτητας των μεσονίων B^+ στην ενέργεια κέντρου μάζας 7 TeV. Η σύγκριση των αποτελεσμάτων με θεωρητικές προβλέψεις από υπολογισμούς στα πλαίσια της Κβαντικής Χρωμοδυναμικής είναι χρήσιμη ώστε να αποφανθούμε για την ισχύ των προβλέψεων στην ενέργεια του LHC, ιδιαίτερα μετά από τις πρόσφατες εξελίξεις των θεωρητικών υπολογισμών που οδήγησαν σε καλή συμφωνία με τα δεδομένα από το Tevatron [11]. Επιπλέον, η μέτρηση της παραγωγής των μεσονίων B^+ είναι χρήσιμη, γιατί μπορεί να επιτευχθεί με καλύτερη ακρίβεια από αυτή των θεωρητικών προβλέψεων, οι οποίες έχουν αβεβαιότητα που φτάνει και το 40%. Έτσι, οι συγκρίσεις των μετρήσεων με τις θεωρητικές προβλέψεις είναι σημαντικές για την μελέτη της εξάρτησης των θεωρητικών προβλέψεων από αυθαίρετες παραμέτρους αλλά και για άλλους πειραματικούς σκοπούς. Χάρη στην εξαιρετική γεωμετρική κάλυψη και απόδοση των ανιχνευτών στο LHC, οι μετρήσεις, και συνεπώς ο έλεγχος των προβλέψεων της θεωρίας σε σύγκριση με το πείραμα, μπορούν να πραγματοποιηθούν σε πολύ μεγαλύτερο εύρος εγκάρσιας ορμής και ωκύτητας από ό,τι έχει μελετηθεί στο παρελθόν.

Η διαφορική ενεργός διατομή παραγωγής B^+ μεσονίων σε συγκρούσεις πρωτονίων μετριέται με την σχέση

$$\frac{\mathrm{d}^2\sigma(pp \to B^+X)}{\mathrm{d}p_\mathrm{T}\mathrm{d}y} \cdot \mathscr{B} = \frac{N^{B^+}}{L_\mathrm{int} \cdot \Delta p_\mathrm{T} \cdot \Delta y} \ ,$$

όπου $\mathscr{B}$ είναι η πιθανότητα διάσπασης του B^+ στο συγκεκριμένο κανάλι, που είναι $(6.03 \pm 0.21) \times 10^{-5}$ και προκύπτει από τον συνδυασμό των γνωστών τιμών για την

πιθανότητα διάσπασης του B^+ σε $J/\psi\, K^+$ και του J/ψ σε δύο μιόνια [9], N^{B^+} είναι ο αριθμός των διασπάσεων του σήματος, $L_{\rm int} \equiv \int L\,{\rm d}t$ είναι η ολοκληρωμένη φωτεινότητα που αντιστοιχεί στο δείγμα και $\Delta p_{\rm T}$, Δy είναι τα πλάτη των διαμερίσεων στην κατανομή της εγκάρσιας ορμής ($p_{\rm T}$) και ωκύτητας (y). Υποθέτοντας ότι τα θετικά και τα αρνητικά μεσόνια B παράγονται με ίση πιθανότητα (κάτι που βρέθηκε ότι ισχύει στην κινηματική περιοχή που πρόκειται να μελετήσουμε, σύμφωνα με θεωρητικούς υπολογισμούς αλλά και με μετρήσεις από τα δεδομένα), ο αριθμός των διασπάσεων σήματος N^{B^+} δίνεται από τον ζυγισμένο μέσο όρο των δύο ανακατασκευασμένων φορτισμένων καταστάσεων σε κάθε διαμέριση $(p_{\rm T}, y)$, διορθωμένο για την απόδοση και την γεωμετρική αποδοχή του ανιχνευτή

$$N^{B^+} = \frac{1}{A}\frac{N^{B^+}_{\rm reco}}{\varepsilon^{B^+}} = \frac{1}{A}\frac{N^{B^-}_{\rm reco}}{\varepsilon^{B^-}} = \frac{1}{A}\frac{N^{B^\pm}_{\rm reco}}{\varepsilon^{B^+} + \varepsilon^{B^-}}\ ,$$

όπου $N^{B^\pm}_{\rm reco}$ είναι ο αριθμός των ανακατασκευασμένων διασπάσεων σήματος που μετριέται στα δεδομένα από την αναλλοίωτη μάζα των μεσονίων B (θετικά και αρνητικά φορτισμένων), A είναι η αποδοχή των κινηματικών κριτηρίων επιλογής που εφαρμόζουμε στα μ, K μιας διάσπασης σήματος, και $\varepsilon^{B^{+(-)}}$ είναι όροι που αφορούν την απόδοση του ανιχνευτή και των αλγορίθμων για την ανακατασκευή γεγονότων σήματος. Απαιτούνται διαφορετικοί όροι για θετικά και αρνητικά φορτισμένα B μεσόνια εξαιτίας της διαφορετικής ενεργού διατομής αλληλεπίδρασης θετικά και αρνητικά φορτισμένων K με την ύλη, που οδηγεί σε διαφορετική απόδοση ανακατασκευής. Η μέτρηση του $N^{B^\pm}_{\rm reco}$ γίνεται με μια μέθοδο προσαρμογής στα δεδομένα χρησιμοποιώντας την αναλλοίωτη μάζα των υποψήφιων B^+ γεγονότων για τον διαχωρισμό του σήματος από το υπόβαθρο. Οι όροι $\varepsilon^{B^{+(-)}}$ και A προκύπτουν από προσομοίωση της ανακατασκευής γεγονότων σήματος στον ανιχνευτή. Η προσομοίωση ελέγχεται κατάλληλα ώστε να διαπιστωθεί εάν η μοντελοποίηση των διαφόρων στοιχείων που αφορούν την ανακατασκευή του σήματος ανταποκρίνονται στην πραγματικότητα. Διάφορα επιμέρους στοιχεία που υπεισέρχονται στον όρο απόδοσης εκτιμώνται από τα δεδομένα και έπειτα η προσομοίωση διορθώνεται κατάλληλα ώστε να λαμβάνεται υπόψη η διαφορά ανάμεσα στα δεδομένα και την προσομοίωση, εφόσον υφίσταται τέτοια διαφορά. Κατά τους ελέγχους αυτούς εκτιμάται και το συστηματικό σφάλμα στον προσδιορισμό των όρων απόδοσης και αποδοχής. Συνυπολογίζοντας το στατιστικό σφάλμα και τα συστηματικά σφάλμα της μεθόδου για τον

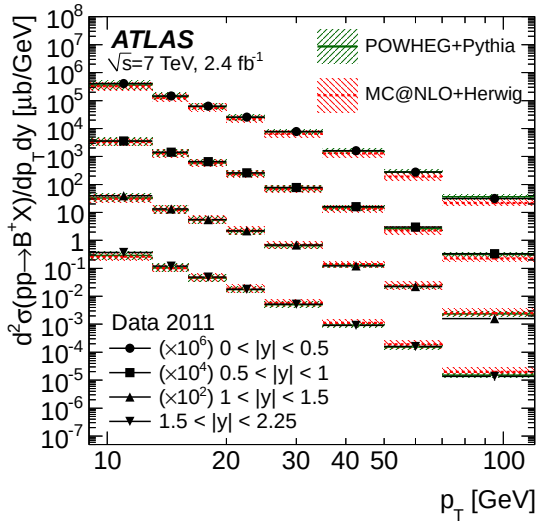

Σχήμα 5: Διαφορική ενεργός διατομή παραγωγής B^+ μεσονίων ως συνάρτηση της εγκάρσιας ορμής και ωκύτητας. Τα σημεία αντιστοιχούν στα δεδομένα και συγκρίνονται με προβλέψεις των θεωρητικών υπολογισμών των πλαισίων POWHEG και MC@NLO. Τα σκιασμένα πλαίσια γύρω από τις θεωρητικές προβλέψεις αντιστοιχούν στην αβεβαιότητα των θεωρητικών υπολογισμών.

προσδιορισμό του αριθμού γεγονότων σήματος, καταλήγουμε ότι η μέτρηση της διαφορικής ενεργου διατομής έχει συνολική αβεβαιότητα της τάξης του 10%.

Τα αποτελέσματα για την ενεργό διατομή παραγωγής μεσονίων B^+ παρουσιάζονται στα παρακάτω σχήματα, όπου και συγκρίνονται με αντίστοιχες θεωρητικές προβλέψεις. Στο σχήμα 5 φαίνεται η ενεργός διατομή παραγωγής ως συνάρτηση της εγκάρσιας ορμής σε τέσσερις περιοχές ωκύτητας. Η μέτρηση συγκρίνεται με προβλέψεις των θεωρητικών υπολογισμών του πλαισίου POWHEG και του πλαισίου MC@NLO. Για ευκολότερη σύγκριση στο σχήμα 6 φαίνεται ο λόγος της μέτρησης ως προς την θεωρητική πρόβλεψη ξεχωριστά για POWHEG και MC@NLO. Τα δεδομένα επιβεβαιώνουν τις προβλέψεις του πλαισίου POWHEG σε όλες τις περιοχές ωκύτητας. Το πλαίσιο MC@NLO προβλέπει χαμηλότερη ενεργό διατομή από αυτή που παρατηρείται στα δεδομένα στις μικρές τιμές εγκάρσιας ορμής. Επιπλέον, προβλέπει ότι η κατανομή της εγκάρσιας ορμής φθίνει γρηγορότερα από ό,τι παρατηρείται στα δεδομένα στην περιοχή κεντρικής ωκύτητας ($|y| < 1$), ενώ στην πρόσθια περιοχή ωκύτητας ($|y| > 1$) παρατηρείται το αντίθετο, δηλαδή η κατανομή της εγκάρσιας ορμής φθίνει πιο αργά από ό,τι παρατηρείται στα

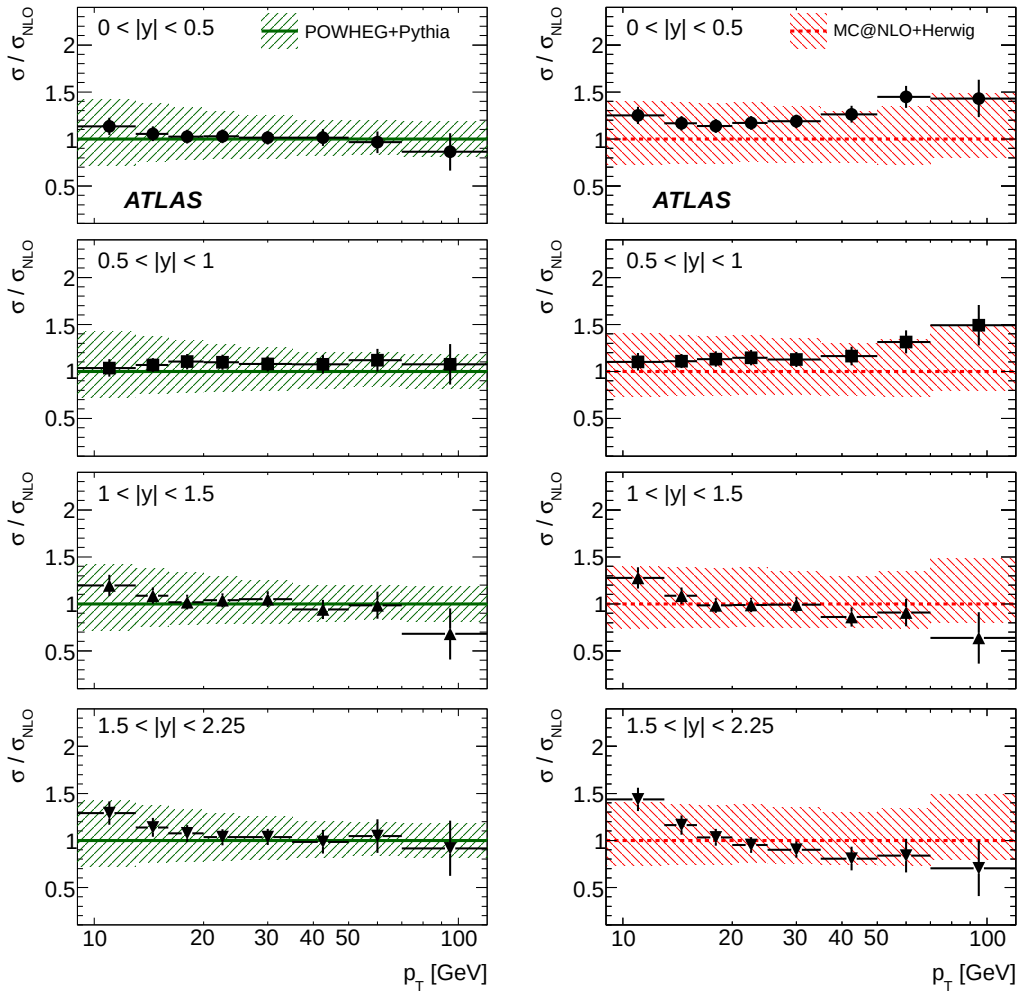

Σχήμα 6: Λόγος της μέτρησης της διαφορικής ενεργού διατομής παραγωγής B^+ μεσονίων ως προς τις προβλέψεις των θεωρητικών υπολογισμών των πλαισίων POWHEG και MC@NLO σε διαμερίσεις εγκάρσιας ορμής σε τέσσερις περιοχές ωκύτητας. Τα σημεία αντιστοιχούν στα δεδομένα και το σφάλμα τους αντιστοιχεί στη συνολική αβεβαιότητα της μέτρησης που προκύπτει από το συνυπολογισμό του στατιστικού και του συστηματικού σφάλματος. Τα σκιασμένα πλαίσια γύρω από τις θεωρητικές προβλέψεις αντιστοιχούν στην αβεβαιότητα των θεωρητικών υπολογισμών.

δεδομένα.

Ολοκληρώνοντας τη μέτρηση αυτή ως προς την εγκάρσια ορμή ή την ωκύτητα εξάγουμε την ενεργό διατομή ως συνάρτηση της ωκύτητας ή της εγκάρσιας ορμής αντίστοιχα. Στο σχήμα 7 φαίνεται η ενεργός διατομή ως συνάρτηση της εγκάρσιας ορμής και συγκρίνεται με τις προβλέψεις από υπολογισμούς της μεθόδου FONLL, όπου διαπιστώνεται καλή συμφωνία. Στο ίδιο σχήμα φαίνεται η αντίστοιχη μέτρηση του πειράματος CMS [12] και διαπιστώνεται ότι η μέτρηση που παρουσιάζεται σε αυτή τη διατριβή εκτείνεται σε μεγαλύτερες τιμές της εγκάρσιας ορμής. Η περιοχή των μεγάλων τιμών της εγκάρσιας ορμής είναι ενδιαφέρουσα για τον έλεγχο των θεωρητικών προβλέψεων. Τέλος, στο σχήμα 8 φαίνεται η ενεργός διατομή ως συνάρτηση της ωκύτητας και συγκρίνεται με τις προβλέψεις όλων των θεωρητικών πλαισίων που προαναφέρθηκαν. Οι θεωρητικές προβλέψεις είναι συμβατές με τη μέτρηση, αν λάβουμε υπόψη την αβεβαιότητα των θεωρητικών προβλέψεων που είναι περίπου 30% και είναι παρόμοια για όλα τα θεωρητικά πλαίσια.

Ολοκληρώνοντας τη μέτρηση σε όλη την κινηματική περιοχή ($9\ \text{GeV} < p_{\text{T}} < 120\ \text{GeV}$ και $|y| < 2.25$), παίρνουμε την τιμή

$$\sigma(pp \to B^+X) = 10.6 \pm 0.3\ (\text{stat.}) \pm 0.7\ (\text{syst.}) \pm 0.2\ (\text{lumi.}) \pm 0.4\ (\mathscr{B})\ \mu\text{b}\ ,$$

όπου το πρώτο σφάλμα είναι στατιστικό, το δεύτερο συστηματικό, το τρίτο είναι από τον προσδιορισμό της ολοκληρωμένης φωτεινότητας και το τελευταίο από την ανεξάρτητη μέτρηση της πιθανότητας του συγκεκριμένου καναλιού διάσπασης [9]. Η πρόβλεψη της μεθόδου FONLL με την αβεβαιότητά της λόγω επιλογής παράγοντα επανακανονικοποίησης και παραγοντοποίησης και της τιμής της μάζας του κουάρκ b είναι

$$\sigma(pp \to bX) \cdot f_{\bar{b}\to B^+} = 8.6^{+3.0}_{-1.9}\ (\text{scale}) \pm 0.6\ (m_b)\ \mu\text{b}\ ,$$

όπου $f_{\bar{b}\to B^+} = (40.1 \pm 0.8)\%$ είναι η γνωστή τιμή για την πιθανότητα αδρονοποίησης [9]. Οι αντίστοιχες προβλέψεις των πλαισίων POWHEG και MC@NLO είναι 9.4 μb και 8.8 μb, αντίστοιχα, με αβεβαιότητες παρόμοιες με αυτές της πρόβλεψης της μεθόδου FONLL.

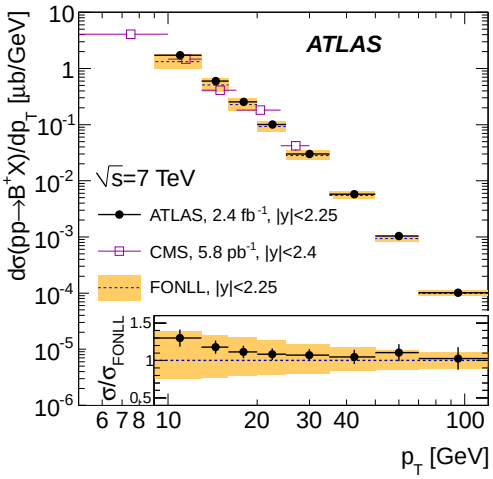

Σχήμα 7: Διαφορική ενεργός διατομή παραγωγής B^+ μεσονίων ως συνάρτηση της εγκάρσιας ορμής. Τα σημεία με σφάλματα αντιστοιχούν στη μέτρηση της ενεργού διατομής με το συνολικό σφάλμα (στατιστικό και συστηματικό) στο εύρος ωκύτητας $|y| < 2.25$. Τα πειραματικά σημεία συγκρίνονται με αποτελέσματα από το πείραμα CMS από μια μέτρηση που καλύπτει το εύρος $p_{\mathrm{T}} < 30$ GeV και $|y| < 2.4$ [12] και με τις προβλέψεις της μεθόδου FONLL [13] μαζί με την αβεβαιότητα των θεωρητικών υπολογισμών, χρησιμοποιώντας τη γνωστή τιμή για την πιθανότητα αδρονοποίησης $f_{\bar{b}\to B^+} = (40.1 \pm 0.8)\%$ [9]. Επιπλέον, στο κάτω μέρος του σχήματος φαίνεται ο λόγος της μέτρησης της ενεργού διατομής ως προς την θεωρητική πρόβλεψη μαζί με τις αβεβαιότητές τους.

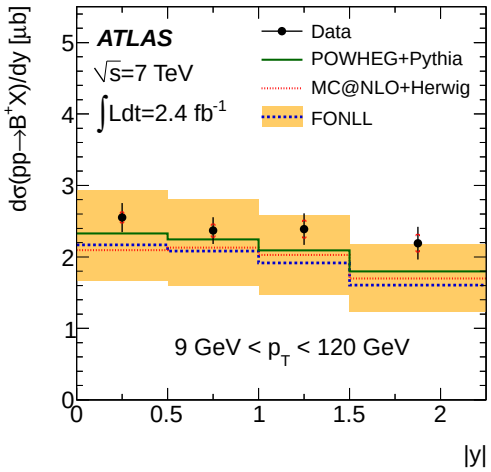

Σχήμα 8: Διαφορική ενεργός διατομή παραγωγής B^+ μεσονίων ως συνάρτηση της ωκύτητας. Τα σημεία με σφάλματα αντιστοιχούν στη μέτρηση της ενεργού διατομής με το συνολικό σφάλμα (οι κόκκινες γραμμές υποδεικνύουν το στατιστικό μέρος του σφάλματος) στο εύρος εγκάρσιας ορμής 9 GeV $< p_{\mathrm{T}} <$ 120 GeV. Προβλέψεις των θεωρητικών πλαισίων POWHEG, MC@NLO και FONLL δίνονται προς σύγκριση. Οι προβλέψεις της μεθόδου FONLL δίνονται μαζί με τα άνω και κάτω όρια αβεβαιότητας, ενώ οι αντίστοιχες προβλέψεις των POWHEG, MC@NLO έχουν παρόμοιες αβεβαιότητες που δεν εμφανίζονται στο σχήμα.

Συμπεράσματα

Στόχος ανάλυσης που προηγήθηκε ήταν η μέτρηση της διαφορικής ενεργού διατομής για την παραγωγή B^+ μεσόνιων ώστε να μελετηθεί η ισχύς των θεωρητικών υπολογισμών της Κβαντικής Χρωμοδυναμικής. Η μέτρηση πραγματοποιήθηκε με δείγμα ολοκληρωμένης φωτεινότητας 2.4 fb^{-1} με δεδομένα από συγκρούσεις πρωτονίων σε ενέργεια 7 TeV στο κέντρο μάζας, τα οποία συλλέχθηκαν το 2011 με τον ανιχνευτή ATLAS στο LHC. Η ενεργός διατομή μετρήθηκε ως συνάρτηση της εγκάρσιας ορμής και της ωκύτητας στο εύρος 9 GeV $< p_{\text{T}} <$ 120 GeV και $|y| < 2.25$ και δίνεται με συνολική αβεβαιότητα 7%–30%, με την κύρια πηγή αβεβαιότητας να είναι συστηματική. Η μέτρηση αυτή εκτείνεται σε σχέση με το αποτέλεσμα από το πείραμα CMS στην ίδια ενέργεια σε υψηλότερες τιμές εγκάρσιας ορμής, η οποία είναι μια ενδιαφέρουσα περιοχή για τις συγκρίσεις με τις θεωρητικές προβλέψεις. Ελέγχθηκαν οι προβλέψεις της μεθόδου FONLL καθώς και άλλων προσεγγίσεων οι οποίες υλοποιούνται στα θεωρητικά πλαίσια Powheg και MC@NLO. Οι θεωρητικοί υπολογισμοί φέρουν αβεβαιότητα από την επιλογή της κλίμακας επανακανονικοποίησης και παραγοντοποίησης, αλλά και της επιλογής της τιμής της μάζας του κουάρκ b, της τάξης του 20%–40%. Μέσα στα όρια αυτής της αβεβαιότητας, οι θεωρητικοί υπολογισμοί είναι σε συμφωνία με τη μέτρηση της ενεργού διατομής αλλά και με την περιγραφή της εξάρτησης από την εγκάρσια ορμή και την ωκύτητα. Για το MC@NLO παρατηρείται μια ιδιαιτερότητα, καθώς η εξάρτηση της ενεργού διατομής από την εγκάρσια ορμή δεν είναι σε καλή συμφωνία με τα δεδομένα όταν συγκρίνεται σε επιμέρους περιοχές κεντρικής ($|y| < 1$) και πρόσθιας ωκύτητας ($|y| > 1$) στο εύρος που καλύπτεται από την παρούσα μέτρηση ($|y| < 2.25$). Σημειώνουμε εδώ ότι η ίδια συμπεριφορά έχει αναφερθεί στη μέτρηση της παραγωγής πιδάκων τροχιών που προέρχονται από κουάρκ b [14] κατά τη σύγκριση των θεωρητικών προβλέψεων με τα δεδομένα σε παρόμοιες περιοχές ωκύτητας. Η μεθόδος FONLL δίνει προβλέψεις για την ενεργό διατομή που είναι σε καλή συμφωνία με τα δεδομένα, υποθέτοντας τη γνωστή τιμή για την πιθανότητα αδρονοποίησης $f_{\bar{b}\to B^+}$, η οποία προέκυψε από ανεξάρτητες πειραματικές μετρήσεις. Εστιάζοντας στην περιοχή μεγάλων τιμών εγκάρσιας ορμής, οι προβλέψεις της FONLL αναμένεται να είναι πιο ακριβείς από εκείνες των άλλων θεωρητικών πλαισιών. Οι προβλέψεις του Powheg, καθώς και εκείνες της FONLL, βρέθηκαν

συμβατές με τη μετρούμενη διαφορική ενεργό διατομής μέχρι περίπου τα 100 GeV. Η προσέγγιση του POWHEG έχει παρόλα αυτά το πλεονέκτημα να παρέχει πλήρη περιγραφή της τελικής κατάστασης και δείχνει να είναι καλύτερη επιλογή γεννήτορα γεγονότων με κουάρκ b.

Τα αποτελέσματα της παρούσας διατριβής για την παραγωγή b αδρονίων, που πραγματοποιήθηκε με την ανακατασκευή του μεσονίου B^+ αποκλειστικά στην διάσπαση σε $J/\psi\, K^+$, μπορεί να συγκριθεί με παρόμοιες μετρήσεις του πειράματος ATLAS. Η παραγωγή b αδρονίων έχει μετρηθεί ανακατασκευάζοντας μερικώς τις διασπάσεις τους σε J/ψ [15], καλύπτοντας ένα ευρύ φάσμα εγκάρσιας ορμής του J/ψ μεσονίου (από περίπου 3 GeV μέχρι περίπου 40 GeV) σε τέσσερις περιοχές ωκύτητας στο εύρος $|y| < 2.4$. Η ίδια μέτρηση έχει γίνει και στο πείραμα CMS σε παρόμοιο εύρος ορμής και ωκύτητας [16], ενώ και στις δύο περιπτώσεις κάποιες μικρές διαφορές έχουν παρατηρηθεί σε υψηλές τιμές ορμής (παρόμοιο σχόλιο γίνεται στην αναφορά [13]). Η παρούσα μέτρηση βοηθά να διευκρινιστεί το ζήτημα αυτό, καθώς εκτείνεται σε μεγαλύτερες τιμές ορμής και δεν παρατηρείται κάποια προφανής απόκλιση. Επίσης, η παραγωγή b αδρονίων έχει μετρηθεί με διασπάσεις σε D^* μεσόνια μαζί με μιόνια στην τελική κατάσταση [17] εξετάζοντας παρόμοια κινηματική περιοχή. Όπως και στο αποτέλεσμα που παρουσιάζεται στην παρούσα διατριβή, οι θεωρητικές προβλέψεις υπολείπονται όσον αφορά την παραγωγή μεσονίων, αν και η παρατηρούμενη διαφορά καλύπτεται από την μεγάλη αβεβαιότητα των θεωρητικών προβλέψεων. Στο ίδιο συμπέρασμα οδηγούν και οι μετρήσεις του πειράματος CMS από μελέτες παραγωγής B μεσονίων σε διάφορα κανάλια διάσπασης ($B^\pm \to J/\psi\, K^\pm$ [12], $B_s^0 \to J/\psi\, K_s^0$ [18], $B_s^0 \to J/\psi\, \phi$ [19], $\Lambda_b^0 \to J/\psi\, \Lambda^0$ [20]). Επιπλέον, με το πείραμα LHCb έχει μετρηθεί η ενεργός διατομή παραγωγής B^+ μεσονίων με τη διάσπαση σε $B^+ \to J/\psi\, K^+$ στην πρόσθια περιοχή ($2 < y < 4.5$) [21], επιδεικνύοντας καλή συμφωνία με τις προβλέψεις της μεθόδου FONLL.

Συνοψίζοντας τα παραπάνω, συμπεραίνουμε ότι υπάρχει καλή κατανόηση της παραγωγής b κουάρκ στο LHC με βάση τις υπάρχουσες θεωρητικές προβλέψεις, ενώ στην παρούσα μελέτη και σε άλλες αντίστοιχες οι μετρήσεις επιτυγχάνουν ακρίβεια καλύτερη από εκείνη των θεωρητικών προβλέψεων. Με αυτό τον τρόπο δίνεται κίνητρο για την πραγματοποίηση θεωρητικών υπολογισμών ανώτερης τάξης που θα δίνουν προβλέψεις με μικρότερη αβεβαιότητα. Επιπλέον, μετά τον έλεγχο των υπολογισμών στα πλαίσια της

Κβαντικής Χρωμοδυναμικής, μπορούμε να εκμεταλλευτούμε τα διαθέσιμα αποτελέσματα και τις μεθόδους που περιγράφηκαν σε αυτή την διατριβή, καθώς και τον πλούτο των διαθέσιμων δεδομένων από την λειτουργία του LHC το 2012 (περίπου 20 fb^{-1} στα 8 TeV) για την εξέταση και άλλων σπανιότερων διαδικασιών στις οποίες η διαδικασία που μελετήθηκε στην παρούσα εργασία χρησιμοποιείται ως σημείο αναφοράς.

Βιβλιογραφία

[1] R. K. Ellis, W. J. Stirling, and B. R. Webber, *QCD and collider physics*. Camb. Monogr. Part. Phys. Nucl. Phys. Cosmol. 8 (1996).

[2] M. Cacciari, M. Greco, and P. Nason, *The p_{T} spectrum in heavy flavor hadroproduction*, JHEP **05** (1998) 007, `arXiv:hep-ph/9803400`.

[3] M. Cacciari, S. Frixione, and P. Nason, *The p_{T} spectrum in heavy flavor photoproduction*, JHEP **03** (2001) 006, `arXiv:hep-ph/0102134`.

[4] P. Nason, *A new method for combining NLO QCD with shower Monte Carlo algorithms*, JHEP **11** (2004) 040, `arXiv:hep-ph/0409146`.

[5] S. Frixione, P. Nason, and G. Ridolfi, *A positive-weight next-to-leading-order Monte Carlo for heavy flavour hadroproduction*, JHEP **09** (2007) 126, `arXiv:0707.3088 [hep-ph]`.

[6] S. Frixione and B. R. Webber, *Matching NLO QCD computations and parton shower simulations*, JHEP **06** (2002) 029, `arXiv:hep-ph/0204244`.

[7] S. Frixione, P. Nason, and B. R. Webber, *Matching NLO QCD and parton showers in heavy flavor production*, JHEP **08** (2003) 007, `arXiv:hep-ph/0305252`.

[8] ATLAS Collaboration, *The ATLAS Experiment at the CERN Large Hadron Collider*, JINST **3** (2008) S08003.

[9] J. Beringer et al., *Review of Particle Physics*, Phys. Rev. **D 86** (2012) 010001.

[10] C. ATLAS, *Observation of the $B^{\pm} \to J/\psi(\mu^{+}\mu^{-})K^{\pm}$ resonance in ATLAS*, Tech. Rep. ATLAS-CONF-2010-098, CERN, Geneva, Sep, 2010.

[11] M. Cacciari, S. Frixione, M. Mangano, P. Nason, and G. Ridolfi, *QCD analysis of first b cross-section data at 1.96 TeV*, JHEP **07** (2004) 033, arXiv:hep-ph/0312132.

[12] CMS Collaboration, *Measurement of the B^+ production cross section in pp collisions at $\sqrt{s} = 7$ TeV*, Phys. Rev. Lett. **106** (2011) 112001, arXiv:1101.0131 [hep-ex].

[13] M. Cacciari, S. Frixione, N. Houdeau, M. L. Mangano, P. Nason, et al., *Theoretical predictions for charm and bottom production at the LHC*, JHEP **10** (2012) 137, arXiv:1205.6344 [hep-ph].

[14] ATLAS Collaboration, *Measurement of the inclusive and dijet cross-sections of b-jets in pp collisions at $\sqrt{s} = 7$ TeV with the ATLAS detector*, Eur. Phys. J. **C 71** (2011) 1846, arXiv:1109.6833 [hep-ex].

[15] ATLAS Collaboration, *Measurement of the differential cross-sections of inclusive, prompt and non-prompt J/ψ production in proton-proton collisions at $\sqrt{s} = 7$ TeV*, Nucl. Phys. **B 850** (2011) 387, arXiv:1104.3038 [hep-ex].

[16] CMS Collaboration, *J/ψ and $\psi(2S)$ production in pp collisions at $\sqrt{s} = 7$ TeV*, JHEP **02** (2012) 011, arXiv:1111.1557 [hep-ex].

[17] ATLAS Collaboration, *Measurement of the b-hadron production cross section using decays to $D^{*+}\mu^- X$ final states in pp collisions at $\sqrt{s} = 7$ TeV with the ATLAS detector*, Nucl. Phys. **B 864** (2012) 341, arXiv:1206.3122 [hep-ex].

[18] CMS Collaboration, *Measurement of the B^0 production cross section in pp collisions at $\sqrt{s} = 7$ TeV*, Phys. Rev. Lett. **106** (2011) 252001, arXiv:1104.2892 [hep-ex].

[19] CMS Collaboration, *Measurement of the strange B meson production cross section with J/ψ ϕ decays in pp collisions at $\sqrt{s} = 7$ TeV*, Phys. Rev. **D 84** (2011) 052008, arXiv:1106.4048 [hep-ex].

[20] CMS Collaboration, *Measurement of the Λ_b cross section and the $\bar{\Lambda}_b$ to Λ_b ratio with $J/\psi\Lambda$ decays in pp collisions at $\sqrt{s} = 7$ TeV*, Phys. Lett. **B 714** (2012) 136, arXiv:1205.0594 [hep-ex].

[21] LHCb Collaboration, R. Aaij et al., *Measurement of the $B^\pm$ production cross-section in pp collisions at $\sqrt{s} = 7$ TeV*, JHEP **04** (2012) 093, arXiv:1202.4812 [hep-ex].

Introduction

The quest for finding out what is the fundamental entity from which our universe is made of is exciting. Democritus first expressed the beautiful idea of entities he called ἄτομα (read atoma, meaning those that cannot be split) that must be the fundamental ingredients from which all matter is made of. It is fascinating that this idea was a result of pure philosophical thought. Centuries later, remarkable discoveries have been made, leading to the identification of the *atom* - as our physics textbooks name it. We found later that what we had named 'atom' has nothing to do with the original idea as it has structure, consists of certain particles (protons, neutrons, electrons) and can be easily decomposed. So scientists kept looking for the truly fundamental, leading to the foundation of particle physics.

Particle physics today, however, has gone much further than just discovering the elementary particles and is closely related to astrophysics. By studying the interactions of the elementary particles an elegant theory has been established, called the Standard Model (SM), with which we have achieved the description of extremely complicated physical phenomena to unprecedented accuracy. Therefore the SM provides a well-tested 'template' for constructing a more universal theory which will answer much more fundamental questions. Such theoretical models, called Grand Unified Theories (GUTs), assume the existence of a fundamental entity, called the *string*, from which all known particles originate. The validity of such models lies beyond any chance of experimental confirmation at the moment. However, one cannot neglect the rich phenomenology accompanying these models: unification of forces, extra dimensions, multiple universes...

The progress in particle accelerators and detection techniques over the past 30

years was of extreme importance to the establishment of the SM. For example, it was the S$p\bar{p}$S at CERN which offered the ground for the discovery of the $W^{\pm}$ and Z bosons and, consequently, for the confirmation of the electroweak unification. Then with LEP collider at CERN and with Tevatron collider at Fermilab, a conclusive picture of the SM has been drawn, but still some important issues remain open. The Large Hadron Collider (LHC) at CERN was built to probe a new energy regime, elucidating the mechanism of spontaneous symmetry breaking by finding the Higgs boson, and put ambitious phenomenological theoretical models to the test. The recent discovery of a Higgs-like particle justified the purpose of building the LHC to the society, but for us, scientists, it is only the beginning of a new era with an endless list of studies that need to be made in order to both measure its properties and probe searches for new physics.

The quest is still on: we need to explore nature and find the truly fundamental constituent from which our universe is made of. Supersymmetry (SUSY), aspects of which are commonly inherited by many GUTs, provides solutions to problematic parts of the SM by predicting a partner particle for each of the known particles of the SM and also more than one Higgs bosons. This has a cosmological impact, as it can introduce candidates for the large amount of dark matter that we observe in the universe. With the LHC we aim at new discoveries that could be matched to predictions of SUSY or, in the absence of new discoveries, we will be able to set stringent limits on the validity of SUSY models. At the same time, we look for hints for extra-dimensions and a variety of exotic signatures beyond the SM.

The research for this thesis was carried out from 2009 to 2013 within the ATLAS experiment, starting at a time of preparations for LHC operations which were resumed in 2010, and was completed by analyzing data recorded in 2011. During the efforts for the commissioning and testing of the muon spectrometer before LHC operations, I contributed to the development of the Data Quality Monitoring Framework for the assessment of the quality of the reconstructed data from the muon spectrometer. The framework was tested with cosmic-ray muons and simulated data and provided useful information during the early LHC operations, when the detector was operating for the first time after the accelerator was turned on. The subject of this thesis was chosen

such in order to both understand the detector performance and exploit the early LHC data for the extraction of physics results which are of interest to the scientific community. The production of $b\bar{b}$ pairs is abundant at the energy of the LHC, offering a good choice for studies with the first data of ATLAS.

The exclusive decay channel $B^+ \rightarrow J/\psi\, K^+$ with $J/\psi \rightarrow \mu^+\mu^-$ was a natural choice for this purpose: it is produced in abundance at the LHC, has a large branching ratio with respect to other B-meson decays, a final state that can be fully reconstructed and offers a clean signature to trigger on, that is the dimuon decay of a J/ψ meson. Via direct reconstruction of this decay channel, I was able to prove the observation of the production of the first heavy flavour events at ATLAS with just 300 nb^{-1} of data and to validate the performance of the muon spectrometer, inner detector and vertexing algorithms by reproducing the well-known properties of $B^{\pm}$ mesons with a measurement of their mass and lifetime. The next item, which is the actual goal on which this thesis concentrates, was the measurement of the differential production cross-section of B^+ mesons in a wide range of p_{T} and y, extending previous measurements to the interesting high-p_{T} region up to about 100 GeV, allowing detailed comparisons with the available theoretical predictions. The understanding of heavy quark production at the new energy regime is of interest to theorists and also a prerequisite to searches for new physics that include b quarks, like $H \rightarrow b\bar{b}$, where it contributes as background. Moreover, the method for the cross-section measurement using this decay channel sets the ground for new interesting B-physics measurements in which $B^+ \rightarrow J/\psi\, K^+$ is used as a reference channel. Such measurements involve the production rate and angular properties of rare muonic and very rare purely muonic B-meson decays, which are interesting because they are means to indirect searches for new physics phenomena.

The structure of this thesis is as follows. In Chapter 1, a short summary of the theoretical background behind heavy flavour production is presented, followed by a discussion on the motivation for such studies at the LHC. Chapter 2 gives the technical design parameters of the LHC and Chapter 3 gives an overview of the ATLAS detector. Then, the reconstruction of the relevant to this analysis physics objects in the ATLAS detector is described in Chapter 4. Chapter 5 introduces the

Data Quality Monitoring Framework which was used during data-taking, focusing on the parts where I have contributed the most, namely the monitoring of single-muon and dimuon off-line reconstruction. Chapter 6 gives the details of data and MC samples used for this analysis. In Chapter 7, the analysis for the $B^{\pm}$ meson using data collected in 2010 is presented. This analysis led to the first observation of $B^{\pm}$ meson production at ATLAS and to a measurement of the $B^{\pm}$ mass and lifetime. Chapter 8 provides the main physics result of this thesis obtained with data recorded in 2011, namely the B^{+} differential production cross-section measurement, and reports the results in comparison with the theory predictions. Chapter 9 discusses the results, comparing them to other experimental measurements and to the theoretical prediction for b-quark production at $\sqrt{s} = 7$ TeV. In addition, conclusions and an outlook for future studies involving the $B^{+} \to J/\psi\, K^{+}$ decay channel are given.

Chapter 1

Theoretical background

This chapter gives a short description of the Standard Model, which is the collection of field theories that describe all of the observed phenomena in particle physics up to date, regarding the electromagnetic, strong and weak interactions. The basics of Quantum Chromodynamics are presented, in order to understand the steps than comprise the production of B mesons, from $b\bar{b}$ production to b-quark fragmentation and hadronization. As the main goal of this thesis is to test experimentally the theoretical calculations of b-hadron production, the formulation of how these calculations are performed is also given. For a more detailed description, the reader may refer to existing literature [1, 2, 3]. Finally, the properties of the $B^{\pm} \to J/\psi\, K^{\pm}$ decay are discussed in order to support the choice of this channel for the study of b-hadron production.

1.1 The Standard Model of Particle Physics

The Standard Model (SM) is a relativistic quantum gauge field theory of fundamental particles and their interactions. It was brought to its current form in the 1960s and has been tested over the years by numerous experiments, so far with great success. According to the SM, matter consists of spin-$\frac{1}{2}$ particles (fermions) organized in three categories (generations) with identical characteristics but increasing mass. For each fermion there is an identical particle (anti-particle) of opposite charge. In

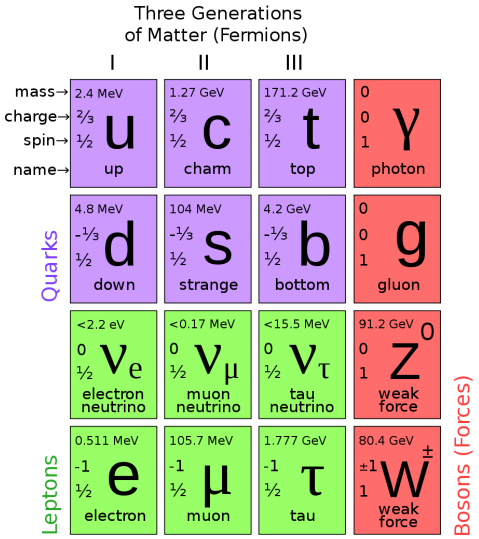

Figure 1.1: The fundamental particles of the Standard Model, organized in three generations of fermions and four force-carrying gauge bosons. For each fermion, an identical particle of opposite charge exists (not shown in the table), named anti-particle.

the SM, electromagnetic, weak and strong interactions are mediated by spin-1 particles (bosons), while a proper description of gravity within the same context is not available yet.

All the particles of the SM shown in Figure 1.1 have been observed, directly or indirectly, including a Higgs boson that was recently discovered by the ATLAS and CMS experiments [4, 5]. This is a scalar, spin-0, particle which appears as a consequence of the Higgs mechanism after the spontaneous electroweak symmetry breaking. Through this mechanism, as a consequence of the interaction with the Higgs field, the vector bosons and the fermions acquire mass.

Although many of the SM predictions have been confirmed with astonishing precision, there are still several open questions that the SM theory does not explain. The SM has 19 free parameters. It does not include gravity, does not explain the different masses of fermions, neither the number of generations nor the origin of the CP violation observed in the universe.

The SM provides a unified approach for the description of electromagnetic, weak

and strong interactions. The interactions arise through the requirement that the theory is invariant under local gauge transformations of the $U(1)_Y \times SU(2)_L \times SU(3)_C$ symmetry group. The indices refer to the conserved quantity in each transformation: weak hypercharge Y, weak isospin L and color C, respectively. The $U(1)_Y \times SU(2)_L$ group describes the electromagnetic and the weak interactions, unified into the *electroweak* interaction, and $SU(3)_C$ describes the strong interaction.

For the $B^{\pm} \rightarrow J/\psi\, K^{\pm}$ decay that is studied in this thesis, all three interactions are relevant. The production of B mesons involves the strong interaction; this thesis concentrates on this part which will be described in more detail in the next sections. Their decay to J/ψ occurs via a $b \rightarrow c$ transition that is mediated by the weak interaction and, finally, the J/ψ meson decay to opposite-charge muons is an electromagnetic process (see Figure 1.2).

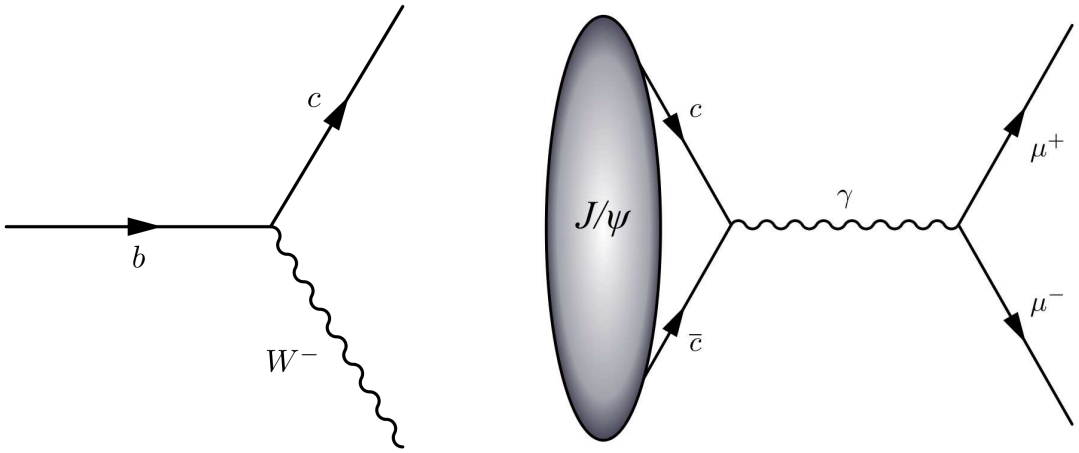

Figure 1.2: *Left:* The $b \rightarrow c$ transition, mediated by a W^- boson. *Right:* The decay of the J/ψ meson ($c\bar{c}$) to muons via a virtual photon.

1.2 Quantum Chromodynamics

Quantum Chromodynamics (QCD) is the $SU(3)_C$ component of the SM that describes the strong interactions of quarks and gluons. In QCD there is an additional quantum number, introduced originally to explain how quarks coexist in hadrons without violating the Pauli exclusion principle. It is named *color charge*, taking three

possible values, "red", "green", "blue", with the red+green+blue combination being "color-neutral". Quarks carry color and anti-quarks carry anti-color, while all hadrons should be color-neutral. Then baryons, which are bound states of three quarks, must consist of a red, a blue and a green quark. Mesons are formed from a quark carrying a color and an anti-quark carrying the same anti-color, so that they are also color-neutral. The gluons, being the generators of the $SU(3)_C$ symmetry group, have eight independent color states that consitute a color octet.

QCD comes with two basic properties, *confinement* and *asymptotic freedom*. Confinement dictates that color states do not exist freely in nature, but only in color-neutral bound states (color singlets). Once a colored final-state particle is produced, like a pair of b quarks ($b\bar{b}$), it undergoes *fragmentation* (see next section) and hadronizes by pulling $q\bar{q}$ pairs from the vacuum to form a color-neutral bound state. Asymptotic freedom deducts from the fact that the strong coupling constant decreases as the interaction distance becomes smaller [6], allowing us to treat partons inside hadrons essentially as free particles.

1.3 b-quark production at colliders

In pp collisions at the LHC, $b\bar{b}$ production can be attributed to three parton-level production subprocesses, shown in Figures 1.3 and 1.4. These are:

- *Flavor creation* (FCR), involving two incoming gluons or quarks which annihilate to produce outgoing heavy quarks.
- *Flavor excitation* (FEX), which involves a b quark from the sea of one proton that is scattered by a parton from the other colliding proton.
- *Gluon splitting* (GSP), involving an outgoing gluon from a $gg \rightarrow gg$ process that splits into a $b\bar{b}$ pair.

FCR is the leading-order (LO) mechanism in α_s (probability $\propto {\alpha_s}^2$). Next-to-leading order (NLO) contributions from these diagrams consider gluon emissions or a self coupling loop. FEX and GSP mechanisms are also considered as NLO diagrams

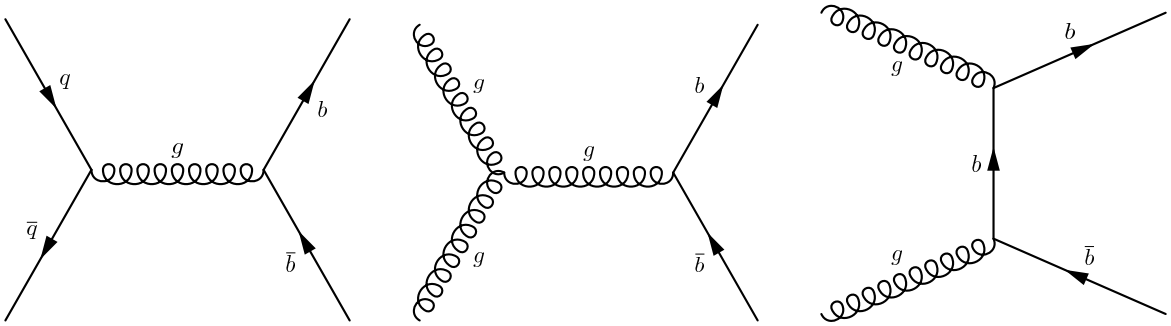

Figure 1.3: Leading-order production mechanism of $b\bar{b}$ pairs (flavor creation).

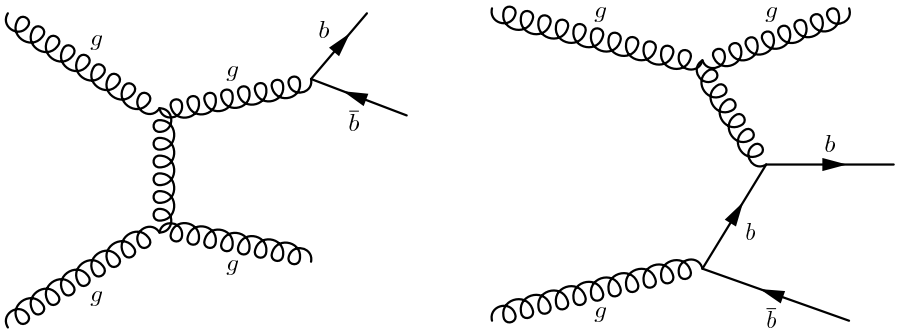

Figure 1.4: Next-to-leading order production mechanisms of $b\bar{b}$ pairs. On the left, heavy quarks are produced by gluon splitting and on the right by flavor excitation.

(probability $\propto {\alpha_s}^3$). Although one expects NLO contributions to be suppressed by a factor of α_s with respect to LO, this is not the case for heavy flavor production at the high energies of the LHC; actually FEX and GSP contribute more than the LO diagrams, as seen in Figure 1.5.[1]

1.4 *b*-quark fragmentation

After a heavy quark is produced, it goes through the *fragmentation process*, which can be factorized in two steps. In the first, produced b and $\bar{b}$ quarks radiate gluons, losing part of their energy. This is a strong process described by QCD and is calculable by theoretical calculations and Monte Carlo techniques implemented in particle gen-

[1]Taking the case of GSP for example, one finds that $gg \to gg$ scattering at the LHC is strongly favored against $gg \to q\bar{q}$ by one-two orders of magnitude. Even though reduced by $\sim \alpha_s$, the contribution of GSP is still larger than that of the LO FCR.

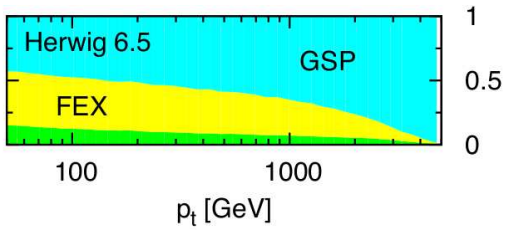

Figure 1.5: Breakdown of the inclusive b-jet spectrum into the three major hard underlying channels contributions: flavor creation (FCR, green), flavor excitation (FEX, yellow) and gluon splitting (GSP, cyan). Figure taken from Ref. [7].

erators. Pertubation theory is applicable because in this high-energy regime, where the energy scale $Q^2 \gg \Lambda_{\mathrm{QCD}}$,[1] the strong coupling constant α_s is small. This part is usually referred to as the *pertubative* fragmentation. As b and $\bar{b}$ quarks draw away from each other, the strong interaction between them gets stronger (the color-force potential increases with distance, $V(r) \propto r$). At some point, the energy of the field becomes sufficient to pull a $q\bar{q}$ pair from the vacuum, and this is repeated until all quarks couple to form color-neutral bound states. Here is where mesons and baryons are formed by pulling one or more lighter quarks from the vacuum, respectively, and the process is referred to as *hadronization*. This part of the quark fragmentation process is non-pertubative and cannot be determined analytically. To draw the line between the pertubative and the non-pertubative parts of the fragmentation an arbitrary parameter is defined, the *factorization* scale. It can be proven that the hadronic cross-sections, when calculated up to all orders, are independent of the choice of this scale. However, the calculations are usually performed up to a finite order and have a dependence on the choice of the factorization scale that becomes less significant when going to higher orders.

[1] Λ_{QCD} is a parameter in QCD used to define the energy scale at which the running strong coupling constant $\alpha_s(Q)$ becomes strong. Its value is about 200 MeV, which corresponds to the typical size of a hadron ($1/200$ MeV$^{-1} \sim 1$ fm) and is a free parameter in the theory, determined from experiments.

1.5 b-hadron production cross-section

The total cross-section for inelastic scattering of two incoming partons can be written as

$$\sigma = \sum_{i,j} \int \mathrm{d}x_1 \, \mathrm{d}x_2 \, f_i(x_1, {\mu_\mathrm{F}}^2) \, f_j(x_2, {\mu_\mathrm{F}}^2) \, \hat{\sigma}_{i,j}(p_1, p_2, \alpha_s(\mu_\mathrm{R}^2), Q^2/\mu_\mathrm{R}, Q^2/\mu_\mathrm{F}), \ . \quad (1.1)$$

In this formula, i, j run for the partons in the colliding hadrons, with x being the proton momentum fraction carried by each parton. With f, we denote the parton distribution functions (PDFs) for each interacting parton inside the proton, defined at a factorization scale μ_F; PDFs incorporate the non-pertubative effects of the fragmentation. With $\hat{\sigma}_{i,j}$, we denote the cross-section of the short-distance interaction, that is the hard process leading to $b\bar{b}$ production ($ij \rightarrow b\bar{b} + X$). Since the strong coupling, α_s, is small at high energies, $\hat{\sigma}$ can be calculated as a pertubation series of α_s, given by

$$\hat{\sigma} = (\alpha_s)^2 \sum_{\nu=0}^{n} C_\nu \cdot (\alpha_s)^\nu \ , \quad (1.2)$$

where C_ν are functions of the kinematic variables and the factorization and renormalization scales; their expression depends on the renormalization scheme [3]. The order of the approximation is $\nu + 2$.

At leading order ($n = 0$), the parton scattering cross-section is calculated exactly as for a QED process. At higher orders, exact calculations are not possible because of singularities introduced by collinear and soft emitted gluons. Instead, the factorization theorem [8] allows the non-pertubative component to be factored out from the integral of Equation (1.1) and be calculated independently of the hard-process cross-section. The factorization theorem is an essential property of QCD allowing singularities to be absorbed into the PDFs, for which phenomenological models and parametrized functions receiving input from experimental data are employed. The calculation of the heavy-quark cross-section then is a matter of determining the cross-section coefficients C_ν for different contributing parton subprocess diagrams up to some order of α_s and convoluting them with the structure functions.

Theoretical calculations for inclusive heavy-quark production at order ${\alpha_s}^2$ have been made more than twenty years ago by Nason, Dawson and Ellis (NDE) [9, 10].

These calculations come with non-negligible renormalization/factorization scale dependence and with limited validity for $p_{\mathrm{T}} \gg m$, where p_{T} and m is the transverse momentum and the mass of the b quark, respectively. The latter originates from the presence of large logarithms of powers of p_{T}/m, accompanying each power of α_s in the pertubative expansion. The leading and next-to-leading logarithms become divergent in the high energy limit and are calculated by a resummation approach. The contribution of these logarithmic terms has been evaluated to next-to-leading logarithmic (NLL) accuracy and is matched[1] to the fixed-order exact NLO calculation; the theoretical framework in which this procedure is performed is referred to as FONLL [11, 12].

In parallel to the above, new theoretical tools have become available, which emerged from the successful matching of NLO QCD calculations with parton shower (PS) Monte Carlo programs, like HERWIG and PYTHIA. The POWHEG [13, 14] and MC@NLO [15,16] frameworks realize the NLO+PS approach and can provide predictions for fully defined exclusive final states, while guaranteeing that inclusive quantities retain full NLO accuracy. Some differences between the FONLL and NLO+PS methods are noted in Ref. [17], according to which the NLO+PS methods should be viewed as approaches that work at small and moderate energies, and that are bound to fail at some large transverse momentum scale. This is because the NLO+PS methods implement the GSP and FEX diagrams only at order of ${\alpha_s}^3$, which is the lowest-order contribution to these processes. At small and moderate p_{T}, the NLO+PS approaches have the same accuracy with FONLL.

Regarding the b-quark fragmentation, a functional form was first given by Kartvelishvili et al. [18], while different parameterizations are also available by Peterson and et al. [19] and Bowler [20]. The parameters for the fragmentation functions are determined best from experimental data from e^+e^- collisions [21] and can be treated as universal, in order to give input for theoretical predictions at hadron colliders. The fragmentation function is convoluted with the predicted cross-section for bare b-quark

[1] *Matching* is a term commonly used to describe the separation of NLO matrix elements according to multiplicity, which is useful in order to avoid double-counting terms which are present both in the FO and the NLL resummed expression.

production in order to obtain the differential cross-section for b-hadron production. The integral of the fragmentation function equals one, so that the overall probability of a b quark to fragment into a hadron is one. The probability of the b quark to pick a specific light quark is referred to as the *fragmentation fraction*; for $\bar{b} \to B^+$, it is $40.1 \pm 0.8\%$ [22]. Therefore, the prediction for the B^+ production is the result of the convolution of the b-quark production cross-section with the fragmentation function, multiplied by the B^+ fragmentation fraction.

The procedure described above is closer to what is performed within FONLL. The Kartvelishvili parametrization is used, with parameters obtained from data containing an admixture of b-hadrons. In the NLO+PS methods, fragmentation is handled by the individual PS MC program and tuned using experimental data. PYTHIA implements the Lund string model [23] with the Bowler modification [24] of the Lund symmetric fragmentation function [25]. HERWIG [26], employed in the MC@NLO package, uses a cluster model [27], instead.

1.6 $B^{\pm} \to J/\psi(\mu^+\mu^-)\, K^{\pm}$ decay

B mesons may deduct from excited states (B^*, B^{**}) that decay fast (through electromagnetic or strong interactions) to ground states. A list of the ground-state B mesons and their properties is given in Table 1.1. Then B mesons decay weakly with the selected decay occurring through a $b \to c$ transition, as shown in Figure 1.6. They are characterized by a long lifetime and high mass and, as a result, the decay vertex is displaced with respect to the vertex of the primary interaction by a measurable distance while the final-state particles are of high momentum. These characteristics make the experimental identification of the B mesons quite easy.

The $B^{\pm} \to J/\psi\, K^{\pm}$ decay channel, chosen to be studied in this thesis, has a rather large branching ratio with respect to other B-meson decays. Considering also the significant branching ratio of $J/\psi \to \mu^+\mu^-$ (OZI suppression, see Chapter 2.5 from Ref. [2]) and the long lifetimes of muons and $K^{\pm}$ mesons, it can be seen that the $B^{\pm} \to J/\psi\, K^{\pm}$ decay has experimental characteristics that make this choice quite reasonable for studies with early data from the LHC.

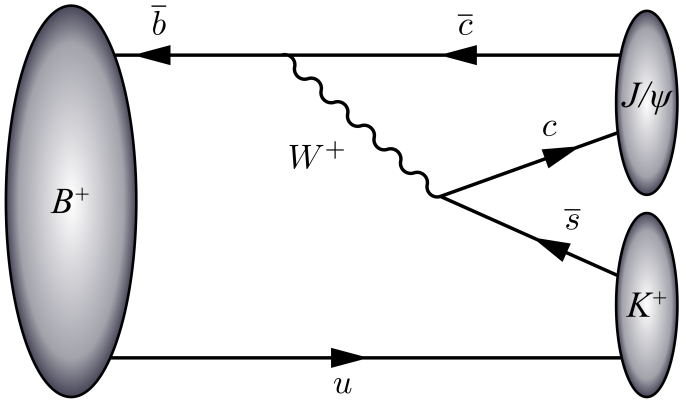

Figure 1.6: Leading-order diagram for the decay of a B^+ meson ($u\bar{b}$) to J/ψ ($c\bar{c}$) and K^+ ($u\bar{s}$).

B meson	Quark content	Mass (MeV)	Mean lifetime (ps)
B^+	bu	5279.26 ± 0.17	1.641 ± 0.008
B_d^0	$\bar{b}d$	5279.58 ± 0.17	1.519 ± 0.007
B_s^0	$\bar{b}s$	5366.77 ± 0.24	1.516 ± 0.011
B_c^+	$\bar{b}c$	6274.5 ± 1.8	0.452 ± 0.033

Table 1.1: List of ground-state B mesons with their measured masses and mean lifetimes, from Particle Data Group [22]. The quoted lifetime for B_s^0 is the average of the lifetimes of the heavy and light eigenstates.

1.7 Motivation for b-hadron production studies at the LHC

As already mentioned in the previous section, the b-hadron production cross-section has been predicted with next-to-leading-order (NLO) accuracy for more than twenty years [9, 10] and more recently it has been predicted with fixed order plus next-to-leading-logarithms (FONLL) calculations [11, 12]. These predictions have been tested at S$p\bar{p}$S collider (CERN) [28, 29] and at the Tevatron collider (Fermilab) [30, 31, 32, 33, 34, 35, 36, 37, 38, 39]. These measurements made a significant contribution to the understanding of heavy-quark production in hadronic collisions [40]. However, the dependence of the theoretical predictions for b-quark production on the factorization and renormalization scales, and the b-quark mass m_b [10], results

in theoretical uncertainties of up to 40%. In addition, measurements of b-hadron production cross-sections are of theoretical interest at higher $\sqrt{s}$ [41] and also for B mesons of higher p_{T} [40], in order to validate the accuracy of the FONLL calculations and the NLO+PS approaches. Therefore, it is important to perform precise measurements of b-hadron production cross-sections at the Large Hadron Collider (LHC) to provide further tests of QCD calculations for heavy-quark production at higher centre-of-mass energies. Thanks to the excellent performance of the LHC detectors and their extended coverage, such tests can be realized in wider transverse momentum and rapidity ranges that what studied previously at Tevatron. Because of the expected large cross-section for b-quark production, such studies are both feasible with the early data from the LHC and a prerequisite to many interesting B-physics studies (namely rare B-meson decays) and new-physics searches where $b\bar{b}$ production is a background.

Bibliography

[1] F. Halzen and D. Martin, *Quarks and Leptons*. Wiley (1984).

[2] D. Griffiths, *Introduction to Elementary Particles*. Wiley VCH (1987).

[3] R. K. Ellis, W. J. Stirling, and B. R. Webber, *QCD and collider physics*. Camb. Monogr. Part. Phys. Nucl. Phys. Cosmol. 8 (1996).

[4] ATLAS Collaboration, *Observation of a new particle in the search for the Standard Model Higgs boson with the ATLAS detector at the LHC*, Phys. Lett. **B 716** (2012) 1–29, `arXiv:1207.7214 [hep-ex]`.

[5] CMS Collaboration, *Observation of a new boson at a mass of 125 GeV with the CMS experiment at the LHC*, Phys.Lett. **B 716** (2012) 30–61, `arXiv:1207.7235 [hep-ex]`.

[6] D. J. Gross and F. Wilczek, *Ultraviolet Behavior of Non-Abelian Gauge Theories*, Phys. Rev. Lett. **30** (1973) 1343–1346. `http://link.aps.org/doi/10.1103/PhysRevLett.30.1343`.

[7] G. Zanderighi, *Accurate predictions for heavy quark jets*, `arXiv:0705.1937 [hep-ph]`.

[8] J. C. Collins, D. E. Soper, and G. F. Sterman, *Factorization of Hard Processes in QCD*, Adv. Ser. Direct. High Energy Phys. **5** (1988) 1–91, arXiv:hep-ph/0409313 [hep-ph].

[9] P. Nason, S. Dawson, and R. K. Ellis, *The total cross-section for the production of heavy quarks in hadronic collisions*, Nucl. Phys. **B 303** (1988) 607.

[10] P. Nason, S. Dawson, and R. K. Ellis, *The one particle inclusive differential cross section for heavy quark production in hadronic collisions*, Nucl. Phys. **B 327** (1989) 49.

[11] M. Cacciari, M. Greco, and P. Nason, *The p_{T} spectrum in heavy flavor hadroproduction*, JHEP **05** (1998) 007, arXiv:hep-ph/9803400.

[12] M. Cacciari, S. Frixione, and P. Nason, *The p_{T} spectrum in heavy flavor photoproduction*, JHEP **03** (2001) 006, arXiv:hep-ph/0102134.

[13] P. Nason, *A new method for combining NLO QCD with shower Monte Carlo algorithms*, JHEP **11** (2004) 040, arXiv:hep-ph/0409146.

[14] S. Frixione, P. Nason, and G. Ridolfi, *A positive-weight next-to-leading-order Monte Carlo for heavy flavour hadroproduction*, JHEP **09** (2007) 126, arXiv:0707.3088 [hep-ph].

[15] S. Frixione and B. R. Webber, *Matching NLO QCD computations and parton shower simulations*, JHEP **06** (2002) 029, arXiv:hep-ph/0204244.

[16] S. Frixione, P. Nason, and B. R. Webber, *Matching NLO QCD and parton showers in heavy flavor production*, JHEP **08** (2003) 007, arXiv:hep-ph/0305252.

[17] M. Cacciari, S. Frixione, N. Houdeau, M. L. Mangano, P. Nason, et al., *Theoretical predictions for charm and bottom production at the LHC*, JHEP **10** (2012) 137, arXiv:1205.6344 [hep-ph].

[18] V. Kartvelishvili, A. Likhoded, and V. Petrov, *On the Fragmentation Functions of Heavy Quarks Into Hadrons*, Phys. Lett. **B 78** (1978) 615.

[19] C. Peterson, D. Schlatter, I. Schmitt, and P. M. Zerwas, *Scaling Violations in Inclusive e+ e- Annihilation Spectra*, Phys. Rev. **D 27** (1983) 105.

[20] M. Bowler, *e^+e^- production of heavy quarks in the string model*, Z. Phys. **C 11** (1981) 169–174. http://dx.doi.org/10.1007/BF01574001.

[21] M. Cacciari, P. Nason, and C. Oleari, *A Study of heavy flavored meson fragmentation functions in e+ e- annihilation*, JHEP **0604** (2006) 006, arXiv:hep-ph/0510032 [hep-ph].

[22] J. Beringer et al., *Review of Particle Physics*, Phys. Rev. **D 86** (2012) 010001.

[23] B. Andersson, G. Gustafson, G. Ingelman, and T. Sjostrand, *Parton fragmentation and string dynamics*, Phys. Rep. **97** (1983) 31.

[24] M. G. Bowler, e^+ e^- *production of heavy quarks in the string model*, Z. Phys. **C 11** (1981) 169.

[25] B. Andersson, G. Gustafson, and B. Soderberg, *A general model for jet fragmentation*, Z. Phys. **C 20** (1983) 317.

[26] G. Corcella, I. Knowles, G. Marchesini, S. Moretti, K. Odagiri, et al., HERWIG *6: An event generator for hadron emission reactions with interfering gluons (including supersymmetric processes)*, JHEP **01** (2001) 010, `arXiv:hep-ph/0011363`.

[27] B. R. Webber, *A QCD model for jet fragmentation including soft gluon interference*, Nucl. Phys. **B 238** (1984) 492.

[28] UA1 Collaboration, C. Albajar et al., *Beauty production at the CERN proton-antiproton collider*, Phys. Lett. **B 186** (1987) 237.

[29] UA1 Collaboration, C. Albajar et al., *Measurement of the bottom quark production cross section in proton-antiproton collisions at* $\sqrt{s} = 0.63$ *TeV*, Phys. Lett. **B 213** (1988) 405.

[30] CDF Collaboration, D. Acosta et al., *Measurement of the ratio of b quark production cross sections in* $\overline{p}p$ *collisions at* $\sqrt{s} = 630$ *GeV and* $\sqrt{s} = 1800$ *GeV*, Phys. Rev. **D 66** (2002) 032002.

[31] CDF Collaboration, F. Abe et al., *Measurement of the bottom quark production cross section using semileptonic decay electrons in* $p\bar{p}$ *collisions at* $\sqrt{s} = 1.8$ *TeV*, Phys. Rev. Lett. **71** (1993) 500.

[32] CDF Collaboration, F. Abe et al., *Measurement of the B meson differential cross section* $d\sigma/dp_{\mathrm{T}}$ *in* $p\bar{p}$ *collisions at* $\sqrt{s} = 1.8$ *TeV*, Phys. Rev. Lett. **75** (1995) 1451.

[33] CDF Collaboration, D. Acosta et al., *Measurement of the* B^+ *total cross section and* B^+ *differential cross section* $d\sigma/dp_{\mathrm{T}}$ *in* $p\bar{p}$ *collisions at* $\sqrt{s} = 1.8$ *TeV*, Phys. Rev. **D 65** (2002) 052005.

[34] D0 Collaboration, S. Abachi et al., *Inclusive* μ *and b-quark production cross sections in* $p\bar{p}$ *collisions at* $\sqrt{s} = 1.8$ *TeV*, Phys. Rev. Lett. **74** (1995) 3548.

[35] D0 Collaboration, B. Abbott et al., *Small angle muon and bottom quark production in $p\bar{p}$ collisions at $\sqrt{s} = 1.8$ TeV*, Phys. Rev. Lett. **84** (2000) 5478, arXiv:hep-ex/9907029.

[36] D0 Collaboration, B. Abbott et al., *Cross section for b jet production in $\bar{p}p$ collisions at $\sqrt{s} = 1.8$ TeV*, Phys. Rev. Lett. **85** (2000) 5068, arXiv:hep-ex/0008021.

[37] CDF Collaboration, D. Acosta et al., *Measurement of the J/ψ meson and b-hadron production cross sections in $p\bar{p}$ collisions at $\sqrt{s} = 1960$ GeV*, Phys. Rev. **D 71** (2005) 032001, arXiv:hep-ex/0412071.

[38] CDF Collaboration, A. Abulencia et al., *Measurement of the B^+ production cross section in $p\bar{p}$ collisions at $\sqrt{s} = 1960$ GeV*, Phys. Rev. **D 75** (2007) 012010.

[39] CDF Collaboration, T. Aaltonen et al., *Measurement of the b-hadron production cross section using decays to $\mu^- D^0 X$ final states in $p\bar{p}$ collisions at $\sqrt{s} = 1.96$ TeV*, Phys. Rev. **D 79** (2009) 092003.

[40] M. Cacciari, S. Frixione, M. Mangano, P. Nason, and G. Ridolfi, *QCD analysis of first b cross-section data at 1.96 TeV*, JHEP **07** (2004) 033, arXiv:hep-ph/0312132.

[41] J. C. Collins and R. K. Ellis, *Heavy-quark production in very high energy hadron collisions*, Nucl. Phys. **B 360** (1991) 3.

Chapter 2

The Large Hadron Collider

The Large Hadron Collider (LHC) [1] is a circular accelerator of ∼27 km circumference, installed in LEP's existing tunnel at CERN in a depth ranging from about 50 to 175 m underground. The LHC is the largest and highest-energy existing particle accelerator, designed to accelerate protons up to 7 TeV with peak luminosity $L = 10^{34}\,\mathrm{cm}^{-2}\mathrm{s}^{-1}$, and also heavy-ions (^{208}Pb) to an energy of about 2.76 TeV per nucleon.

To exploit the full discovery potential of the LHC, four major detectors are installed at different points around the LHC ring and are considered as independent experiments, all run by international collaborations. These are (in alphabetic order):

- ALICE (A Large Ion Collider Experiment), devoted to lead-ion collisions in order to study the properties of quark gluon plasma,
- ATLAS (A Toroidal LHC ApparatuS), a general-purpose experiment, designed for high-p_{T} physics and with the ability to detect whatever may come out of pp collisions at the LHC,
- CMS (Compact Muon Solenoid), a general-purpose experiment much alike to ATLAS,
- LHCb, devoted to b-physics studies, with special focus on CP violation and rare B-meson decays.

In addition to the above, three experiments of significantly smaller scale also exist named TOTEM (TOTal cross-section, Elastic scattering and diffraction dissociation Measurement at the LHC), LHCf (LHC forward) and MOEDAL (MOnopole and Exotics Detector At the LHC), built for different objectives.

The purpose of this Chapter is to give a brief description of the LHC, regarding its operation principles and its technical specifications.

2.1 Proton acceleration

Protons are extracted from a bottle of hydrogen gas and are then accelerated to 90 keV by a radio frequency quadrupole (RFQ2). To reach the energy of 7 TeV, they are going through a complex of different accelerators (see Figure 2.1). Firstly, protons are sent to a linear accelerator, called LINAC2, where they speed up to 50 MeV. Secondly, they are injected to the Proton Synchrotron Booster, which boosts them to 1.4 GeV. The protons are then inserted in another circular accelerator, called Proton Synchrotron (PS), where they reach the energy of 25 GeV. The beam is then sent to the Super Proton Synchrotron (SPS) where it is accelerated up to 450 GeV. In the last stage, protons are fed to the LHC where they reach the energy of 7 TeV after being accelerated for 20 minutes. Specifically, LHC has two storage rings where it accelerates two independent beams, one moving clockwise and one anti-clockwise. Each beam consists of 2808 bunches with $1.15 \cdot 10^{11}$ protons each. The bunches travel at almost the speed of light, with frequency equal to $f = 11.245$ kHz and period $T = 1/f \sim 9 \cdot 10^{-5}$ s. The distance between two consecutive bunches is 7.5 m, so keeping in mind that protons travel at almost the speed of light, one can easily calculate that the collisions will happen every 24.95 ns.

For the acceleration of the protons, the LHC is equipped with 1232 superconducting dipole magnets (see Figure 2.2), 14.3 m each, placed around the ring, providing a magnetic field of 8.33 T. Each magnet has two sets of coils producing opposing fields for the acceleration of two beams of particles of the same charge in opposite directions. Liquid helium is used for cooling of the magnets down to 1.9 K. In addition, there are also 392 quadrupole, 688 sextupole and 168 octupole magnets for focusing

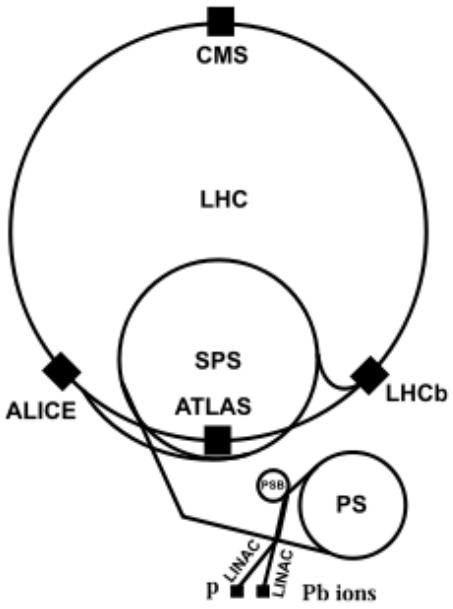

Figure 2.1: The LHC injection complex. The LINAC2, PSB, PS and SPS machines are used as pre-accelerating phases of the two counter rotating proton beams that are finally inserted into the LHC ring.

the beams. The above and also other basic design parameters of the LHC machine are summarized in Table 2.1.

Collisions of the accelerated protons occur at the four interaction regions where the experiments are located. To avoid parasitic collisions inside the common beam pipe, the two beams have been designed to collide with a sufficiently large crossing angle (this affects negatively the peak luminosity). The beams are squeezed as much as possible at the collision point to increase the chances of a collision (see Figure 2.3), while protons that do not interact, continue to circulate around the LHC ring. The number of protons in the bunches decreases with time due to collisions and interactions in the beam pipe. Eventually, after some time, the beams are dumped controllably (unless the beams are lost due to field instabilities that may occur) and a new fill is done.

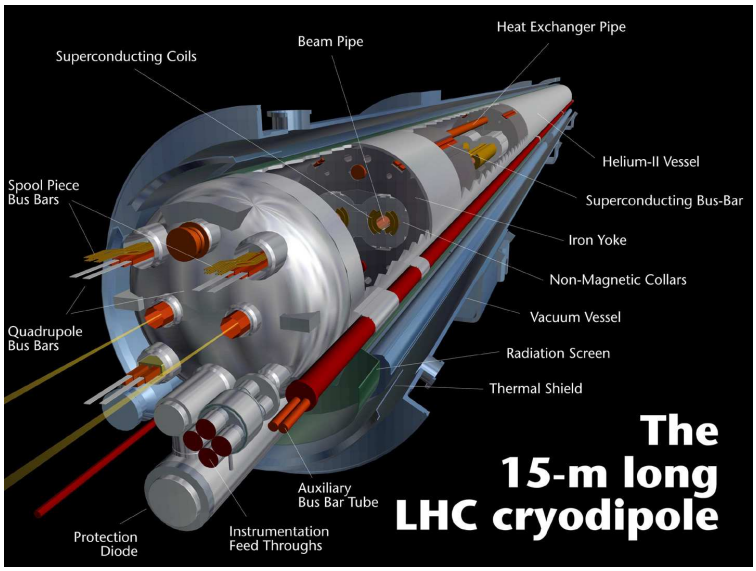

Figure 2.2: Sketch of an LHC dipole.

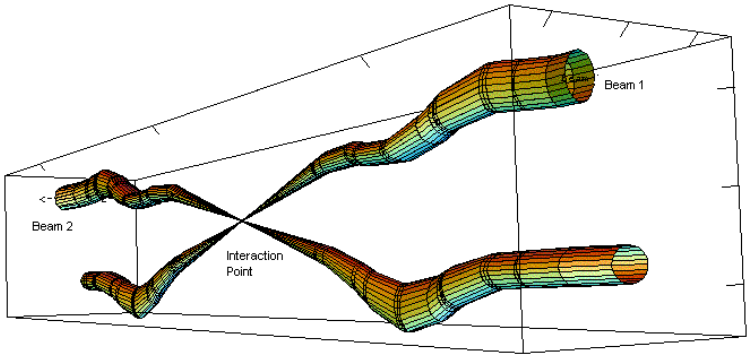

Figure 2.3: Representation of the intersection of beams in ATLAS.

Parameter	**Value**
Proton beam energy	7 TeV
Number of bunches per beam	2808
Number of particles per bunch	$1.15 \cdot 10^{11}$
Circulating beam current	0.584 A
RMS of bunch length	7.55 cm
Peak luminosity	10^{34} cm^{-2} s^{-1}
Collision time interval	24.95 ns
Number of main bends	1232
Field of main bends	8.33 T

Table 2.1: Values of basic design parameter of the LHC machine.

2.2 Beam parameters

The beam size can be expressed in terms of two quantities, the transverse emittance ϵ and the amplitude function β. Emittance is a measure of the parallelism of a beam and has units of length. Low emittance means bigger concentration of particles of nearly the same momentum which results in higher probability of particle interactions. The emittance measured on the plane transverse to the beam is the transverse emittance ϵ_{T}. The emittance is a function of the beam momentum, with higher beam energies leading to lower values of emittance. Because of this, it is usually more convenient to use the normalized emittance, $\epsilon_n = \gamma \cdot \epsilon_{\mathrm{T}}$, with γ being the Lorentz factor, which is constant under acceleration. The normalized emittance is useful because it can be used in the comparison of the beam properties in the various parts of the accelerator complex.

The amplitude function β is determined by the accelerator magnet configuration and relates to the focusing of the beam. It can be expressed in terms of the cross-sectional size of the bunch ($\Sigma^2 = \Sigma_x \cdot \Sigma_y$) and ϵ_n:

$$\beta = \frac{\pi \cdot \Sigma^2}{\epsilon_n} \ . \tag{2.1}$$

From the above equation it is clear that β has units of length and is proportional to the beam size *Sigma*. A useful quantity is β^*, which is the distance from the interaction point at which the beam size becomes double. The design values for the

β^* quantity and the normalized transverse emittance are:

$$\beta^* = 0.55 \text{ m} \quad , \quad \epsilon_n = 3.75 \text{ } \mu\text{m} \ .$$

2.3 Luminosity determination

Apart from the center-of-mass energy, another important parameter of a collider is the instantaneous luminosity, L. It is defined from beam parameters and its importance in physics analysis is that it relates the event or collision rate R to the cross-section σ of the process:

$$R = L \cdot \sigma \ . \tag{2.2}$$

Given a process with known cross-section, one can estimate the event rate for this process with this formula (or measure the cross-section from the observed event rate).

To estimate the instantaneous luminosity of the LHC [2], inelastic pp collisions can be used, so that the luminosity will be given by

$$L = \frac{R_{\text{inel}}}{\sigma_{\text{inel}}} = \frac{\mu \, n_b f_r}{\sigma_{\text{inel}}} \ , \tag{2.3}$$

where μ is the average number of inelastic interactions per bunch crossing, n_b is the number of bunches per beam and f_r is the revolution frequency. However, the inelastic pp cross-section, σ_{inel}, needs to be measured at the energy of the LHC, so an alternative method is used for the determination of the absolute instantaneous luminosity directly from the machine parameters:

$$L = \frac{n_b \, f_r \, n_1 \, n_2}{2\pi \Sigma_x \, \Sigma_y} \tag{2.4}$$

where n_1, n_2 are the numbers of particles in each of the two colliding bunches and Σ_x, Σ_y characterize the widths of the horizontal and vertical beam profiles. Typically, the Σ_x, Σ_y profiles are measured with *van der Meer* scans, also called just luminosity scans. The scans are performed by moving the beams across each other in steps of known distance first in the horizontal (x) and then in the vertical (y) direction. The relative interaction rates are measured as a function of the beam separation distance

in each direction. The resulting distributions are gaussian with the maximum rate at zero separation and are fitted to extracts the values of Σ_x and Σ_y.

Luminosity scans are carried out relatively infrequently, as their purpose is to calibrate the results of event-counting techniques which determine the luminosity using

$$L = \frac{\mu_{\text{obs}}\, n_b f_r}{\sigma_{\text{obs}}} \ , \tag{2.5}$$

where $\mu_{\text{obs}}\,(= \varepsilon \cdot \mu)$ is the average number of *observed* inelastic interactions per bunch crossing in the luminosity detectors, obtained after applying corrections of including detector efficiency and acceptance (ε) , and $\sigma_{\text{obs}}\,(= \varepsilon \cdot \sigma_{\text{inel}})$ is the corresponding cross-section. Therefore, with the luminosity scans σ_{obs} is determined without relying on explicit measurements of σ_{inel}. Then different methods which provide μ_{obs} from raw event counts are used to measure the absolute luminosity either in real time, providing feedback for the tuning of the accelerator, or off-line, with more precise calibration and careful evaluation of results.

Bibliography

[1] O. S. Brüning, P. Collier, P. Lebrun, S. Myers, R. Ostojic, J. Poole, and P. Proudlock, *LHC Design Report*. CERN-2004-003-V-1.

[2] ATLAS Collaboration, *Improved luminosity determination in pp collisions at $\sqrt{s} = 7$ TeV using the ATLAS detector at the LHC*, `arXiv:1302.4393 [hep-ex]`.

Chapter 3

The ATLAS detector

The ATLAS experiment [1] uses a general purpose detector consisting of an inner tracker, a calorimeter and a muon spectrometer. The inner detector (ID) directly surrounds the interaction point and is embedded in an axial 2 T magnetic field. The ID is enclosed by a calorimeter system (CS) containing electromagnetic and hadronic sections. The CS is surrounded by a large muon spectrometer (MS) inside an air-core toroidal magnet system. An overview of the ATLAS detector including all subsystems can be seen in Figure 3.1. In the next sections details are given for the various subsystems.

3.1 Coordinate system

ATLAS uses a right-handed coordinate system (x, y, z) with its origin at the center of the detector (nominal interaction point). The z-axis is along the beam pipe, the x-axis points to the centre of the LHC ring and the y-axis points upward. In the transverse plane, x-y, ϕ ($\in [-\pi, \pi]$) is the azimuthal angle around the beam pipe. In polar coordinates, θ ($\in [0, \pi]$) is the polar angle from the z-axis.

Quantities like momentum p and energy E are usually given in the transverse plane, where in this case the transverse components of these two quantities are defined as:

$$p_{\mathrm{T}} = p \cdot \sin\theta, \;\; E_{\mathrm{T}} = E \cdot \sin\theta \; . \tag{3.1}$$

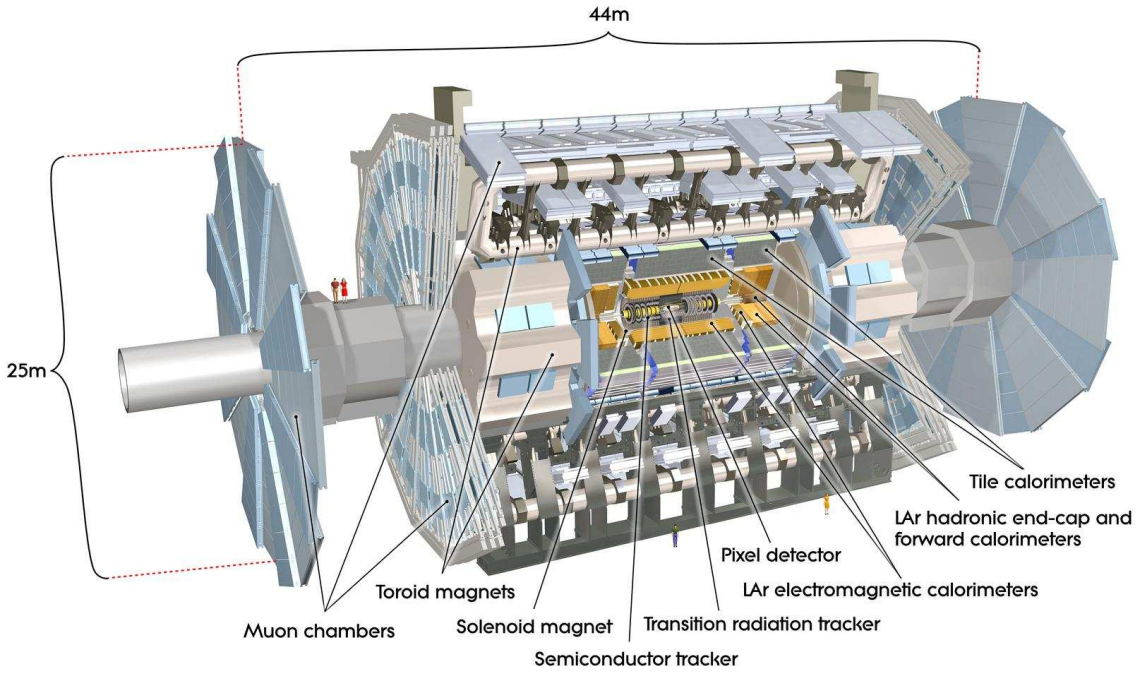

Figure 3.1: The ATLAS detector and subsystems.

Another important quantity that is widely used in particle physics experiments is the rapidity (noted with y from now on, but not to be confused with y coordinate) which is defined by

$$y = \frac{1}{2} \ln \frac{E + p_z}{E - p_z} \tag{3.2}$$

where p_z is the z-component of the momentum of a particle of energy E. Rapidity is a Lorentz-invariant quantity, and for particles travelling at energies much larger than their mass, it can be written as a function of θ, defining pseudorapidity:

$$\eta \equiv -\ln \left(\tan \frac{\theta}{2} \right) \ . \tag{3.3}$$

Pseudorapidity is also useful, especially when the exact mass and momentum of the particle is not known. Lastly, we define the distance between the direction of two particles in the η and ϕ plane as

$$\Delta R = \sqrt{(\Delta\eta)^2 + (\Delta\phi)^2} \ , \tag{3.4}$$

where $\Delta\eta = |\eta_1 - \eta_2|$ and $\Delta\phi = |\phi_1 - \phi_2| - \kappa \cdot 2\pi$, with $\kappa = +1$ if $|\phi_1 - \phi_2| > \pi$ and $\kappa = 0$ otherwise.

3.2 Magnet system

The purpose for the Magnet System is to bend the trajectories of charged particles and allow independent momentum measurements in the ID and the MS sub-detectors. The Magnet System in ATLAS is built using superconducting magnets cooled by liquid helium at 4.8 K. A solenoid magnet (see Figure 3.2) surrounds the ID and

Figure 3.2: The ATLAS solenoid providing the magnet field in the ID.

provides it with an axial field of 2 T at the center and 0.5 T at the edges, parallel to the beam axis. It has been optimized to minimize the thickness of the material in front of the electromagnetic calorimeter and has a contribution of 0.66 radiation lengths. For this purpose, the solenoid windings and the LAr calorimeter share the same cryogenic system. The solenoid is a single layer coil wounded on the inside of a cylinder with an inner radius of 1.23 m and outer radius of 1.28 m, with a 5.8 m length. The flux of the magnetic field is returned via the steel of the hadronic calorimeter. A magnet system of three toroids provides the magnetic field for the MS. The barrel toroid consists of eight superconducting coils circularly positioned

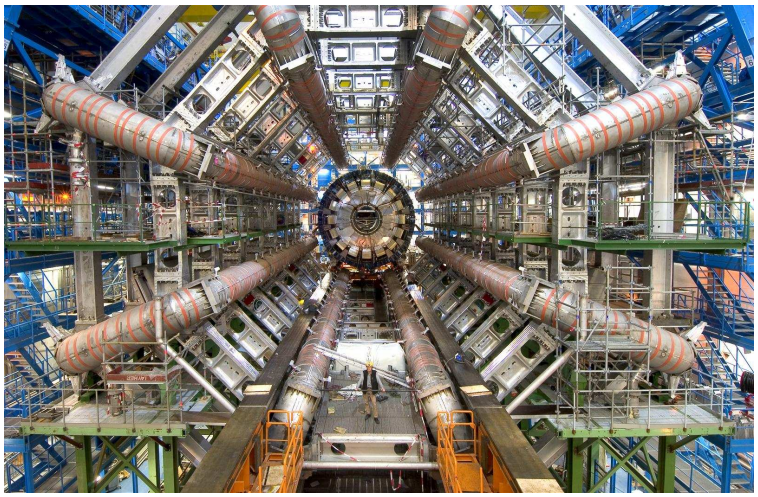

Figure 3.3: The ATLAS barrel toroid, comprising eight coils which provide the magnet field in the MS.

around the beam axis (see Figure 3.3), while in the end-cap regions two extra toroids (one in each end-cap) have been employed (see Figure 3.4). The magnetic field lines follow the azimuthal direction and are perpendicular to the solenoidal field lines. The size of the magnet system in the barrel region is 25.3 m in length, with inner and outer diameters of 9.4 m and 20.1 m respectively. The resulting strength of the magnetic field is 0.5 T in the central region and 1 T in the end-caps.

3.3 Inner detector

The Inner Detector is the innermost part of the ATLAS detector. It is contained inside a 7 m long envelope with radius of 1.15 m and the whole system is immersed inside the 2 T magnetic field formed by the central solenoid, described in the previous section. It is divided in three subsystems which, in order of radial distance from the collision point, are: the Pixel Detector, the Semiconductor Tracker (SCT) and the Transition Radiation Tracker (TRT). These three, although technically independent, act complementary to fulfill the basic experimental duties carried out by the ID, which are track reconstruction and vertexing. A schematic representation of the ID and its three sub-systems is shown in Figure 3.5. The ID is installed at the closest

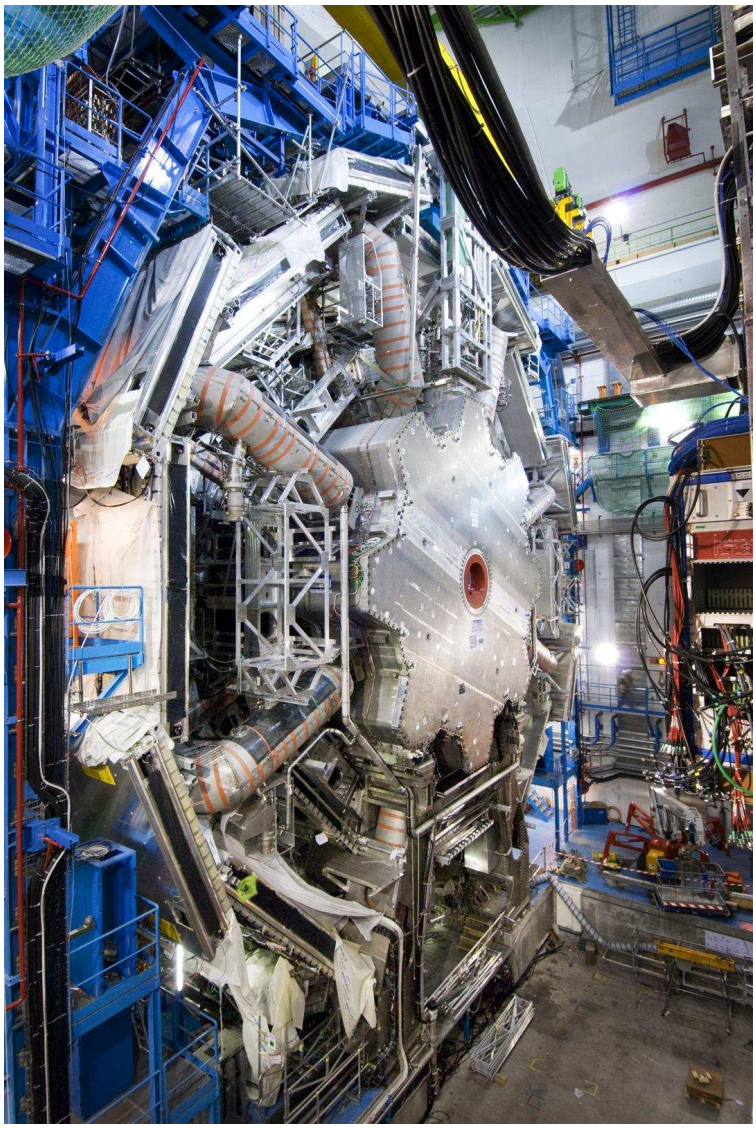

Figure 3.4: One of the two ATLAS end-cap toroids in its position fitting between the barrel toroid coils.

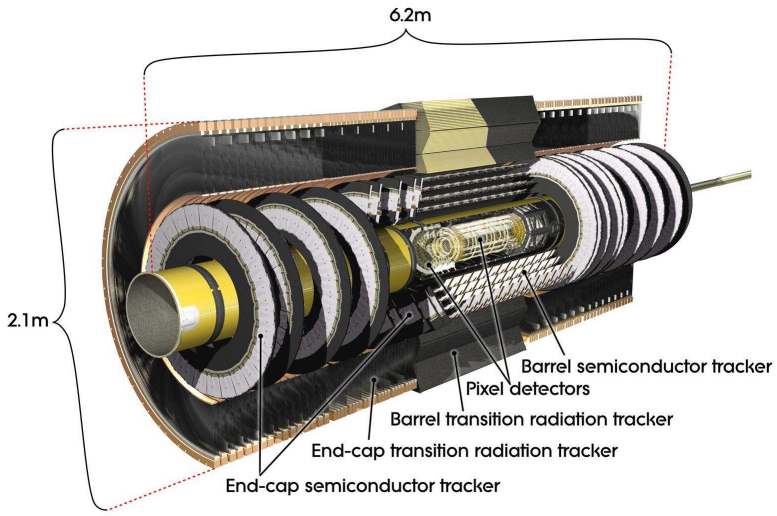

Figure 3.5: View of the Inner Detector of ATLAS.

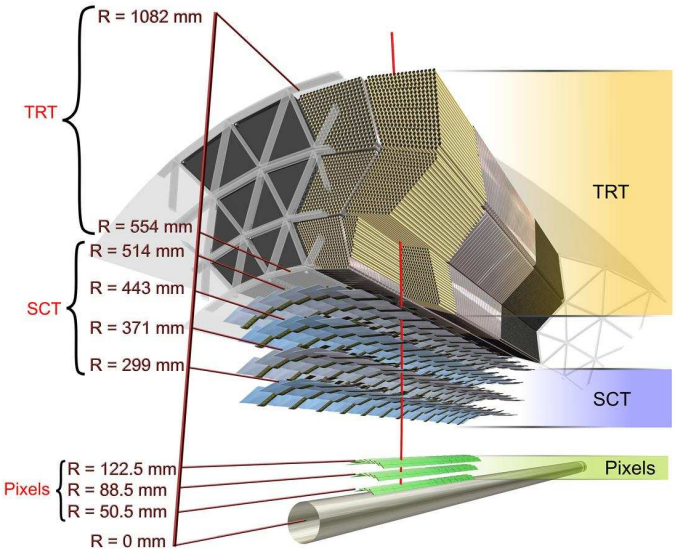

Figure 3.6: The Inner Detector comprises three subsystems. The innermost system is the Pixel Detector while the middle is the SemiConductor Tracker. Both use silicon as the detecting technology. The outermost part is the Transition Radiation Tracker which uses the straw tube technology.

distance from the interaction point, where about 1000 particles emerge every 25 ns (for the design bunch spacing). For this reason, radiation tolerance of the detecting elements was considered carefully during the design. Moreover, it is important to maintain efficient pattern recognition and high resolution of momentum and vertex measurements. Therefore, after about three years of operation (2010–2013), the first layer of the Pixel Detector from the interaction point (B-layer) is going to be replaced because of radiation damage, whereas the other parts and the SCT and TRT are expected to withstand large particle fluxes for over ten years at nominal luminosity. Regarding performance, the ID has very fine granularity to reduce occupancy levels and high efficiency in track reconstruction. Precision measurements are achieved by combining the three systems; the Pixel Detector and the SCT provide few space point measurements but with high precision and at the same time TRT improves pattern recognition and momentum resolution by contributing 36 hits per track on average. A more detailed description of the ID subsystems follows.

Pixel Detector

The operation principle of the Pixel Detector is based on a modular unit of detector substrates and integrated read-out electronics. The active material is silicon arranged into rectangles (pixels) of size 50×400 μm^2 and thickness 250 μm. There are three layers of such units in the barrel region at radial distances from the interaction point of 5.05 cm, 8.85 cm and 12.25 cm while in the end-caps the pixel units are arranged on three disks on each side at distances of 49.5 cm, 58.0 cm and 65.0 cm. The overall rapidity coverage of the pixel detector is $|\eta| < 2.5$. The B-layer, located closer to the collision point than any other detector element, guarantees optimal impact parameter resolution and, accompanied with the other two layers of pixels, provides high precision space-point measurements of intrinsic accuracy 10 μm in R-ϕ and 115 μm in the z direction and also the ability to reconstruct tracks of short lived particles and their corresponding vertex. The accuracy is similar in the end-cap region where the pixel disks are present. In total, the Pixel Detector has 80.4 million read-out channels.

Semiconductor Tracker

The SCT is the intermediate subsystem of the ID and its basic building block is a module consisting of two layers of silicon micro-strip wafers glued back to back and a hybrid system containing the read-out electronics. In the barrel there are four layers of such modules giving four precise space-point measurements located at radii of 30, 37, 45 and 52 cm, while at the end-caps modules are arranged perpendicularly to the beam axis on 9 disks on each side, extending from 85.4 cm to 272.0 cm in z axis and with an outer radius of 56 cm. In total there are 2112 modules in the barrel and 1976 modules in the end-caps. Instead of pixels, the SCT uses silicon strip technology with a strip pitch of 80 μm and each layer consists of 768 strips. The two layers of silicon wafers are rotated by 40 mrad stereo angle with respect to each other to allow for second coordinate measurement. The resolution in the R-ϕ plane is 22 μm and in the z coordinate is 580 μm.

The particle detection principle for the SCT (as well as for the Pixel Detector) is based on the ionization caused by charged particles when they traverse the silicon bulk. Ionisation produces electrons and holes (positive-charge ions) which drift in opposite directions under the influence of the electric field created by a potential difference applied to the two sides of silicon wafer. Charges are collected at each end of the detector and after the signal is amplified, is read out through the electronics. In order to reduce noise from leakage currents emerging in silicon's bulk because of thermal excitation and radiation damage of the detector, the SCT operates at a temperature of -7 °C.

Transition Radiation Tracker

TRT is the subsystem of the ID which is further away from the interaction point and uses different technology than the other two ID subsystems. It extends radially from 56 cm to 107 cm and is capable of providing on average 36 measurements per track with intrinsic accuracy of 130 μm. It uses straws of only 4 mm in diameter and 144 cm length that are filled with a gas mixture of 70% Xe, 20% CO_2 and 10% CF_4 and have a sense wire in the centre of 30 μm diameter.

The operation principle of the TRT is based on the ionization of the gas by the passage of a charged particle. The drift time of electrons, produced at the ionization and collected at the wire, provides discrimination between tracking hits and hits from transition radiation, which is the radiation emitted by charged particles in the X-ray range when they traverse the boundary between two substances with different dielectric properties. This is used to enhance the identification of electrons and their discrimination against pions, while the intensity of the transition radiation depends on the energy of the particle.

3.4 Calorimeters

The ATLAS Calorimetric System (CS) is located between the ID and the MS and is divided into electromagnetic, hadronic and forward calorimeter parts. The electromagnetic calorimeter covers the range $|\eta| \leq 3.2$ and the hadronic calorimeter, including the forward calorimeter, extends up to $|\eta| \leq 4.9$. The different parts and technologies of the CS are described briefly in the following sections and a schematic view is given in Figure 3.7. The CS is designed to satisfy multiple objectives. It is

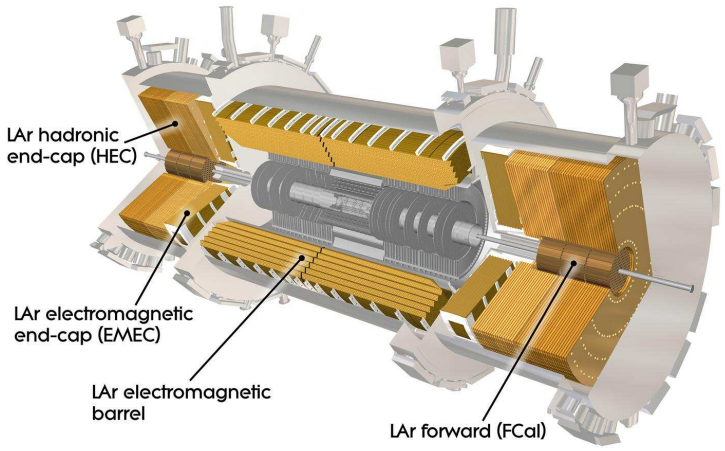

Figure 3.7: View of the Calorimetric System of ATLAS.

responsible for

- precise measurements of the energy of electrons, photons and jets,
- the determination of the missing transverse energy, which requires both excellent energy measurement resolution and hermeticity,
- the identification of particles (electrons and photons, mainly) from the shower shape of particles and the longitudinal energy leakage, and
- the determination of the spatial isolation of particles, extremely valuable to suppression of the background in various searches for rare processes.

The CS is also important for muons. It can provide muon identification independently of the MS which can be used to study the performance of the MS. Moreover, it limits the amount of particles that escape to the MS to a minimum, realized by the thickness of the calorimeter which corresponds to more than 22 radiation lengths[1] (X_0) in the barrel region and more than 24 X_0 in the end-caps. At the same time, the amount of the material in the CS is crucial for the reconstruction of muons, as they lose energy and also undergo multiple scattering while traversing the calorimeters. The loss of energy in the CS sets a threshold on the lowest amount of energy that a muon can have in order to reach the MS, while multiple scattering degrades the momentum resolution, especially for low-energy muons.

Electromagnetic Calorimeter

The ATLAS electromagnetic calorimeter (LArEM) is detector using liquid argon as active material and steel-coated lead as absorber. It is characterized by the accordion-shaped structure of its detection elements, chosen to provide uniformity of the detector in ϕ. When electrons or photons enter the LArEM, they initiate cascades of electrons and photons from successive bremsstrahlung irradiation and electron-positron pair creation. In the end, the largest fraction of the initial energy of

[1]The radiation length of a material is defined as the mean distance in which the energy of a traversing electron is reduced by a factor of 1/e.

the electron/photon is absorbed by the material. The choice of liquid argon is justified by its radiation hardness and its fast and linear response. The LArEM consists of the barrel part, covering $|\eta| < 1.4575$, and two end-cap parts covering $1.375 < |\eta| < 3.2$. In the range $|\eta| < 2.5$, in which the LArEM and the ID overlap, the LArEM has three compartments (front, middle and back), each of them segmented in cells of different sizes. The cell granularity is finer at the front compartment, allowing precision position measurements along the η coordinate, and coarser at the back compartment. In the end-caps, the granularity varies with η. An additional active layer of liquid argon is placed before the front compartment (presampler), useful to corrections of the energy losses of incident particles due to the detector material before the calorimeter.

Hadronic Calorimeter

The ATLAS hadronic calorimeter, similarly to all the other subdetectors, is divided into one barrel and two end-cap sections. Like the LArEM, it is segmented in three compartments with varying cell granularity. The barrel part ($|\eta| < 1.7$) is the Tile Hadronic Calorimeter (TileCal), using tiles of plastic scintillator as active material embedded in iron absorbers. For the hadronic end-cap calorimeter (HEC) ($1.5 < |\eta| < 3.2$), the use of liquid-argon technology is imperative due to the high radiation levels, and the absorbing material is copper.

Forward Calorimeter

The ATLAS Forward Calorimeter (FCAL) occupies the pseudo-rapidity range $3.1 < |\eta| < 4.9$, employing liquid-argon technology. Its coverage is well outside the acceptance of both the ID and MS, and thus cannot be used for precision measurements related to reconstructed tracks of charged particles. However, FCAL is as important as the rest of the CS system because it provides hermeticity in calorimetry thus reliable measurement of the missing energy in each event and also jet energy measurements in the very forward region.

3.5 Muon spectrometer

The muon spectrometer of ATLAS has been designed to provide identification and momentum measurement of muons in the range $|\eta| < 2.7$ with full azimuthal coverage and trigger in the range $|\eta| < 2.4$. This can be done for muons of momenta of a few GeV up to momenta of the TeV scale and independently of the ID, providing thus the so-called *stand-alone* momentum measurement. For stand-alone reconstruction, the resolution is ∼3% for muons with $p_{\mathrm{T}} = 50$ GeV and around 10% for muons with $p_{\mathrm{T}} = 1$ TeV. The MS can also operate combined with the other subdetectors, especially with the ID, for full track reconstruction of muons.

Due to cost considerations, radiation tolerance and performance requirements, four different technologies of muon-detection chambers are used. Monitored Drift Tubes (MDTs) and Cathode Strip Chambers (CSCs) provide precise position measurements in the bending plane in $|\eta| < 2.0$ and $2.0 < |\eta| < 2.7$, respectively. In addition, Resistive Plate Chambers (RPCs) and Thin Gap Chambers (TGCs) with a coarse position resolution but a fast response time are used primarily to trigger muons in the ranges $|\eta| < 1.05$ and $1.05 < |\eta| < 2.4$, respectively, and also to provide measurements in the non-bending plane. Details for each subsystem follow.

Monitored drift tubes

The detection elements of the MDTs are aluminium tubes of 30 mm diameter and 400 μm thickness, filled with a gas mixture of Ar/CO_2 (93%:7%) at 3 bar absolute pressure. In the center of each tube there is a tungsten-rhenium (W-Re) wire of 50 μm diameter which acts as the anode while the tube wall is the cathode, forming a potential difference of 3080 V. An MDT chamber consists of two sets of either three of four layers of tubes, with the chambers at the inner station having more detecting layers for better granularity. Each set of layers, called multi-layer, is separated from the other by a mechanical spacer. After the installation of each chamber in its permanent position in the spectrometer, mechanical deformations are *monitored* by an optical alignment system, justifying the naming of this type of chambers. A schematic representation of an MDT chamber is seen in Figure 3.8.

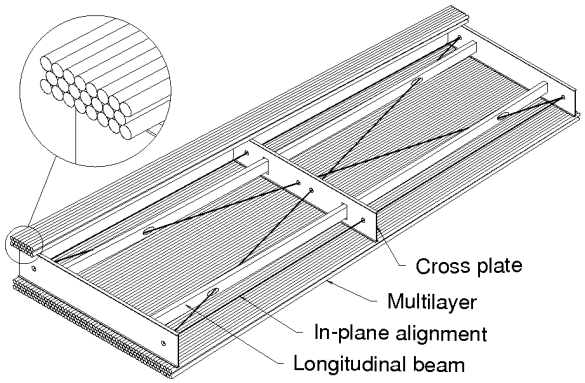

Figure 3.8: Sketch of a Monitored Drift-Tube chamber.

The detection principle of an MDT is as follows. When a charged particle traverses the tube, it ionizes the gas and liberates electrons from the gas atoms. Under the influence of the electric field, electrons start drifting towards the wire and at the same time positive ions drift in opposite direction towards the tube's wall. Primary electrons, while moving towards the wire accelerated by the electric field, acquire more energy and cause the ionization of more atoms, creating an avalanche near the wire where the potential is highest. The secondarily produced ions drift toward the tube wall traversing the whole distance from the wire to the wall. The signal induced on the wire propagates to the end of the tube, where an amplifier followed by a discriminator feeds the pulse to the time-to-digital converter (TDC) installed on the chamber.

Cathode-strip chambers

The CSCs are multi-wire proportional chambers that substitute the MDT technology in the forward, high-activity regions. The CSCs are designed to provide high spatial and time resolution, measurement of two coordinates at a high-rate environment. They are made of cathode planes segmented into strips in orthogonal directions. The plane with the strips perpendicular to the wires provides the precision coordinate, while the one parallel to the wires provides the transverse (ϕ) coordinate. A schematic representation of the above is shown in Figure 3.10. The chambers are filled with gas mixture of Ar/CO_2 (80% : 20%) and ionization of the gas caused by the

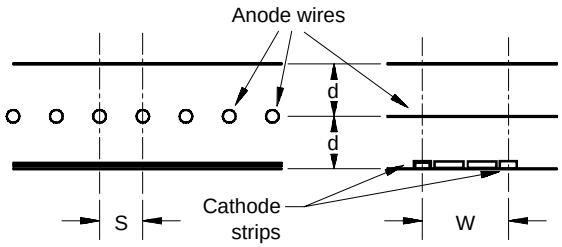

Figure 3.9: Sketch of a Cathode-Strip Chamber.

passage of a charged particle is transformed into an electron avalanche near the wires. The position of the track is obtained by interpolation between the charges induced by the avalanche on neighboring cathode strips. The expected resolution of the CSC system is about 60 μm in the bending plane and 5 mm in the transverse coordinate. The ability to operate in a high-rate environment is mainly due to the small electron drift times, which are of the order of 40 ns, resulting in timing resolution of 7 ns. This also allows the CSCs to be used as trigger chambers in this region.

Resistive-plate chambers

The RPCs are gaseous detectors which provide triggering for the MDT chambers and also measurement of two coordinates. They are made of two parallel resistive electrode-plates of phenolic-melaminic plastic laminate which are separated by each other by insulating spacers forming a gas gap of 2 mm. The gap is filled with a gas mixture containing mainly $C_2H_2F_4$ (94.7%). The electric field, which is created between the plates, is about 4.9 kV/mm and allows the production of electron avalanches along the tracks of ionizing particles towards the anode. The signal is read out from metallic strips, which are mounted on the outer faces of the two resistive plates and are perpendicular to each other. These are called η and ϕ strips because they are parallel and orthogonal to the MDT wires and determine the η or ϕ coordinate, respectively. The spatial resolution is roughly 1 cm while timing resolution is 2 ns. A schematic view of a cross section of an RPC is shown in Figure 3.10.

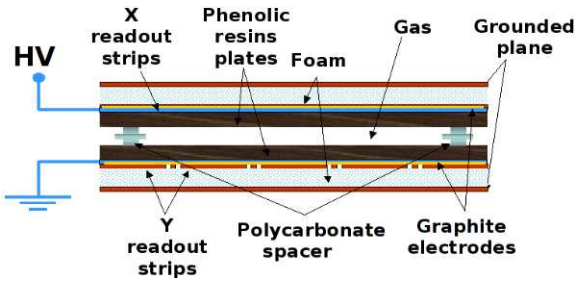

Figure 3.10: Sketch of a Resistive-Plate Chamber.

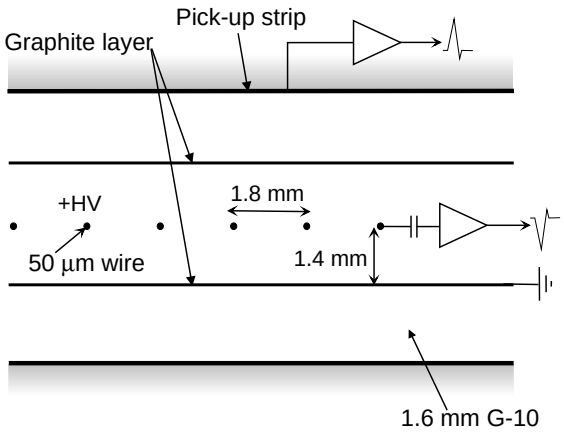

Figure 3.11: Sketch of a Thin-Gap Chamber.

Thin-gap chambers

The TGCs are used for triggering and measurement of two coordinates similarly to the CSC system and they are installed in the end-cap regions. They are multi-wire proportional chambers which consist of two cathode plates forming a 2.8 mm gas gap. The anode wires are located in the middle of the two plates and the distance from each other is 1.8 mm. The gas mixture used is n$-C_5H_{12}$ (n-pentane) and CO_2. The high electric field around the TGC wires and the small wire-to-wire distance lead to very good time resolution for the large majority of the tracks (except for those that pass midway between two wires, where the drift field vanishes). This setup is illustrated in Figure 3.11. The bending coordinate is measured by groups of TGC wires while the azimuthal coordinate is measured by the radial strips.

3.6 Trigger system

Considering that recording a collision event requires about 1 MB of storage space and also that ATLAS is designed to operate at 25 ns bunch crossings, it becomes clear that there is an enormous amount of data coming from the LHC per second. In order to cope with computing and storage limitations while retaining the potential of studying various physics processes, ATLAS deploys a sophisticated trigger system [2] to distinguish potentially interesting events and reduce the amount of data that are eventually stored.

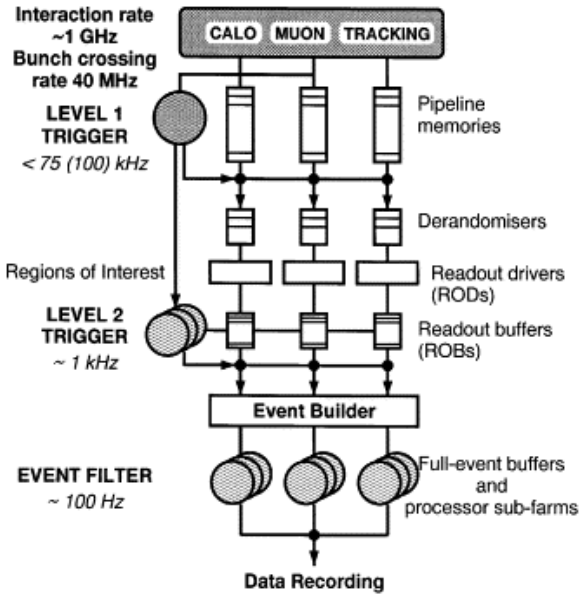

Figure 3.12: The ATLAS trigger system.

Figure 3.12 shows the three levels of the ATLAS trigger system: the hardware-based Level-1 trigger and the two-stage High Level Trigger (HLT), comprising the Level-2 trigger and Event Filter (EF). At Level-1, signals are received from the calorimeters and muon spectrometer (RPCs and TGCs). Concerning the muon trigger, it searches for patterns of hits corresponding to different p_{T} thresholds, thus defining Regions of Interest (ROIs) around these Level-1 hit patterns. The time necessary for Level-1 to decide whether such an ROI is defined in order to reject or keep the event is 2.5 μs. ROIs then serve as seeds for the muon reconstruction at the

HLT. At Level-2, information is retrieved from different parts of the detector in order to extract an better estimation of the location and p_{T} of the object within no more than 40 ms, and reduce the event rate below 3.5 kHz. The final decision is taken at the EF, where dedicated and highly selective algorithms incorporate all the detector information through the Event Builder and achieve a position and momentum resolution close to that provided by the offline muon reconstruction. For this purpose, the EF reconstruction runs on a dedicated computer cluster near the ATLAS site. The EF system dedicates 4 s of processing time per event to decide whether the event should be recorded or not and reduces the event rate to about 200 Hz.

Events that are selected by the trigger system are sorted accordingly in *data streams*, depending on signature (muon, electron, jet, or other) that allowed the event to be selected. I.e. the *muon* stream contains events that are selected by muon triggers. The rate of data coming from the muon stream corresponds to about 20% of the total bandwidth. Besides data streams that are used for physics analysis, there is a *calibration* stream collecting data that are used for the calibration of the detectors (rate about 30% of the total bandwidth) and also an *express* stream used for monitoring purposes (about 5%).

B-Physics Triggers

As already mentioned, ATLAS can record data with a rate of about 200 Hz. The bandwidth is balanced for the various ATLAS physics groups and the trigger rate dedicated to B-physics is typically 20 Hz. In ATLAS, the B-physics program and trigger is thus mostly relying on muonic final states. The main signatures searched by the B-physics triggers are single muons or dimuons with various transverse momentum thresholds and dimuon vertices various invariant mass cuts. A description of the available trigger algorithms is given in Ref. [2].

3.7 Data format and Computing

The reconstruction of signals received from the detector, as well as the physics analysis tools, is implemented within *Athena*, the ATLAS software framework. The reconstruction chain starts from byte-stream data (RAW), that is is output of the HLT. The output of reconstruction algorithms is producing Event Summary Data (ESD), in which physics objects like tracks and muons are built following the principles of object-oriented programming. Most physics applications should be able to run on ESD, which keep extended information from the detector. Then Analysis Object Data (AOD) are derived from ESD, including all the necessary information and objects that are suitable for physics analysis. At this level, analysis-specific selections on the amount of information and the type of events can be applied on AOD to provide Derived AOD (DAOD) or Derived Physics Data (DPD), which are technically identical to AOD but significantly smaller in size than AOD and can be stored in small-scale computing facilities for fast and efficient user analysis.

For the storage and processing of the data from ATLAS and the LHC, in general, a large-scale grid infrastructure has been developed, the Worldwide LHC Computing Grid (WLCG). It is a global collaboration of more than 150 computing centres in nearly 40 countries, linking up national and international grid infrastructures. In the WLCG, there is an hierarchical structure of facilities. The Tier-0 computing center is the heart of the grid. It is located at CERN and keeps a copy of all data received from the detectors. After reconstruction of the data, ESD and AOD are distributed to Tier-1 and Tier-2 centers so that they become available for physicists to run their physics analysis.

Bibliography

[1] ATLAS Collaboration, *The ATLAS Experiment at the CERN Large Hadron Collider*, JINST **3** (2008) S08003.

[2] ATLAS Collaboration, *Performance of the ATLAS Trigger System in 2010*, Eur. Phys. J. **C 72** (2012) 1849, `arXiv:1110.1530 [hep-ex]`.

Chapter 4

Reconstruction of physics objects

Following the hardware description of the inner detector and muon spectrometer subsystems in the previous chapter, in this one the basic concepts behind the reconstruction of relatively stable particles relevant for this thesis, namely charged hadrons and muons, are presented. In addition, vertex reconstruction is also discussed, as it is of particular importance for the reconstruction of unstable particles like J/ψ mesons and b-hadrons. For a detailed description of the procedure of track and vertex reconstruction, the interested reader may refer to Ref. [1]. Performance studies with data from 2010 and 2011 LHC operations are shown in Ref. [2].

4.1 Inner detector tracks

The inner detector employs three technically independent subsystems which act complementary in order to reconstruct tracks of charged particles. The Pixel and the SCT (see Section 3.3) provide few but high-precision space-point measurements (three and eights hits per track on average, respectively). The TRT improves pattern recognition and momentum resolution by contributing 36 hits per track on average, which allow an accurate measurement of the curvature of the track. The baseline algorithm designed for the efficient reconstruction of primary charged particles is the *inside-out* strategy. It starts by finding a track candidate in the pixel and SCT detectors (silicon track) and then extends the trajectories of successfully fitted tracks

to the TRT to reconstruct a full ID track. The main steps are:

- **pattern recognition:** Three-dimensional space-points are formed from clusters of silicon pixels or from the intersection of the front and backside silicon strips in an SCT module. Space-points that are compatible with a minimum p_{T} of 400 MeV are selected as track seeds. Then a fast Kalman filter is used to associate additional silicon hits moving away from the interaction point. If the track seeds can be extended to contain a minimum of 7 silicon hits, a track candidate is formed.

- **ambiguity solving:** At this step, a dedicated process is followed to resolve ambiguities from tracks sharing the same hits and also to distinguish fake tracks from those originating from a real particle trajectory. This process takes into account the number of hits-on-track and number of "holes", defined as the absence of hits in the passage of the track through a detector element, in order to assign a "score" to each track candidate. Shared hits between tracks are assigned to the track with the highest score and are removed from the other track. After the ambiguity solving process, tracks are required to have at least 7 associated hits, otherwise they are not used for further processing.

- **TRT track extension:** Silicon tracks, formed during the previous steps, are refitted with the addition of TRT hits that are compatible with the silicon track direction. The refitted track is compared with the original silicon track using the track scoring mechanism. The refitted track is kept, unless the silicon track has a higher score, where in this case the silicon track is kept.

In a second stage, a complementary procedure follows that performs a track search starting from segments reconstructed in the TRT and extends them inwards by adding silicon hits, which is referred to as *back-tracking*. This is designed to reconstruct secondary tracks that originate from particles produced in the interactions of primary particles. Finally, tracks with a TRT segment but no extension into the silicon detectors are referred to as TRT-standalone tracks. Both back-tracking and TRT-standalone reconstruction have severe drawbacks in high-luminosity environments and

are not considered in the analysis for this thesis.

4.2 Vertices

Most of the reconstructed tracks from a proton-proton collision will originate from the collision point, indicating the *primary vertex* of that collision. As more than one *pp* interactions may occur in a given bunch crossing, it is probable that many primary vertices can be reconstructed per event, while all vertices should lie within the *beam spot*, a region that is defined by the geometrical properties of the colliding beams. The beam spot is described by a Gaussian with the standard deviation of ∼5 cm in the direction of the beam and ∼15 μm in the transverse plane.

Primary vertices

The reconstruction of primary vertices comprises the primary vertex finding algorithm, dedicated to associate reconstructed tracks to vertex candidates, and the vertex fitting algorithm, dedicated to reconstruct the vertex position and its corresponding error matrix. An iterative vertex finding algorithm is used [2]. First, ID tracks compatible with originating from the interaction region are selected and a vertex seed is found by looking for the global maximum in the distribution of z_0-parameter of the tracks (z-coordinate of the distance of closest approach of the track to the beam-spot center). Taking as input the seed position and the tracks around it, the vertex position is determined using a χ^2-based vertex fitting algorithm. The beam-spot position is used to constrain the vertex fit, with significant impact on vertices reconstructed out of very few tracks. Tracks incompatible with the vertex by more than 7σ are used to seed a new vertex. This procedure is repeated until no unassociated tracks are left in the event or no additional vertex can be found.

Reconstructed primary vertices are sorted according to the sum of ${p_{\mathrm{T}}}^2$ of the constituent tracks. In analyses of 2010 and 2011 data, the usual choice of primary vertex is the one with the highest $\sum {p_{\mathrm{T}}}^2$, which is usually the one having the best vertex fit quality, as well.

Secondary vertices

The J/ψ meson decays fast ($t \sim 10^{-23}$ sec) and, if produced promptly in pp collisions, its decay vertex lies on the primary vertex within the uncertainty of its reconstructed position. For J/ψ mesons produced in decays of b-hadrons, their decay vertex is displaced with respect to the primary vertex by a measurable distance, due to the relatively long lifetime ($t \sim 10^{-12}$ sec) of b-hadrons. Therefore, tracks originating from such decays can be used to identify *secondary vertices* in order to measure the b-hadron lifetime or distinguish prompt from non-prompt J/ψ production. In the case of a $B^+ \rightarrow J/\psi(\mu^+\mu^-)\ K^+$ decay, the secondary vertex is determined from three tracks, the muons and the charged kaon. To improve the resolution of the reconstructed decay vertices, kinematic constraints are posed on the vertex fit. In the case of the $B^\pm$, in addition to requiring that all three tracks originate from the same point, the dimuon invariant mass is constrained to the well-known J/ψ mass, which compensates for detector resolution on the determination of the muon momenta and has a significant improvement effect on the reconstructed B^+ mass resolution.

4.3 Muons

The ATLAS Muon spectrometer provides muon identification and reconstruction up to $|\eta| < 2.7$ for muons with p_{T} ranging from 1 GeV to more than 1 TeV. Muon reconstruction is based on drift-radius measurements (hits) in MDTs, which provide an accurate measurement of the η coordinate, while the ϕ coordinate is taken from hits in the RPCs and TGCs, and also CSCs in the forward region (η measurements of these chambers are also used in track fitting but do not improve the resolution).

As a first step, within a single chamber, patterns are defined as collections of hits consistent with a trail left by a traversing muon and are subjected to a straight-line track fit (given the large radius of the muon trajectory in the bending plane, within a chamber this is a good approximation, see Figure 4.1, right). Based on the χ^2 per degree of freedom of the resulting fit, high-quality segments are selected and used as seeds for the next step, where a full track fit is performed from track segments in

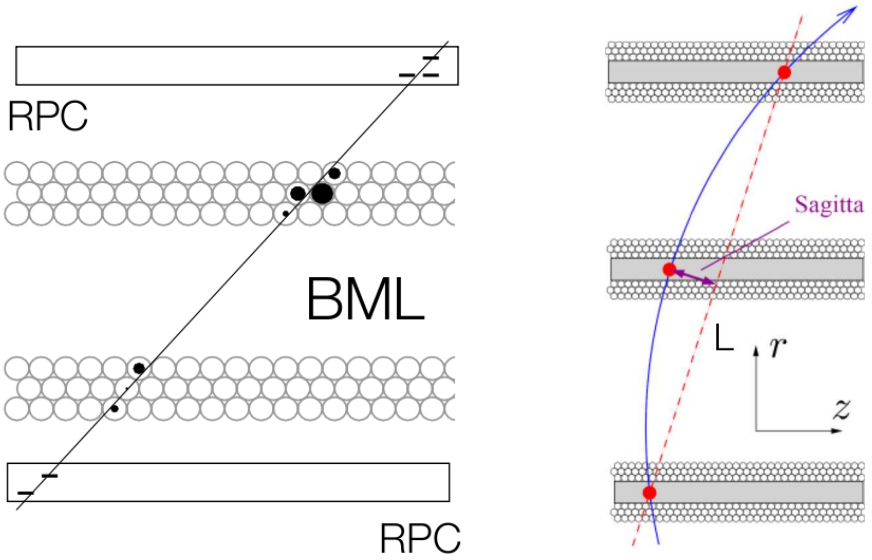

Figure 4.1: Sketch of a muon track segment formation from drift-radius measurements in the two multi-layers of an MDT chamber (left). Trigger hits from RPCs or TGCs are also used, but only to select hits in a given bunch crossing. A full muon track is fitted after combining segments from three MDT stations, and the p_{T} is measured from the sagitta of the three super-points (see text) of resulting track (right).

the three stations of MDT chambers. In the middle of each chamber and between multilayers, a *super-point* is defined. From the three super-points the sagitta of the track is formed which is used for the measurement of the muon p_{T}. Examples of fitting muon segments and tracks are shown in Figure 4.1.

The conditions for muon identification and reconstruction are quite different in the central and forward rapidity region and also at low-p_{T}. Therefore three categories of reconstructed muons are defined, depending on the reconstruction strategy that is followed [3]:

- **Stand-alone muons** are tracks reconstructed in the MS, as described above, extrapolated back to the interaction point taking into account multiple scattering and energy losses in the traversed material. Tracking information from the ID is not used, so this type of reconstructed muons has larger background contamination and worse momentum and spatial resolution than what can be achieved by muons in the next categories. However, stand-alone muons are useful in order to extend muon identification beyond the coverage of the ID up to

$|\eta| = 2.7$.

- **Combined muons** are tracks reconstructed in the MS which are associated to tracks in the ID. A fit is performed using the combined information from the ID and MS, achieving higher purity and better resolution than the ID, especially in the end-cap region. For low-p_{T} muons, fluctuations of the energy loss in the calorimeters dominate the resolution and make the gain of the combined fit not significant. Due to the ID coverage, combined reconstruction is limited to $|\eta| < 2.5$.

- **Segment-tagged muons** are reconstructed from segments that were not associated with an MS track, but that are matched to ID tracks. This type of reconstruction is extremely useful for increasing the acceptance of the MS for muons of low-p_{T} which are bent before reaching the middle and outer stations of the MS, thus lacking the chance of being reconstructed as combined muons, or for muons in the end-cap-barrel transition or $|\eta| \sim 0$ regions, where the muon might have missed one or more stations. As such reconstructed muons do not give a full MS track, they adopt the measured parameters of the associated ID track.

For this thesis, stand-alone muons are not used, as it is important to reconstruct the secondary vertex of the dimuon, thus the ID component of a muon track is needed. The combined muons are of best quality, as they have negligible background (coming from hadrons punching through the calorimeters or decays-in-flight) and better resolution than segment-tagged muons. Nevertheless, depending on the needs posed by the analysis, segment-tagged muons may be used to increase the overall muon reconstruction efficiency at low p_{T}. This is particularly important for B-physics studies where muons of low p_{T} down to a few GeV are used. In the low-p_{T} region ($p_{\mathrm{T}} < 20$ GeV), the p_{T} resolution is dominated by the ID measurements and is about 1.5% [4].

Bibliography

[1] M. Limper, S. Bentvelsen, and A. P. Colijn, *Track and vertex reconstruction in the ATLAS inner detector*. PhD thesis, 2009.

[2] ATLAS Collaboration, *Performance of the ATLAS Inner Detector Track and Vertex Reconstruction in the High Pile-Up LHC Environment*, Tech. Rep. ATLAS-CONF-2012-042. `http://cds.cern.ch/record/1435196`.

[3] ATLAS Collaboration, *The ATLAS Experiment at the CERN Large Hadron Collider*, JINST **3** (2008) S08003.

[4] S. Hassani, L. Chevalier, E. Lancon, J.-F. Laporte, R. Nicolaidou, and A. Ouraou, *A muon identification and combined reconstruction procedure for the ATLAS detector at the LHC using the (MUONBOY, STACO, MuTag) reconstruction packages*, Nucl. Instrum. Meth. **A 572** no. 1, (2007) 77.

Chapter 5

Data Quality Monitoring of the Muon Spectrometer

Data Quality Monitoring (DQM) is an important project within the Data Preparation group. ATLAS has about 140 million electronic channels receiving data with a rate of 100 Hz, and it is essential to monitor the status of data-taking (*on-line* monitoring) and off-line reconstruction (*off-line* monitoring) in order to assess the proper functioning of the detector and reconstruction algorithms, especially during LHC operation. Using predefined algorithms for the analysis of data from dedicated streams, conclusive results are provided during data processing in an automated way. When DQM occurs in the on-line environment, it provides the shifter with current run information that can be used to overcome problems early on. During the off-line reconstruction, the results of on-line monitoring are re-evaluated and, in addition, more complex analysis of physical objects is performed to assess the quality of the reconstructed data and the ability of the detector to reconstruct well-known resonances. My contribution has been in the development of the off-line DQM framework for the muon system.

5.1 On-line, off-line and express streams

The on-line stream receives input from the data acquisition system and offers real-time monitoring (latency of only tenths of seconds) of detector-level quantities. In the on-line environment, this information can flag the shifter to take action to prevent taking faulty data. At this step, there should be reasonable agreement between the on-line environment and the Detector Control System (DCS) status. Part of the muon data collected by the data acquisition system are transferred to dedicated computing farms (calibration centers) for the determination of the calibration parameters needed for muon reconstruction in the MS. Data from the off-line streams become available with latency of about one day), using the full reconstructed ATLAS event information. The express stream is dedicated to monitoring, giving priority to processing of received data in order to provide information from all detector subsystems with only 10% of the full data sample, in order to have conclusive results within a few hours, using old values for the calibration parameters from a database.

5.2 Off-line Muon Data Quality Monitoring

The purpose of off-line muon DQM [1] is to perform more complex and fine-grained checks of the data to determine their quality and provide useful feedback to the hardware experts and various physics groups. Muon data quality is performed on hit-level quantities, on reconstructed segments and tracks and, finally, on reconstructed physical objects decaying to muons. The organization of the off-line Muon DQM follows this logical and practical order. Four software packages have been developed to cover the needs for each level, named `MuonRawDataMonitoring`, `MuonSegmMonitoring`, `MuonTrackMonitoring` and `MuonPhysicsMonitoring`, where the author has contributed to the development of the last two, mainly. These packages have been developed within the Athena framework and are executed as part of the off-line reconstruction chain in order to produce monitoring histograms. The histogram output is gathered in a ROOT file respecting the aforementioned structure. The histogram output is of use to the off-line shifter, which can obtain the infor-

mation either by running ROOT scripts prepared for this purpose or by browsing the histograms from a publicly available web-page, called *Web Display*.[1] The Web Display is part of the Off-line Data Quality Monitoring Framework (DQMF), which provides the functionality of running pre-defined algorithms automatically on selected histograms to determine the quality of the data. For each histogram, all the corresponding details are given, like the specific check/algorithm applied and its result. A user-friendly code (*red*=problem, *yellow*=potential problem, *green*=no problem) is adopted to flag the result, which propagates to upper levels in order to determine the overall status of a subsystem. In Figures 5.1, 5.2 and 5.3, some representative screen captures are shown for each muon monitoring step, using the DQMF output from a 7M event run (155160, 16–17 May 2010, period B2) from *pp* collision data collected by the express stream. The off-line monitoring software runs on ESD, concurrently with reconstruction software during the ESD to AOD processing step at Tier-0, and provides the final information on the data quality which is stored in a database. Apart from the express stream, the off-line monitoring software runs also on the full statistics from the off-line streams, providing a useful tool for experts to perform analysis using the extended output from the ROOT files.

5.2.1 Muon Raw Data Monitoring

This is the first step of monitoring where hit-level quantities are monitored such as occupancies and correlations between different chambers. The main goal at this level is to check the readout chain from the on-line to the off-line environment.

5.2.2 Muon Segment and Track Monitoring

At this step the reconstruction of tracks and segments is monitored by looking at quantities such as track/segment parameters describe the position of the track perigee, direction of the track and also hit multiplicities, occupancies and fit quality parameters; this information is used to check calibration constants, chamber efficien-

[1]Look for Tier-0 Histograms in `https://atlasdqm.cern.ch/webdisplay`.

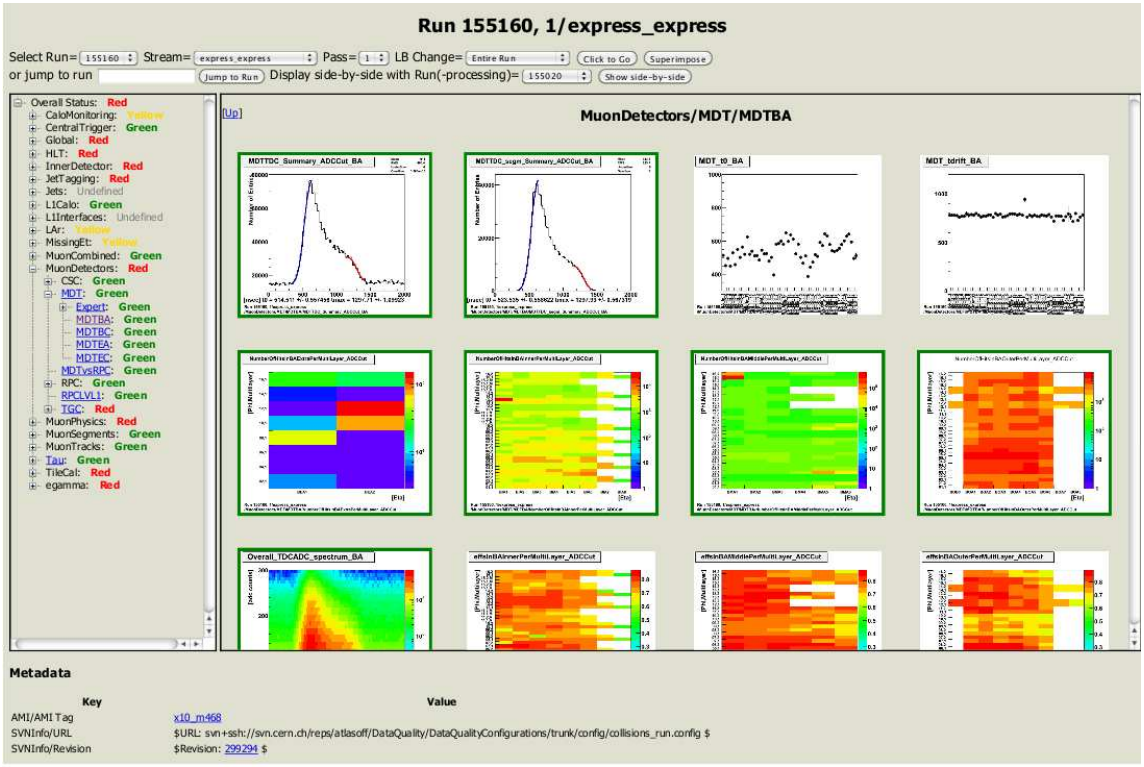

Figure 5.1: Selected output from Raw Data Monitoring package in DQMF Web Display. Shown is a list of histograms for MDTs in side-A of the barrel region. By clicking on each histogram, all corresponding details are given. In the left side pane it can be seen that similar output exists for all regions of the MS and also for RPCs, TGCs and CSCs.

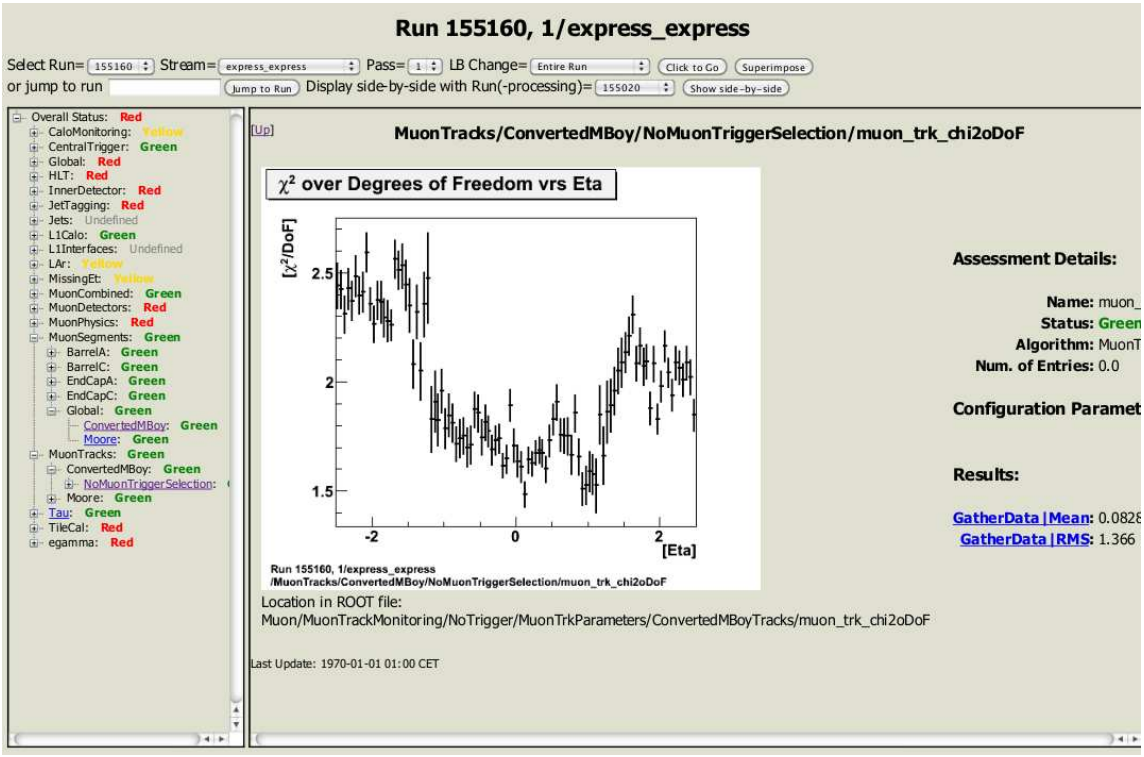

Figure 5.2: Selected output from Muon Track Monitoring package in DQMF Web Display. Shown is a profile histogram of the quality of muon track fitting, demonstrated by the χ^2 per degree of freedom, as a function of η.

cies and detector resolution. Part of the Muon Track Monitoring code was developed as part of my MSc. thesis, in which more detailed examples are given in Ref. [2]. More details on Muon Segment Monitoring can be found in a relevant MSc. thesis by V. Kouskoura [3].

5.2.3 Muon Physics Monitoring

Physics Monitoring is the last step of Muon Monitoring, where the reconstruction of dimuon decays of known resonances such as J/ψ and Z is used a monitoring tool for the MS performance. The important quantities from which we can extract valuable information are the dimuon event yields and the dimuon invariant mass. For a given run where statistics are limited, the goal is to make sure that the data include well

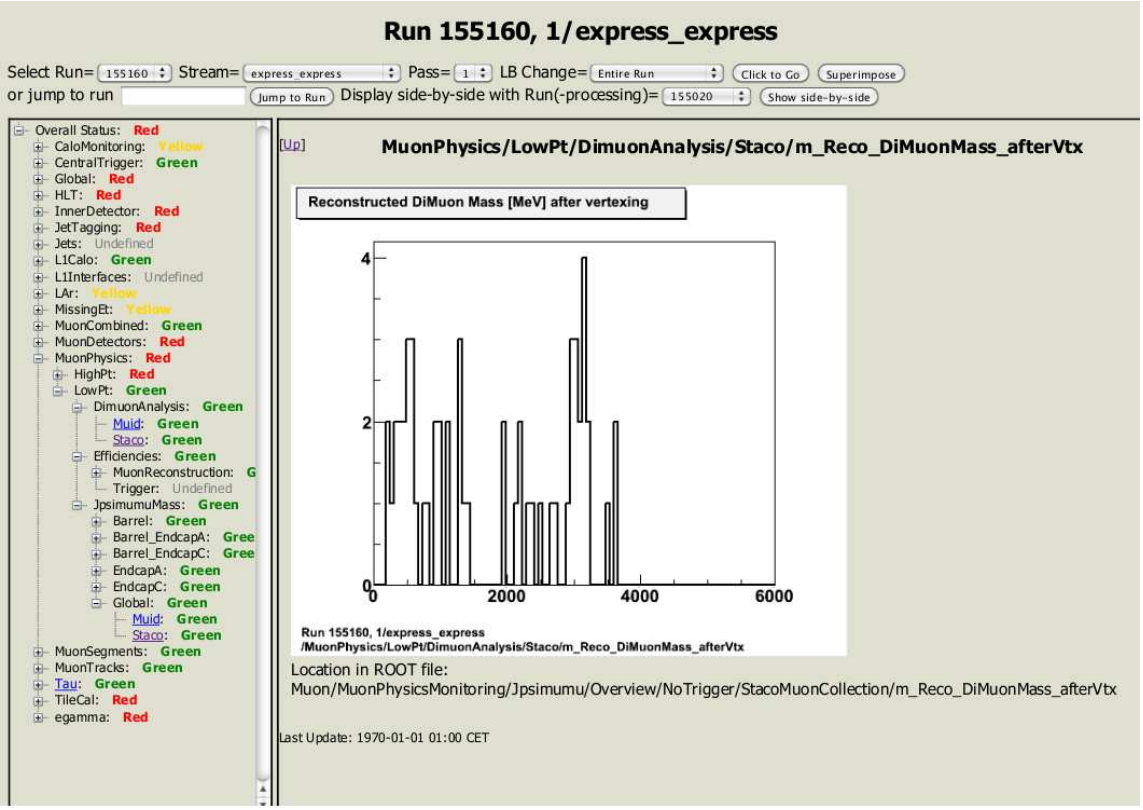

Figure 5.3: Selected output from Muon Physics Monitoring package in DQMF Web Display. Shown is a histogram of the dimuon invariant mass in the range 0–6 GeV, with a clear excess of reconstructed events at the J/ψ mass region.

reconstructed objects and can be used for physics analysis. With higher statistics (from long runs or from integration of data from different runs), more detailed checks can be made on the mass position and width to detect various sources of bias which introduce deterioration of resolution, such as detector misalignment, magnetic field uncertainty and material effects.

Bibliography

[1] N. Benekos, M. Bianco, G. Chiodini, I. A. Christidi, J. Coggeshall, A. Cortes-Gonzalez, D. Fortin, J. Griffiths, A. Guida, O. M. Harris, K. A. Johns, V. Kaushik, V. Kouskoura, X. Lei, T. M. Liss, I. Nomidis, and C. Petridou,

Muon Offline Monitoring at Tier-0 using cosmics and FDR data, Tech. Rep. ATL-COM-MUON-2009-042 (restricted to ATLAS). `https://cds.cern.ch/record/1223323`.

[2] I. Nomidis, *Offline Muon Data Quality Assurance in ATLAS*, Master's thesis, 2009. `http://invenio.lib.auth.gr/record/113625`.

[3] V. Kouskoura, *Data quality assurance of the ATLAS muon spectrometer and monitoring with cosmic data*, Master's thesis, 2009. `http://invenio.lib.auth.gr/record/114205`.

Chapter 6

Data and simulation

This chapter gives details about the collection of the data samples and the preparation of simulated samples used in this thesis and is organized as follows. In Section 6.1 the evolution of luminosity is shown, along with details on the used triggers and pile-up conditions for the 2010 and 2011 data samples. In Section 5, the aspects of Data Quality Monitoring of the ATLAS muon spectrometer are presented, as this project is an integral part of the data-taking procedure, with important contributions from the author. Lastly, Section 6.2 gives details on the simulation of the $b\bar{b}$ process, highlighting difficulties which are relevant B-physics studies in ATLAS.

6.1 Data samples

Data for this thesis were collected during 2010 and 2011, when the LHC was operating with proton beams colliding at $\sqrt{s} = 7$ GeV.

Data 2010

The total integrated luminosity delivered[1] and recorded by ATLAS during 2010 is about 45 pb^{-1}. During this period, the peak instantaneous luminosity was increas-

[1]The delivered luminosity accounts for the luminosity delivered from the start of stable beams until the LHC requests ATLAS to turn the sensitive detector off to allow a beam dump or beam studies.

ing, reaching a maximum of $2.1 \cdot 10^{32}$ cm^{-2} sec^{-1}. The evolution of the integrated luminosity with time is shown in Figure 6.1, together with the maximum of the average number of pp interactions per bunch crossing[1] observed per day. The 2010 data

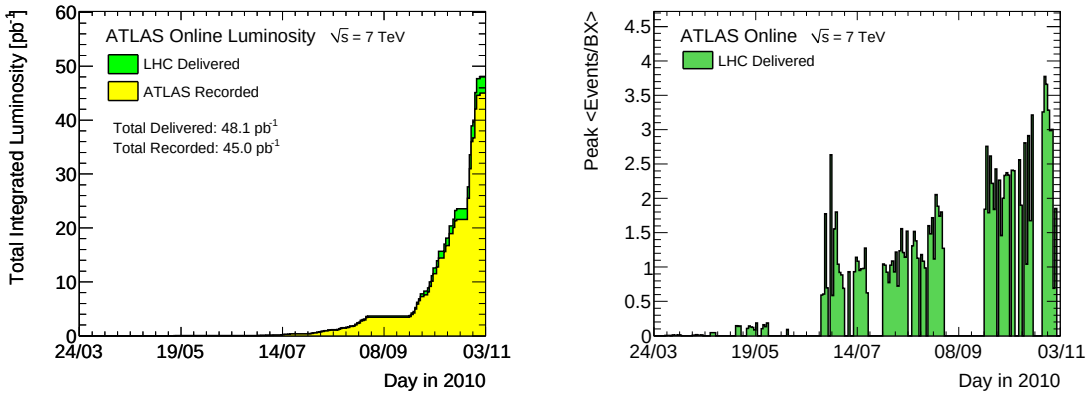

Figure 6.1: Cumulative luminosity (left) versus day delivered to and recorded by ATLAS during stable beams and for pp collisions at $\sqrt{s} = 7$ TeV in 2010. The maximum of the average number of interactions per bunch crossing observed per day (right) ranged from about one to 3.8.

sample is of relatively low luminosity and pile-up, which allowed single muon triggers with very loose thresholds to operate.

Data 2011

The performance of the LHC increased drastically in 2011, delivering more than 5 fb^{-1} in about 5 months. During this period, the peak instantaneous luminosity reached a maximum of $3.65 \cdot 10^{33}$ cm^{-2} sec^{-1}. The evolution of the integrated and peak luminosity with time is shown in Figure 6.2, where it can be seen that significant improvement was achieved after a Technical Stop of the LHC in September. The distribution of the mean number of pp interactions per bunch-crossing is shown in Figure 6.3 before and after September's Technical Stop, when β^* was reduced from 1.5 m to 1 m.

[1]This number corresponds to the mean of the poisson distribution on the number of interactions per crossing. It is calculated from the instantaneous luminosity as $\mu = L \cdot \sigma_{\text{inel}}/(n_b \cdot f_r)$, where L is the instantaneous luminosity, σ_{inel} is the inelastic cross-section which we take to be 71.5 mb, n_b is the number of colliding bunches and f_r is the LHC revolution frequency.

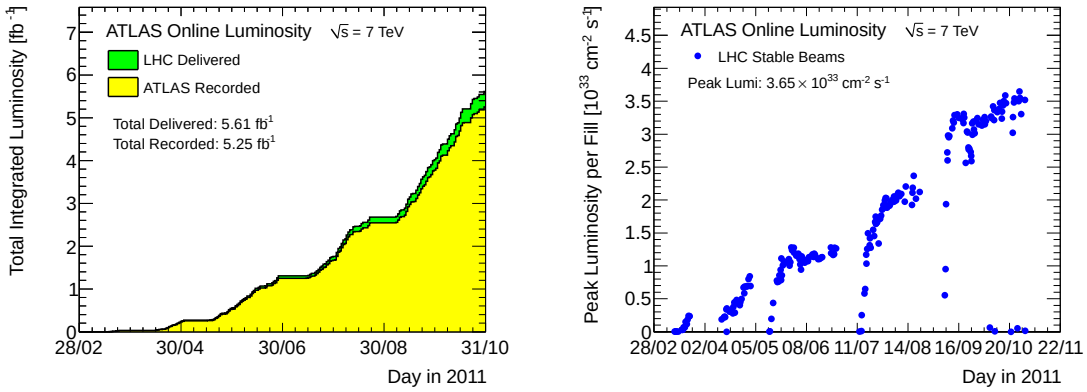

Figure 6.2: Cumulative (left) and peak luminosity (right) versus day delivered to and recorded by ATLAS during stable beams and for pp collisions at $\sqrt{s} = 7$ TeV in 2011.

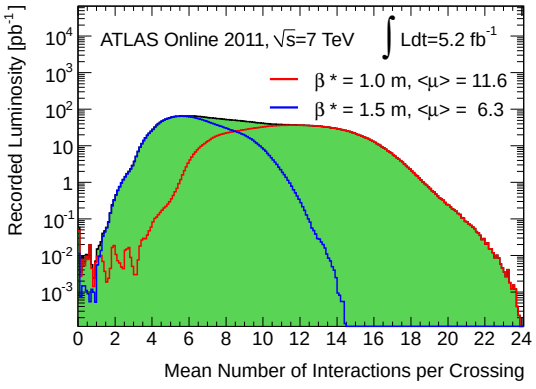

Figure 6.3: Luminosity-weighted distribution of the mean number of interactions per crossing for LHC operation in 2011.

Trigger conditions changed dramatically in 2011 and the p_{T} thresholds of the available un-prescaled single muon triggers were significantly higher than in 2010. This is not optimal for B-physics studies, so data for the analysis of this thesis were selected with a dimuon trigger which requires the presence of at least two muon candidates with $p_{\mathrm{T}} > 4$ GeV (a more detailed description of this trigger is given in Section 8.2). After the significant increase of the luminosity in September 2011, this trigger was also prescaled. Therefore, the analysis is restricted to the data sample from the LHC operation in early 2011, from April to August.

Good-run list selection

Both 2010 and 2011 data samples are subjected to a set of quality criteria, which require proper functioning of the detector subsystems which are relevant for the analysis (ID and MS). Selected events are also required to have occurred during stable beams, meaning that the colliding bunch of each beam if filled with protons so that collisions were possible. The quality of the data is determined by the Data Preparation group per luminosity block and is stored in a good-run list (GRL). The names of the used GRLs for 2010 and 2011 data are given in Table 6.1. For 2010, the resulting integrated luminosity with this GRL is calculated to be 39.4 pb^{-1} with an uncertainty of 3.4%. For 2011 it is 2.4 fb^{-1} with an uncertainty of 1.8% [1].

	2010	2011
Data tag	data10_7TeV	data11_7TeV
Run periods	B–I	B2, D–J, K1–K4
Physics trigger	(various)	EF_2mu4_Jpsimumu
GRL	DetStatus-v21-pro05_Muon	DetStatus-v36-pro10_Muon.xml
Total luminosity	39 nb^{-1}	2.4 fb^{-1}

Table 6.1: Shown are the details of the integrated luminosity calculation, performed with the tool found in https://atlas-lumicalc.cern.ch.

6.2 Monte Carlo simulation

In the analysis two Monte Carlo (MC) samples are used. The first sample simulates the signal $B^{\pm} \to J/\psi\, K^{\pm} \to \mu^+\mu^-\, K^{\pm}$, while the second simulates $b\bar{b}$ production, with $b\bar{b} \to J/\psi\, X \to \mu^+\mu^-\, X$, including the signal and also the backgrounds which are relevant for the analysis. Both samples were generated with PYTHIA 6 [2] using the 2011 ATLAS tune [3]. The response of the ATLAS detector was simulated [4] using GEANT4 [5]. Additional pp interactions in the same and nearby bunch crossings (pile-up) were included in the simulation. In the following subsections, some technical issues regarding the MC sample production are discussed in order to highlight difficulties which are relevant for B-physics studies.

6.2.1 Production of $b\bar{b}$ pairs with Pythia

PYTHIA is a generator that includes all $b\bar{b}$ production mechanisms (flavour creation, flavour excitation, gluon splitting), and also a MC showering program that implements the Lund string model for the fragmentation of the b quark. The probability to obtain a signal $B^{\pm}$ decay from a $b\bar{b}$ pair is given by the branching ratio of the signal process $B^{\pm} \to J/\psi\, K^{\pm}$, with $J/\psi \to \mu^+\mu^-$, which is about 6×10^{-5} [6]. Taking also into account the fragmentation fraction of $\bar{b} \to B^+$ which is about 0.4, this means that, by default, one has to generate at least 100k $b\bar{b}$ events to get just a single B^+ or B^- signal decay. Moreover, a signal decay will not be detected unless the final-state particles are within the fiducial volume of the detector and the trigger system. It is clear from the above that in order to produce a high-statistics sample for a specific channel and ensure that it will contain detectable events, a different approach has to be followed.

A dedicated interface to PYTHIA for B-physics, PYTHIAB [7], is used for this purpose. In order to speed up the generation by producing events with a good chance of being detected, PYTHIAB checks at parton level (before the hadronization) for the presence of $b\bar{b}$ quarks satisfying thresholds in p_{T} and η defined by the user. Moreover, it allows multiple hadronizations of the same parton content and the application

of trigger-like and offline-like selection cuts on the kinematics (p_{T}, η) of the final state particles. Lastly, another important functionality provided by PythiaB is that of forcing a given b-hadron to decay in a specific mode without intervening in the Pythia code; in this case it is the $B^{\pm}$ meson that is forced to decay to $J/\psi\, K^{\pm}$, and then the J/ψ meson is forced to decay to muons.

When applying cuts at generation-level and forcing specific decay modes, the usual approach is to use these requirements only on one quark of a $b\bar{b}$ pair, either on b or $\bar{b}$. Consequently, two independent samples are produced for the $B^{\pm}$ signal. In the first sample, the B^{+} meson is forced to decay to $J/\psi\, K^{+}$, and cuts are posed on the p_{T} and η of the $\bar{b}$ quark and final-state particles (muons, kaons) to ensure that the signal decay products are inside the detector acceptance; no requirements are used for the b quark. In the second sample, the corresponding procedure to produce B^{-} signal events is followed, applying cuts on the b quark, instead. The reason for that is clear: if both b and $\bar{b}$ quarks are forced to decay in the same signal mode in the same event satisfying fiducial kinematic cuts, we end up with an unrealistic sample in which every event contains two signal decays and many combinatorial solutions. In the case of the production of the inclusive $b\bar{b} \to J/\psi\, X$ sample, requirements are applied to the $\bar{b}$-quark only, forcing it to decay to modes containing a J/ψ meson in the final state (including feed-down from higher $c\bar{c}$ states). For example, in this sample the $B^{+} \to J/\psi\, K^{+}$ decay is found in abundance, while the probability of finding a $B^{-} \to J/\psi\, K^{-}$ decay is tiny, due to its actual branching ratio. The cuts posed at generation level for the production of the various MC samples are given in Table 6.2.

Sample	Process	b-quark		$\bar{b}$-quark		muons		kaons	
108540	$B^{+} \to J/\psi\, K^{+}$	-	-	2.5	2.5	2.5	2.5	0.5	2.5
108541	$B^{-} \to J/\psi\, K^{-}$	2.5	2.5	-	-	2.5	2.5	0.5	2.5
108411	$b\bar{b} \to J/\psi\, X$	-	-	4	2.5	4	2.5	-	-

Table 6.2: Cuts on b and $\bar{b}$ quarks and final state particles, posed at generation level to enhance the production of signal decays inside the fiducial volume of the detector. For the pair of numbers quoted for each particle type, the first number is the minimum p_{T} in GeV that is required and the second is the maximum $|\eta|$ required. Dashes in some fields indicate that no requirement was applied.

By default, PYTHIA includes only a few b-hadron decays, so for the production of the inclusive $b\bar{b} \to J/\psi\, X$ sample a dedicated effort was made to include as many processes as possible, using input from PDG for the branching ratios of various b-decays [8].

In addition to the samples listed in Table 6.2, which are official ATLAS samples with full detector simulation, another sample of private production is used. This has not gone through detector-simulation and was produced with same settings as for the signal MC samples but without any cuts on the final-state particles, in order to estimate the kinematic acceptance of the analysis cuts used for the cross-section measurement (see Section 8.4.1).

6.2.2 Correction of angular properties

In the signal decay $B^{\pm} \to J/\psi\, K^{\pm}$, the J/ψ meson is produced isotropically, while the $J/\psi \to \mu^+\mu^-$ decay is not isotropic (see Appendix A). PYTHIA does not consider spin-momentum correlations in the $J/\psi \to \mu^+\mu^-$ decay, as well as for all complex sequencial B of D-meson decays and CP violating decays. This should be corrected for by reweighting generated events so that the correct angular properties are reproduced. Alternatively, the EVTGEN event generator [9] can be used, which takes care of this problem. It is not, however, the baseline generator for the official B-physics sample production in ATLAS, as it is significantly slower than PYTHIA.

Figure 6.4 shows the distribution of $\cos\theta^*$ for PYTHIA and EVTGEN where θ^* is the angle between the positively charged muon and the kaon in the J/ψ meson rest frame. In the case of PYTHIA where the J/ψ meson decays isotropically, this distribution is flat. The correct distribution is given by $\sin^2\theta^*$, which is the case for EVTGEN. In the same Figure, it is shown that the same result as for EVTGEN is achieved by reweighting the events generated with PYTHIA to the correct distribution. It must be noted that the shown distributions were obtained from samples generated without any cuts on the final-state particles. The PYTHIA sample without such cuts is used for the acceptance calculation, where the effect of this reweighting procedure is significant.

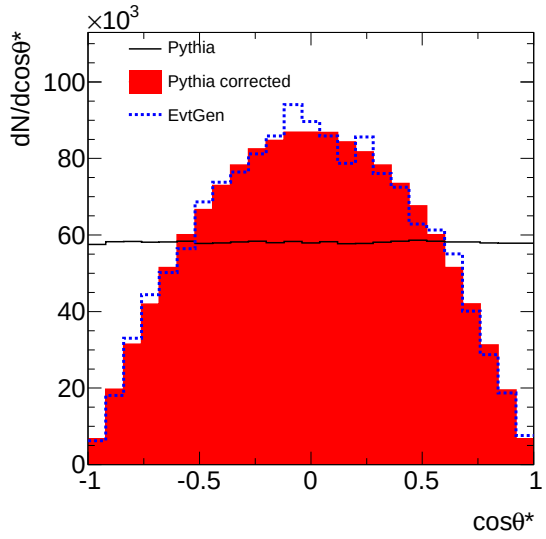

Figure 6.4: Spin-momentum alignment of the leptons in the decay of J/ψ meson is such that the zero helicity is conserved.

6.3 Pile-up

In the high-luminosity environment of the LHC, most hard-scattering events have additional softer interactions occurring in the same bunch crossing, called *in-time pile-up*. The number of additional interactions follows a Poisson distribution with a mean determined from the beam parameters. The beam parameters changed in the middle of 2011 LHC operation, with a significant effect on pile-up, as can be seen in Figure 6.3. It is noted that the number of additional interactions in a given bunch crossing is determined from the number of reconstructed vertices.

In-time pile-up is included in the MC simulation. To account for the different pile-up conditions during 2011, MC samples include four different configurations, as can be seen in Table 6.3. Each configuration is assigned a run number and uses different pile-up conditions and trigger menus, in accordance with the various periods of data-taking. Simulated events with run number 189751 are not used for the analysis of the first half of the 2011 data, as they use a have different pile-up setup and trigger menu, corresponding to the high-luminosity second half if the full 2011 data sample. Events in the simulation are not produced equally for the different configurations; they are produced following ratios determined by the integrated luminosities corresponding to

the relevant data-taking periods. Usually, these ratios are not known *a priori*, when the MC sample production occurs, so they are corrected *a posteriori* with an event-reweighting procedure. In this case, where the pile-up and trigger conditions are stable and these ratios well-defined, such a procedure was found to have a negligible effect on the various parts of this analysis.

MC run number	$\langle N_{\mathrm{PV}} \rangle$
180164	4.3
183003	4.4
186169	5.1
189751	7.5

Table 6.3: The average number of reconstructed vertices per event, $\langle N_{\mathrm{PV}} \rangle$, given for four different configurations in the MC simulation. Each configuration is assigned a run number. The last configuration (189751) corresponds to the high-luminosity data-taking periods.

Bibliography

[1] ATLAS Collaboration, *Improved luminosity determination in pp collisions at $\sqrt{s} = 7$ TeV using the ATLAS detector at the LHC*, `arXiv:1302.4393 [hep-ex]`.

[2] T. Sjostrand, S. Mrenna, and P. Z. Skands, PYTHIA *6.4 Physics and Manual*, JHEP **05** (2006) 026, `arXiv:hep-ph/0603175`.

[3] ATLAS Collaboration, *ATLAS tunes of Pythia 6 and Pythia 8 for MC11*, Tech. Rep. ATL-PHYS-PUB-2011-009. `http://cds.cern.ch/record/1363300`.

[4] ATLAS Collaboration, *The ATLAS Simulation Infrastructure*, Eur. Phys. J. **C 70** (2010) 823, `arXiv:1005.4568 [physics.ins-det]`.

[5] GEANT4 Collaboration, S. Agostinelli et al., *GEANT4: A Simulation toolkit*, Nucl. Instrum. Meth. **A 506** (2003) 250.

[6] J. Beringer et al., *Review of Particle Physics*, Phys. Rev. **D 86** (2012) 010001.

[7] M. Smizanska, *PythiaB, an interface to Pythia6 dedicated to simulation of beauty events*, Tech. Rep. ATL-COM-PHYS-2003-038 (restricted to ATLAS).

[8] E. V. Bouhova-Thacker, *Model for $b\bar{b} \to J/\psi\, X$ generation*, Tech. Rep. (restricted to ATLAS). `https://twiki.cern.ch/twiki/pub/AtlasProtected/BPhysWorkingGroupBEventsGenerators/Btojpsix_note.pdf`.

[9] D. J. Lange, *The EvtGen particle decay simulation package*, Nucl. Instrum. Methods **A 462** (2001) 152. `http://www.sciencedirect.com/science/article/pii/S0168900201000894`.

Chapter 7

Observation and lifetime measurement of $B^{\pm}$ mesons

During the early periods of data taking from pp collisions, there was high interest in reconstructing well-known resonances in order to validate the performance of the ATLAS detector. After the observation of J/ψ mesons decaying to two muons, observing $B^{\pm}$ mesons decaying to $J/\psi K^{\pm}$ was the next challenge. Using the first data recorded by ATLAS in 2010, an analysis for the observation of $B^{\pm}$ meson production was conducted, in order to provide the first B-physics result of the experiment. The $B^{\pm} \rightarrow J/\psi\, K^{\pm}$ and $J/\psi \rightarrow \mu^{+}\mu^{-}$ signals were used as "standard candles" in the initial phase of data-taking for the assessment of the performance of the inner detector and muon spectrometer and also of the techniques involved in measurements of b-hadron masses, lifetimes, production rates and angular properties. With measurements of the well-known mass and lifetime of these signals which I performed, the performance of the inner detector was validated for mass and vertex reconstruction.

In Section 7.1, the details of the analysis that led to the observation of $B^{\pm}$ mesons with a few pb^{-1} are given. Using the full 2010 dataset of about 40 pb^{-1}, a simultaneous (two-dimensional) likelihood fit method was employed for the measurement of the $B^{\pm}$ mass and lifetime, described in Section 7.2.

7.1 Observation analysis

Clear evidence of $B^{\pm}$ production was already seen with a few hundreds of nb^{-1} (see Figure 7.1), which was reported to the ATLAS collaboration on 3 August 2010.[1] The data sample was growing fast, so the analysis was repeated with larger statistics to provide a publishable result [1].

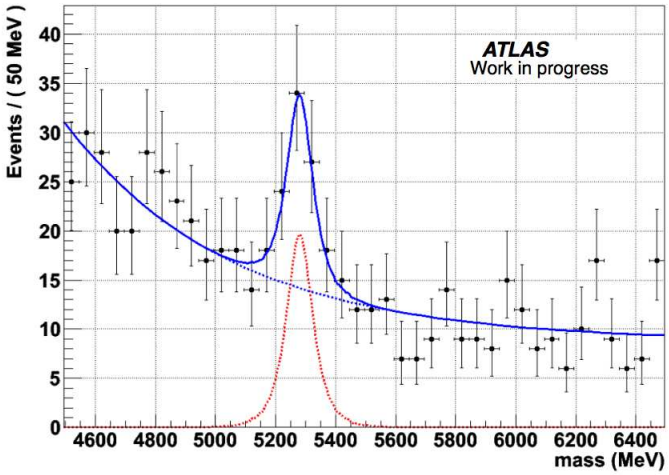

Figure 7.1: Invariant mass of $J/\psi\, K^{\pm}$ using 290 nb^{-1} of data recorded in early in 2010, showing a clear excess of events at the $B^{\pm}$ mass. The continuous blue line indicates the result of a fit to the $B^{\pm}$ candidates, returning a total of 49 ± 13 signal events over a background of about 94 events. The reconstructed $B^{\pm}$ mass returned by the fit is 5280 ± 16 MeV, consistent with the world-averaged value of 5279.17 ± 0.29 MeV [2].

7.1.1 Data sample and event selection

The data sample for the observation analysis was collected during LHC operation with protons colliding at $\sqrt{s} = 7$ TeV between 24th June and 29th August 2010 (data-taking periods D–F). For the reconstruction of the signal decay, the muon and tracking systems are of particular importance. Only data where both subdetectors were fully operational, and where the LHC beams were declared to be stable, are considered for physics analysis. The data were collected in a period of rising instantaneous

[1] Link to presentation (restricted to ATLAS): `https://indico.cern.ch/conferenceDisplay.py?confId=72824`.

luminosity of the LHC, and the trigger conditions varied considerably over this time. Consequently, the trigger selections differ depending on the period of data taking. In the beginning, when the High-Level Trigger (HLT, see Section 3.6) was not active, single and dimuon triggers at Level-1 were used, without any p_{T} threshold for muons. At later periods the HLT was activated and events passing a variety of single and dimuon triggers were accepted, with thresholds ranging from 4 to 10 GeV. For higher luminosity runs the HLT single muon triggers with low thresholds were prescaled; events passing these triggers were accepted nevertheless. Applying these requirements of data quality and trigger, the data sample corresponds to 3.4 pb^{-1}. This luminosity estimate has an uncertainty of 11% [3].

Track selection

Tracks to be considered as muon candidates are required to pass certain quality criteria, based on the numbers of hits in the pixel, SCT and TRT detectors, according to standard recommendations provided by the ATLAS Muon Combined Performance group. For the data considered here, the selections on the track quality require at least one hit in the pixel detector and at least six hits in the SCT. Tracks reconstructed in the ID that are matched with combined or segment-tagged muons are selected as muon candidates. The matching is done between ID tracks and the ID components of reconstructed muons. In this analysis the muon track parameters are taken from the ID measurement alone, as the resolution for low-p_{T} muons is driven by the ID track reconstruction. The same track quality criteria are applied to tracks selected as potential $K^{\pm}$ candidates.

Reconstruction of J/ψ candidates

To veto events triggered by cosmic-ray muons and ensure that there is one pp collision, we require that there is at least a reconstructed primary vertex in the event with at least three associated tracks. Then to identify J/ψ candidates, events must have at least one pair of reconstructed muons of opposite charge.

Muon pairs are fitted using a vertexing algorithm [4] constraining the tracks to

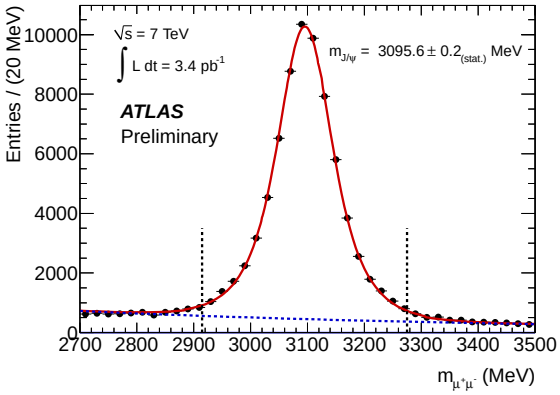

Figure 7.2: Invariant mass of oppositely signed dimuons. Dimuons in the shown range are fitted to derive the reconstructed J/ψ mass, with its value shown with its statistical uncertainty. Dimuons with an invariant mass within the range indicated by the dashed vertical lines, which corresponds to $\pm 3\sigma$ of the reconstructed J/ψ mass, are considered as $J/\psi \to \mu^+\mu^-$ candidates and are used to select $B^{\pm}$ mesons.

originate from a common vertex and the refitted track parameters returned by the algorithm are used to derive the momenta of muons and the dimuon invariant mass. In each pair, the highest-p_{T} muon should have a p_{T} of at least 4 GeV, and the other a p_{T} of at least 2.5 GeV. Muon pairs fitted successfully to a common vertex with $\chi^2/N_{\mathrm{d.o.f.}} < 10$ are retained in the mass range 2700–3500 MeV, and their invariant mass is shown in Figure 7.2. Dimuons are considered as $J/\psi \to \mu^+\mu^-$ candidates if their invariant mass lies in a 3σ window (± 180 MeV) around the reconstructed J/ψ mass, corresponding to the mass range 2915–3275 MeV. The reconstructed J/ψ mass was obtained with a maximum likelihood method, where the J/ψ signal is described using a Gaussian with per-candidate uncertainties and a linear background description; for details, see [5]. If more than two muons are found in the event, all the allowed charge combinations are made to find J/ψ candidates. If multiple J/ψ candidates are found in the event, which happens in about 2% of the total number of events, we consider all of them in the formation of $B^{\pm}$ candidates. A total of 75k J/ψ candidates fulfilling the above criteria are found in the preselected events.

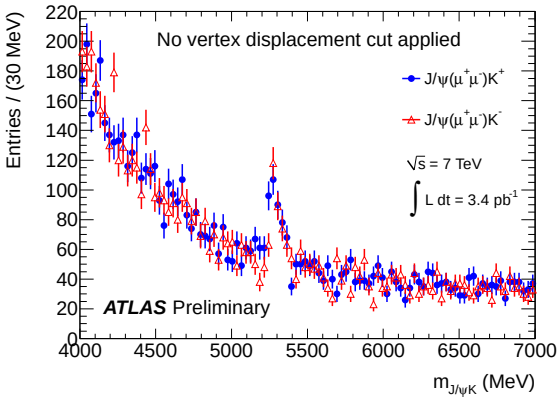

Figure 7.3: Invariant mass distributions of selected $J/\psi\,K^+$ (solid circles) and $J/\psi\,K^-$ candidates (triangles) in the mass range 4000–7000 MeV.

Reconstruction of $B^{\pm}$ candidates

Dimuon track pairs passing the J/ψ candidate selection presented above are again fitted to a common vertex with an additional third track having p_{T} greater than 2.5 GeV. The three-track vertex fit is performed by constraining the muon tracks to the J/ψ world average mass and assigning the kaon mass to the third track. Fitted triplets are considered to be $B^{\pm} \to J/\psi\,K^{\pm}$ candidates if the vertex fit is of good quality, requiring $\chi^2/N_{\mathrm{d.o.f.}} < 6$, and the p_{T} of the three-track combination is greater than 10 GeV. A total of 13k candidates fulfilling the above criteria are found in a wide mass range 4000–7000 MeV. Figure 7.3 shows the invariant mass distribution of these $J/\psi\,K^{\pm}$ candidates, separated by charge. The signal peak is clearly seen in both the positive and negative-charge combinations on top of the background, which has different contributions and shapes in the low and high-mass sidebands. B mesons which are only partially reconstructed as B^+/B^- candidates populate the low-mass sideband. The high-mass sideband is dominated by the flat background formed by random combinations of J/ψ with tracks coming from the primary vertex. In this figure, good response of the inner detector in reconstructing both positive and negative tracks is seen which allows to combine both B^+ and B^- candidates in the analysis to double the statistics.

7.1.2 Per-candidate invariant mass fit

To extract the signal properties ($B^{\pm}$ mass and resolution) and number of signal events in the data sample, an unbinned maximum likelihood fit is performed using $J/\psi\, K^{\pm}$ candidates in a restricted mass range from 5000 to 5600 MeV. The likelihood function is defined by:

$$L = \prod_{i=1}^{N} f_{sig}\, S(m_i) + (1 - f_{sig})\, B(m_i) \tag{7.1}$$

where m_i is the $J/\psi\, K^{\pm}$ invariant mass of the i-th candidate and N is the total number of $J/\psi\, K^{\pm}$ candidates in the chosen invariant mass range. S and B are probability density functions that model the $B^{\pm}$ signal and background shapes in this mass range. For the signal, the mass is modelled with a Gaussian distribution:

$$S(m_i) \equiv \frac{1}{\sqrt{2\pi}(s \cdot \delta m_i)} \exp\left[-\frac{(m_i - m_{B^{\pm}})^2}{2(s \cdot \delta m_i)^2}\right] \tag{7.2}$$

whose mean value $m_{B^{\pm}}$ will be taken as the reconstructed $B^{\pm}$ mass (one the free parameters of the fit), and the width of the gaussian is the product $s \cdot \delta m_i$. The mass error δm_i is calculated for each $J/\psi\, K^{\pm}$ candidate from the covariance matrix associated with the three-track vertex fit and f_{sig} represents the signal fraction. The scale factor s accounts for differences between the per-candidate errors on the candidate masses (calculated from tracking parameters) and the overall mass resolution. Ideally, the value of this parameter is 1. For the background, the mass distribution is modelled with a linear function:

$$B(m_i) \equiv 1 + b \cdot m_i \tag{7.3}$$

where b is the slope of the linear background. Because of partially reconstructed B mesons and kinematic reflections, no attempt is made to model the background far from the $B^{\pm}$ mass region. In the mass region $5000 - 5600$ MeV a linear approximation of the background is adequate, given the available statistics.

The fit has four free parameters: f_{sig}, $m_{B^{\pm}}$, s and b. Their values and covariant-error matrix returned by the fit are used to calculate the number of $B^{\pm}$ signal decays

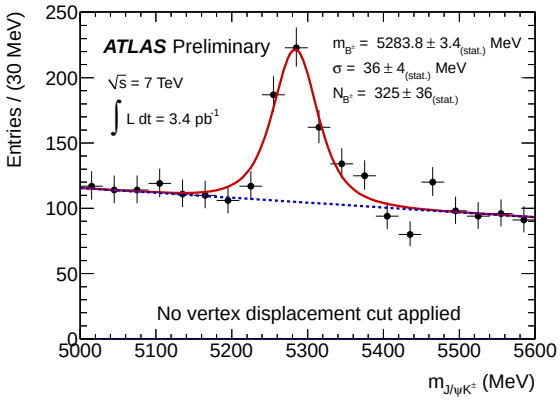

Figure 7.4: Invariant mass of $J/\psi\, K^{\pm}$ candidates in a narrow mass window. The solid line is the projection of the result of the unbinned maximum likelihood fit to all $J/\psi\, K^{\pm}$ candidates in the shown mass range. The dashed line is the projection for the background component of the same fit. The results of the fit for the number of signal events, the reconstructed $B^{\pm}$ mass and its resolution are also shown with their statistical uncertainties.

N_{sig}, the mass resolution σ_m and the number of background events N_{bkg} in the mass interval $m_{B^{\pm}} \pm 3\sigma_m$. The mass resolution σ_m is defined as half of the width of the $B^{\pm}$ mass distribution for which the integral of S retains 68.3% of N_{sig} symmetrically around the fitted mass $m_{B^{\pm}}$. The uncertainty of σ_m is calculated using the covariance matrix of the fit. The number of background events N_{bkg} in the mass interval $m_{B^{\pm}} \pm 3\sigma_m$ and its error is calculated from f_{sig}, b, N and the error matrix of the fit.

The fit is applied as described above, and the result is shown in Figure 7.4. The $B^{\pm}$ mass returned by the fit is 5283.8 ± 3.4 MeV, which is consistent with the world average of 5279.17 ± 0.29 MeV [2]. The signal mass resolution σ_m is 36 ± 4 MeV, in agreement with the expectation from simulation (39 MeV). The $B^{\pm}$ signal extracted from the data sample, which corresponds to an integrated luminosity of 3.4 pb^{-}1, is 325 ± 36 and the background is 756 ± 87. As a check, the properties of B^{+} and B^{-} signal events have been extracted separately with the same fit method and were found to be consistent [1]. With this study we conclude to the good performance of the ID and MS in reconstructing the $B^{\pm} \to J/\psi(\mu^{+}\mu^{-})\, K^{\pm}$ decay and reproducing the known mass of $B^{\pm}$ mesons with the first data recorded in 2010.

7.2 Lifetime measurement

A characteristic of the B mesons is their long lifetime, resulting in a measurable displacement of their decay vertex (secondary vertex). This can be used, therefore, for the identification of b hadrons and b jets, in general. With the selection of $B^{\pm}$ signal events and a measurement of their lifetime, the performance of secondary vertex reconstruction in the ID is evaluated. Using pp collision data from the early LHC operation in 2010, an analysis for the simultaneous measurement of the $B^{\pm}$ meson mass and lifetime was performed to validate the reconstruction of $B^{\pm}$ mesons with the ATLAS detector by reproducing their well-known properties (mass and lifetime). The analysis employs a simultaneous (two-dimensional) likelihood fit to the invariant mass and proper decay time of $B^{\pm}$ candidates in order to disentangle the signal component from the background in the proper-time distribution.

7.2.1 Data sample and event selection

The full 2010 data sample is used for the $B^{\pm}$ mass and lifetime measurement. Due to the increasing luminosity of the collider, the trigger conditions were not stable, so a list of unprescaled triggers is used, considering the triggers with the lowest-p_{T} thresholds per data-taking period.[1] Using this list of triggers and after data quality selections, the integrated luminosity of the resulting data sample corresponds to about 35 pb^{-1}.

Event selection for the lifetime measurement is similar to the one described in the previous section for the observation of $B^{\pm}$ meson production, with small variations on certain requirements because of the different needs posed by the different fit methods. Muons reconstructed either as combined or segment-tagged are used, requiring at least one combined muon per J/ψ candidate, in order to maintain good mass resolution and signal-to-background ratio. The invariant mass selection for the $B^{\pm}$ candidates

[1] Following official recommendations: (access restricted to ATLAS) `https://twiki.cern.ch/twiki/bin/viewauth/Atlas/MuonTriggerPhysicsTriggerRecommendations`. The list of used triggers is: `EF_mu0_missingRoi`, `EF_mu0_rpcOnly`, `EF_mu0_outOfTime1`, `EF_mu4_MSonly`, `EF_mu6_MSonly`, `EF_mu10_MSonly`, `EF_mu4`, `EF_mu6`, `EF_mu10`, `EF_mu4_DiMu_FS`, `EF_mu4_DiMu`, `EF_2mu4`, `EF_2mu4_DiMu`, `EF_mu4_Jpsimumu`.

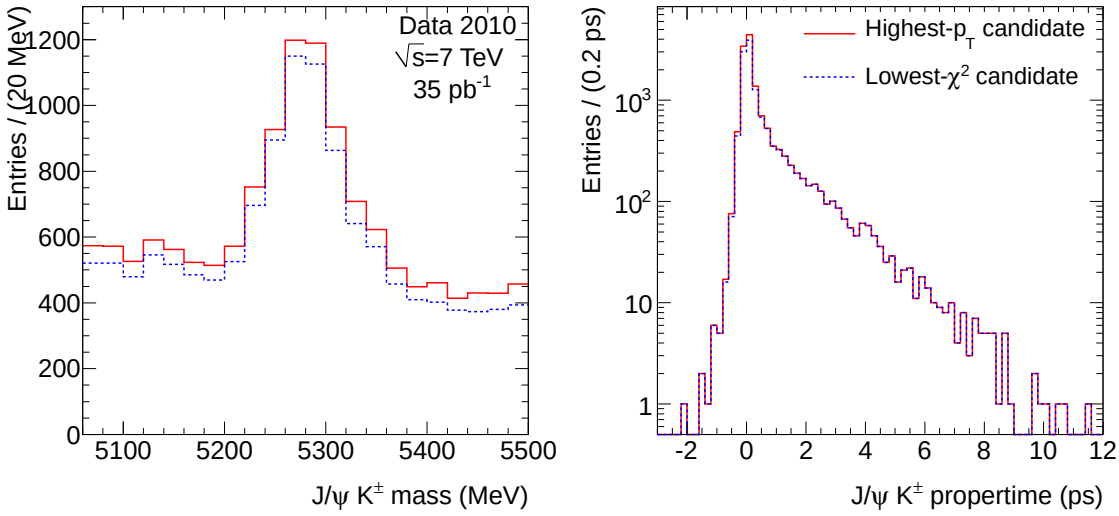

Figure 7.5: Invariant mass (left) and proper decay time (right) of selected $J/\psi\, K^{\pm}$ candidates, using different definitions for the preferred $B^{\pm}$ solution in events where multiple exist. Histograms drawn with a continuous line (red) are obtained using the candidate with the highest p_{T} as the preferred solution and histograms with a dashed line (blue) are obtained using the candidate with the best vertex-fit quality.

is stricter than in the previous section, set to 5060–5500 MeV respectively and is justified later in this Chapter. Moreover, only one $B^{\pm}$ candidate is selected when multiple ones survive all the selection steps in the event; the candidate with the highest p_{T} is selected, which is usually the one having the best vertex fit quality, as well. Following the above selection requirements, we end up with a sample of 13.5k events which is used for the mass-lifetime fit. The invariant mass and proper decay time (defined in the next section) of selected candidates in shown in Figure 7.5. To see the effect of the definition of the preferred solution, when multiple exist, we compare in this Figure the mass and propertime distributions obtained with two different definitions: the first is the one used, where the $B^{\pm}$ candidate with the highest p_{T} is chosen, and the second is using the candidate with the best vertex-fit quality (lowest χ^2) as the preferred solution. The second definition is found to have slightly better background rejection. However, it was found to have a slightly lower signal efficiency in MC simulation, so the first definition is chosen in the analysis, instead.

7.2.2 Definition of proper decay time

For each $B^{\pm}$ meson candidate, the flight distance L from the primary to the secondary vertex ($L \equiv |\vec{L}| = |\vec{r}_B - \vec{r}_{\rm PV}|$) is measured in the lab frame, from which we derive the proper decay time τ using the Lorentz factor:

$$\tau = \frac{t}{\gamma} = \frac{L}{\beta\gamma} = \frac{L \cdot m_{B^{\pm}}}{p} \ , \tag{7.4}$$

where we used the relativistic expressions $\beta = \upsilon/c \equiv \upsilon$ and $p = \gamma m_0 \upsilon$ ($m_0 \equiv m_{B^{\pm}}$) and the world-average value of the $B^{\pm}$ mass for $m_{B^{\pm}}$. Taking the projections of the decay length and momentum on the transverse plane, where the determination of L and p is more accurate, the previous expression becomes

$$\tau = \frac{L_{xy} \cdot m_{B^{\pm}}}{p_{\rm T}} \ , \tag{7.5}$$

where $L_{xy} = \vec{L} \cdot \vec{p_{\rm T}}/p_{\rm T}$, it is the signed projection of the flight distance on the direction of the $B^{\pm}$ transverse momentum, as shown in Figure 7.6. This projection is a better approximation of the decay length, because the momentum is measured with better precision than that of the vertex position (although this may not be evident in the Figure, in which the difference between the direction of the B^{+} transverse momentum and the direction of the primary to the secondary (B^{+}) vertex has been artificially enhanced for demonstration purposes.

More than one primary vertex is usually found in the event, as the average number of interactions goes up to 3.8 in the high-luminosity runs (see Section 6.1). In such events, it is assumed that the $B^{\pm}$ candidate was produced in the vertex whose constituent tracks have the highest $\sum {p_{\rm T}}^2$; this vertex is defined as the primary vertex for the decay length calculation. Different definitions of the primary vertex have been used and point out the same vertex in more than 99% of the times. The result for the lifetime measurement was found to be insensitive to this definition.

For an unbiased calculation of the decay length, the position of the the primary vertex must be determined independently from that of the secondary vertex. It is possible, however, that tracks of a $B^{\pm}$ candidate are selected by the vertexing algorithm to built the primary vertex. In these cases, the primary vertex is refitted

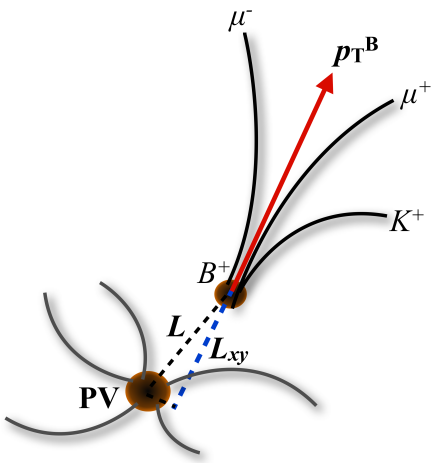

Figure 7.6: Schematic representation of the transverse decay length (L_{xy}) from the primary vertex to the B^+ decay vertex, which is used in the determination of the B^+ proper decay time. It is extracted from the vector pointing from the primary to the B^+ decay vertex ($\boldsymbol{L}$), projected on the direction of the transverse momentum of the B^+ candidate ($\boldsymbol{p_T}^{\boldsymbol{B}}$).

after removing the tracks used to reconstruct the $B^{\pm}$ candidate and the decay-length calculation uses the position of the refitted vertex.

7.2.3 Sources of background

There are various sources of background to the signal process which can be categorized according to their invariant mass shape in the $B^{\pm}$ mass region. Fully and partially reconstructed b-hadron decays contribute to a non-flat invariant mass shape, as can be seen in Figure 7.7.

The decay $B^{\pm} \to J/\psi\,\pi^{\pm}$ where the kaon mass is wrongly assigned to the pion is an example of a fully reconstructed b-hadron decay which is misidentified as a signal decay, and produces a broad resonance structure inside the signal region. This decay is Cabibbo-suppressed with respect to the signal decay with a relative ratio:

$$R = \frac{\mathscr{B}(B^+ \to J/\psi\,\pi^+)}{\mathscr{B}(B^+ \to J/\psi\,K^+)} = 0.048 \pm 0.004 \tag{7.6}$$

according to the world-average values [2] of the branching ratios of the signal and this decay.

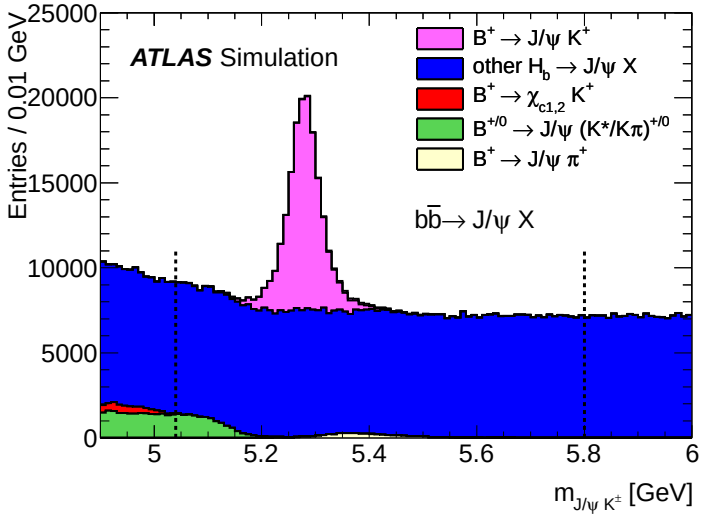

Figure 7.7: The invariant mass of reconstructed $J/\psi\, K^{\pm}$ candidates from fully simulated $b\bar{b} \to J/\psi\ X$ decays, demonstrating various sources of background and the corresponding signal. The dashed lines indicate the chosen fitted region for the cross-section measurement (see next Chapter), while for the lifetime measurement a tighter mass region is used. Other background contributions from J/ψ mesons produced promptly in pp collisions (prompt J/ψ background, see text) are not shown.

From the bulk of partially reconstructed b-hadron decays which can be misidentified as signal decays, we deal with the following decays, as they are resonant in the signal mass region:

- $B^{\pm} \to \chi_c\, K^{\pm} \to \gamma\, J/\psi\, K^{\pm}$, where the energy of the photon is not considered, so the distribution of $m_{J/\psi K}$ is resonant with a peak at about $m_{B^{\pm}} - (m_{\chi_c} - m_{J/\psi})$, where $m_{B^{\pm}}$, m_{χ_c}, $m_{J/\psi}$ are the masses of the respective mesons; above 5.04 GeV the contribution of this background is negligible, so the lower bound of the invariant mass range in which we select $B^{\pm}$ candidates is chosen such that we avoid to include it in the fit model.

- $B^{\pm/0} \to J/\psi\, K^{*\pm/0} \to J/\psi\, (K\,\pi)^{\pm/0}$ and $B^{\pm/0} \to J/\psi\, (K\,\pi)^{\pm/0}$, where the pion is not considered in the construction of the decay vertex, so the distribution of $m_{J/\psi K}$ is resonant with a peak at $m_{B^{\pm}} - m_{\pi}$, where m_{π} is the mass of the pion.

Other partially reconstructed b-hadron decays are either negligible or produce resonant structures outside the signal region and are not considered.

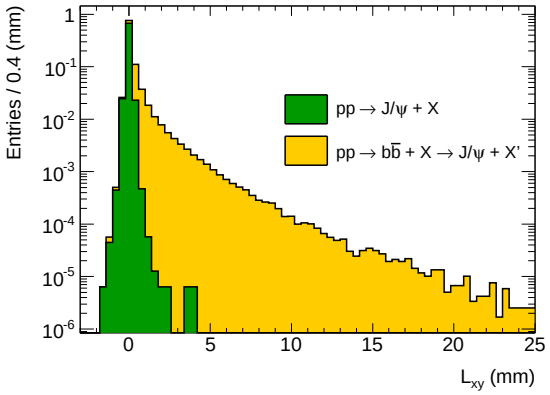

Figure 7.8: Transverse decay length distribution of reconstructed $B^{\pm} \to J/\psi\, K^{\pm}$ candidates in the mass range 5.06–5.5 GeV from simulation. The histograms are the distributions of simulated MC events. The gaussian distribution around zero is the background from fully simulated $pp \to J/\psi(\mu^+\mu^-) + X$ events (prompt background). The distribution with the long-lived tail is from simulated $b\bar{b} \to J/\psi(\mu^+\mu^-) + X$ events, in which the signal process is also included. The sum of the two MC distributions is normalized to unity, with a relative normalization of the non-prompt component over total of 0.28 [6].

The resonant backgrounds that were described above, sit on top of combinatorial background, which is either random combinations of J/ψ mesons or of dimuon from b-hadron decays with a random track.

These random combinations are referred to as combinatorial background, which is the dominant background in this analysis.[1] Events from promptly produced J/ψ mesons will be referred to as *prompt* J/ψ background, while events from J/ψ that originate from a b-hadron decay will referred to as *non-prompt* J/ψ background. The distinction between these two components is evident when measuring the displacement of the $B^{\pm}$ candidate from the primary vertex. For example, Figure 7.8 shows the transverse decay length for these two sources of J/ψ mesons from simulation.

Besides the combinatorial background originating from $b\bar{b} \to J/\psi + X$ decays, the non-resonant dimuon+X combinatorial background from $b\bar{b}$ and $c\bar{c}$ decays is found to be negligible. It was evaluated by looking at the sidebands of the J/ψ signal peak

[1]This is a reducible background which in principle can be suppressed with both secondary-vertex displacement and direction requirements; however, it was chosen not to implement these requirements in the present work.

in the dimuon invariant mass distribution.

7.2.4 Mass-lifetime fit method

An unbinned maximum likelihood fit to the reconstructed invariant mass and proper decay time of the selected candidates is performed to extract the mass and lifetime of the $B^{\pm}$ meson. The invariant mass and the propertime are fitted simultaneously in order to disentangle the signal from long-lived background which originates mainly from b-hadrons decaying to J/ψ which are only partially reconstructed. The likelihood function is

$$\mathscr{L} = \prod_{i=1}^{N} P\left(m_i, \tau_i | m_s, \tau_s\right) = \prod_{i=1}^{N} \left[f_s \cdot S_m \cdot S_\tau + (1 - f_s) \cdot B_m \cdot B_\tau\right] \ , \tag{7.7}$$

where m_i and τ_i is the invariant mass and propertime of the i-th $B^{\pm}$ candidate, m_s and τ_s is the $B^{\pm}$ mass and lifetime (parameters of interest). The total number of selected $B^{\pm}$ candidates is denoted by N and the fraction of signal events is f_s, so that the number of signal events is given by $f_s \cdot N$. With S_m, S_τ we denote the probability density functions (pdfs) modeling the signal mass and propertime distributions. Similarly, B_m and B_τ are pdfs for the mass and propertime distributions of the background, respectively.

The invariant mass shape of the signal is dominated by the detector resolution, assumed to be gaussian, so the signal pdf is

$$S_m \equiv S_m(m_i | m_s, \sigma_m) = \frac{1}{\sqrt{2\pi}\sigma_m} \exp\left[-\frac{(m_i - m_s)^2}{2\sigma_m^2}\right] \ , \tag{7.8}$$

where σ_m is the mass resolution. The signal pdf for the proper decay time is an exponential of slope τ_s, smeared with the detector resolution,

$$S_\tau \equiv S_\tau(\tau_i, \delta_{\tau_i} | \tau_s) = \exp\left(-\frac{\tau_i'}{\tau_s}\right) \otimes R_\tau(\tau_i' - \tau_i, \delta_{\tau_i}) \ , \tag{7.9}$$

where $\delta_{\tau_i} = s_\tau \cdot \sigma_{\tau_i}$, it is the per-candidate error of the proper decay time returned by the vertexing algorithm, σ_{τ_i}, scaled by a constant, s_τ, and R_τ is the propertime resolution function:

$$R_\tau \equiv R_\tau(\tau_i, \delta_{\tau_i}) = \frac{1}{\sqrt{2\pi}\delta_{\tau_i}} \exp\left(-\frac{\tau_i^2}{2\delta_{\tau_i}^2}\right) \ . \tag{7.10}$$

The scaling factor s_τ should equal one if the track parameter errors are gaussian and their propagation in the propertime calculation is done properly. We allow for a small scaling of the per-candidate errors as a fine-tuning parameter in the fit and also as a cross-check of the error calculation.

The background has two components; one is for the description of the prompt J/ψ background, and another is for the non-prompt J/ψ background:

$$\begin{aligned} B_m &= f_{b1} B_m^{\text{prompt}} + (1 - f_{b1}) B_m^{\text{non-prompt}} \\ B_\tau &= f_{b1} B_\tau^{\text{prompt}} + (1 - f_{b1}) B_\tau^{\text{non-prompt}} \ , \end{aligned} \tag{7.11}$$

with f_{b1} being the fraction of the prompt component. The prompt J/ψ background is flat in invariant mass ($B_m^{\text{prompt}} \equiv 1$) . It is of zero lifetime and its proper time distribution is defined by the resolution model R_τ. An additional component is considered for the description of badly reconstructed candidates appearing as exponential tails of this background component in the proper decay time distribution, so the propertime pdf for the prompt J/ψ background is

$$\begin{aligned} &B_\tau^{\text{prompt}} \equiv B_\tau^{\text{prompt}}(\tau_i, \delta_{\tau_i}, b_1, \tau_0) = \\ &= b_1 \frac{1}{\sqrt{2\pi}\delta_{\tau_i}} \exp\left(-\frac{\tau_i^2}{2\delta_{\tau_i}^2}\right) + (1 - b_1) \exp\left(-\frac{|\tau_i'|}{\tau_0}\right) \otimes R_\tau(\tau_i' - \tau_i, \delta_{\tau_i}) \ , \end{aligned} \tag{7.12}$$

where b_1 is the fraction of the gaussian-like component and τ_0 is the propertime slope of a symmetric exponential around zero, convolved with the resolution function R_τ. The non-prompt background has two components. The first represents the partially reconstructed b-hadron decays like

$$B^{\pm/0} \to J/\psi\, K^{*\pm/0} \to J/\psi\, (K\,\pi)^{\pm/0} \ \ , \ B^{\pm/0} \to J/\psi\, (K\,\pi)^{\pm/0} \ , \tag{7.13}$$

where in the final state the pion is not associated to the vertex of the $B^{\pm}$ candidate. The energy of the missing pion affects the invariant mass shape by shifting the reconstructed $B^{\pm}$ mass to lower values and the resulting shape can be described with a complementary error function:

$$\text{erfc}(m_i) = 1 - \text{erf}\left(\frac{m_i - m_0}{s_0}\right) \ , \tag{7.14}$$

where m_0 is the position of the center of the function, approximately a pion mass lower than the $B^{\pm}$ mass, and s_0 is the slope of the error function. Not considering the pion in the reconstruction of the $B^{\pm}$ momentum affects its direction with respect to the direction of the original b-hadron, therefore L_{xy} is always underestimated and results in shorter lifetime than that of the b-hadron. The second component of the non-prompt J/ψ background is the case where the J/ψ meson from a b-hadron decay is combined with a random track not originating from the same decay. The resulting invariant mass shape is non-resonant and is modelled with an exponential. The resulting proper-lifetime of this component is mostly shorter than that of the actual b-hadron, as its direction is poorly represented by the $B^{\pm}$ candidate and L_{xy} is underestimated, and it also has a longer lifetime component. Then according to the above, the mass pdf for the non-prompt J/ψ background is written as

$$\begin{aligned} B_m^{\text{non-prompt}} &\equiv B_m^{\text{non-prompt}}(m_i, |m_0, s_0, s_1, b_{m1}) = \\ &= b_{m1} \exp\left(-\frac{m_i}{s_1}\right) + (1 - b_{m1}) \operatorname{erfc}(m_i | m_0, s_0) \ , \end{aligned} \tag{7.15}$$

where s_1 is slope of the exponentially dropping invariant mass of the non-prompt J/ψ background and $b_{\tau 1}$ is its fraction. The proper time pdf for the non-prompt background is given from the addition of two exponentials convolved with the resolution function R_τ:

$$\begin{aligned} B_\tau^{\text{non-prompt}} &\equiv B_\tau^{\text{non-prompt}}(\tau_i, \delta_{\tau_i} | \tau_{\text{eff1}}, \tau_{\text{eff2}}, b_{\tau 1}) = \\ &= \left[b_{\tau 1} \exp\left(-\frac{\tau_i'}{\tau_{\text{eff1}}}\right) + (1 - b_{\tau 1}) \exp\left(-\frac{\tau_i'}{\tau_{\text{eff2}}}\right) \right] \otimes R_\tau(\tau_i' - \tau_i, \delta_{\tau_i}) \ , \end{aligned} \tag{7.16}$$

with τ_{eff1}, τ_{eff2} being the effective lifetimes for the two constituents of the non-prompt J/ψ background (one being of short lifetime, 'short-lived', and the other being of longer lifetime, 'long-lived') and $b_{\tau 1}$ is the fraction of the first. The $B^{\pm} \to J/\psi\, \pi^{\pm}$ background is not modelled in the mass-lifetime fit as to keep the number of fit parameters to a minimum. It was found that it does not affect the fit results because of its small contribution. Considering the lifetime, it can be treated as signal, while it has a small effect on the $B^{\pm}$ mass position.

The full list of parameters used in the mass-lifetime fit is given in Table 7.1, along with the results of the fit to data for each parameter. The projections of the likelihood

Parameter	Fit value	Description
Signal mass pdf (S_m)		
m_s	5278.4 ± 0.8 MeV	$B^{\pm}$ mass
σ_m	33.9 ± 0.9 MeV	mass resolution
f_s	0.228 ± 0.005	signal fraction
Signal propertime pdf (S_τ)		
τ_s	1.63 ± 0.04 ps	$B^{\pm}$ lifetime
Background mass pdf (B_m)		
s_1	-0.0012 ± 0.0005	slope of exponential
m_0	5168 ± 12 MeV	center of error function
s_0	30 ± 15	slope of error function
b_{m1}	0.91 ± 0.04	fraction of exponential
Background propertime pdf (B_τ)		
f_{b1}	0.67 ± 0.01	fraction of prompt J/ψ b/g
b_1	0.91 ± 0.02	fraction of gaussian core of prompt J/ψ b/g
$b_{\tau 1}$	0.42 ± 0.03	fraction of 'long-lived' non-prompt b/g
τ_{eff1}	1.44 ± 0.08 ps	lifetime of 'long-lived' non-prompt b/g
τ_{eff2}	0.22 ± 0.02 ps	lifetime of 'short-lived' non-prompt b/g
τ_0	0.23 ± 0.03 ps	lifetime (exponential tails) of prompt b/g
s_τ	1.04 ± 0.02	per-candidate error scaling factor

Table 7.1: Parameters used in the mass-lifetime likelihood fit. The quoted values are the results of the fit with statistical uncertainty.

function on binned data of the invariant mass and proper decay time are shown in Figure 7.9. The quality of the fit is indicated by the pull distributions of the resulting fit, shown in the same figure. Pulls are defined as

$$\text{pull} = \frac{n_{\text{data}} - n_{\text{fit}}}{\delta n_{\text{data}}} \ , \tag{7.17}$$

where n_{data} is the number of candidates in a given bin in data, with a statistical uncertainty of δn_{data}, and n_{fit} is the prediction of the fit. The values obtained for the reconstructed $B^{\pm}$ mass and lifetime are

$$m_{B^{\pm}} = 5278.4 \pm 0.8 \text{ MeV} \ , \ \tau_{B^{\pm}} = 1.63 \pm 0.04 \text{ ps} \ ,$$

both consistent with the world-averaged values. The results of the fit for all parameters are given in Table 7.1.

A detailed study of systematics including effects of the detector alignment, expected to be 1-2% [7], was not performed for the purposes of this study, as with this

fit we aimed to provide a test of the ID performance and not a precision measurement. However, the stability of the fit has been validated with variations in the event selection and the fit model. The variations in the event selection include the choice of the invariant mass range, the definition of primary vertex and using or not all multiple solutions and, if not, changing the definition of the preferred solution, when multiple exist. The variations of the fit model include the choice of signal and background mass pdf and the choice of different scaling factors for the signal and background. In all cases, the resulting values for the $B^{\pm}$ mass and lifetime do not change, within their statistical precision. To conclude, the results of this test demonstrate the excellent performance of the ATLAS inner detector and muon spectrometer with the very first data from LHC.

Bibliography

[1] C. ATLAS, *Observation of the $B^{\pm} \to J/\psi(\mu^+\mu^-)K^{\pm}$ resonance in ATLAS*, Tech. Rep. ATLAS-CONF-2010-098, CERN, Geneva, Sep, 2010.

[2] J. Beringer et al., *Review of Particle Physics*, Phys. Rev. **D 86** (2012) 010001.

[3] ATLAS Collaboration, *Luminosity determination using the ATLAS Detector*, Tech. Rep. ATLAS-CONF-2010-060. `http://cds.cern.ch/record/1281333`.

[4] V. Kostyukhin, *VKalVrt - package for vertex reconstruction in ATLAS*, Tech. Rep. CERN-ATL-PHYS-2003-031. `http://cds.cern.ch/record/685551`.

[5] ATLAS Collaboration, *First observation of the $J/\psi \to \mu^+\mu^-$ resonance in ATLAS pp collisions at $\sqrt{s} = 7$ TeV*, Tech. Rep. ATLAS-CONF-2010-045. `http://cds.cern.ch/record/1277685`.

[6] ATLAS Collaboration, *Measurement of the differential cross-sections of inclusive, prompt and non-prompt J/ψ production in proton-proton collisions at $\sqrt{s} = 7$ TeV*, Nucl. Phys. **B 850** (2011) 387, `arXiv:1104.3038 [hep-ex]`.

[7] *Measurement of the Average B Lifetime with the ATLAS Detector*, Tech. Rep. ATLAS-CONF-2011-145, CERN, Geneva, Oct, 2011.

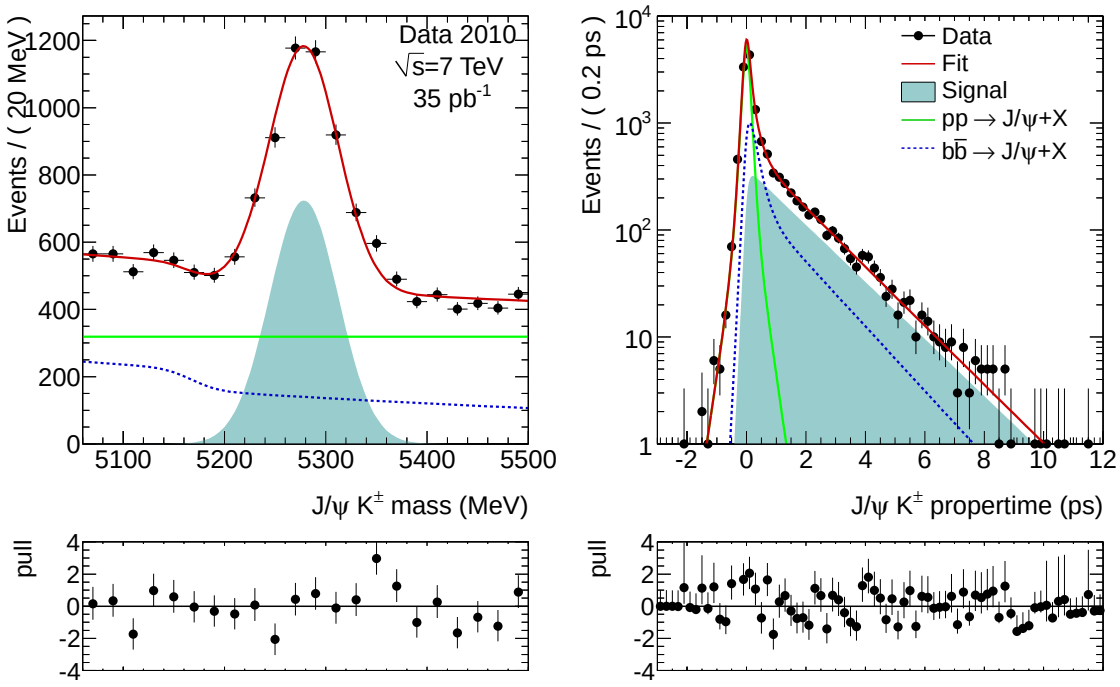

Figure 7.9: The invariant mass (left) and proper decay time (right) distributions of reconstructed $B^{\pm}$ candidates from data. The red line is the projection of the unbinned simultaneous likelihood fit to the invariant mass and proper time of $B^{\pm}$ candidates. The fit has separate components for the signal, prompt and non-prompt J/ψ background, also shown in the figure. A total of about 3080 signal events are found in the data sample, with mass 5278.4 ± 0.8(stat.) GeV and lifetime 1.63 ± 0.04(stat.) ps . Below each figure, the pull distributions are shown for the comparison of the fit result to data.

Chapter 8

Cross-section measurement of B^+ production

Measurements of B-meson production are important for the understanding of the b-quark properties. In this Chapter, the results for the differential cross-section of B^+ production are presented as a function of transverse momentum and rapidity. Note that results are reported for B^+ meson production, but are derived from both charged states using $B^\pm \to J/\psi\, K^\pm$ decays, under the assumption that in the phase space accessible by this measurement the B^+ and B^- production cross-sections are equal. This assumption is in agreement with the predictions of NLO Monte Carlo generators and is also valid within the precision of the measurement, as will be shown later in this Chapter, where the results are presented. Comparisons of the measured cross-sections with theoretical predictions from different approaches that were discussed in Section 1.5 are also shown. The shapes of $\mathrm{d}\sigma/\mathrm{d}p_\mathrm{T}$ and $\mathrm{d}\sigma/\mathrm{d}y$ can be used to probe the fragmentation mechanism and also basic attributes of the theory predictions, such as the factorization/renormalization scale dependence. As it will be shown, the theoretical uncertainties, mainly due to the scale dependence, are large (up to 40%), while the experimental measurements can reach much better precision. This makes measurements of b-hadron production useful for the comparisons with theory and also important for experimental purposes, in order to have more accurate determinations of $b\bar{b}$ production as a background to many interesting processes and searches for new

particles, like the search for the Higgs boson in its decay to a $b\bar{b}$ pair.

8.1 Outline of the measurement

The differential cross-section for B^+ meson production in pp collisions is given by

$$\frac{\mathrm{d}^2\sigma(pp \to B^+X)}{\mathrm{d}p_\mathrm{T}\mathrm{d}y} \cdot \mathscr{B} = \frac{N^{B^+}}{L_\mathrm{int} \cdot \Delta p_\mathrm{T} \cdot \Delta y} \ , \tag{8.1}$$

where $\mathscr{B}$ is the total branching ratio of the signal decay, which is $(6.03 \pm 0.21) \times 10^{-5}$, obtained by combining the world averaged values of the branching ratios for $B^+ \to J/\psi\, K^+$ and $J/\psi \to \mu^+\mu^-$ [1], N^{B^+} is the number of $B^+ \to J/\psi\, K^+$ signal decays produced, $L_\mathrm{int} \equiv \int L\, \mathrm{d}t$ is the integrated luminosity of the data sample and Δp_T, Δy are the widths of p_T and y intervals. Assuming that B^+ and B^- mesons are produced in equal numbers[1], N^{B^+} is derived from the average yield of the two reconstructed charged states in a (p_T, y) interval, after correcting for detector effects and acceptance:

$$N^{B^+} = \frac{1}{A}\frac{N^{B^+}_\mathrm{reco}}{\varepsilon^{B^+}} = \frac{1}{A}\frac{N^{B^-}_\mathrm{reco}}{\varepsilon^{B^-}} = \frac{1}{A}\frac{N^{B^\pm}_\mathrm{reco}}{\varepsilon^{B^+} + \varepsilon^{B^-}} \ , \tag{8.2}$$

where $N^{B^\pm}_\mathrm{reco}$ is the number of reconstructed signal events, obtained from data with a fit to the invariant mass distribution of $B^\pm$ candidates, A is the acceptance of the kinematic cuts imposed on the final state particles of the signal decay and $\varepsilon^{B^{+(-)}}$ are efficiency factors for the reconstructed $B^{+(-)}$ signal decays. Regarding the efficiency factors $\varepsilon^{B^{+(-)}}$, separate corrections are needed for B^+ and B^- signal decays, because the different interaction cross-section of K^+ and K^- with the detector material results in different reconstruction efficiencies for the two charged mesons. After giving the details on the used data sample and the describing the event selection in Section 8.2, the method for the extraction of the number of signal events $N^{B^\pm}_\mathrm{reco}$ is explained in Section 8.3. More details about the correction factors A and $\varepsilon^{B^{+(-)}}$ are given in Section 8.4.

[1]This assumption was tested with NLO MC and was found to be accurate to about 99.5% in the phase space accesible by ATLAS. Later in this Chapter, where results from data are reported, it is shown that the assumption of equal B^+ and B^- production is valid within the presicion of the available data.

8.2 Data sample and event selection

The first half of the full 2011 data sample is used for the $B^{\pm}$ cross-section measurement. Events for the analysis were selected with a dimuon trigger that was unprescaled during this data-taking period. The used trigger requires two muon ROIs at Level-1 without requirements on p_{T}. A full track reconstruction of dimuon candidates was performed by the HLT (Level-2 and EF) where both muons were required to have $p_{\mathrm{T}} > 4$ GeV. At the EF level, a dedicated B-physics algorithm (`EF_2mu4_Jpsimumu`) was used to apply additional requirements, loosely selecting events compatible with J/ψ mesons decaying into a muon pair. Specifically, the muons had to be of opposite charge and fit successfully to a common vertex. The quality of the vertex fit was required to be good ($\chi^2/N_{\mathrm{d.o.f.}} < 10$) and the invariant mass of the dimuon had to be in the J/ψ signal region (2.5–3.5 GeV). Using this trigger and after data quality selections, the resulting data sample corresponds to 2.4 pb^{-1} (see also Section 6.1).

As for the $B^{\pm}$ observation analysis and lifetime measurement, tracks reconstructed in the ID that are matched to tracks reconstructed in the MS are selected as muon candidates. Tracks selected as muon or $K^{\pm}$ candidates are subject to the same selection criteria, which are given in Appendix B.

The event must contain at least a reconstructed primary vertex with at least three associated tracks. Then to identify J/ψ candidates, the procedure is the same as described in previous Chapter for the observation and lifetime measurement. For the cross-section measumerent, only combined muons are considered for the formation of J/ψ candidates. This ensures that high-quality muons are used in the analysis, offering better resolution in J/ψ mass, lower background rates and are accompanied by precise reconstruction efficiency measurements. In analysis of 2010 data, the use of segment-tagged muons was imperative in order to increase the signal yield, while this is not an issue in the analysis of the bulk of 2011 data.

Thus, $J/\psi \to \mu^+\mu^-$ candidates are selected in a wide mass range 2.7–3.5 GeV, found to be 100% efficient for selecting signal events. No further vertex quality requirement is posed on J/ψ candidates, other than the $\chi^2/N_{\mathrm{d.o.f.}}$ selection on trigger level. Due to the trigger acceptance, muons can be identified in the range $|\eta| <$

2.4. However the trigger efficiency measurement is limited to $|\eta| < 2.3$, because of poor statistics at the edge of the acceptance. To ensure that accurate efficiency measurements are used, J/ψ candidates are required to have $|y^{\mu\mu}| < 2.25$ and the muons are required to have $p_{\mathrm{T}} > 4$ GeV and $|\eta| < 2.3$. In each event, the muons of the J/ψ candidates are required to be the ones that fired the trigger, so both offline reconstructed muons must match a EF trigger object in ϕ and η, requiring $\Delta R = \sqrt{(\Delta\phi)^2 + (\Delta\eta)^2} < 0.01$. If multiple J/ψ candidates are found in the event, we consider all of them in the formation of $B^{\pm}$ candidates.

The muon tracks of the selected J/ψ candidates are again fitted to a common vertex with an additional third track with p_{T} greater than 1 GeV. The three-track vertex fit is performed by constraining the muon tracks to the J/ψ mass [1]. The $K^{\pm}$ mass is assigned to the third track and the $\mu^+\mu^- K^{\pm}$ invariant mass is calculated from the refitted track parameters returned by the vertexing algorithm. Regarding the quality of the three-track vertex fit, a global χ^2 involving all three tracks is used and must be $\chi^2/N_{\mathrm{d.o.f.}} < 6$. This selects about 99% of signal events while rejecting more than 60% of total background events (more details will be given in Section 8.4.6). We retain B^+ and B^- candidates with $p_{\mathrm{T}} > 9$ GeV and $|y| < 2.25$ in the mass range 5.040–5.800 GeV (Figure 8.1). The number of selected $B^{\pm}$ candidates per event is shown in Figure 8.2 and the average candidate multiplicity is 1.3. Multiple $B^{\pm}$ candidates result mainly from random combinations of tracks with selected J/ψ mesons produced promptly in pp collisions. More than 90% of the signal is found in events with only one $B^{\pm}$ candidate. Although a veto on events with multiple candidates could improve the signal over background ratio (which was done for the lifetime measurement), we choose to allow multiple solutions in order to avoid the determination of the signal rejection for such a veto. Figure 8.3 shows the invariant mass distribution for events with more than one $B^{\pm}$ candidates ($N_{B^{\pm}} > 1$), where it can be clearly seen that there is a small signal contribution. Moreover, the low and high-mass sidebands of the $B^{\pm}$ signal region in this distribution show that multiple combinatorial solutions result in non-resonant background which is trivial to model and cannot affect the estimation of the signal yield.

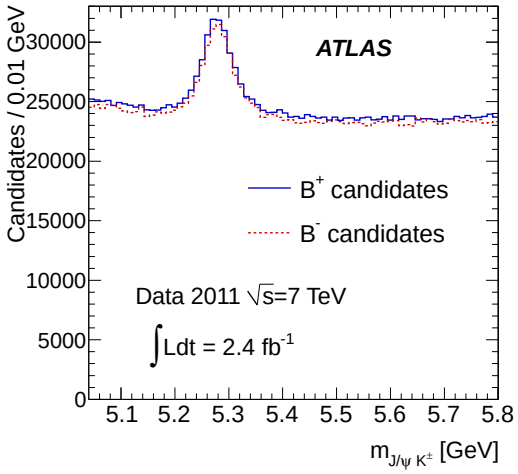

Figure 8.1: Histograms of the invariant mass of the selected B^+ (continuous line) and B^- (dashed line) candidates. No efficiency correction is applied. The lower yield of B^- with respect to B^+ candidates is due to the different reconstruction efficiencies for positively and negatively charged hadrons (pions, kaons), resulting from different interaction cross sections with the detector material.

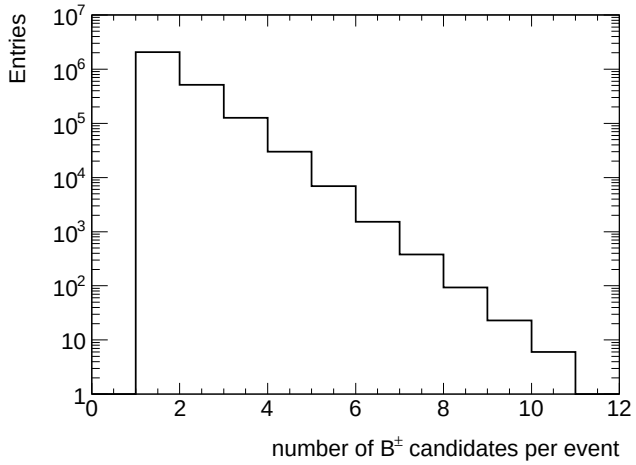

Figure 8.2: $B^{\pm}$ candidate multiplicity after all selection cuts have been applied.

8.3 Signal yield extraction

The number of signal events (signal yield) is obtained from data with a binned maximum likelihood fit to the invariant mass of the selected candidates. The choice of a binned likelihood instead of the unbinned likelihood that was used in the ob-

servation and mass-lifetime analysis (see Chapter 7) is motivated by the large size of the data sample. The binned likelihood fit is much faster and allows many studies of systematics to be performed. The various sources of background were identified and categorized according to their behaviour in the invariant mass spectrum in Section 7.2.3. First, the likelihood function is defined in Section 8.3.1, along with the probability density functions (pdfs) for the modeling of the signal and background. Then the parameters for signal and background pdfs are extracted from MC simulation, as explained in Sections 8.3.2 and 8.3.3. Finally, the fits to the data are performed in intervals of p_{T} and $|y|$ of the $B^{\pm}$ mesons, and the results are reported in Section 8.3.4.

8.3.1 Likelihood

To obtain the signal yield from a given invariant mass distribution, a binned maximum likelihood method is used. The likelihood function is defined by:

$$\mathscr{L} = \prod_{i=1}^{N} P\left(m_i|f_s\right) = \prod_{i=1}^{N} \left[f_s \cdot S(m_i|\boldsymbol{\alpha}_s) + (1-f_s) \cdot B(m_i|\boldsymbol{\alpha}_b)\right] \ , \tag{8.3}$$

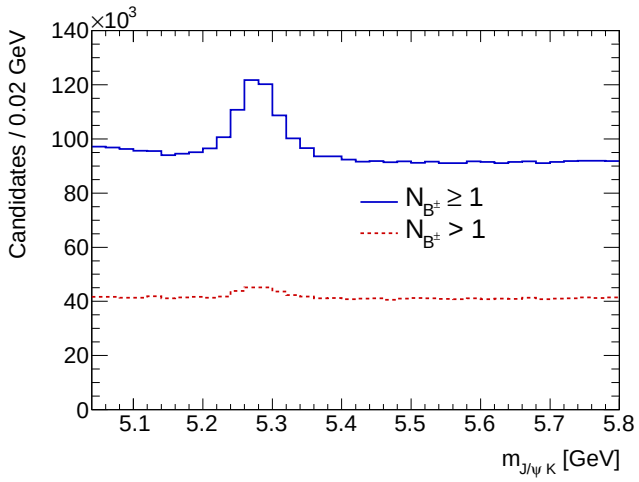

Figure 8.3: Shown with the continuous line is the invariant mass histogram of selected $B^{\pm}$ candidates. The invariant mass of candidates coming from events with multiple $B^{\pm}$ solutions (which is a subset of all selected candidates) is shown with the dashed line histogram. Such events are enriched in background with a flat mass shape while there is a small but non-zero signal contribution.

where m_i is the number of counts in the i-th bin of $J/\psi\, K^{\pm}$ invariant mass, f_s is the signal fraction (parameter of interest) and $\boldsymbol{\alpha}_s$, $\boldsymbol{\alpha}_b$ are sets of nuisance parameters which enter the signal and the background pdfs, S and B, respectively. The number of bins is denoted by N and the total number of selected $B^{\pm}$ candidates is given by $\sum_{i=1}^{N} m_i$, which multiplied by f_s returns the number of signal events. In the next paragraphs, we give the definitions of the signal and background pdfs, and motivate the choice of function for the description of each component in the fit.

The invariant mass shape of the signal is dominated by the resolution of the detector which, to a good approximation, follows a gaussian profile. The signal pdf is defined as the sum of two gaussians with fractions f_1 and $1-f_1$, and different widths σ_1, σ_2, both centered at the reconstructed mass of $B^{\pm}$, $m_{B^{\pm}}$:

$$S(m_i|\boldsymbol{\alpha}_s) \equiv S(m_i|f_1,\sigma_1,\sigma_2,m_{B^{\pm}}) = f_1 \cdot G(m_i|m_{B^{\pm}},\sigma_1) + (1-f_1)\cdot G(m_i|m_{B^{\pm}},\sigma_2) \tag{8.4}$$

where $G(m_i|\mu,\sigma) = \frac{1}{\sqrt{2\pi}\sigma}\exp\left[-\frac{(m_i-\mu)^2}{2\sigma^2}\right]$. The second gaussian is considered in order to account for the fact that not all events have the same resolution.

The pdf includes three components for the background. The partially reconstructed b-hadron decays where the pion of the decay is not associated to the decay vertex (see Section 7.2.3 have an invariant mass which has a turn-on shape, due to a constant amount of missing energy corresponding to a pion mass. The mass of these decays is modeled with a complementary error function. The $B^{\pm} \to J/\psi\,\pi^{\pm}$ decay, in which the kaon mass is wrongly assigned to the pion, produces resonant mass shape similar to the signal, but the wrong mass assignment causes the mass distribution of this decay to be displaced with respect to the $B^{\pm}$ mass, have worse resolution and a high-mass tail; a Crystal Ball function is used to model this background. Last, the remaining background is mainly combinatorial and its invariant mass distribution is modeled with an exponential function. The total background pdf is

$$\begin{aligned} B(m_i|\boldsymbol{\alpha}_b) &\equiv B(m_i|f_2,m_0,s_0,f_3,m_c,\sigma_c,\alpha_c,n_c,\beta) \\ &= f_2\cdot \mathrm{erfc}(m_i|m_0,s_0) + f_3\cdot C(m_i|m_c,\sigma_c,\alpha_c,n_c) + (1-f_2-f_3)\cdot\exp(\beta\cdot m_i)\ . \end{aligned} \tag{8.5}$$

In the above, the complementary error function, erfc, is defined as:

$$\mathrm{erfc}(m_i|m_0, s_0) = 1 - \mathrm{erf}\left(\frac{m_i - m_0}{s_0}\right) \tag{8.6}$$

where m_0, s_0 are two parameters which determine the position and the slope of the error function, and the Crystal Ball function, C, is defined as:

$$C(m_i|m_c, \sigma_c, \alpha_c, n_c) =$$

$$= \begin{cases} \frac{1}{\sqrt{2\pi}\sigma_c} \exp\left[-\frac{(m_i - m_c)^2}{2\sigma_c}\right], & \text{for } \frac{m_i - m_c}{\sigma_c} > -\alpha_c \\ \frac{1}{\sqrt{2\pi}\sigma_c} \left(\frac{n_c}{|\alpha_c|}\right)^{n_c} \exp\left(-\frac{|\alpha_c|^2}{2}\right) \left(\frac{n_c}{|\alpha_c|} - |\alpha_c| - \frac{m_i - m_c}{\sigma_c}\right)^{-n_c}, & \text{for } \frac{m_i - m_c}{\sigma_c} \leq -\alpha_c \end{cases} \tag{8.7}$$

where m_c and σ_c define the mean and width of the gaussian component of the Crystal Ball function, n_c is a power-law exponent and α_c defines the transition point between the gaussian and the power-law function.

8.3.2 Signal modeling

A sample of fully simulated signal events is used to study and extract their invariant mass shape. We require that selected $B^\pm$ candidates are matched to a true signal decay in order to remove combinatorial background events formed by a J/ψ meson from a signal decay and a random track from the decay of the other b-quark or from a pile-up vertex. To describe the invariant mass of signal events, we use the sum of two gaussians as it was explained in eq. 8.4. Then the fit is performed in (p_T, y) intervals to extract the values of the parameters which define the shape of the signal pdf, which are σ_1, σ_2 and f_1. The mass position is used as a free parameter when fitting the four rapidity intervals, integrated over p_T, as shown in Figure 8.4. The derived mass value from the fit in a given rapidity interval is then fixed when fitting all the p_T intervals of this rapidity. This is done to avoid fluctuations of $m_{B^\pm}$ in bins with low statistics, taking into account that $m_{B^\pm}$ does not depend on p_T. The fits to MC-simulated signal events in (p_T, y) intervals are shown in Figure 8.5. The values of the signal pdf parameters (σ_1, σ_2, f_1) change significantly with p_T and $|y|$. We use the weighted average of the widths of the two gaussian components of the signal pdf,

$\langle\sigma\rangle = f_1\sigma_1 + (1-f_1)\sigma_2$, as a measure of the mass resolution; its p_{T} and y dependence is shown in Figure 8.6. In Figure 8.4, the result of the fit to the invariant mass of simulated signal events in four rapidity regions is shown, and the selected function for the invariant mass describes the signal very well.

8.3.3 Background modeling

The complementary error function that is used to model the partially reconstructed b-hadron decays was given in Equation (8.6). Its position and shape are determined from the parameters m_0 and s_0, respectively. The slope of the error function is correlated to the mass resolution, so it is expected to vary with rapidity. To obtain the values for these parameters, a binned maximum likelihood fit is performed to a subset of the fully simulated inclusive $b\bar{b} \to J/\psi\, X$ sample, selecting only the b-hadron decays in which a final-state pion is not considered in the reconstruction of the b-hadron decay vertex (see previous section). In Figure 8.7, the result of the fit in four rapidity regions is shown and the invariant mass distribution of these background events is found to be well-described with the selected function. Then the fit is performed in (p_{T}, y) intervals, to extract the values of the parameters m_0, s_0, which define the shape of the function. The fits are shown in Figure 8.8, and the resulting values of the parameters are shown in Figure 8.9 and 8.10. A small variation of these parameters with p_{T} and y of the $B^{\pm}$ candidate is seen. In the fits for the cross-section, the pdf parameters for this background are constrained to the values obtained for the corresponding fit to the events from MC simulation.

The $B^{\pm} \to J/\psi\,\pi^{\pm}$ decay is modeled with the Crystal Ball function that was defined in Equation (8.7). The shape of this function is also expected to vary with rapidity due to detector resolution. We extract the shape of this background in four rapidity regions, neglecting the p_{T} variation of the mass shape, which is small. This is also done with a binned maximum likelihood fit to the mass of $B^{\pm} \to J/\psi\,\pi^{\pm}$ events that are extracted using MC truth information from the simulated $b\bar{b} \to J/\psi\, X$ sample. The fits are shown in Figure 8.11.

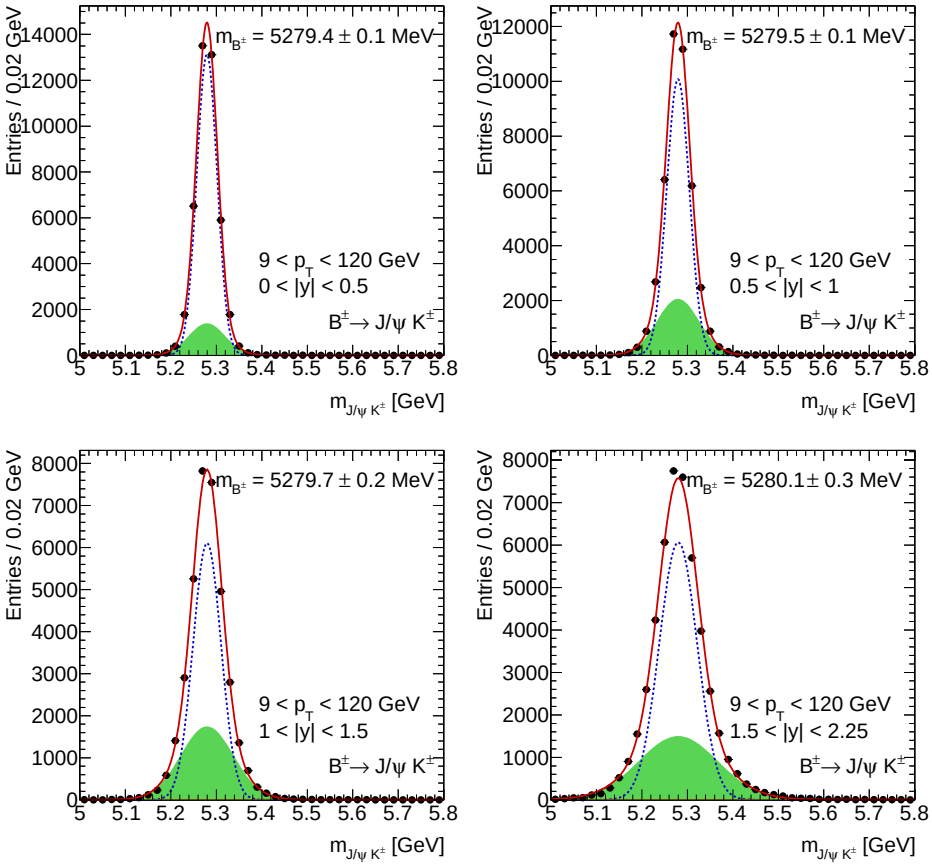

Figure 8.4: Invariant mass distributions of fully simulated $B^\pm \to J/\psi\, K^\pm$ decays in four rapidity intervals. Each interval contains about 40k reconstructed events. The points with error bars are simulated data and the solid line is the result of the binned maximum likelihood fit. The likelihood function is the sum of two gaussians, shown with a dashed line and a solid area, respectively. The quoted numbers are the resulting values of the reconstructed $B^\pm$ mass in each interval.

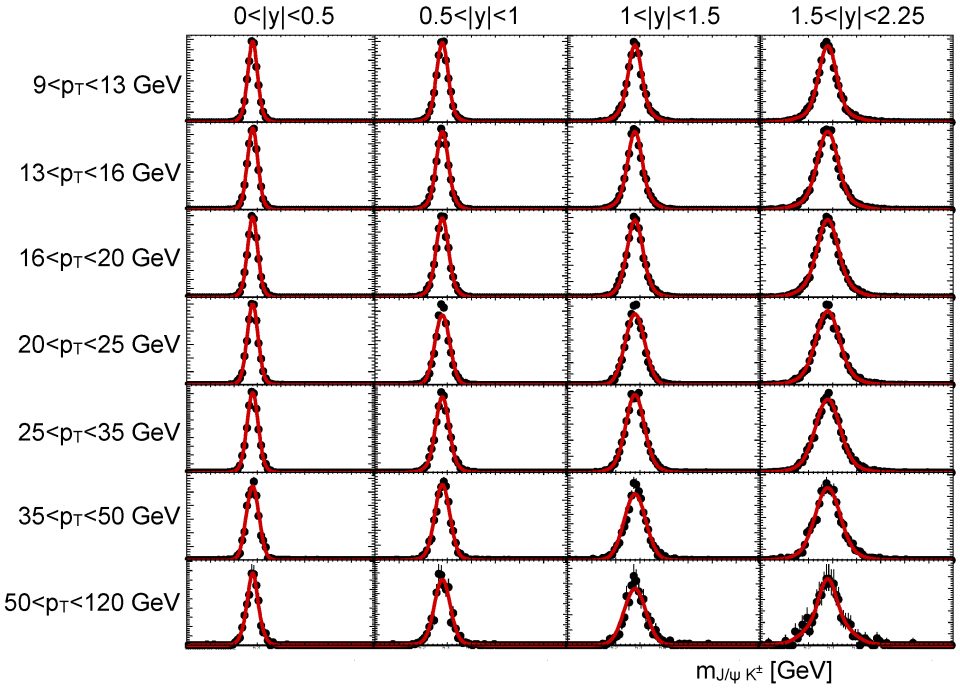

Figure 8.5: The invariant mass distributions of fully simulated signal decays in (p_{T}, y) intervals. Points are simulated data. The solid line is the result of a binned maximum likelihood fit in mass range 5.0–5.8 GeV (same for all subfigures), using the sum of two gaussians to describe the mass shape of the selected events.

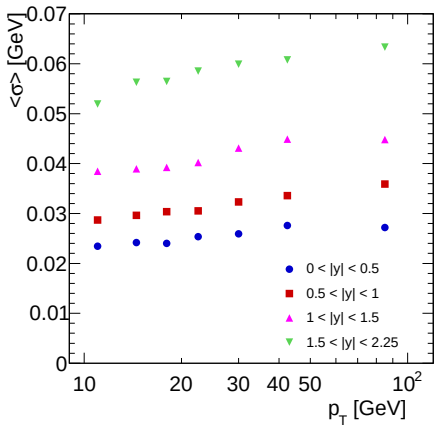

Figure 8.6: The average resolution $\langle\sigma\rangle = f_1\sigma_1 + (1 - f_1)\sigma_2$, where σ_1 and σ_2 are the widths of the two gaussians comprising the signal pdf and f_1 is the fraction of the first gaussian, is shown in (p_{T}, y) intervals, as obtained from fits to MC-simulated signal events.

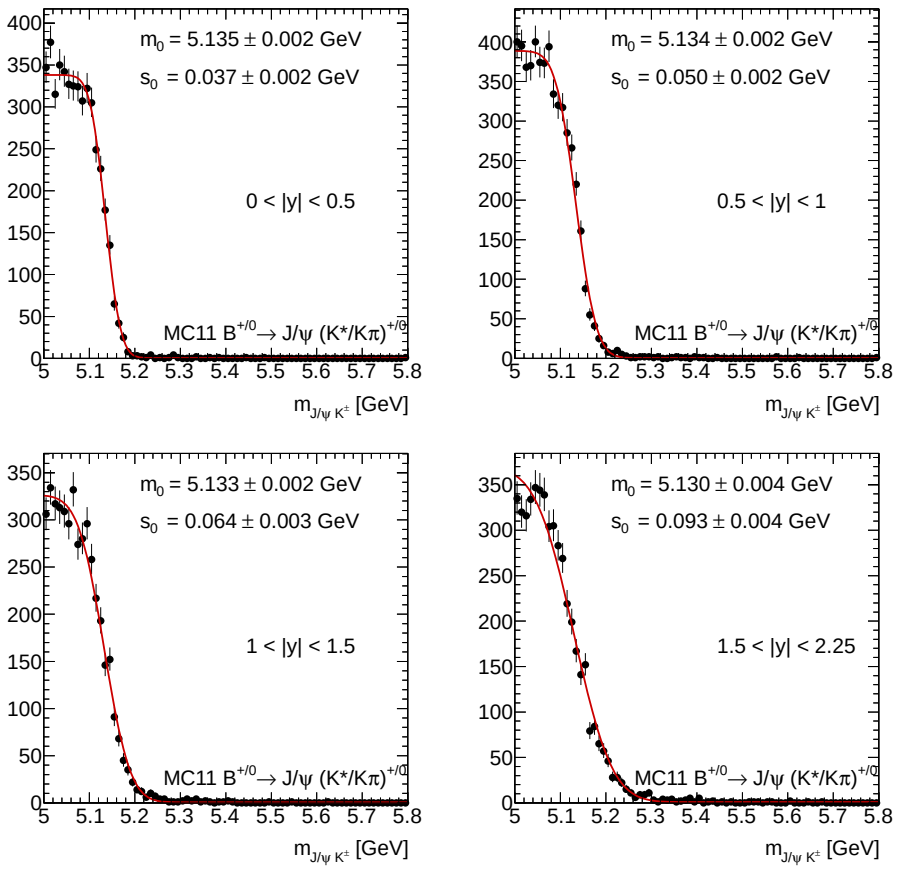

Figure 8.7: Invariant mass of partially reconstructed b-hadron decays in which a pion is not considered in the reconstruction of the secondary vertex, selected from the inclusive MC sample $b\bar{b} \rightarrow J/\psi\, X$ in the four slices of rapidity. The invariant mass shape of this background component is modeled using an error function. The line indicates the result of the binned likelihood fit that is used to extract the parameters which define the position and slope of the error function.

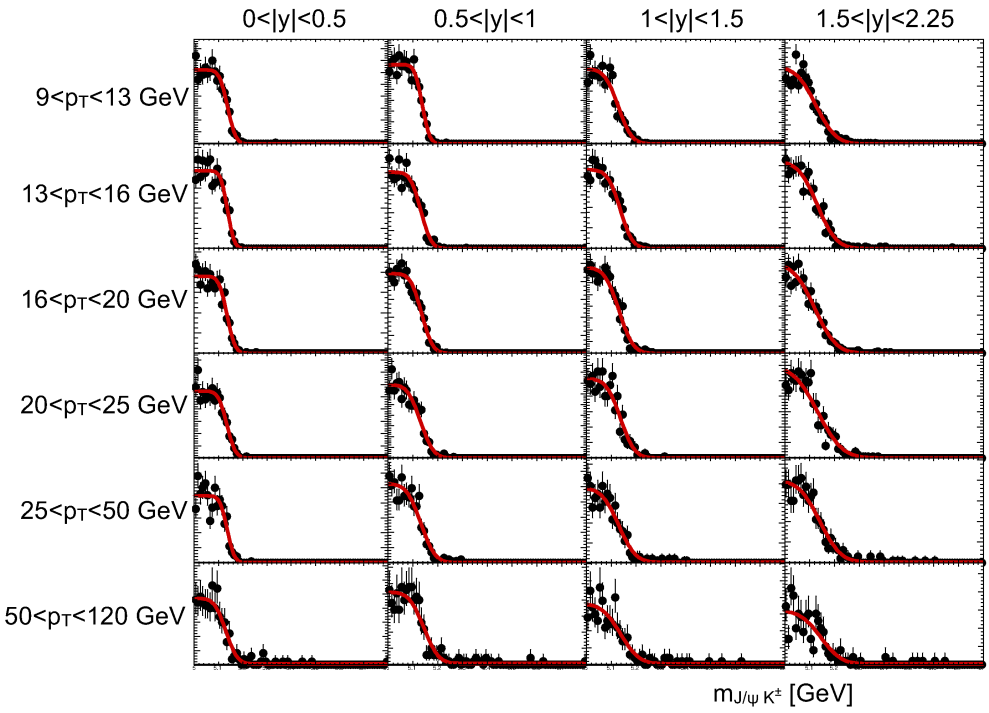

Figure 8.8: Invariant mass distributions of simulated partially reconstructed b-hadron decays in which a final-state pion is not associated to the decay vertex in (p_{T}, y) intervals. Points with are simulated signal events. The solid line is the result of a binned maximum likelihood fit in mass range 5.0–5.8 GeV (same for all subfigures), using an error function to model the invariant mass shape of the selected events.

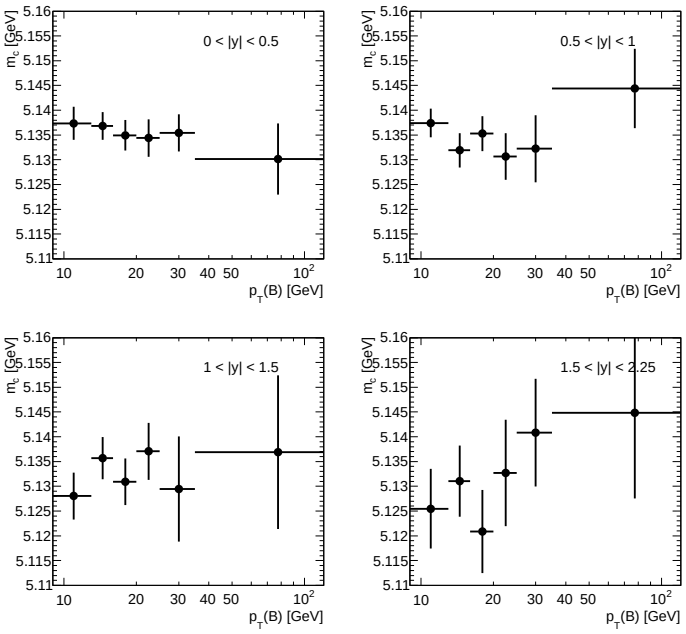

Figure 8.9: Values of the parameter m_0 (position of the error function) obtained from fits to simulated events from partially reconstructed b-hadron decays.

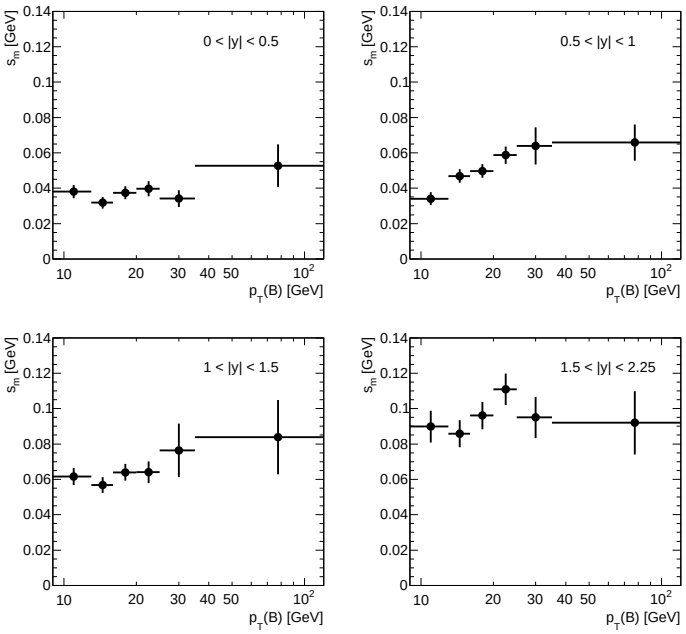

Figure 8.10: Values of the parameter s_0 (slope of the error function) obtained from fits to simulated events from partially reconstructed b-hadron decays.

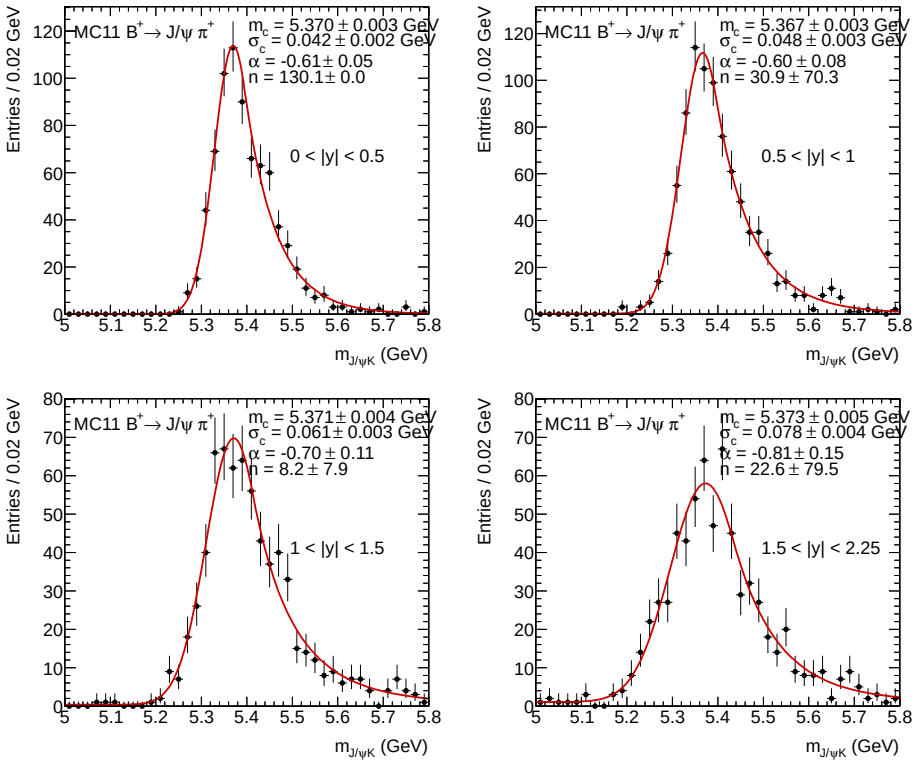

Figure 8.11: The invariant mass of simulated $B^{\pm} \to J/\psi\,\pi^{\pm}$ decays in which the kaon mass is wrongly assigned to the pion, obtained in four intervals of rapidity. This background is modeled using a Crystal Ball function and the line indicates the result of a binned likelihood fit. The resulting fit parameters which define the position and shape of the Crystal Ball function in each interval are also shown.

8.3.4 Fitting procedure in the data

To extract the signal yield from data, first the shapes of the signal and background pdfs are obtained from fits to signal and background events from MC simulation. In previous sections, it was shown that these shapes depend on the p_{T} and y of the $B^{\pm}$ meson candidate, so they are extracted separately for each (p_{T}, y) interval, except for the $B\pm$ signal mass position and the pdf parameters for the $B^{\pm} \to J/\psi\,\pi^{\pm}$ background, which are obtained in the four y intervals. Then the data are fitted in the same (p_{T}, y) interval, constraining the shapes of the signal and background to the results from the fits to MC-simulated events and leaving their normalization free. The fit model comprises 14 parameters for the description of the signal and background, which are strongly correlated. If one leaves free to fluctuate all parameters of the fit model, tests with MC-simulated signal+background samples have shown that the fit behaves as if it is over-parametrized. As a result, the signal and background pdf parameters obtain unrealistic values, especially in (p_{T}, y) intervals where the background contamination is larger, the mass resolution is worse and the available statistics small. By constraining the parameters which define the shape of the signal and background, we recover the stability of the fit in all (p_{T}, y) intervals and control potential biases in the estimation of the signal yield. The parameters that are constraint to the values obtained from fits to MC event samples are:

- σ_1, σ_2, f_1, which define the shape of the signal pdf,
- m_0, s_0, which define the shape of the error function modeling the partially reconstructed b-hadrons, and
- m_c, σ_c, α_c, n_c, which define the shape of the Crystal Ball function modeling $B^{\pm} \to J/\psi\,\pi^{\pm}$ decays.

The normalization of the Crystal Ball function, f_3, is constrained to the fraction of the world-average values for their branching ratios and is corrected for the different acceptance and efficiency of the two decay modes, as given by:

$$R' = \frac{N_{\mathrm{rec}}^{J/\psi\,\pi^{\pm}}}{N_{\mathrm{rec}}^{J/\psi\,K^{\pm}}} = \frac{\sigma(pp \to B^{\pm}\,X \to J/\psi\,\pi^{\pm}\,X) \cdot \varepsilon^{J/\psi\,\pi^{\pm}}}{\sigma(pp \to B^{\pm}\,X \to J/\psi\,K^{\pm}\,X) \cdot \varepsilon^{J/\psi\,K^{\pm}}} = R \cdot \frac{\varepsilon^{J/\psi\,\pi^{\pm}}}{\varepsilon^{J/\psi\,K^{\pm}}}\ , \qquad (8.8)$$

where R is the fraction of the branching ratios of the two decay modes (see eq. 7.6) and $\varepsilon^{J/\psi\,\pi^\pm}$, $\varepsilon^{J/\psi\,K^\pm}$ are the overall acceptance and efficiency corrections for the two decay modes. With MC simulation of the two decay modes, we find that $\varepsilon^{J/\psi\,\pi^\pm}/\varepsilon^{J/\psi\,K^\pm} = 1.1 \pm 0.1$. The reconstructed $B^\pm$ mass at which the signal pdf is centered, $m_{B^\pm}$, is obtained from data by fitting the invariant mass of the selected candidates in four rapidity intervals (see Figure 8.12), and is constrained throughout the fits in $p_{\rm T}$ intervals in each rapidity interval. This is done to avoid fluctuations of $m_{B^\pm}$ in intervals with limited statistics. Therefore, when fitting the data in each $(p_{\rm T}, y)$ interval, the free parameters are the normalization of the signal f_s the normalization of the partially reconstructed b-hadron decays f_2 and the slope of the combinatorial background β.

From Figure 8.12, where the signal yields in four rapidity regions are given, we get a total number of about 126500 $B^\pm$ signal events observed in data in the full $p_{\rm T}$ and y range covered by this analysis. These events populate eight intervals of $p_{\rm T}$ and four rapidity intervals for the double-differential cross-section measurement. In Figure 8.13 the fit in an interval of intermediate $p_{\rm T}$ and central rapidity is exemplified, in which all the components of the fit are distinguishable. All fits to data in the 32 $(p_{\rm T}, y)$ intervals are shown in Figures 8.14-8.17 and the resulting signal yields, not corrected for efficiency and acceptance, are reported in Table 8.1. The quality of the fits is demonstrated by the residual distributions, shown beneath each figure, and by the corresponding value of Pearson's χ^2 test.

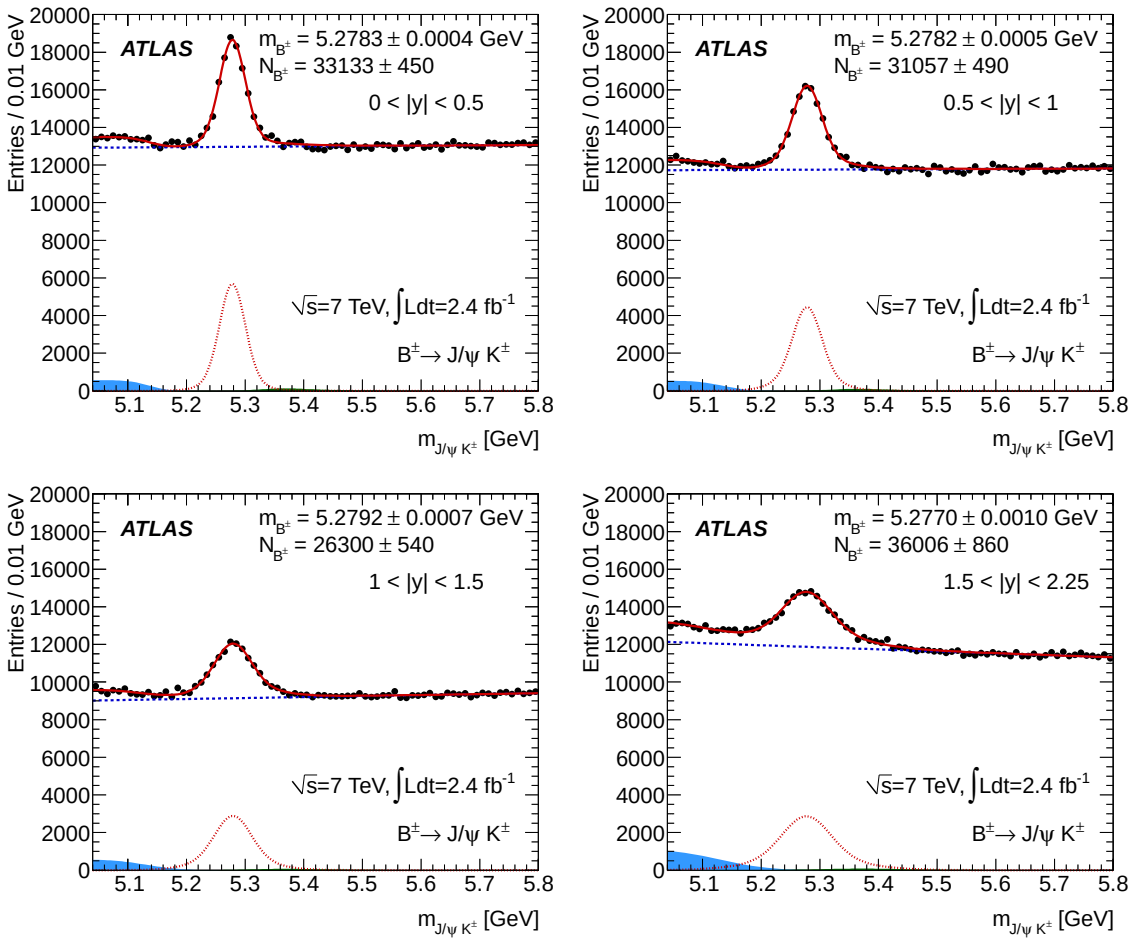

Figure 8.12: Fits to invariant mass distributions of $B^\pm$ candidates in the four rapidity regions. Points are data. The solid line is the result of the binned maximum likelihood fit in the shown mass range. The components of the fit for the signal and the background are shown. The quoted numbers are the signal yields and the reconstructed $B^\pm$ mass, as obtained from each fit.

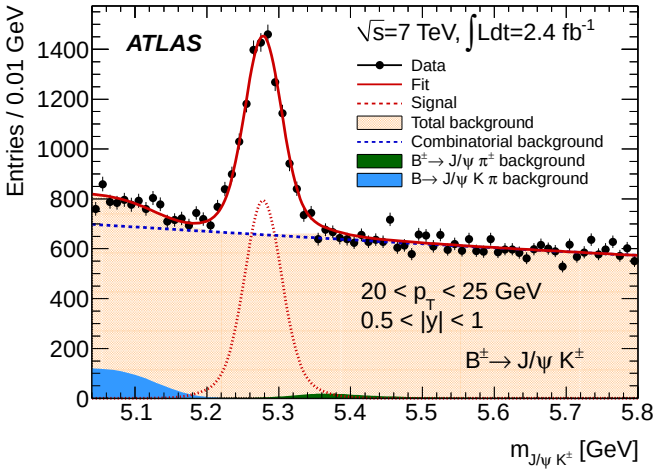

Figure 8.13: Fit to invariant mass of $B^{\pm}$ candidates in an intermediate p_{T} interval in a central rapidity region. The points with error bars are data and the solid line is the result of the binned maximum likelihood fit. The various components of the fit for the signal and the background are also shown.

Table 8.1: Signal yields from fits to $B^{\pm}$ candidates in (p_{T}, y) intervals, quoted with their statistical uncertainty returned by the fit.

$B^{\pm}$ p_{T} range	$B^{\pm}$ rapidity range			
[GeV]	$0 < \lvert y\rvert < 0.5$	$0.5 < \lvert y\rvert < 1$	$1 < \lvert y\rvert < 1.5$	$1.5 < \lvert y\rvert < 2.25$
9 - 13	6478 ± 301	5059 ± 311	4238 ± 334	6226 ± 506
13 - 16	7160 ± 213	6456 ± 236	5757 ± 264	7813 ± 423
16 - 20	7327 ± 168	7379 ± 191	5982 ± 207	8221 ± 337
20 - 25	5510 ± 124	5569 ± 138	4697 ± 152	6161 ± 244
25 - 35	4520 ± 100	4531 ± 113	3907 ± 123	5015 ± 188
35 - 50	1615 ± 57	1674 ± 65	1302 ± 68	1517 ± 101
50 - 70	380 ± 27	399 ± 31	316 ± 33	344 ± 43
70 - 120	87 ± 12	97 ± 16	51 ± 11	52 ± 12

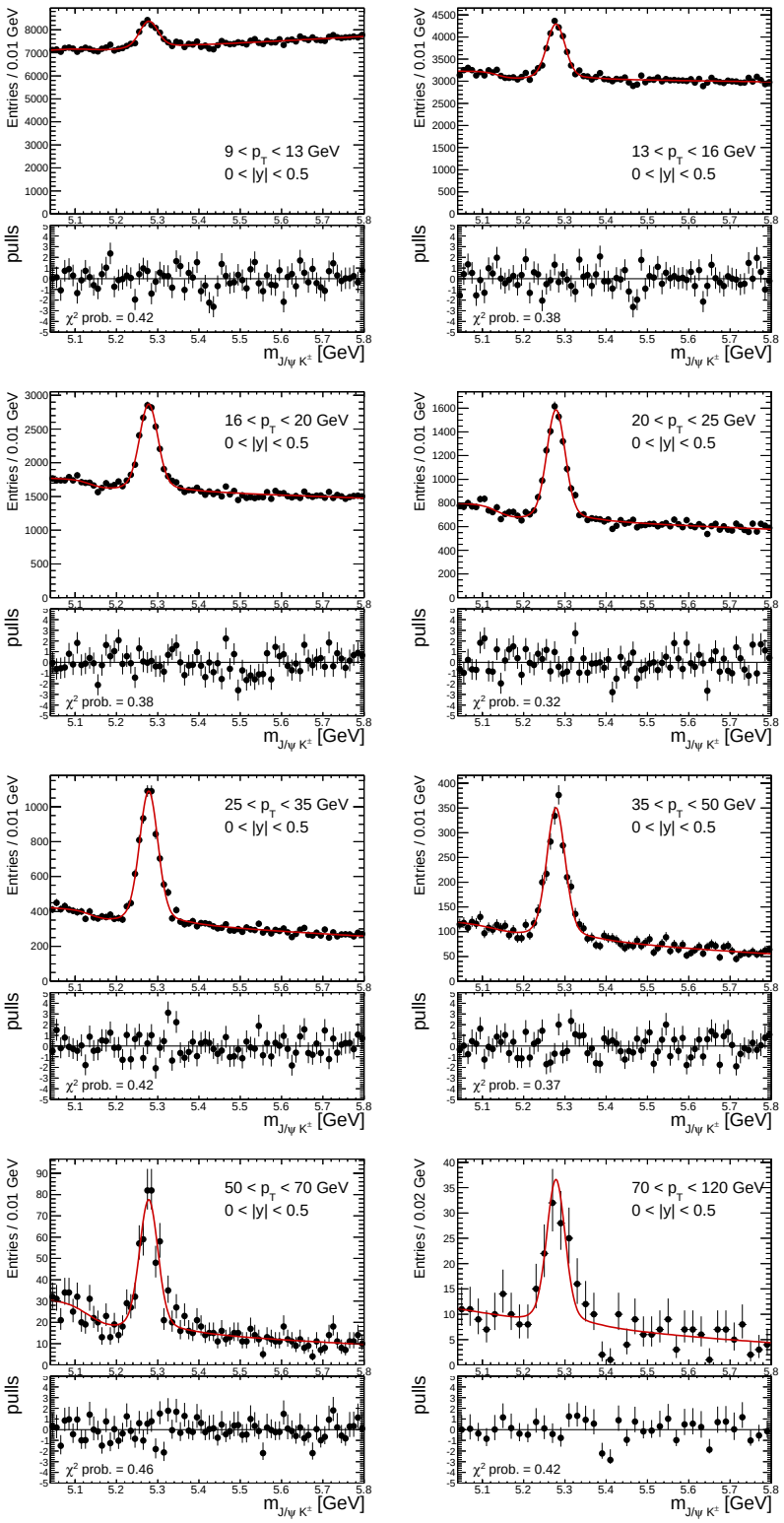

Figure 8.14: Mass fits to data for $B^{\pm}$ candidates in eight p_{T} intervals in $0 < |y| < 0.5$.

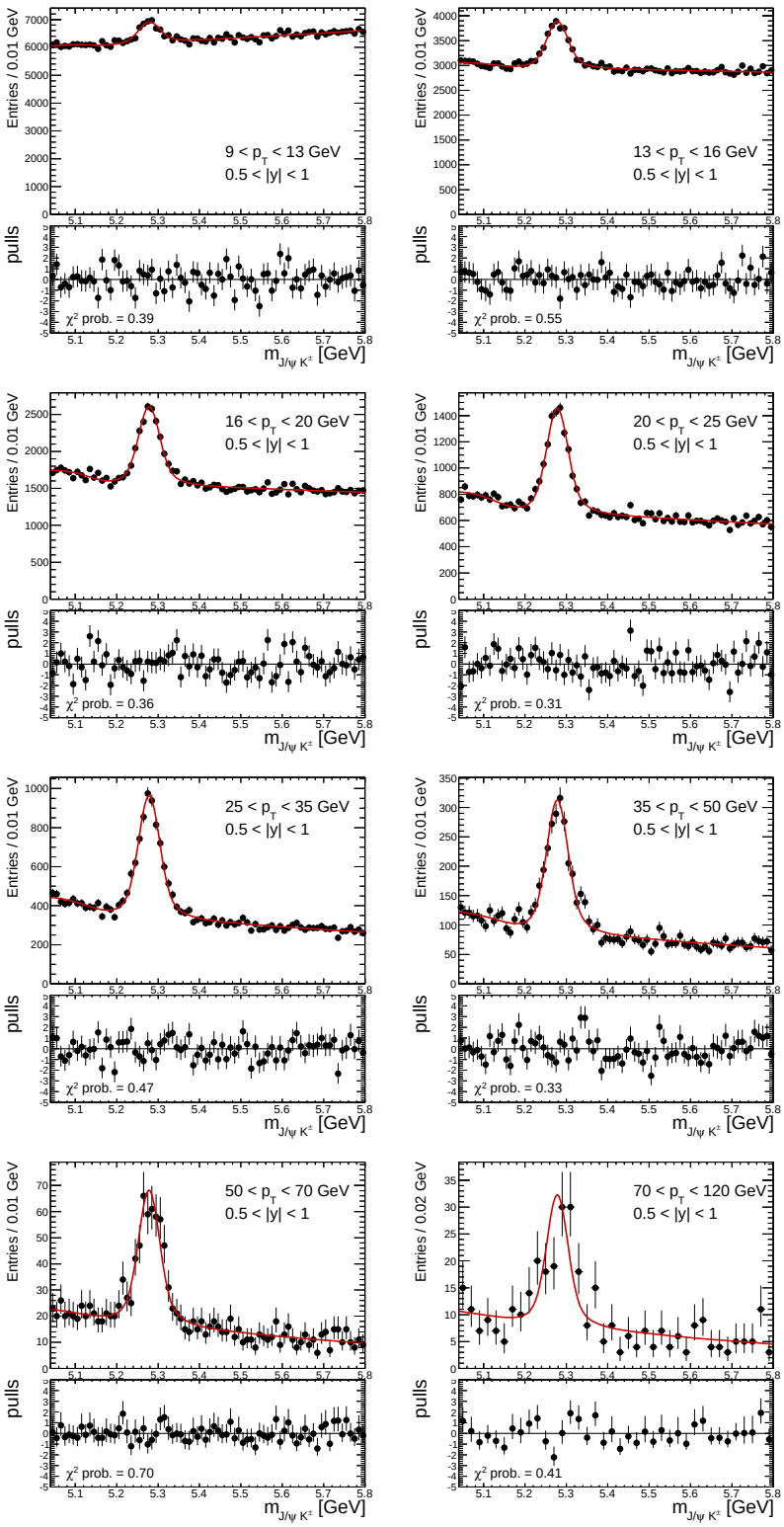

Figure 8.15: Mass fits to data for $B^{\pm}$ candidates in eight p_{T} intervals in $0.5 < |y| < 1$.

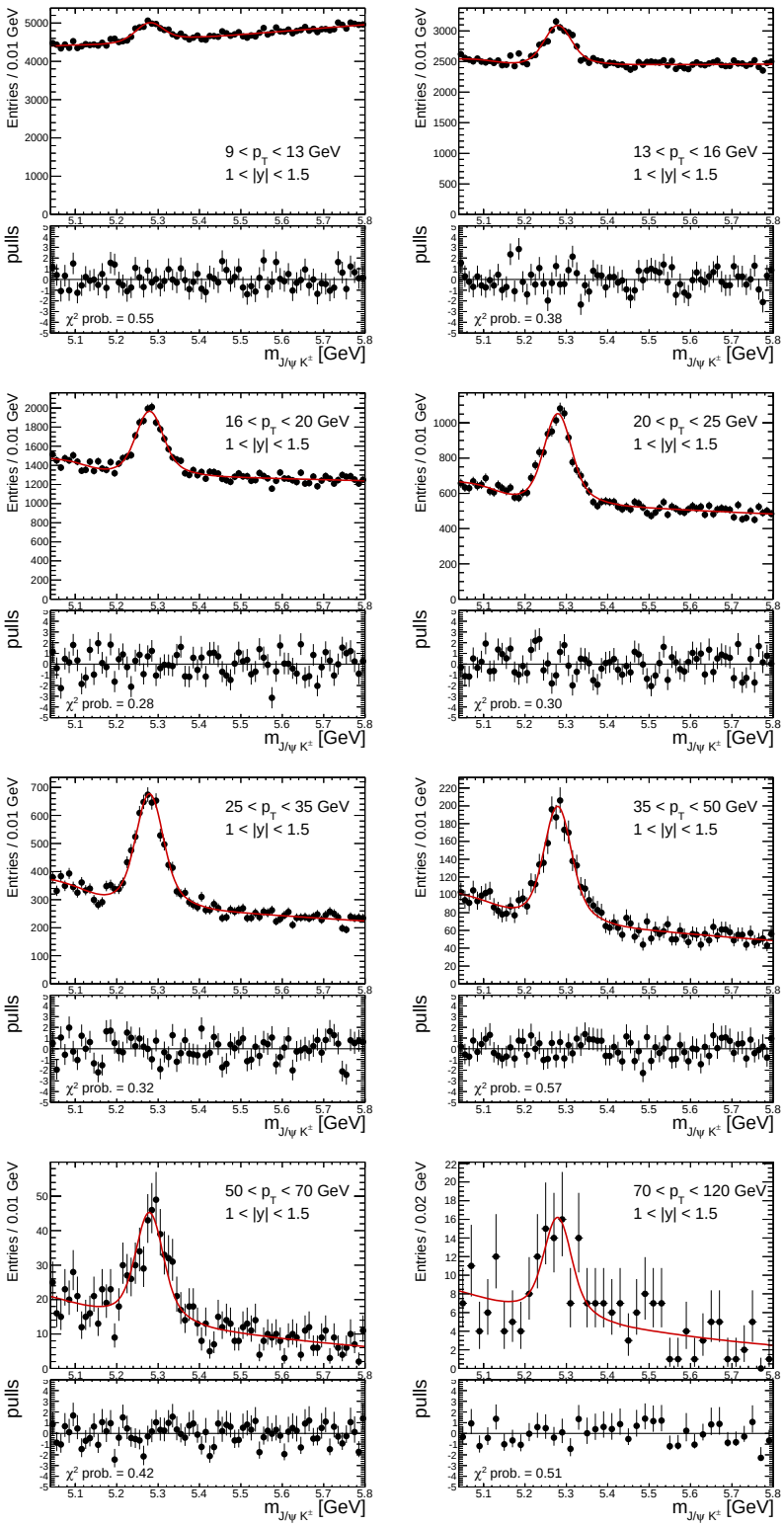

Figure 8.16: Mass fits to data for $B^{\pm}$ candidates in eight p_{T} intervals in $1 < |y| < 1.5$.

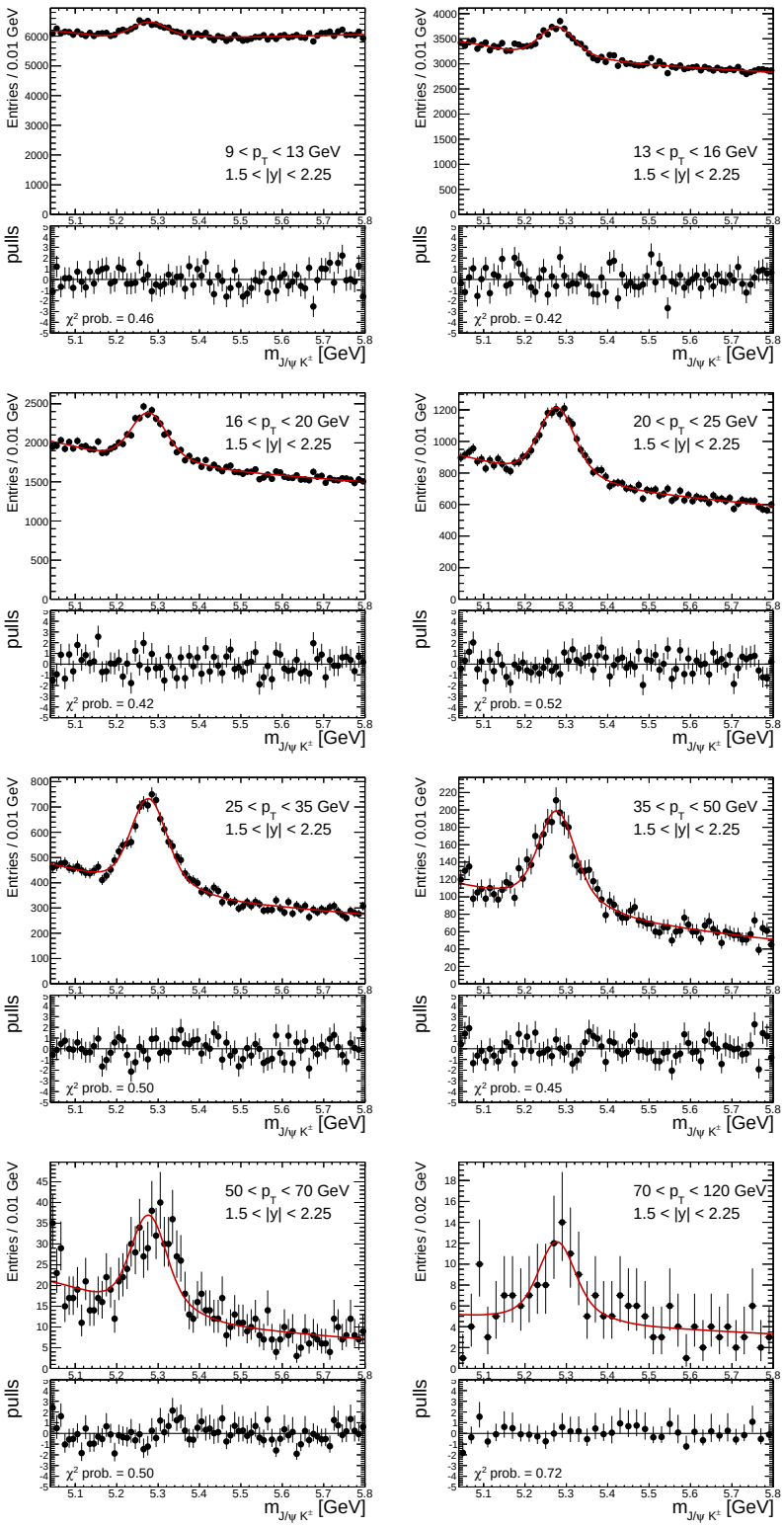

Figure 8.17: Mass fits to data for $B^{\pm}$ candidates in eight p_{T} intervals in $1.5 < |y| < 2.25$.

8.4 Corrections to the signal yield

8.4.1 Signal acceptance

The kinematic acceptance is the probability that the decay products of a B^+ meson with transverse momentum $p_{\rm T}$ and rapidity y falls into the fiducial volume of the detector. An average acceptance correction is extracted in each $(p_{\rm T}, y)$ interval using a sample of signal decays generated with PYTHIA, in which no kinematic cuts are applied to the final state particles. Then to emulate the fiducial volume of the detector and trigger, the following kinematic cuts are used:

$$p_{\rm T}^K > 1 \ \ {\rm GeV} \ , \ |\eta^K| < 2.5 \ \ , \ \ p_{\rm T}^\mu > 4 \ \ {\rm GeV} \ , \ |\eta^\mu| < 2.3 \ \ , \ \ |y^{J/\psi}| < 2.25$$

resulting in the acceptance map shown in Figure 8.18, in which the acceptance ranges from about 4% in the lowest $p_{\rm T}$ bins up to more than 80% in the highest $p_{\rm T}$ bins. A binomial error is assigned to the acceptance in each bin, which ranges from 1% to 4% (relative to the acceptance) from low to high $p_{\rm T}$ bins.

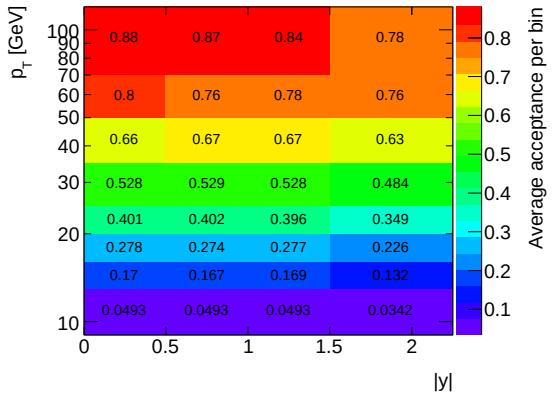

Figure 8.18: Map of the average acceptance for signal events in each $(p_{\rm T}, y)$ bin used in the analysis, obtained from generated $B^+ \to J/\psi(\mu^+\mu^-)\, K^+$ decays.

8.4.2 Signal efficiency

The efficiency factors for B^+ and B^- are obtained from MC simulation in the same manner. In the following, ε^{B^-} is implicitly referred to, together with ε^{B^+}. The

efficiency for B^+ events is defined as the product of trigger, muon reconstruction (ID and MS), kaon reconstruction and vertexing efficiencies:

$$\varepsilon^{B^+} = \varepsilon^{J/\psi}_{\text{trigger}} \cdot \varepsilon^{\mu^+} \cdot \varepsilon^{\mu^-} \cdot \varepsilon^{K^+}_{\text{ID}} \cdot \varepsilon^{\mu\mu K}_{\text{vertex}} = \varepsilon^{J/\psi}_{\text{trigger}} \cdot \varepsilon^{\mu^+}_{\text{MS}} \cdot \varepsilon^{\mu^-}_{\text{MS}} \cdot (\varepsilon^{\mu}_{\text{ID}})^2 \cdot \varepsilon^{K^+}_{\text{ID}} \cdot \varepsilon^{\mu\mu K}_{\text{vertex}} \ . \quad (8.9)$$

In the above equation, $\varepsilon^{\mu^+}_{\text{MS}}$ and $\varepsilon^{\mu^-}_{\text{MS}}$ are the efficiencies for reconstructing μ^+ and μ^- in the MS, which differ for muons of low p_{T} due to the toroidal magnetic field bending muons with positive (negative) charge towards higher (lower) pseudorapidity. The trigger efficiency, $\varepsilon^{J/\psi}_{\text{trigger}}$, depends on the ability of the trigger to identify muons of given p_{T} and η as decay products of a J/ψ meson. The trigger efficiency includes independent and correlated terms between the two muons, as will be explained later.

The overall signal efficiency ε^{B^+} for a given (p_{T}, y) interval is obtained from MC simulated signal events from the fraction

$$\varepsilon^{B^+} = \frac{N^{B^+}_{\text{MC, reco}}}{N^{B^+}_{\text{MC, gen}}} \ , \quad (8.10)$$

where the denominator is the number of signal events generated in the given (p_{T}, y) interval and the numerator is the number of signal events reconstructed in the same (p_{T}, y) interval that pass all the offline selection requirements. Bin-to-bin migration effects are included in the efficiency definition of Equation (8.10), as the signal events which are reconstructed in a (p_{T}, y) interval are not required to be generated in the same interval. The overall signal efficiency obtained with this fraction corrects for all the individual efficiencies appearing in Equation (8.9). However, it has to be verified that the simulation reproduces each these efficiencies well. The trigger and muon reconstruction efficiencies are measured explicitely in the data using auxiliary single and dimuon triggers and tag-and-probe methods [2] and the simulation is corrected with per-event weights to reproduce the efficiencies measured with data. The derived weights, $w^{\mu^+}_{\text{MS}}$, $w^{\mu^-}_{\text{MS}}$, $w^{J/\psi}_{\text{trigger}}$ are applied in each event, so that $N^{B^+}_{\text{MC, reco}}$ in Equation (8.10) is now defined as

$$N^{B^+}_{\text{MC, reco}} = \sum_{i=1}^{N^{\text{events}}_{\text{MC}}} (w^{\mu^+}_{\text{MS}})_i \cdot (w^{\mu^-}_{\text{MS}})_i \cdot (w^{J/\psi}_{\text{trigger}})_i \ . \quad (8.11)$$

The efficiency for reconstructing muons in the ID, $\varepsilon^{\mu}_{\text{ID}}$, and the vertexing efficiency, $\varepsilon^{\mu\mu K}_{\text{vertex}}$ is found to be 99% in both cases and well reproduced by the simulation, thus

no scale factor is applied. The reconstruction efficiency of hadrons in the ID was verified in Ref. [3] for data and simulation; for the kaons used in this analysis, it is obtained from simulation. In the next sections, the muon trigger efficiency, the muon and kaon reconstruction efficiencies and the $B^{\pm}$ vertexing efficiency are presented, as obtained from simulation, and are compared to the measurements with data.

8.4.3 Muon reconstruction efficiency

The muon reconstruction and trigger efficiencies are measured from the data using a sample enriched in J/ψ mesons with a tag-and-probe technique. The method for the measurement and the result from data is taken from [2]. For this thesis, the method is reproduced on MC-simulated events to extract weights with which the simulation is corrected in order to reproduce the efficiencies measured in data (see Equation (8.11)). The basic idea behind the method is given below.

The tag-and-probe technique is a common approach followed in the measurement of efficiencies without relying on simulation, and is usually referred to as a 'data-driven' method. With this method, one can measure the efficiency of a specific detector sub-system, relying on information from other independent detector sub-systems. To measure the efficiency of reconstructing muons in the MS, for instance, one can select muons that are reconstructed in the ID, without requiring any kind of information from the MS. These are called 'probe' muons as they can be used to measure the reconstruction efficiency of the MS with respect to the ID from the fraction $N^{\text{probes}}_{\text{pass}}/(N^{\text{probes}}_{\text{pass}} + N^{\text{probes}}_{\text{fail}})$, where $N^{\text{probes}}_{\text{pass(fail)}}$ is the number of probes that pass (fail) an additional requirement which justifies whether they were also reconstructed in the MS or not. The critical point in the tag-and-probe method is to ensure the purity of the sample of probes. In the case where we want to measure the MS efficiency, this means that we need to select probes that are true muons instead of pions/kaons, without requiring MS information. In this implementation of the method, the purity of the sample of probes is ensured by identifying dimuon decays of J/ψ mesons. The presence of at least one true muon of high quality ('tag' muon) is required, which provides an indication of a $J/\psi \to \mu^+\mu^-$ decay. Selected probes, in pairs with tag

muons, are considered as J/ψ candidates and should have characteristics compatible with a $J/\psi \to \mu^+\mu^-$ decay.

The measurement of the muon reconstruction efficiency is done on a sample of events collected with single-muon triggers, with thresholds on p_{T} varying from 4 GeV to 40 GeV. A tag muon must be identified as a combined muon, associated with an ID track of good quality based on hits in SCT, TRT and pixel detectors, and must be the one which fired the trigger in the event. The probe muon must be a good ID track which, in pair with a tag muon, fulfills the following requirements:

- Probe + tag muon pair must fit successfully to a common vertex.
- Probe + tag muon pair must have an invariant mass in the J/ψ signal region.
- Probes and tag muons must be sufficiently separated in η and ϕ in the trigger and in reconstruction algorithms.

After this selection, the resulting sample of tag+probe (muon+track) pairs is used to measure the MS efficiency, by checking if the probe track is associated to a reconstructed combined muon (thus giving a muon+muon pair). Then the single-muon reconstruction efficiency of the MS is defined as:

$$\varepsilon_{\mathrm{MS}} = \frac{N_{\mu+\mu}}{N_{\mu+\mathrm{trk}}} \ ,$$

where $N_{\mu+\mu}$ and $N_{\mu+\mathrm{trk}}$ are the yields of J/ψ mesons reconstructed from two fully reconstructed muons or a muon and an ID track, respectively. The muon+track and muon+muon samples are not background-free, so the yields are extracted with a fitting procedure using the invariant mass of the tag+probe pairs, before and after requesting the association with the MS.

Following the procedure as described above, the muon reconstruction efficiency of the MS is measured with respect to the ID in bins of p_{T} and $q \cdot \eta$ of the muon. Due to the toroidal magnetic field, muons with positive (negative) charge are bent towards higher (lower) pseudorapidity. This introduces a charge dependence in the muon reconstruction efficiency. We calculate efficiencies as a function of charge-signed pseudorapidity as negative muons at positive rapidities are affected in the

same manner as positive muons in negative rapidities. The charge dependence is particularly noticeable at low p_{T} and high η, where the muon can be bent outside of the geometrical acceptance of the detector.

The single-muon reconstruction efficiencies are obtained from a sample of fully simulated $J/\psi \to \mu^+\mu^-$ decays, in which only true muons originating from a J/ψ meson decay are used, and is shown in Figure 8.19. The efficiency map from MC-simulated events is compared to the one derived from data to obtain scale factors ($\varepsilon^{\mathrm{data}}/\varepsilon^{\mathrm{MC}}$), which are used to correct the MC simulation in order to reproduce the efficiencies measured in data. The resulting scale factors, derived from the division of the 2-d maps from data and MC simulation, are shown in Figure 8.20. The error associated to the scale factor is dominated by the statistical accuracy of the data-driven efficiency measurement and includes the uncertainty due to statistics in the MC-simulated sample.

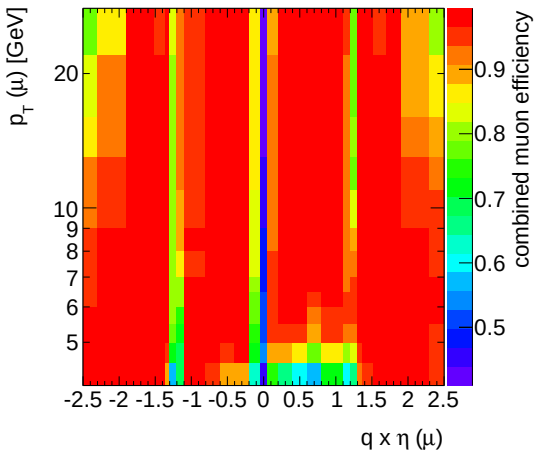

Figure 8.19: Map of the combined muon reconstruction efficiency, obtained from MC-simulated events.

8.4.4 Trigger efficiency

As for the muon reconstruction efficiency, the method for the measurement of the muon trigger efficiency and the result from data is taken from [2]. It is a tag-and-probe method, the basic idea of which is similar to the one described in the

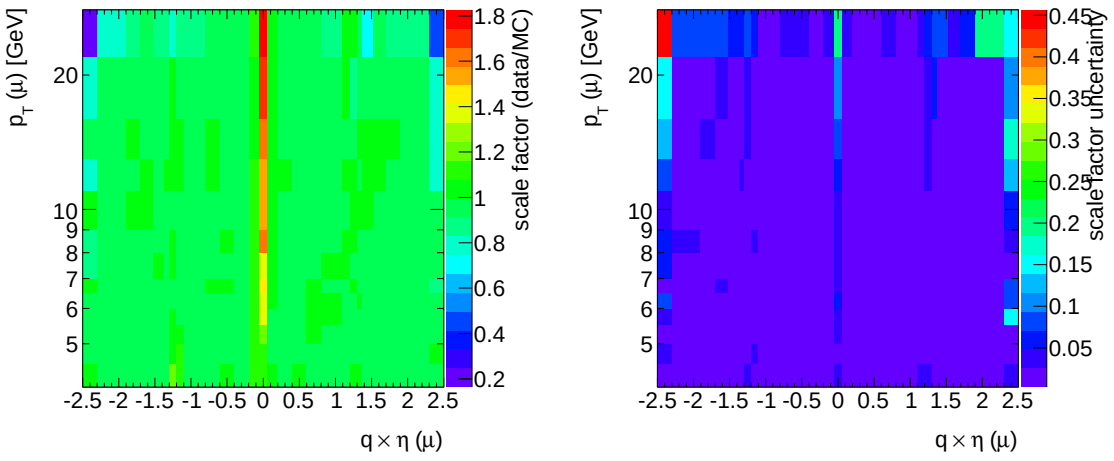

Figure 8.20: Scale factors for the combined muon reconstruction efficiency (left), obtained from the comparison of data to MC simulation, and its associated error (right).

previous section for the measurement of the muon reconstruction efficiency. In its implementation for the measurement of the trigger efficiency, auxiliary single and dimuon triggers are used, while a significant complication arises from the fact that correlations between the two muons need to be taken into account. For this thesis, the method is reproduced on MC-simulated events to extract weights with which the simulation is corrected in order to reproduce the efficiencies measured in data (see Equation (8.11)). The method for the efficiency measurement and the extraction of weights is described in detail below.

The standard trigger used in the cross-section analysis to select dimuons from J/ψ mesons is `EF_2mu4_Jpsimumu`, which was described in Section 8.2. Its efficiency for a given muon pair (μ_1, μ_2) originating from the decay of a J/ψ meson can be factorized as

$$\varepsilon_{\text{trigger}}^{\mu_1,\mu_2} = \varepsilon_{\text{ROI}}^{\mu_1} \cdot \varepsilon_{\text{ROI}}^{\mu_2} \cdot c_{\mu\mu} \ , \tag{8.12}$$

where $\varepsilon_{\text{ROI}} \equiv \varepsilon_{\texttt{EF\_mu4}}$ is the efficiency of the trigger to identify a single muon, determined in bins of p_{T} and $q \cdot \eta$ of the muon, and $c_{\mu\mu}$ is a correction term to account for correlations between the two muons and is a function of $|y|$ of the dimuon and the opening angle between the muons. To estimate the single-muon trigger efficiency, the tag-and-probe method used dimuon resonances reconstructed in events collected

with a single-muon trigger. The muon that fired the single-muon trigger is defined as the tag, while the other muon is used as the probe, checking whether it can be associated to an `EF_mu4` trigger object to estimate the single-muon efficiency. In the available data sample, the single-muon trigger with the lowest p_{T} threshold which is also un-prescaled, is `EF_mu18`.

For the estimation of $\varepsilon_{\mathrm{ROI}}$ and $c_{\mu\mu}$, three auxiliary triggers are used:

1. `EF_2mu4_DiMu`: a dimuon trigger similar to the standard trigger used in the analysis, where no cut is made on dimuon invariant mass;

2. `EF_2mu4_DiMu_NoVtx_NoOS`: a dimuon trigger similar to the previous trigger, where no cuts are made on dimuon vertex quality or charge of the two muons;

3. `EF_mu18`: a single-muon trigger with a p_{T} threshold of 18 GeV, which is the lowest of the available un-prescaled triggers in data.

Although the standard trigger used is `EF_2mu4_Jpsimumu`, the efficiency measurements are performed for `EF_2mu4_DiMu`, which allows the use of both J/ψ and $\Upsilon \to \mu^+\mu^-$ decays for the trigger efficiency measurement. Both triggers have the same efficiency in selecting signal J/ψ events, as their only difference is the additional requirement of the '`Jpsimumu`' trigger to select dimuons with invariant mass around the J/ψ and ψ' mass ($2.5 < m_{\mu\mu} < 4.3$ GeV), which does not reject signal events. Thus, the efficiency measurements and scale factors that we extract are common for the two triggers.

The single-muon trigger efficiency is extracted with this formula:

$$\varepsilon_{\mathrm{ROI}}(p_{\mathrm{T}}^{\mu}, q\cdot\eta^{\mu}) = \frac{(N_{\mu\mu}\,|\,\texttt{EF\_mu18}\ \&\ \texttt{EF\_2mu4\_DiMu})}{(N_{\mu\mu}\,|\,\texttt{EF\_mu18})}\frac{1}{c_{\mu\mu}(\Delta R_{\mu\mu}, |y_{\mu\mu}|)}\ , \qquad (8.13)$$

where $(N_{\mu\mu}\,|\,\texttt{EF\_mu18})$ is the number of dimuons which fire the single-muon trigger and $(N_{\mu\mu}\,|\,\texttt{EF\_mu18}\ \&\ \texttt{EF\_2mu4\_DiMu})$ is the number of dimuon pairs which fire both the single and the dimuon triggers. From their fraction, the efficiency of identifying a single-muon ROI is obtained.[1] However, two things should be considered for a valid

[1]This definition includes the assumption that the probability of a muon to fire the `EF_mu4` trigger, given that it fires the `EF_mu18`, is one. This assumption has been tested with MC-simulated events and was found to be valid.

measurement: the efficiency of the additional requirements posed by the dimuon trigger algorithm (vertexing and opposite-charge) and the efficiency of the trigger to distinguish overlapping ROIs. The J/ψ mesons selected by such a high-p_{T} single-muon trigger are boosted and their dimuon decays have a small opening angle (ΔR). For $\Delta R < 0.3$, ROIs begin to overlap and trigger algorithms become deficient because only one ROI is identified in this case. Moreover, the presence of a second muon close to the first may affect the identification efficiency of both muons positively or negatively. Effects from such correlations in the estimation of the single-muon efficiency are also accounted for with the $c_{\mu\mu}$ correction term, as shown in above equation.

Therefore, we define the dimuon correction $c_{\mu\mu}$, which is the product of two efficiencies, c_a and $c_{\Delta R}$. The first, c_a, corresponds to the efficiency of dimuon vertexing and opposite-charge requirements and is extracted from the fraction

$$c_a(|y_{\mu\mu}|) = \frac{(N_{\mu\mu} \,|\, \texttt{EF\_2mu4\_DiMu})}{(N_{\mu\mu} \,|\, \texttt{EF\_2mu4\_DiMu\_noVtx\_noOS})} \tag{8.14}$$

for dimuons with $\Delta R > 0.3$, and the result from MC simulation is shown in Figure 8.21 in bins of dimuon rapidity. We identify three regions of rapidity in which

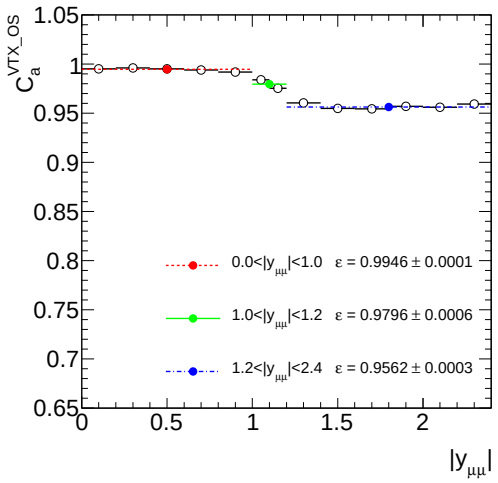

Figure 8.21: The efficiency of the vertex quality and opposite charge requirements from MC simulation, given in three regions of rapidity in which this efficiency is relatively constant.

this factor is stable, which are $|y_{\mu\mu}| < 1$, $1 < |y_{\mu\mu}| < 1.2$ and $1.2 < |y_{\mu\mu}| < 2.4$. The

second, $c_{\Delta R}$, is the efficiency of the dimuon trigger to distinguish overlapping ROIs, extracted from the fraction:

$$\rho_{\Delta R}(\Delta R, |y_{\mu\mu}|) = \frac{(N_{\mu\mu} \,|\, \texttt{EF\_mu18} \;\&\; \texttt{EF\_2mu4\_DiMu})}{(N_{\mu\mu} \,|\, \texttt{EF\_mu18})} \,. \tag{8.15}$$

To disentangle various effects entering this fraction, muons are required to be of $p_{\mathrm{T}} > 8$ GeV, which ensures that the muons are at the plateau of the `EF_mu4` efficiency, and then plot the distribution of $\rho_{\Delta R}$ in the three $|y_{\mu\mu}|$ regions in which c_a is stable. In Figure 8.22, the distribution $\rho_{\Delta R}$ is shown, as obtained from J/ψ and Υ mesons from MC simulation. Due to the high-p_{T} selection, we find no J/ψ mesons in the MC-simulated sample with $\Delta R > 0.3$, so in this region the $\Upsilon(1S)$ meson is used instead of J/ψ, both in data and MC simulation. This combination allows accurate determination of $\rho_{\Delta R}$ both at small ΔR, where dimuon events mainly originate from decays of boosted J/ψ mesons, and also at large ΔR where dimuon events are only available from Υ meson decays. The resulting distributions are fitted with an error function to describe its turn-on shape (Figure 8.22). The shape of the error function corresponds to the $c_{\Delta R}$ correction. Its normalisation is irrelevant at this point, since what we aim to represent with this quantity is the efficiency of the trigger to distinguish overlapping ROI. As explained earlier, the total dimuon correction is defined as:

$$c_{\mu\mu} = c_a \cdot c_{\Delta R} \tag{8.16}$$

and the result we obtain from MC simulation is shown in Figure 8.23, compared to the same result from data. Within the large uncertainty of the measurement from the data, a good agreement is seen with MC simulation.

Using the measurement of $c_{\mu\mu}$, we estimate the single-muon trigger efficiency in MC-simulated events using Equation 8.13 in bins of muon p_{T} and $q \cdot \eta$, and the result is shown in Figure 8.24. Comparing the result from MC simulation with data, we derive data/MC scale factors. The single-muon trigger efficiency from data is derived separately for data recorded during periods B-G and H-J ,due to a change in trigger definition. Therefore, two maps of scale factors are extracted, shown in Figure 8.25.

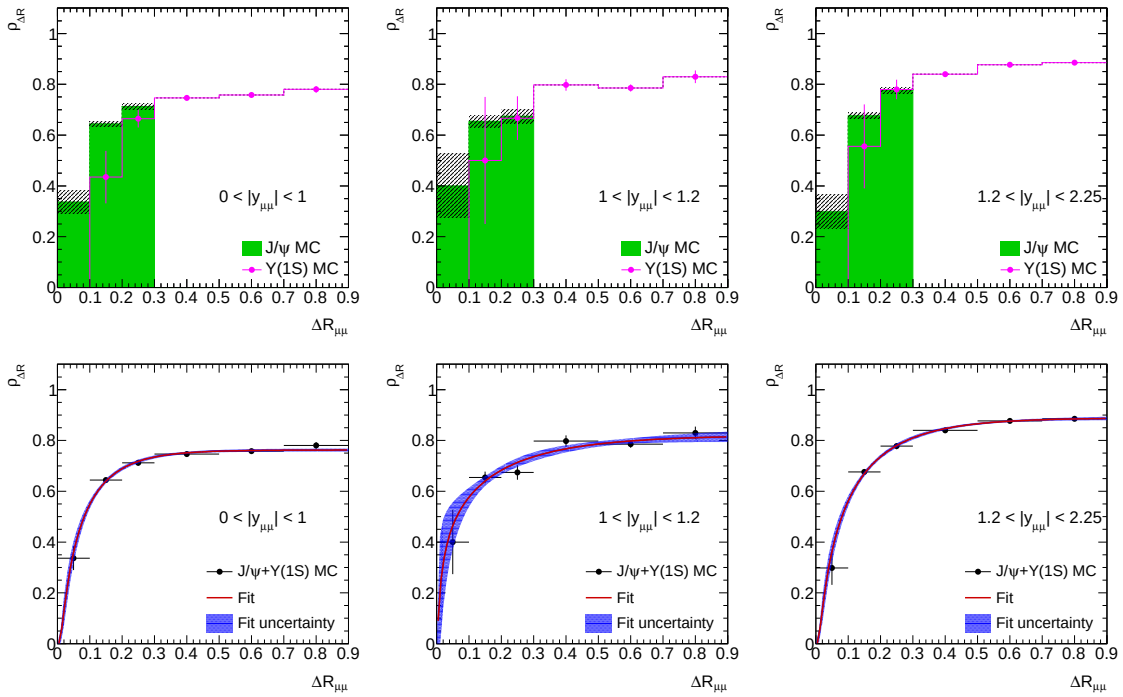

Figure 8.22: The distribution of $\rho_{\Delta R}$ (see Eq. 8.15), which is proportional to the efficiency of the trigger to separate overlapping ROIs, $c_{\Delta R}$, is shown in three dimuon rapidity regions, as obtained from simulated J/ψ and Υ meson decays (top). To extract $c_{\Delta R}$, the $\rho_{\Delta R}$ distribution is obtained from J/ψ mesons for $\Delta R < 0.3$ and $\Upsilon(1S)$ mesons for $\Delta R > 0.3$, and is fitted in each rapidity region with an error function.

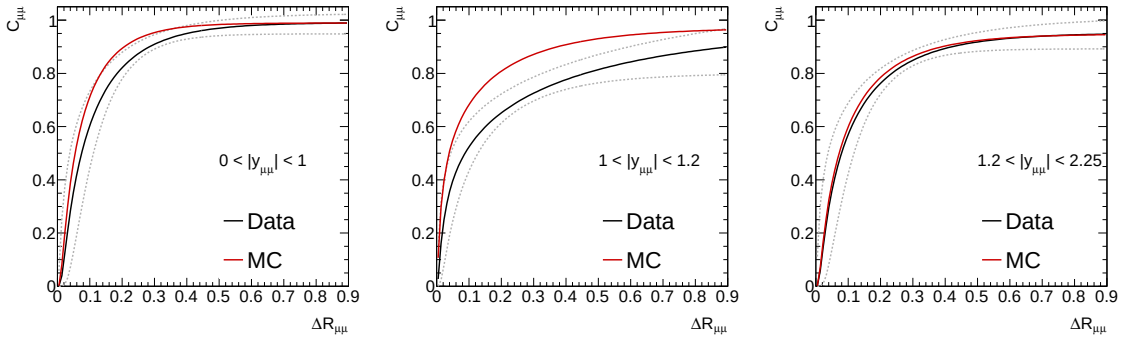

Figure 8.23: Dimuon trigger corrections in data and MC simulation for three dimuon rapidity regions. The dashed line indicates the uncertainty of the measurement from data.

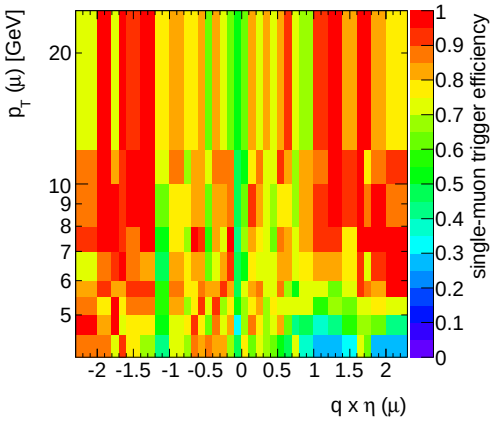

Figure 8.24: Map of the single-muon trigger efficiency, obtained from MC-simulated events.

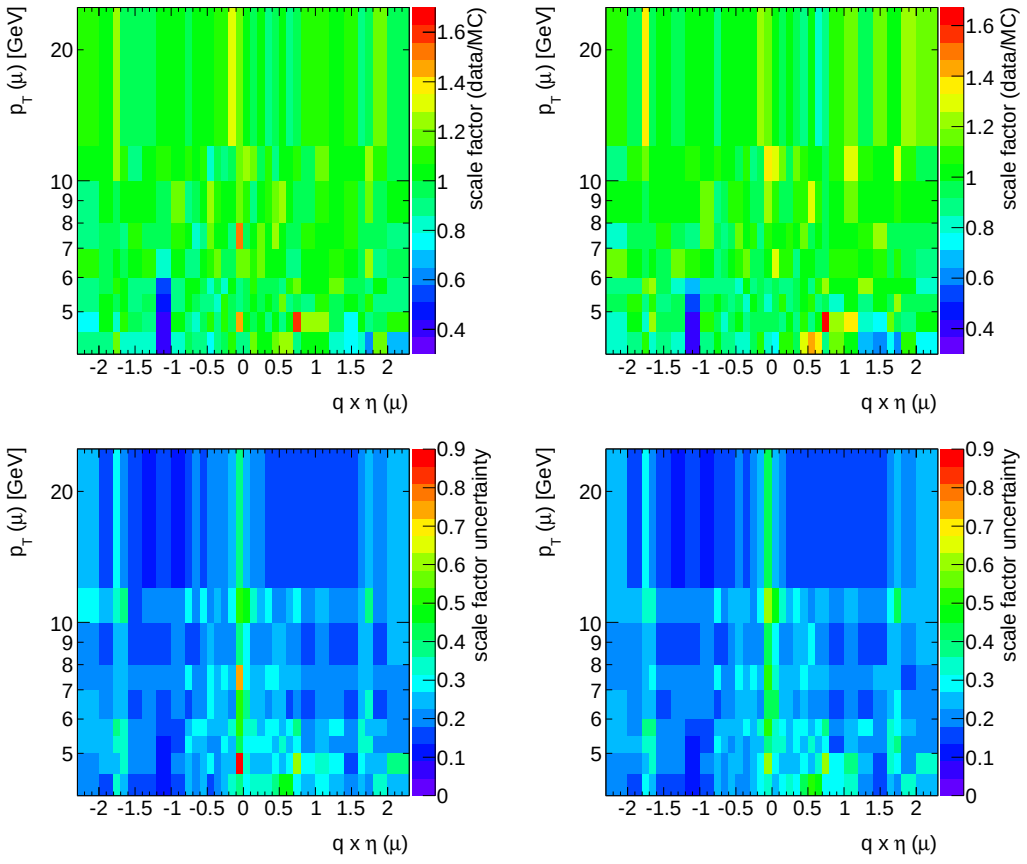

Figure 8.25: Maps of single-muon trigger efficiency scale factor (top) and their error (bottom) derived from MC simulation. Due to a change in trigger definition, efficiency and scale factors are given separately for periods B-G (left) and periods H-J (right).

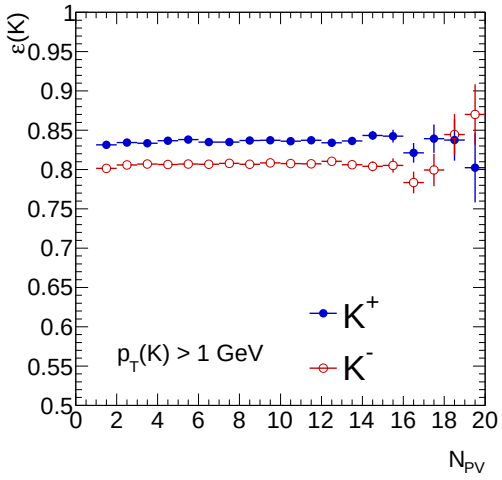

Figure 8.26: Efficiency of reconstructing K^+ (points) and K^- mesons (circles) as a function of the number of reconstructed vertices in the event.

8.4.5 Kaon reconstruction efficiency

The reconstruction efficiency of charged hadrons in the ID was verified in Ref. [3] for data and simulation; for the kaons used in this analysis, it is obtained from simulation. Charged kaons have a relatively large decay length (∼3.7 m) and can traverse all the ID layers before reaching the calorimeters. Their reconstruction efficiency is related to their interaction with the material of the ID and is obtained from the MC simulation based upon GEANT4.

In this analysis, the reconstruction efficiency for kaons having $p_{\mathrm{T}} > 1$ GeV and $|\eta| < 2.5$ is studied with MC simulation and found to be 83.6% (80.7%) for K^+ (K^-) mesons and also independent of pile-up, as shown in Figure 8.26. The charge asymmetry of the kaon efficiency is a result of negative kaons interacting more with the detector material, as nuclei have a higher probability to interact with K^- mesons. The charge asymmetry of the kaon efficiency is expressed as

$$A_K = \frac{\varepsilon_{K^+} - \varepsilon_{K^-}}{\varepsilon_{K^+} + \varepsilon_{K^-}} \ . \tag{8.17}$$

This asymmetry has been measured with data in an independent analysis [4] and found to be $A_K = 0.0105 \pm 0.0056$ for kaons of $p_{\mathrm{T}} > 2.5$ GeV. We studied the kaon reconstruction efficiency with MC-simulated events and the efficiency of kaons with

$p_{\mathrm{T}} > 2.5$ GeV is found to be $\varepsilon_{K^+} = 85\%$ and $\varepsilon_{K^-} = 82.6\%$. This translates to an asymmetry of 0.014 that is consistent with the result from data.

8.4.6 $B^{\pm}$ vertexing efficiency

Selected $B^{\pm}$ candidates are required to satisfy a loose requirement on the quality of the three-track vertex fit, which is characterized by the χ^2 per degree of freedom. We require $\chi^2/N_{\mathrm{dof}} < 6$, which is found to be about 99% efficient in selecting signal events in MC, fairly independent of p_{T} and y of the $B^{\pm}$ meson. The high signal efficiency and background rejection of the chosen requirement is demonstrated in Figure 8.27, using the invariant mass of $B^{\pm}$ candidates. A very loose cut on the vertex quality is employed ($\chi^2/N_{\mathrm{d.o.f.}} < 10000$) which retains 100% of signal events according to simulation, as hardly any signal is expected to have $\chi^2/N_{\mathrm{d.o.f.}} > 200$. The chosen value of this loose cut is a starting value, in order to set a limit to the number of background events written in the analysis ntuples. In the Figure it is shown that hardly any signal can be found in the events rejected by the tight cut used in the analysis.

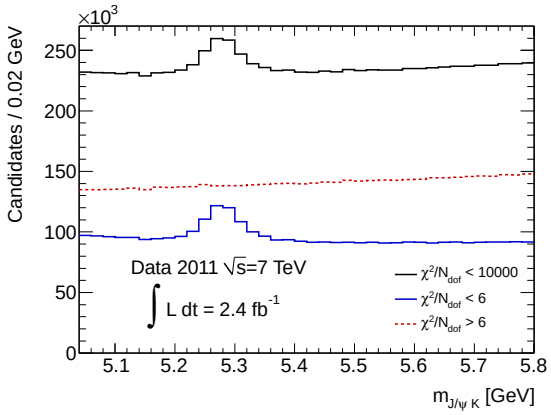

Figure 8.27: Invariant mass distribution of $B^{\pm}$ candidates that fulfill a loose vertex selection ($\chi^2/N_{\mathrm{d.o.f.}} < 10000$), shown with the black line histogram. The invariant mass distribution of $B^{\pm}$ candidates which pass (fail) the tight vertex selection of the analysis ($\chi^2/N_{\mathrm{d.o.f.}} < 6$) is shown with the blue continuous (red dashed) line histogram.

A study has been done to verify the $B^{\pm}$ vertexing efficiency with data, using the

ratio

$$\varepsilon_{\text{vertex}}^{\mu\mu K} = \frac{(N^{B^\pm} \mid \chi^2/N_{\text{dof}} < 6)}{(N^{B^\pm} \mid \chi^2/N_{\text{dof}} < 10000)} \ , \tag{8.18}$$

where $N^{B^\pm}$ in the numerator and the denominator are signal yields obtained with fits to the invariant mass of candidates passing the tight and loose vertex selections, respectively. The fit strategy followed is the same as described in Section 8.3.4 with fits performed in the four rapidity regions for better statistical precision. The result for the $B^\pm$ vertexing efficiency is seen in Figure 8.28, compared to the expectation from simulation. Systematics from the fit will mostly cancel in the ratio of Equation 8.18, so the statistical uncertainty of the fits in the data is used to assign a binomial error to the vertexing efficiency in each bin. Within the available statistical precision, the data-derived estimation agrees with the expectation from simulation. Moreover, the

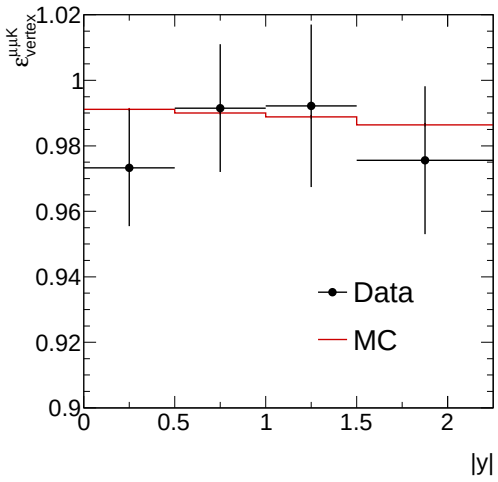

Figure 8.28: $B^\pm$ vertexing efficiency measured with data in four bins of rapidity (dots with error bars), compared to the expectation from simulation (red histogram).

effect of pile-up on the $B^\pm$ vertexing efficiency has been studied with MC simulation, showing negligible deterioration with the increase of the number of reconstructed vertices (see Figure 8.29).

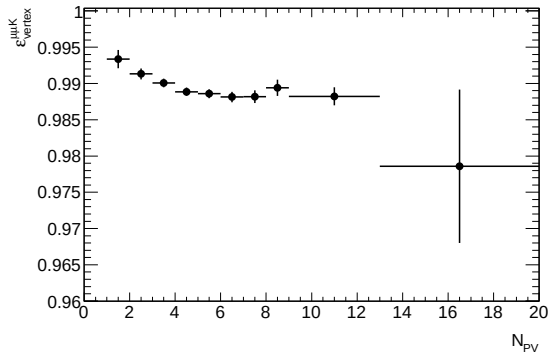

Figure 8.29: $B^{\pm}$ vertexing efficiency as a function of the number of reconstructed vertices in the event, obtained from simulated signal events.

8.4.7 B^+ / B^- efficiency difference

The efficiency of B^+ and B^- signal decays is different, due to the charge asymmetry of the kaon reconstruction efficiency, which was explained in Section 8.4.5. We obtain the difference of the efficiency for reconstructing B^+ and B^- signal decays in bins of $|y|$ and p_{T} from simulation. In Figure 8.30, shown are the reconstruction efficiencies (ommiting the trigger selection) for B^+ (ε^{B^+}) and B^- (ε^{B^-}), together with their relative difference, $\Delta\varepsilon/\varepsilon = (\varepsilon^{B^+} - \varepsilon^{B^-})/\varepsilon^{B^+}$. We can assume no significant rapidity dependance of the efficiency difference and thus derive its value in the eight p_{T} bins used in this analysis from the plot of $\Delta\varepsilon/\varepsilon$ vs p_{T}.

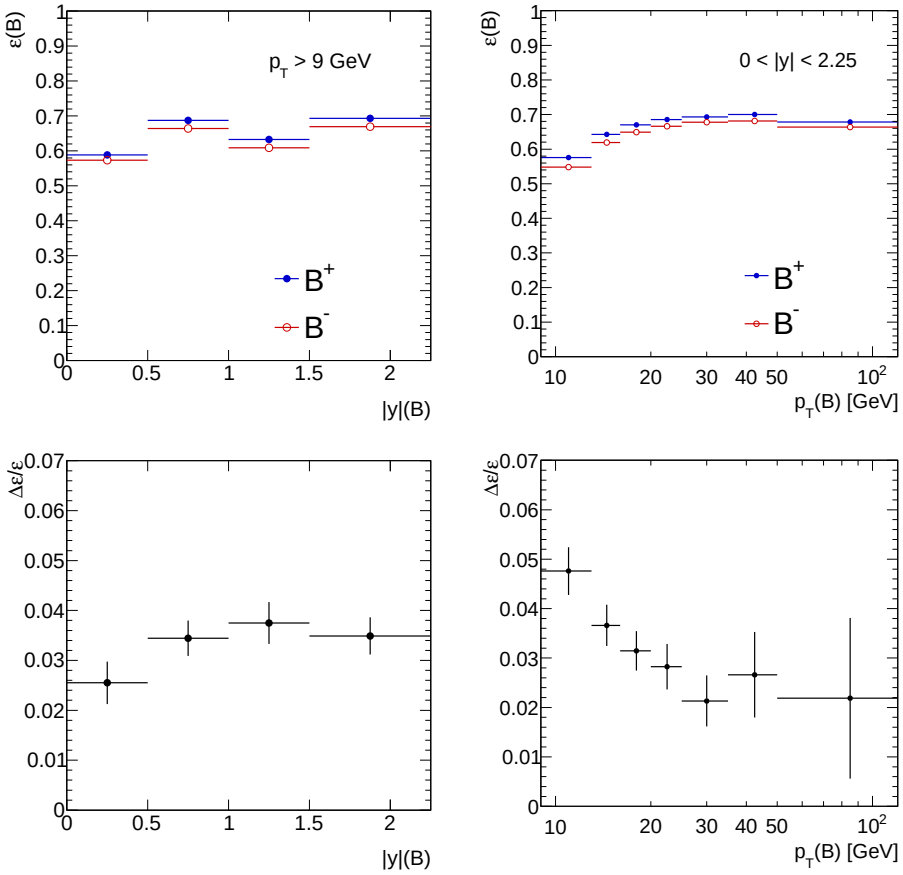

Figure 8.30: The signal efficiency (top) and the efficiency difference (bottom) for reconstructing B^+ and B^- signal events (no trigger selection applied) in bins of rapidity (left) and transverse momentum (right), obtained from MC. The error bars correspond to the statistical uncertainty of the MC simulation.

8.4.8 B^+ efficiency after corrections

The overall signal efficiency for B^+ mesons, incorporating all effects that were discussed in Section 8.4.2, is shown in Figure 8.31. The Figure shows also the effect of applying the weights for muon reconstruction and trigger efficiency (see Sections 8.4.3 and 8.4.4, respectively). The B^+ signal efficiency is increasing with p_{T} as an effect of the increasing reconstruction efficiency of muons and kaons. At high p_{T}, there is a significant drop of efficiency due to the dimuon trigger, mainly.[1] The efficiency for B^- mesons is obtained by correcting the B^+ efficiency according to the relative difference shown in 8.30, as a function of p_{T}.

8.5 Systematic uncertainties

Various sources of systematic uncertainty on the measurement of the B^+ production cross-section are considered and discussed in the next sections. A list of these uncertainties is given in Table 8.2, along with their range in the four rapidity intervals. Their breakdown in (p_{T}, y) intervals is given in Figure 8.32. In the same figure, the total systematic uncertainty, including the uncertainties from the luminosity and branching ratio, is compared to the statistical precision of the measurement.

Trigger efficiency systematics

As explained in Section 8.4.4, the trigger efficiency is obtained in bins of p_{T} and $q \cdot \eta$ of the muon, where q is the muon charge, using a tag-and-probe method on data. Then, the correction weights (scale-factors) for the trigger efficiency, $w^{J/\psi}_{\mathrm{trigger}}$, are obtained from the fraction of the measured efficiency from data over the expectation from simulation in each $(p_{\mathrm{T}}, q \cdot \eta)$ bin (see Figure 8.25). As the statistical component of the uncertainty associated with the weights for the trigger efficiency is dominant, the uncertainty on the cross-section is derived from a series of pseudo-experiments by

[1] The trigger becomes deficient in separating ROIs of dimuons with very small opening angle ΔR (see Figure 8.22), which is the case for muons from decays of boosted J/ψ mesons originating from decays of high-p_{T} B^+ mesons.

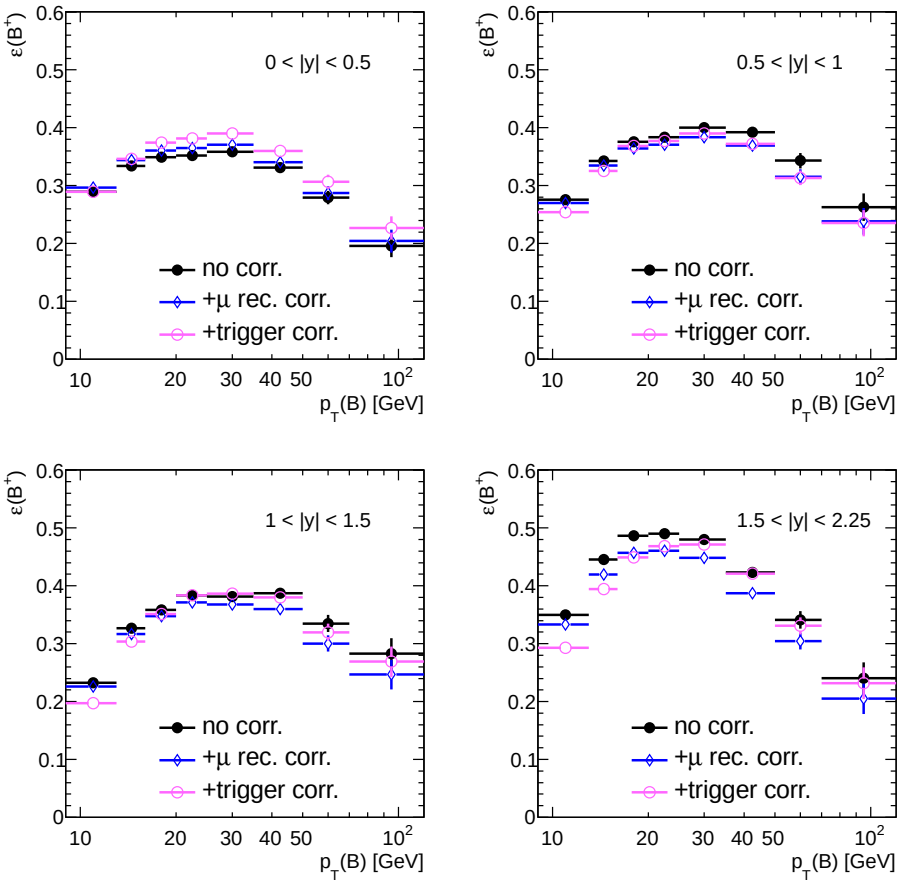

Figure 8.31: The signal efficiency for B^+ events, obtained from MC simulation before and after applying corrections for trigger and muon reconstruction, given in p_{T} intervals in the four rapidity regions defined in this analysis. The error bars correspond to the statistical uncertainty of the MC simulation and do not include uncertainties from the used scale factors.

Table 8.2: The statistical and total systematic uncertainties on the cross-section measurement. The contributions from the various sources of systematic uncertainty are also given. The quoted numbers are the lower and upper values over the p_{T} intervals for the four rapidity intervals.

	Relative uncertainty [%]			
Source	$\|y\| < 0.5$	$0.5 < \|y\| < 1$	$1 < \|y\| < 1.5$	$1.5 < \|y\| < 2.25$
Statistical uncertainty	2.2–14	2.5–17	3.2–22	3.8–24
Total systematic uncertainty	6.7–14	6.5–13	6.9–16	7.6–18
1. Trigger	3.8–7.4	3.2–6.2	3.4–7.0	3.6–8.8
2. Invariant mass fit	1.8–3.4	1.7–5.3	2.4–8.9	2.6–7.6
3. Kaon reconstruction	2.2	2.2–2.4	2.5–2.9	3.5–4.0
4. Acceptance	0.9–3.5	0.9–3.6	1.0–4.2	1.0–5.8
5. Muon reconstruction	0.5–1.3	0.5–1.7	0.5–2.1	0.6–5.4
6. $B^{\pm}$ vertexing	2.0	2.0	2.0	2.0
7. Branching ratio	3.4	3.4	3.4	3.4
8. Luminosity	1.8	1.8	1.8	1.8
9. Signal efficiency	1.3–10	1.3–9.1	1.3–9.5	1.2–12

allowing the weights to fluctuate randomly under a Gaussian assumption, according to their assigned uncertainty. Each pseudo-experiment provides a modified value for the signal efficiency in each (p_{T}, y) interval of $B^{\pm}$ meson. In each (p_{T}, y) interval, 200 pseudo-experiments are performed to obtain the relative efficiency difference, $(\varepsilon' - \varepsilon)/\varepsilon$, where ε is the nominal and ε' is the modified signal efficiency. The RMS value of the resulting distribution is used as an estimate of the systematic uncertainty in that (p_{T}, y) interval. Figure 8.33 shows the distribution of the relative efficiency difference in each interval.

Fit systematics

For the fit method, three sources of systematic uncertainty are identified and considered to be uncorrelated. These are the shape of the signal pdf, the reconstructed $B^{\pm}$ mass and the shape of the background pdf. Below, the procedure to estimate the systematic uncertainty from each source is described, and the resulting uncertainties are added quadratically to obtain the total systematic uncertainty from the fit method

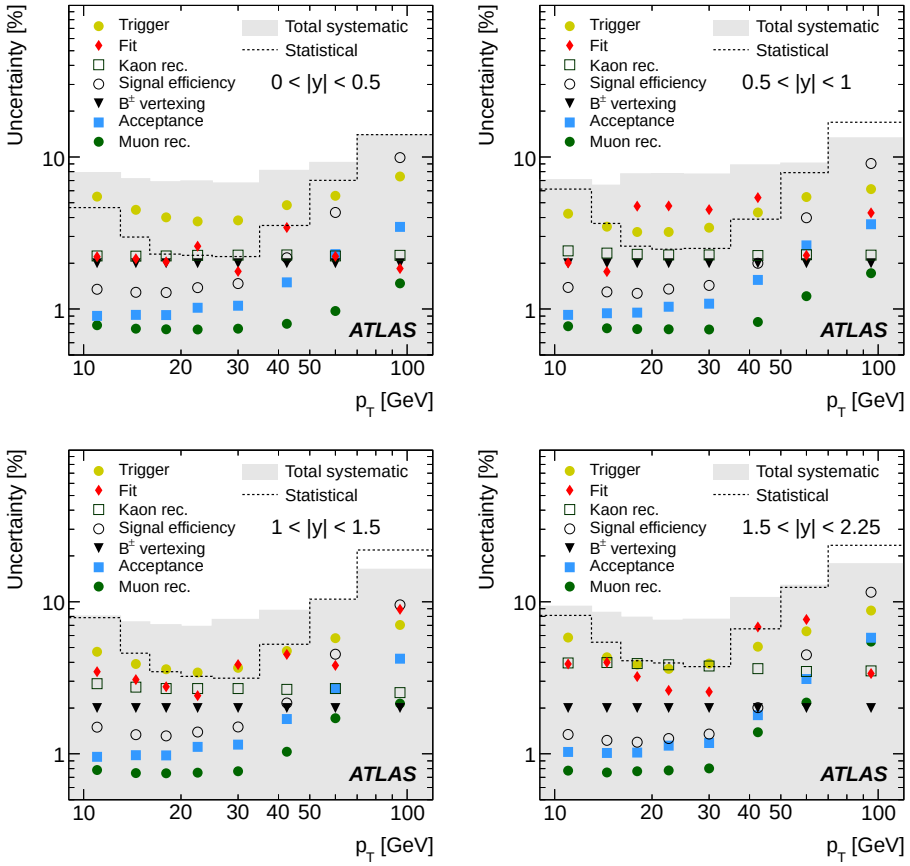

Figure 8.32: Relative systematic uncertainties affecting the cross-section in p_{T} intervals for different rapidity ranges. The total systematic uncertainty (solid area), including uncertainties from luminosity (1.8%) and branching ratio (3.4%), is compared to the statistical uncertainty (dashed line).

in each (p_{T}, y) interval.

1. *Uncertainty on shape of the signal pdf.* This uncertainty is estimated with variations of the fit model, where the values of the signal pdf parameters σ_1, σ_2, f_1 are varied independently within their uncertainties derived from the fit to signal events from MC simulation. From these variations of the fit model, the largest absolute value of the signal yield variation is taken as the systematic uncertainty from the signal pdf shape, in order to account for the large correlations of these parameters. Two alternative pdfs were considered (three Gaussians,

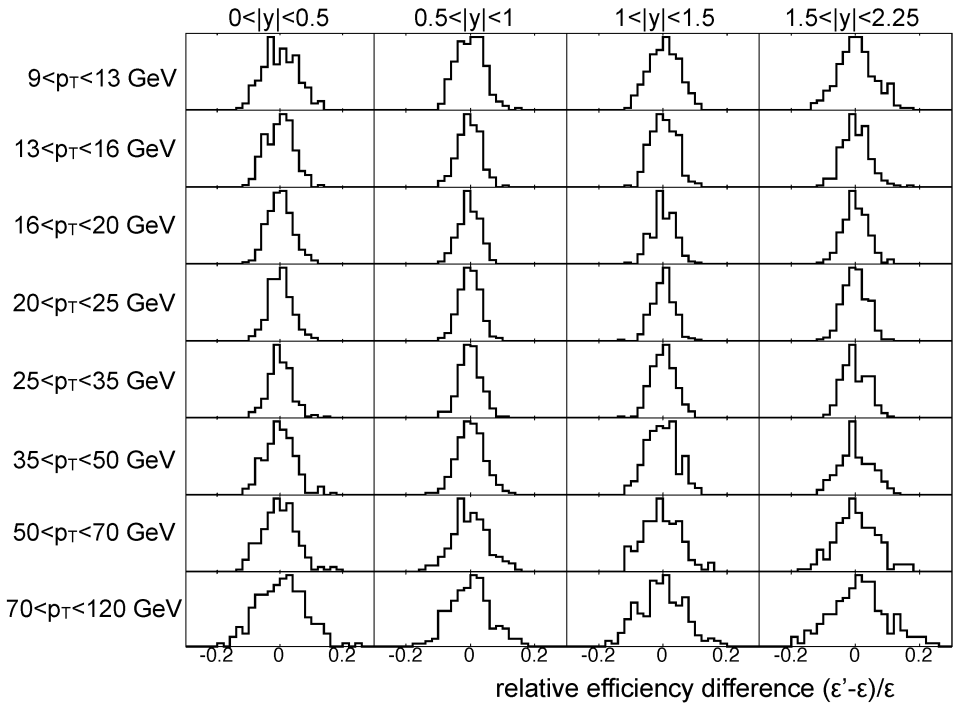

Figure 8.33: Results of 200 pseudo-experiments for estimation of the systematic uncertainty from the trigger efficiency on the cross-section in each (p_{T}, y) interval of the $B^{\pm}$ meson. Each experiment uses random variations of the trigger efficiency weights to obtain the relative efficiency difference, with respect to the nominal signal efficiency. The RMS value of the resulting distribution in each interval is used as an estimate of the systematic uncertainty from the trigger efficiency.

two Crystal Ball + Gaussian) and no significant differences in the signal yield were observed. Among the various sources of systematic uncertainty considered for the fit method, the signal pdf is dominant and its contribution ranges from 1% to 8%.

2. *Uncertainty on the $B^{\pm}$ mass value.* The reconstructed mass $m_{B^{\pm}}$ is obtained from data by fitting the invariant mass of all candidates with $p_{\mathrm{T}} > 9$ GeV in each of the four rapidity intervals. The resulting values are used to fix this parameter when performing the fits in the various (p_{T}, y) intervals and their statistical uncertainties (0.4–1.0 MeV) is used to estimate the systematic uncertainty on

the signal yield. The fits in the various (p_{T}, y) intervals are repeated varying the value of $m_{B^\pm}$ within its statistical uncertainty. The observed difference in the signal yield is smaller than 1%.

3. *Uncertainty on the shape of the background pdf.* The fit includes three components for the description of the background. They are listed below, and each contributes as a possible source of uncertainty. In order to account for the large correlations between the three components, the systematic uncertainty assigned to the background modeling for each (p_{T}, y) interval is obtained after varying each component independently, and taking the largest observed difference in the signal yield.

   (a) Combinatorial background: Using a polynomial instead of exponential shape for the combinatorial bacground, the observed difference in the signal yield ranges from 0.1% to 4%, being larger in higher rapidity and p_{T} intervals.

   (b) $B^\pm \to J/\psi\,\pi^\pm$: For the resonant background from $B^\pm \to J/\psi\,\pi^\pm$, the dominant uncertainty comes from the relative branching fraction of this decay with respect to the signal, which has an uncertainty of 10% [1]. Varying this fraction in the fit within its uncertainty was found to have a small effect on the signal yield ($\sim$1%).

   (c) Partially reconstructed b-hadron decays: The resonant background from partially reconstructed b-hadron decays is modeled with a complementary error function. Varying its parameters within their uncertainties from the fits to background events from MC simulation, the observed difference in the signal yield is smaller than 1%.

Kaon track reconstruction efficiency systematics

The efficiency of hadron reconstruction is determined from MC simulation and validated with data [3], with the uncertainty dominated by the material description.[1] To estimate the systematic uncertainty for hadron reconstruction efficiency, variations in the material description in the MC simulation are performed, using more material for the ID (+5%, +10%) and for the service structures between Pixel and SCT detectors (+20%). For hadrons of $p_{\mathrm{T}} > 0.5$ GeV, where the efficiency is relatively stable with p_{T}, the resulting uncertainty on hadron reconstruction efficiency is considered as a function of η of the hadron, and its value is obtained in five η intervals, as seen in Table 8.3. This uncertainty, convolved with the η distribution of kaons

Relative uncertainty [%] per $\lvert\eta\rvert$ interval				
$\lvert\eta\rvert < 1.3$	$1.3 < \lvert\eta\rvert < 1.9$	$1.9 < \lvert\eta\rvert < 2.1$	$2.1 < \lvert\eta\rvert < 2.3$	$2.3 < \lvert\eta\rvert < 2.5$
2.2	3.2	4.1	4.1	7.1

Table 8.3: Tracking efficiency systematic uncertainty for hadron reconstruction for tracks of $p_{\mathrm{T}} > 0.5$ GeV, taken from Ref. [3].

from signal $B^{\pm}$ decays, translates to an uncertainty of 2% to 4% on the cross-section measurement.

Acceptance systematics

The acceptance in each (p_{T}, y) interval has a relative uncertainty ranging from 1% to 4%, due to the size of the MC sample, which is assigned as systematic uncertainty. Theoretical uncertainties on the acceptance, due to the underlying kinematic distributions modeled by the generator and choice of PDF, were studied and found to be negligible, as will be discussed later in in Section.

[1] In this reference, the tracking efficiency is studied with data of 2010 and the systematic uncertainty is evaluated for an older version of ATLAS simulation samples (MC09). However, results are valid also for data and MC samples of 2011 and 2012, as the track reconstruction algorithms and the material description have not changed.

Muon reconstruction efficiency systematics

For the evaluation of the systematic uncertainty on the cross-section for the muon reconstruction efficiency, the procedure is similar to the one followed for the trigger efficiency. As explained in Section 8.4.3, the muon reconstruction efficiency is obtained in bins of p_{T} and $q \cdot \eta$ of the muon, using a tag-and-probe method on data. This efficiency measurement has an uncertainty which is mainly statistical, and propagates to the muon efficiency weights, w^{μ}_{MS} (Figure 8.20), that we use to correct the MC samples. Then the systematic uncertainty on the cross-section is evaluated from 200 pseudo-experiments, using random variations of the muon efficiency weights, by taking the RMS value of the resulting distribution of the difference observed on the signal efficiency. In addition, there is also an uncertainty coming from the efficiency for reconstructing a muon in the ID with the selection criteria used in this analysis. This efficiency is found to be 99% with a systematic uncertainty of 0.5% for each muon.

$B^{\pm}$ vertexing efficiency systematics

The vertex quality requirement has an efficiency of about 99%, as shown in Figure 8.28. It was estimated with data by comparing the signal yields in four rapidity intervals before and after applying this requirement and is found to be consistent with the expectation from MC simulation. A maximum difference of 2% is observed between the estimate from data and the expectation from MC simulation for this efficiency and is assigned as systematic uncertainty the cross-section.

Branching ratio uncertainty

The total branching ratio of the selected decay, obtained by combining the branching ratios of the decays $B^{\pm} \to J/\psi\, K^{\pm}$ and $J/\psi \to \mu^{+}\mu^{-}$, has an uncertainty of 3.4% [1].

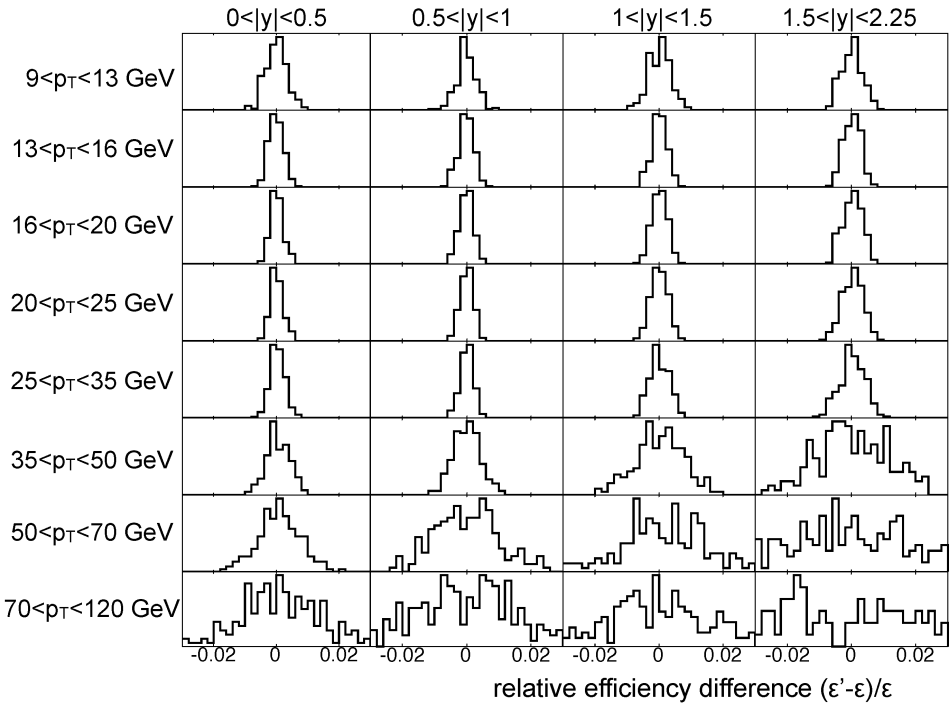

Figure 8.34: Results of 200 pseudo-experiments for estimation of the systematic uncertainty from the muon reconstruction efficiency on the cross-section in each (p_{T}, y) interval of the $B^{\pm}$ meson. Each experiment uses random variations of the muon efficiency weights to obtain the relative efficiency difference, with respect to the nominal signal efficiency. The RMS value of the resulting distribution in each interval is used as an estimate of the systematic uncertainty from the muon efficiency.

Luminosity determination systematics

The luminosity calibration is based on data from van der Meer scans and has an uncertainty of 1.8% [5].

Signal efficiency

The efficiency correction factor for $B^{\pm}$ signal events is obtained from MC simulation (Equation (8.10)). The systematic uncertainty assigned to this factor has two components, which are added in quadrature:

1. *Uncertainty from the size of the MC sample.* A sample of 2M fully simulated signal decays is used for the estimation of the signal efficiency, corresponding to a luminosity similar to that of the data sample. Due to the size of this sample, which is limited by the available computing resources, the efficiency estimation has an uncertainty that is small (∼1%) in most intervals and becomes significant in the high-p_{T} interval 70–120 GeV (∼10%).

2. *Uncertainty from K^+/K^- efficiency asymmetry.* Because of the different interactions of K^+ and K^- mesons with the detector material, the efficiencies for the kaons used in this analysis differ by ∼3.5%, as obtained from simulation and verified with data (see Section 8.4.6). The statistical uncertainty of the estimation of this efficiency difference from data is used to assign a systematic uncertainty of 1%, which propagates to the cross-section through the sum of efficiencies ($\varepsilon^{B^+} + \varepsilon^{B^-}$) in Equation (8.2).

Theoretical uncertainties on the signal efficiency, due to the underlying kinematic distributions modeled by the generator and choice of PDF, were studied and found to be negligible, as will be explained in Section 8.5.

Other systematics

Additional sources of systematic uncertainty were examined, but were found to be less significant. Residual effects related to final-state radiation have been determined to be smaller than 1% and are neglected. Differences in the underlying kinematic distributions modeled by the Pythia and NLO generators, including PDFs, were considered. The impact on the acceptance and the signal efficiency was estimated by reweighting the kinematic distributions of Pythia to those of Powheg and MC@NLO (details can be found in Appendix C). The largest effect is seen in the high-rapidity intervals ($1.5 < |y| < 2.25$), where the maximum relative difference observed is 1%, with a statistical uncertainty of the same order, while in most (p_{T}, y) intervals the effect is very small (∼0.1%). No systematic uncertainty is assigned for this. Bin-to-bin migration of signal events due to finite detector resolution is studied with MC simulation. It is found to be a small effect (<0.5%), which is included in

the definition of signal efficiency (Equation (8.10)) and no systematic uncertainty is assigned for it. Potential effects in the calculation of the signal efficiency due to the difference between the momentum scales in data and MC simulation are expected to be larger in the lower p_{T} intervals used in this analysis, where they were estimated to be smaller than 0.5%, and no systematic uncertainty is assigned for this source either.

8.6 Results

8.6.1 B^+ production cross-section

Using eq. (8.1), the differential cross-section for B^+ production times branching ratio $\mathscr{B}$ is obtained as a function of p_{T} and y of the B^+ meson and the results are shown in Tables 8.4 and 8.5, averaged over each (p_{T}, y) interval. The double-differential cross-section is integrated over p_{T} to obtain the differential cross-section $\mathrm{d}\sigma/\mathrm{d}y$, or over rapidity to obtain $\mathrm{d}\sigma/\mathrm{d}p_{\mathrm{T}}$, and results are reported in Tables 8.6 and 8.7. When summing over the intervals in p_{T} or rapidity, the systematic uncertainty

p_{T} interval [GeV]	$\frac{\mathrm{d}^2\sigma}{\mathrm{d}p_{\mathrm{T}}\mathrm{d}y} \cdot \mathscr{B}(B^+ \to J/\psi K^+) \cdot \mathscr{B}(J/\psi \to \mu^+\mu^-)$ [pb/GeV] $0 < \lvert y\rvert < 0.5$	$0.5 < \lvert y\rvert < 1$
9–13	$24.5 \pm 1.1 \pm 1.7$	$21.7 \pm 1.3 \pm 1.4$
13–16	$8.7 \pm 0.3 \pm 0.6$	$8.5 \pm 0.3 \pm 0.5$
16–20	$3.76 \pm 0.09 \pm 0.22$	$3.9 \pm 0.10 \pm 0.27$
20–25	$1.54 \pm 0.04 \pm 0.09$	$1.57 \pm 0.04 \pm 0.11$
25–35	$0.467 \pm 0.010 \pm 0.027$	$0.468 \pm 0.012 \pm 0.033$
35–50	$0.097 \pm 0.003 \pm 0.007$	$0.095 \pm 0.004 \pm 0.008$
50–70	$0.0165 \pm 0.0012 \pm 0.0014$	$0.0178 \pm 0.0014 \pm 0.0015$
70–120	$0.00188 \pm 0.00026 \pm 0.00025$	$0.00202 \pm 0.00034 \pm 0.00026$

Table 8.4: Differential cross-section measurement for B^+ production multiplied by the branching ratio to the final state, averaged over each (p_{T}, y) interval in the rapidity range $|y| < 0.5$ and $0.5 < |y| < 1$. The first quoted uncertainty is statistical, the second uncertainty is systematic.

from each source is calculated from the linear sum of the contributions from each

p_{T} interval [GeV]	$\frac{\mathrm{d}^2\sigma}{\mathrm{d}p_{\mathrm{T}}\mathrm{d}y} \cdot \mathscr{B}(B^+ \to J/\psi K^+) \cdot \mathscr{B}(J/\psi \to \mu^+\mu^-)$ [pb/GeV] $1 < \lvert y \rvert < 1.5$	$1.5 < \lvert y \rvert < 2.25$
9–13	$23.6 \pm 1.9 \pm 1.7$	$22.3 \pm 1.8 \pm 1.9$
13–16	$8.0 \pm 0.4 \pm 0.5$	$7.1 \pm 0.4 \pm 0.6$
16–20	$3.29 \pm 0.11 \pm 0.20$	$2.90 \pm 0.12 \pm 0.21$
20–25	$1.32 \pm 0.04 \pm 0.08$	$1.08 \pm 0.04 \pm 0.07$
25–35	$0.408 \pm 0.013 \pm 0.028$	$0.312 \pm 0.012 \pm 0.022$
35–50	$0.073 \pm 0.004 \pm 0.006$	$0.055 \pm 0.004 \pm 0.006$
50–70	$0.0135 \pm 0.0014 \pm 0.0013$	$0.0097 \pm 0.0012 \pm 0.0012$
70–120	$0.00095 \pm 0.00021 \pm 0.00015$	$0.00083 \pm 0.00019 \pm 0.00014$

Table 8.5: Differential cross-section measurement for B^+ production multiplied by the branching ratio to the final state, averaged over each (p_{T}, y) interval in the rapidity range $1 < |y| < 1.5$ and $1.5 < |y| < 2.25$. The first quoted uncertainty is statistical, the second uncertainty is systematic.

p_{T} interval [GeV]	$\frac{\mathrm{d}\sigma}{\mathrm{d}p_{\mathrm{T}}} \cdot \mathscr{B}(B^+ \to J/\psi K^+) \cdot \mathscr{B}(J/\psi \to \mu^+\mu^-)$ [pb/GeV] $\lvert y \rvert < 2.25$
9–13	$103 \pm 4 \pm 8$
13–16	$36.0 \pm 0.8 \pm 2.3$
16–20	$15.3 \pm 0.3 \pm 1.0$
20–25	$6.1 \pm 0.1 \pm 0.4$
25–35	$1.81 \pm 0.03 \pm 0.12$
35–50	$0.348 \pm 0.008 \pm 0.028$
50–70	$0.062 \pm 0.003 \pm 0.005$
70–120	$0.0061 \pm 0.0006 \pm 0.0007$

Table 8.6: Differential cross-section measurement for B^+ production multiplied by the branching ratio to the final state, averaged over each p_{T} interval in the rapidity range $|y| < 2.25$. The first quoted uncertainty is statistical, the second uncertainty is systematic.

interval, as they are correlated. Tabulated results of the measurements presented in this paper are available in HepData[1].

Using the world-average value for the branching ratio $\mathscr{B}$, the differential cross-sections obtained are compared to predictions of Powheg (+Pythia) and MC@NLO (+Herwig) and the FONLL approximations. For Powheg and MC@NLO the CT10 [6] param-

[1] HepData repository for the B^+ cross-section results: `http://hepdata.cedar.ac.uk/view/p8401`.

$\lvert y\rvert$ interval	$\frac{\mathrm{d}\sigma}{\mathrm{d}y} \cdot \mathscr{B}(B^+ \to J/\psi K^+) \cdot \mathscr{B}(J/\psi \to \mu^+\mu^-)$ [pb] $9\ \mathrm{GeV} < p_\mathrm{T} < 120\ \mathrm{GeV}$
0.0–0.5	$154 \pm 5 \pm 10$
0.5–1.0	$143 \pm 6 \pm 9$
1.0–1.5	$144 \pm 8 \pm 10$
1.5–2.25	$132 \pm 7 \pm 11$

Table 8.7: Differential cross-section measurement for B^+ production multiplied by the branching ratio to the final state, averaged over each y interval in the p_T range 9 GeV$<$ $p_\mathrm{T} < 120$ GeV. The first quoted uncertainty is statistical, the second uncertainty is systematic.

eterization for the parton distribution function of the proton is used, while for FONLL calculations the CTEQ6.6 [7] parameterization is used. In all cases, a b-quark mass of 4.75 ± 0.25 GeV is used, with the renormalization and factorization scales, μ_r, μ_f, set to $\mu_r = \mu_f = \mu$, where μ has different definitions for the POWHEG, MC@NLO and FONLL predictions.[1] The predictions are quoted with uncertainties due to the b-quark mass and renormalization and factorization scales. Uncertainties from factorization and renormalization scales are estimated by varying them independently up and down by a factor of two [8].

POWHEG and MC@NLO predictions are compared with the double-differential cross-section measurement in Figure 8.35. To allow a better comparison between the measured cross-sections and the NLO predictions, Figure 8.36 shows their ratio for each rapidity range separately for POWHEG and MC@NLO. The data are in good agreement with POWHEG in all rapidity intervals. MC@NLO, however, predicts a lower production cross-section at low p_T and a p_T spectrum that is softer than the data for $|y| < 1$ and harder than the data for $|y| > 1$. In the integration of the four rapidity intervals, this effect averages out and the prediction of the cross-section $\mathrm{d}\sigma/\mathrm{d}p_\mathrm{T}$ is compatible with data.

The FONLL prediction is compared with the measured differential cross-section

[1]For POWHEG: $\mu^2 = m_Q^2 + (m_{Q\bar{Q}}^2/4 - m_Q^2)\sin^2\theta_Q$, where $m_{Q\bar{Q}}$ is the invariant mass of the $Q\bar{Q}$ system and θ_Q is the polar angle of the heavy quark in the $Q\bar{Q}$ rest frame. For MC@NLO: $\mu^2 = m_Q^2 + (p_{\mathrm{T},\,Q} + p_{\mathrm{T},\,\bar{Q}})^2/4$, where $p_{\mathrm{T},\,Q}$ and $p_{\mathrm{T},\,\bar{Q}}$ are the transverse momenta of the produced heavy quark and antiquark respectively, and m_Q is the heavy-quark mass. For FONLL: $\mu = \sqrt{m_Q^2 + p_{\mathrm{T},\,Q}^2}$.

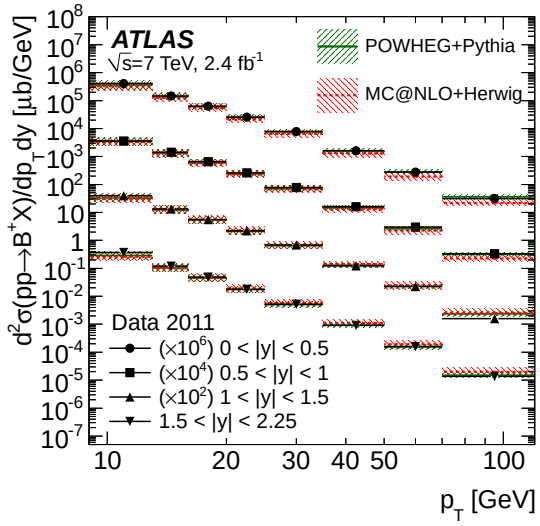

Figure 8.35: Double-differential cross-section of B^+ production as a function of p_{T} and y, averaged over each (p_{T}, y) interval and quoted at its centre. The data points are compared to NLO predictions from POWHEG and MC@NLO. The shaded areas around the theoretical predictions reflect the uncertainty from renormalization and factorization scales and the b-quark mass.

$\mathrm{d}\sigma/\mathrm{d}p_{\mathrm{T}}$ in Figure 8.37. In this Figure, the results from CMS [9] for B^+ meson production as a function of p_{T}, covering the rapidity range $|y| < 2.4$, are shown for comparison. The FONLL prediction is in good agreement with the data concerning the behaviour in rapidity and p_{T}, within the theoretical uncertainties.

All available predictions for $\mathrm{d}\sigma/\mathrm{d}y$ are compared with data in Figure 8.38. The measured cross-section has a small rapidity dependence and is in agreement with the predictions within their uncertainties. The theoretical uncertainties in all cases are large (∼30%) and are similar for the POWHEG, MC@NLO and FONLL predictions.

The integrated B^+ production cross-section in the kinematic range 9 GeV $< p_{\mathrm{T}} <$ 120 GeV and $|y| < 2.25$ is:

$$\sigma(pp \to B^+X) = 10.6 \pm 0.3\ (\mathrm{stat.}) \pm 0.7\ (\mathrm{syst.}) \pm 0.2\ (\mathrm{lumi.}) \pm 0.4\ (\mathscr{B})\ \mu\mathrm{b}.$$

The FONLL prediction, with its theoretical uncertainty from the renormalization and factorization scale and the b-quark mass, is:

$$\sigma(pp \to bX) \cdot f_{\bar{b}\to B^+} = 8.6^{+3.0}_{-1.9}\ (\mathrm{scale}) \pm 0.6\ (m_b)\ \mu\mathrm{b}\ ,$$

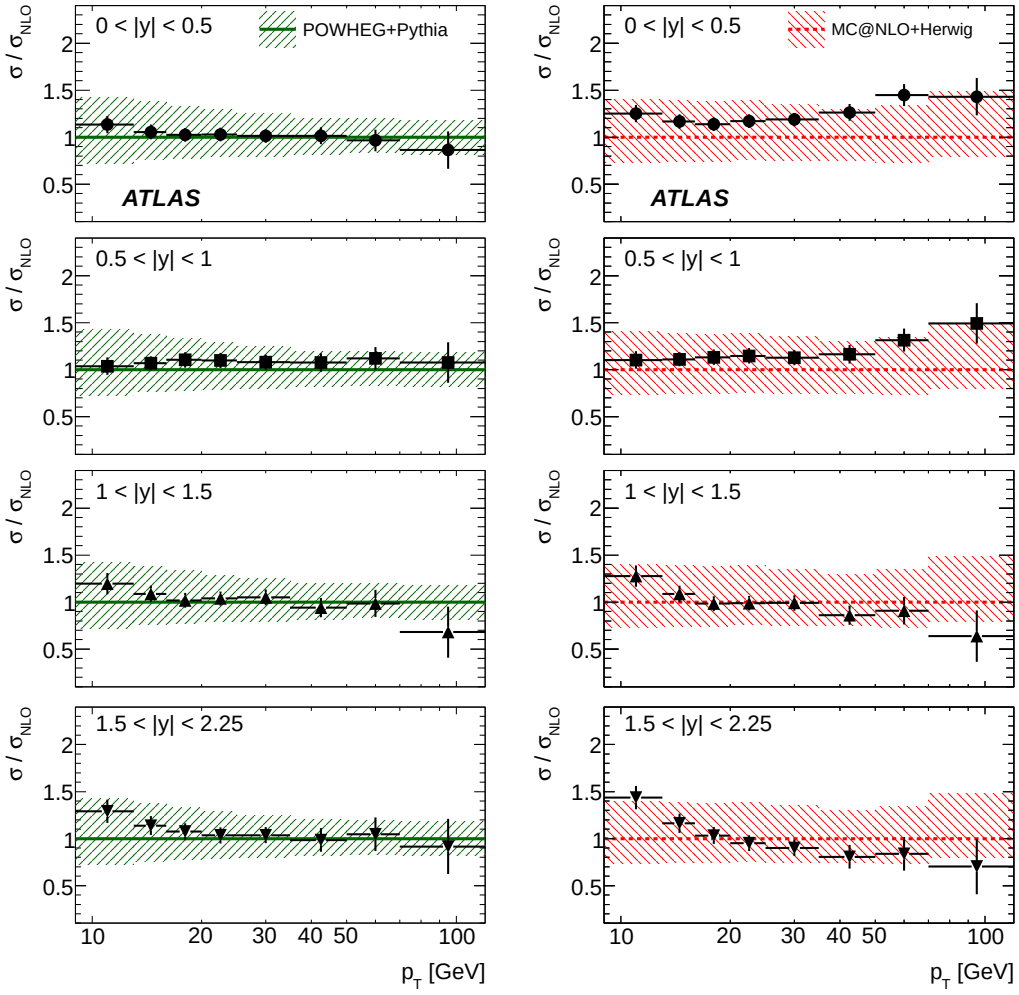

Figure 8.36: Ratio of the measured cross-section to the theoretical predictions ($\sigma/\sigma_{\mathrm{NLO}}$) of POWHEG (left) and MC@NLO (right) in eight p_{T} intervals in four rapidity ranges. The points with error bars correspond to data with their associated uncertainty, which is the combination of the statistical and systematic uncertainty. The shaded areas around the theoretical predictions reflect the uncertainty from renormalization and factorization scales and the b-quark mass.

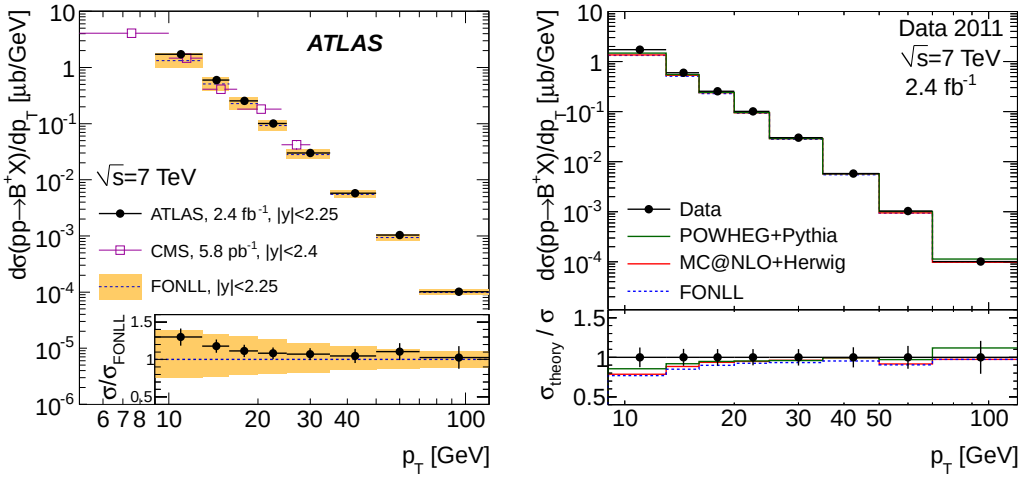

Figure 8.37: Differential cross-section of B^+ production vs p_{T}, integrated over rapidity. The solid circle points with error bars correspond to the differential cross-section measurement of ATLAS with total uncertainty (statistical and systematic) in the rapidity range $|y| < 2.25$, averaged over each p_{T} interval and quoted at its centre. **On the left**, the data points are compared to results from CMS, for a measurement covering $p_{\mathrm{T}} < 30$ GeV and $|y| < 2.4$ [9], and to predictions of the FONLL calculation [8] for b-quark production with its uncertainty, assuming a hadronization fraction of $f_{\bar{b}\to B^+}$ of $(40.1 \pm 0.8)\%$ [1]. Also shown is the ratio of the measured cross-section to the predictions of the FONLL calculation ($\sigma/\sigma_{\mathrm{FONLL}}$). The upper and lower uncertainty limits on the prediction were obtained considering scale and b-quark mass variations. **On the right**, all available theoretical predictions, FONLL, POWHEG and MC@NLO, are compared to the data points. For each prediction, the ratio of the predicted cross-section to the data ($\sigma_{\mathrm{theory}}/\sigma$) is also shown. The uncertainties of the predictions, which for POWHEG and MC@NLO are similar to the uncertainty of FONLL, are not shown.

where $f_{\bar{b}\to B^+} = (40.1 \pm 0.8)\%$ [1] is the world-average value for the hadronization fraction. The corresponding predictions of POWHEG and MC@NLO are 9.4 μb and 8.8 μb, respectively, with theoretical uncertainties similar to the FONLL prediction.

8.6.2 B^+/B^- ratio

We extract the ratio of the production of the two charged states, in order to test the assumption of equal B^+ and B^- production. This is performed by fitting the invariant mass distribution of B^+ and B^- candidates separately in the four rapidity intervals

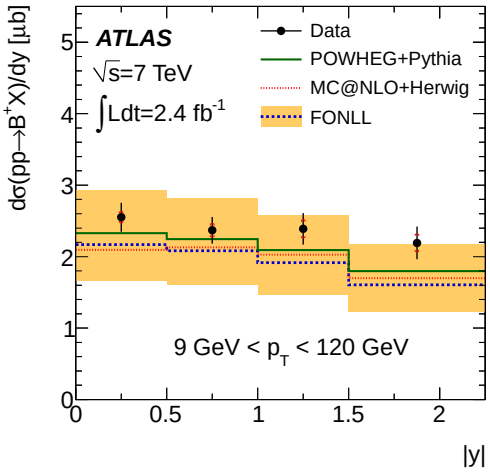

Figure 8.38: Differential cross-section of B^+ production vs rapidity, integrated over p_{T}. Points with error bars correspond to the differential cross-section measurement with total uncertainty (lines on the error bars indicate the statistical component) in the p_{T} range 9 GeV $< p_{\mathrm{T}} <$ 120 GeV, averaged over each rapidity interval and quoted at its centre. POWHEG, MC@NLO and FONLL predictions are also given for comparison. The FONLL prediction is quoted with upper and lower uncertainty limits, which were obtained considering scale and b-quark mass variations. The relevant uncertainties of the predictions of POWHEG and MC@NLO are of the same order and are not shown.

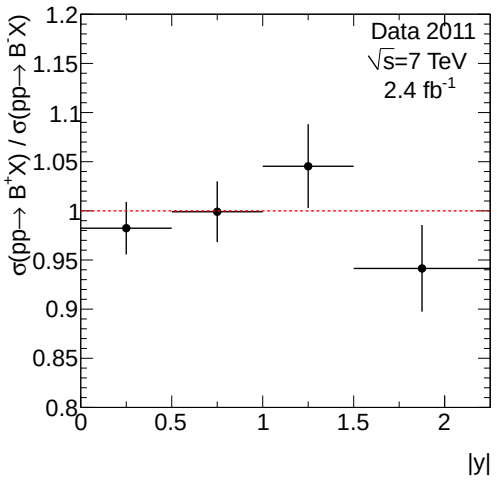

Figure 8.39: Ratio of B^+ over B^- production, corrected for the efficiency difference for reconstructing two charged states, as a function of rapidity. The uncertainty shown is statistical only.

and then correcting for the B^+/B^- efficiency difference (see Section 8.4.7). In the ratio of $\sigma(pp \to B^+X)/\sigma(pp \to B^-X)$, all systematics (luminosity, branching ratio, trigger, acceptance, fit, vertexing) are expected to cancel, except for the systematic for the charge asymmetry of the kaon reconstruction (1%). In Figure 8.39 the ratio of B^+ over B^- meson production is shown with its statistical uncertainty from the fit to data. The statistical uncertainty of the data is 1.8–3.3% and within this uncertainty we see that the ratio the B^+ to B^- production is consistent with unity. We conclude that this analysis is not sensitive to potential asymmetry in the production of B^+ and B^- mesons.

8.7 Discussion of results

A measurement of the differential cross-section for B^+ meson production has been presented. The measurement was performed with 2.4 fb^{-1} of pp collision data at $\sqrt{s} = 7$ TeV, recorded in 2011 with the ATLAS detector at the LHC. The cross-section was measured as a function of transverse momentum and rapidity in the range 9 GeV $< p_{\mathrm{T}} <$ 120 GeV and $|y| < 2.25$, and quoted with a total uncertainty of

7%–30%, with the main source of uncertainty being systematic in most bins, except for the high-p_{T} bins were the statistical uncertainty is larger than the systematics. This measurement extends previous result from CMS at $\sqrt{s} = 7$ TeV [9] at higher p_{T}, which is an interesting region for comparisons with available NLO QCD predictions [8] obtained with two approaches, the NLO+parton shower (PS) and with the FONLL approach.

Predictions from the NLO+PS approach were obtained with the POWHEG and MC@NLO frameworks using PYTHIA and HERWIG for the PS step, and are quoted with an uncertainty from renormalization and factorization scales and b-quark mass of the order of 20%–40%. Within these uncertainties, POWHEG+PYTHIA is in agreement with the measured integrated cross-sections and with the dependence on p_{T} and y. At $|y| < 1$, MC@NLO+HERWIG predicts a lower production cross-section and a softer p_{T} spectrum than the one observed in data, while for $|y| > 1$ the predicted p_{T} spectrum becomes harder than observed in data.[1] The FONLL calculation for $\sigma(pp \to b\,X)$ is compared to the data, assuming a hadronization fraction $f_{\bar{b}\to B^+}$ of $(40.1 \pm 0.8)\%$, and is in good agreement with the measured differential cross-section $\mathrm{d}\sigma/\mathrm{d}p_{\mathrm{T}}$, within the theoretical uncertainty. Focusing on the high-p_{T} region, predictions of FONLL are expected to be more accurate than those of POWHEG and MC@NLO. Predictions of POWHEG+PYTHIA, as well as those of FONLL, are found to be compatible with the measured differential cross-section up to about 100 GeV, while the NLO+PS approach has the advantage of providing a full description of the final state.

The results of this thesis for b-hadron production, obtained with the reconstruction of $B^{\pm}$ mesons decaying exclusively to $J/\psi\,K^{\pm}$, can be compared with similar measurements by the ATLAS collaboration. The inclusive b-hadron production has been measured using $B \to J/\psi\,X$ decays [11], showing a good agreement with FONLL, with a comparison covering a wide range in J/ψ p_{T} (from about 3 GeV up to about 40 GeV) in four slices of rapidity up to $|y| < 2.4$. The same measurement has

[1] We note here that the same behavior has been reported in the measurement of b-jet production [10], when comparing predictions of MC@NLO with the data in different rapidity regions.

been provided by the CMS collaboration in a similar fiducial volume [12] and some small discrepancies have been observed at high p_{T} (also commented in Ref. [8]). The $B^{\pm}$ measurement that has been presented in this thesis helps to clarify this issue. The inclusive b-hadron production has also been measured using $B \to D^{*\pm}\mu^{\mp} X$ decays [13], and the result is reported in a fiducial volume similar to the one used in this thesis for $B^{\pm}$ mesons. As in the result presented in this thesis, an excess is seen in the data with respect to NLO predictions in the low-p_{T} region but is well-within the large theoretical and the experimental uncertainties. The same conclusion has been reached by the CMS collaboration in studies of B-meson production using fully reconstructed exclusive decay channels ($B^{\pm} \to J/\psi\, K^{\pm}$ [9], $B_d^0 \to J/\psi\, K_s^0$ [14], $B_s^0 \to J/\psi\, \phi$ [15], $\Lambda_b^0 \to J/\psi\, \Lambda^0$ [16]). In addition, the LHCb collaboration has measured the $B^{\pm}$ cross-section using the decay to $J/\psi\, K^{\pm}$ in the forward rapidity region $2 < y < 4.5$ [17], demonstrating good agreement with the prediction of FONLL. Summing up the above, we conclude to a good understanding of b-hadron production at the LHC, while in many cases the available measurements achieved accuracy better than that of the theoretical predictions at NLO. This is a motivation for new theoretical calculations at higher orders that will be free of the large dependence on the choice of normalization and factorization scale and, thus, more precise.

Bibliography

[1] J. Beringer et al., *Review of Particle Physics*, Phys. Rev. **D 86** (2012) 010001.

[2] ATLAS Collaboration, *Measurement of Upsilon production in 7 TeV pp collisions at ATLAS*, Phys. Rev. D **87** (2013) 052004.

[3] ATLAS Collaboration, *Charged-particle multiplicities in pp interactions measured with the ATLAS detector at the LHC*, New J. Phys. **13** (2011) 053033, `arXiv:1012.5104 [hep-ex]`.

[4] S. Beale, *Measurement of Kaon charge asymmetry for the $B_s \to \mu^+\mu^-$ analysis*, Tech. Rep. ATL-COM-PHYS-2011-1552 (restricted to ATLAS).

[5] ATLAS Collaboration, *Improved luminosity determination in pp collisions at*

$\sqrt{s} = 7$ *TeV using the ATLAS detector at the LHC*, arXiv:1302.4393 [hep-ex].

[6] H.-L. Lai, M. Guzzi, J. Huston, Z. Li, P. M. Nadolsky, et al., *New parton distributions for collider physics*, Phys. Rev. **D 82** (2010) 074024, arXiv:1007.2241 [hep-ph].

[7] P. M. Nadolsky, H.-L. Lai, Q.-H. Cao, J. Huston, J. Pumplin, et al., *Implications of CTEQ global analysis for collider observables*, Phys.Rev. **D 78** (2008) 013004, arXiv:0802.0007 [hep-ph].

[8] M. Cacciari, S. Frixione, N. Houdeau, M. L. Mangano, P. Nason, et al., *Theoretical predictions for charm and bottom production at the LHC*, JHEP **10** (2012) 137, arXiv:1205.6344 [hep-ph].

[9] CMS Collaboration, *Measurement of the B^+ production cross section in pp collisions at $\sqrt{s} = 7$ TeV*, Phys. Rev. Lett. **106** (2011) 112001, arXiv:1101.0131 [hep-ex].

[10] ATLAS Collaboration, *Measurement of the inclusive and dijet cross-sections of b-jets in pp collisions at $\sqrt{s} = 7$ TeV with the ATLAS detector*, Eur. Phys. J. **C 71** (2011) 1846, arXiv:1109.6833 [hep-ex].

[11] ATLAS Collaboration, *Measurement of the differential cross-sections of inclusive, prompt and non-prompt J/ψ production in proton-proton collisions at $\sqrt{s} = 7$ TeV*, Nucl. Phys. **B 850** (2011) 387, arXiv:1104.3038 [hep-ex].

[12] CMS Collaboration, *J/ψ and $\psi(2S)$ production in pp collisions at $\sqrt{s} = 7$ TeV*, JHEP **02** (2012) 011, arXiv:1111.1557 [hep-ex].

[13] ATLAS Collaboration, *Measurement of the b-hadron production cross section using decays to $D^{*+}\mu^- X$ final states in pp collisions at $\sqrt{s} = 7$ TeV with the ATLAS detector*, Nucl. Phys. **B 864** (2012) 341, arXiv:1206.3122 [hep-ex].

[14] CMS Collaboration, *Measurement of the B^0 production cross section in pp collisions at $\sqrt{s} = 7$ TeV*, Phys. Rev. Lett. **106** (2011) 252001, arXiv:1104.2892 [hep-ex].

[15] CMS Collaboration, *Measurement of the strange B meson production cross section with J/ψ ϕ decays in pp collisions at $\sqrt{s} = 7$ TeV*, Phys. Rev. **D 84** (2011) 052008, arXiv:1106.4048 [hep-ex].

[16] CMS Collaboration, *Measurement of the Λ_b cross section and the $\bar{\Lambda}_b$ to Λ_b ratio with $J/\psi\Lambda$ decays in pp collisions at $\sqrt{s} = 7$ TeV*, Phys. Lett. **B 714** (2012) 136, arXiv:1205.0594 [hep-ex].

[17] LHCb Collaboration, R. Aaij et al., *Measurement of the $B^\pm$ production cross-section in pp collisions at $\sqrt{s} = 7$ TeV*, JHEP **04** (2012) 093, arXiv:1202.4812 [hep-ex].

Conclusions and perspectives

This doctoral thesis has presented an analysis of B^+ meson production using the first pp collision data at $\sqrt{s} = 7$ TeV collected by the ATLAS detector at the LHC. The work for this thesis was carried out in two steps. First, the proper functioning and the good performance of the detector were validated in order to ensure that the data can be used for the extraction of physics results. For this purpose, contributions to the development of the Data Quality Monitoring software for the muon spectrometer have been made to assess the quality of the reconstruction of muons and dimuon resonances. In addition, this thesis presented an analysis of the first data from the LHC collected in 2010. The production of $B^\pm$ mesons in ATLAS was ensured via the direct observation of reconstructed $B^\pm \to J/\psi(\mu^+\mu^-)\, K^\pm$ decays with 3.4 pb^{-1} of data. Then, the full 2010 data sample that corresponds to about 35 pb^{-1} was used for a simultaneous measurement of the $B^\pm$ mass and lifetime. With this measurement the excellent performance of the ATLAS detector in reconstructing the $B^\pm \to J/\psi(\mu^+\mu^-)\, K^\pm$ decay was demonstrated, as the measured $B^\pm$ mass and lifetime are found to be in good agreement with the world-average values. At the second step, following the detector performance studies, was the extraction of the main physics results of the thesis, that is the measurement of the differential production cross-sections for B^+ mesons. The cross-section was measured with 2.4 fb^{-1} of data recorded in 2011 as a function of transverse momentum and rapidity in the range 9 GeV $< p_{\mathrm{T}} <$ 120 GeV and $|y| < 2.25$, and quoted with a total uncertainty of about 10%. This measurement extends the range of B^+ meson production to higher p_{T} values, which is of interest to theorists for comparisons with available NLO QCD predictions from calculations obtained with the FONLL method and with the predictions of the POWHEG and

MC@NLO frameworks. Overall, a good agreement of the predictions with the data is seen. The POWHEG package, using PYTHIA for the fragmentation step, seems to be a good choice for the generation of $b\bar{b}$ events, while for the MC@NLO event generator some features in the predicted kinematics of B^+ mesons that are not compatible with the data have been noted. Predictions of POWHEG+PYTHIA, as well as those of the FONLL method, are found to be compatible with the measured differential cross-section up to about 100 GeV, while the POWHEG approach, as an event generator, has the advantage of providing a full description of the final state. In all cases, the theory predictions have an uncertainty of the order of 20%–40%, larger than the precision of the measurement, due to the choice of renormalization and factorization scales and the b-quark mass. Therefore, the measurement presented in this thesis gives a motivation for theorists to perform calculations at higher orders to reduce the theoretical uncertainty.

Outlook

After testing NLO QCD calculations, we can exploit the wealth of the available data collected until the shutdown of the LHC in early 2013 (about 5 fb^{-1} at 7 TeV and 20 fb^{-1} at 8 TeV) to look into more exciting processes, in which the decay that was studied in this thesis, $B^{\pm} \to J/\psi\, K^{\pm}$, is used as a reference. For example, there is increased interest in the purely muonic decays of B_s^0 and B_d^0 mesons. Its branching ratio is tiny according to the SM predictions ($\sim 10^{-9}$), as flavor-changing neutral currents are allowed only at loop level. If new particles exist, outside the SM, they would contribute in the loop and may enhance the branching ratio significantly. The role of the $B^{\pm} \to J/\psi\, K^{\pm}$ decay is that the branching ratio of $B \to \mu^+\mu^-$ is measured relative to the well-known branching ratio of this decay, allowing the cancellation of common systematics (luminosity, trigger efficiency, etc.). By the time that this thesis is written results have become available, first from LHCb [1] and then from CMS [2], demonstrating first observations of this rare decay with production rates compatible with the SM predictions. Results from ATLAS are also available [3] but were obtained from analysis of only 2.4 fb^{-1} of data, setting an upper limit on the branching ratio

of $B_s^0 \to \mu^+\mu^-$; an update with the full data sample is highly anticipated. In addition to the search for this very rare purely muonic decay, other rare muonic b-hadron decays are also of great interest, sharing the same objective. Decays of the type $B \to \mu^+\mu^- K$, involving a $b \to s\mu^+\mu^-$ transition, are also suppressed but have larger branching ratios ($\sim 10^{-6}$); results exist from studies at the Tevatron [4]. Analysis of the angular properties of these decays can also reveal new physics. High statistics are expected for these decays at the LHC and results are already published from LHCb, using a fraction of the available data sample. Therefore, analysis of the full available data sample will give a better insight in the properties of rare b-hadron decays. The similar topology of the $B^\pm \to J/\psi(\mu^+\mu^-)\, K^\pm$ decay allows the methods developed for its cross-section measurement to be used in such analyses in ATLAS.

In view of the large data sample that will be delivered by the LHC after it resumes operations in 2015 (about $100\,\text{fb}^{-1}$), more studies of rare B decays are planned. However, it should be clarified that B physics is only a part of the interests of the ATLAS experiment. After the recent discovery of the Higgs boson, the attention has been driven to studies of this particle's properties with the large data samples, which will allow precise measurements of its couplings in order to fully determine its nature. Concluding, particle physics is entering a new era, as the LHC will soon start operating at its design energy ($\sqrt{s} = 14$ TeV) and luminosity (10^{34} cm^{-2} s^{-1}). With the high-luminosity LHC we aim to search for new physics beyond the Standard Model and its Higgs mechanism. At the same time, B physics is still going to play a role, as it provides means to indirect searches for new physics.

At this point, this thesis comes to an end... while scientific research will go on exploring the universe of possibilities, driving our future in the most exciting way.

Bibliography

[1] LHCb Collaboration, *Measurement of the $B_s^0 \to \mu^+\mu^-$ branching fraction and search for $B^0 \to \mu^+\mu^-$ decays at the LHCb experiment*, Phys. Rev. Lett. **111** (2013) 101805, `arXiv:1307.5024 [hep-ex]`.

[2] CMS Collaboration, *Measurement of the $B_s^0 \to \mu^+\mu^-$ branching fraction and search for $B^0 \to \mu^+\mu^-$ with the CMS Experiment*, Phys. Rev. Lett. **111** (2013) 101804, arXiv:1307.5025 [hep-ex].

[3] ATLAS Collaboration, *Search for the decay $B_s^0 \to \mu^+\mu^-$ with the ATLAS detector*, Phys. Lett. **B 713** (2012) 387–407, arXiv:1204.0735 [hep-ex].

[4] CDF Collaboration, *Observation of the Baryonic Flavor-Changing Neutral Current Decay $\Lambda_b \to \Lambda\mu^+\mu^-$*, Phys.Rev.Lett. **107** (2011) 201802, arXiv:1107.3753 [hep-ex].

Appendix A

Angular properties of the $B^{\pm} \to J/\psi\, K^{\pm}$ decay

The signal decay involves a scalar meson decaying to a vector (J/ψ) and a scalar meson ($K^{\pm}$). The total angular momentum ($\mathbf{J} = \mathbf{L} + \mathbf{S}$) of the initial state is zero and conserved, therefore the $J/\psi\, K^{\pm}$ final state must have $\mathbf{L} + \mathbf{S} = 0$. We denote the azimuthal (angular momentum) and spin quantum numbers with ℓ and s, and their corresponding secondary quantum numbers (z-axis projections) with m_ℓ and m_s, respectively. The vector meson has $s_1 = 1$, $\mathrm{m}_{s1} = [-1, 0, 1]$, therefore its presence in the final state suggests that $s = 1$, $\mathrm{m}_s = \mathrm{m}_{s1} + \mathrm{m}_{s2} = [-1, 0, 1]$. Consequently, we derive that ℓ must be 1 and m_ℓ such that ensures that the total angular momentum is zero. The final state $|j, j_z\rangle = |0, 0\rangle$ is the combination of states arising from the vector sum of spin and angular momentum,

$$|j, j_z\rangle = |\ell, \mathrm{m}_\ell\rangle|s, \mathrm{m}_s\rangle = |1, \mathrm{m}_\ell\rangle|1, \mathrm{m}_s\rangle$$

for which the total angular momentum is conserved. Thus we derive that the final state is

$$\Psi = \sum c_{ij}|\mathrm{m}_\ell, \mathrm{m}_s\rangle = \frac{1}{\sqrt{3}}\left(|1, -1\rangle - |0, 0\rangle + |-1, 1\rangle\right),$$

where c_{ij} are the Clebsh-Gordan coefficients. Using the expressions of the spherical harmonics $Y_1^{m_\ell}$, we see that for selected spin state ($\mathrm{m}_s = -1, 0, 1$) the wave function is not isotropic, but when averaging over all spin states, the probability density $\Psi^*\Psi$ is

independent of ϕ meaning that J/ψ and $K^{\pm}$ mesons are produced isotropically. Going to the J/ψ rest frame, we can choose the z-axis to be opposite to the direction of the kaon (same with the direction of the B^{+} meson), so that $\theta = 0$ and only one spin state survives, that with a z component that equals zero. The J/ψ meson is produced with zero helicity in the decay. Regarding the angular properties of the decay of a vector meson into lepton pairs, a description is found in Ref. [1]. The decay of J/ψ is described as longitudinally polarized along the z-axis, and the angular distribution is

$$\frac{\mathrm{d}N}{\mathrm{d}\Omega} \propto \frac{\mathrm{d}N}{\mathrm{d}\cos\theta} \propto \sin^2\theta \ ,$$

where θ is the angle of the positive-charge lepton with respect to the z axis in the J/ψ rest frame.

Bibliography

[1] S. Palestini, *Angular distribution and rotations of frame in vector meson decays into lepton pairs*, Phys. Rev. **D 83** (2011) 031503, `arXiv:1012.2485 [hep-ph]`.

Appendix B

MCP recommendations for track selection

Following recommendations from the Muon Combined Performance (MCP) group the track quality selections for the analysis of 2011 data are given below.

- If B-layer hits were expected for the track, it is required to have at least one B-layer hit.
- Number of pixel hits + number of crossed dead pixel sensors > 1
- Number of SCT hits + number of crossed dead SCT sensors ≥ 6
- Number of pixel holes + number of SCT holes < 2
- Let $N = N_{\text{hits}}^{\text{TRT}} + N_{\text{outliers}}^{\text{TRT}}$, where $N_{\text{hits}}^{\text{TRT}}$ and $N_{\text{outliers}}^{\text{TRT}}$ are the number of track TRT hits and TRT outliers, respectively. We require:
  - $N > 5$ and $N_{\text{outliers}}^{\text{TRT}} < 0.9\,N$, if track $|\eta| < 1.9$;
  - $N_{\text{outliers}}^{\text{TRT}} < 0.9\,N$, if track $|\eta| \geq 1.9$ and $N > 5$.

Appendix C

Effect of the imperfect modelling of B^+ kinematics by the generator

In the next paragraphs, details are given on the dependence of the acceptance and the signal efficiency on the B^+ kinematics, as predicted by the used generator. In this analysis, the PYTHIA generator with the AUET2B-LO** tune [**?**] is used as the baseline for the estimation of these corrections. The kinematic distributions for generated $B^{\pm}$ mesons are compared to those predicted by POWHEG and MC@NLO using CT10 [**?**] PDF in Figure C.1. The fact that the p_{T} distribution does not change significantly from LO to NLO supports our choice of PYTHIA as the baseline. In the comparison of the two NLO generators with PYTHIA, MC@NLO shows larger deviation (mainly in y) and is used in the estimation of systematics.

To estimate systematics on ε^{B^+} and A, we reweight events in PYTHIA so that the p_{T} and y distributions match the ones from MC@NLO. The variation we observe on the value of ε^{B^+} and A is assigned as systematic uncertainty deriving from imperfect knowledge of the B^+ kinematics, also accounting for the choice of PDF.

To obtain the weights, two-dimensional fits are performed to derive analytic functions which describe the p_{T}-y distribution of B^+. Neglecting the small correlation of p_{T} and y variables, the analytic function used, is

$$F(p_{\mathrm{T}}, y) = F(p_{\mathrm{T}}) \cdot F(y) \ , \tag{C.1}$$

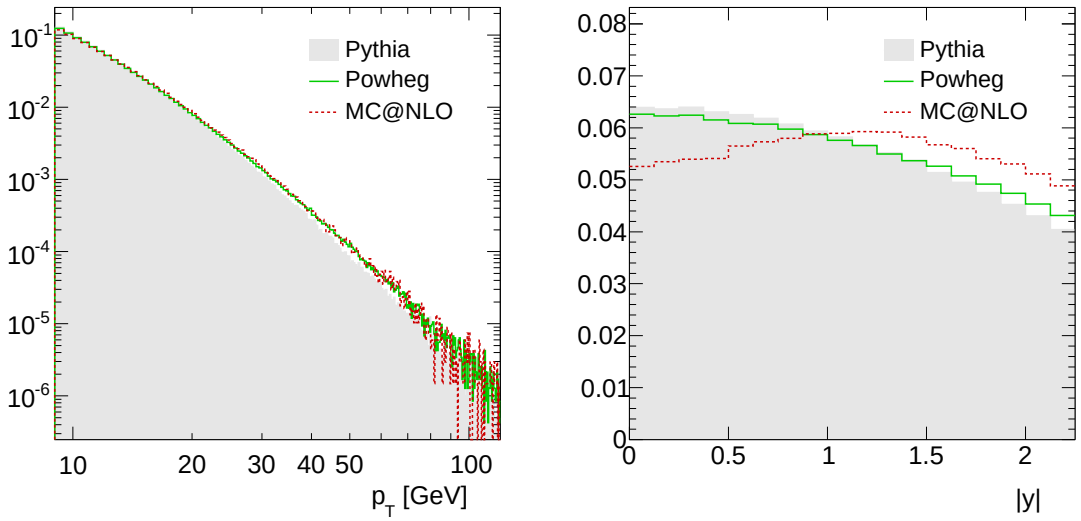

Figure C.1: Predictions of p_{T} and y distributions from POWHEG (green) and MC@NLO (dashed red), compared to PYTHIA (solid grey). All histograms are normalized to unity.

where:

$$F(p_{\mathrm{T}}) = \alpha e^{-k_1 p_{\mathrm{T}}} + (1-\alpha)\frac{p_{\mathrm{T}}}{[1+(\frac{p_{\mathrm{T}}}{k_2 n})^2]^n} \quad , \quad F(y) = A + By + Cy^2 + Dy^3 \qquad \text{(C.2)}$$

The values for the parameters α, A, B, C, D, k_1, k_2, n are obtained separately from the fit to POWHEG, MC@NLO and PYTHIA histograms to define the three functions which describe the shapes of the p_{T}-y distributions for each generator. To make the events from PYTHIA match the kinematics from MC@NLO, event weights are then defined as a function of p_{T} and y, taking the ratio of the corresponding functions:

$$w(p_{\mathrm{T}}, y) = \frac{F_{\mathrm{MC@NLO}}(p_{\mathrm{T}}, y)}{F_{\mathrm{PYTHIA}}(p_{\mathrm{T}}, y)} \; . \qquad \text{(C.3)}$$

As the signal efficiency and acceptance is extracted in (p_{T}, y) intervals, the events have to be weighted so that the kinematics of PYTHIA events in a (p_{T}, y) interval match the ones from MC@NLO in the same interval. Thus, the event weight function $w(p_{\mathrm{T}}, y)$ has to be defined in each interval after normalizing the $F_{\mathrm{MC@NLO}}(p_{\mathrm{T}}, y)$ and $F_{\mathrm{PYTHIA}}(p_{\mathrm{T}}, y)$ in the bin (their integral in the bin equals one). Finally, the signal efficiency and acceptance are re-calculated after weighting the events from PYTHIA using

the derived weight functions. The differences we observe are demostrated in Figure C.2. The effect of the modified kinematics is found to be negligible, expect for some bins in the forward rapidity interval, where the observed difference is as large as the statistical precision. However, such effects are partially correlated and are neglected.

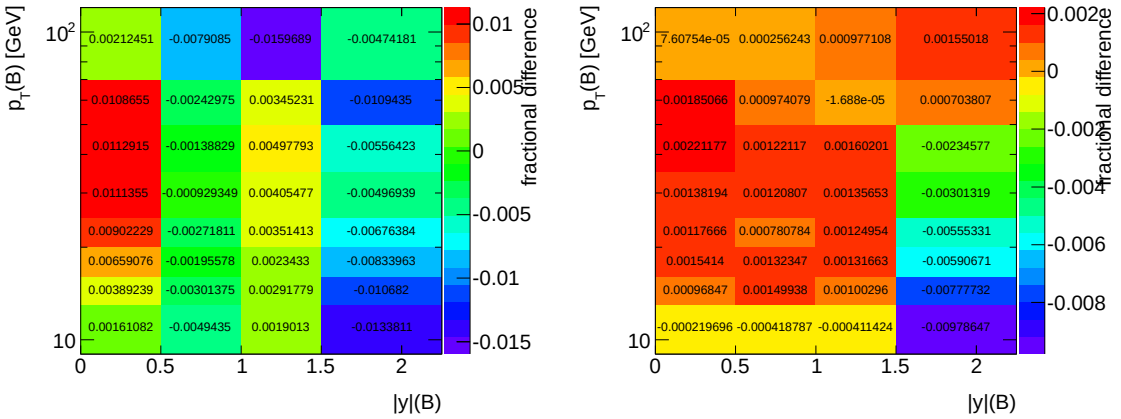

Figure C.2: Variation of signal efficiency (left) and acceptance (right) after reweighting events from PYTHIA to match the kinematics from MC@NLO in each bin. The observed differences are used to estimate the systematic uncertainty on the signal efficiency and acceptance from b-quark kinematics.

Acknowledgements

Ευχαριστώ το πρόγραμμα 'Ηράκλειτος II' για την χρηματοδότηση της ερευνητικής εργασίας στα πλαίσια αυτής τη διατριβής. Το έργο υλοποιήθηκε στο πλαίσιο του Επιχειρησιακού Πρόγραμματος «Εκπαίδευση και Δια Βίου Μάθηση» και συγχρηματοδοτήθηκε από την Ευρωπαϊκή Ένωση (Ευρωπαϊκό Κοινωνικό Ταμείο) και από εθνικούς πόρους.

I thank the Research Funding Program 'Hrakleitus II' for funding the research for this thesis. This research has been co-financed by the European Union (European Social Fund - ESF) and Greek national funds through the Operational Program "Education and Lifelong Learning" of the National Strategic Reference Framework (NSRF).

Completing a PhD thesis was a lifetime project during which I encountered discouraging difficulties. I would have easily abandoned the effort, if it had not been for the endless and unconditional support from the people I worked and lived with. Written below are a few words for those that played a key role in various parts of my PhD studies.

To start with, I consider myself very lucky for joining the Thessaloniki ATLAS group and I enjoyed every minute of work with its members. I have been very privileged to have undoubtedly the most intuitive, smart and supportive advisor anyone could ask for. Prof. Chara Petridou, I thank you for giving me the chance to make my dreams come true. It has been six years already since I first knocked your door hoping for a MSc thesis and since then it has been quite a journey. You guidance has always been excellent and inspiring, putting me back on track when I was lost. Sitting beside you I have taken numerous lessons on how to think, work and react. There is still a lot to learn but I will never develop your unique instinct in physics analysis and I will always come back to you for advice.

I thank Assist. Prof. Dimos Sampsonidis for helping me do the first steps in my PhD and the analysis. I remember times when I had serious trouble understanding things while you were always cool, relaxed and helpful. This spirit is exactly what I needed back then and is what I will try to pass on to my colleagues, following your example. Lecturer Kostas Kordas, I thank you for all the advice you have been giving me all these years and for reminding me why this job is fun, which I usually forget. I

am so inspired by your untold passion and rare ability to conduct and explain science and your classic mottos.

I also need to thank the people of the ATLAS B-physics group that supported the analysis at various steps. I thank Dr. Sandro Palestini for showing excessive interest in improving the cross-section analysis and supporting it at the most crucial times. You have my deepest appreciation not only for identifying problems that were usually overlooked, but also for having the first word on how to overcome them. I thank Dr. Maria Smizanska for guiding the efforts of the first data analysis within the $B \to J/\psi$ group during the exciting times of observing the first $B^{\pm}$ mesons in ATLAS back in 2010. I also thank Dr. James Catmore for developing the software for B-physics analysis and helping in solving software-related problems and Dr. Camilla Maiani for helping me understand the fit methods and sharing her code for mass and lifetime fits so willingly. I am grateful to Dr. Nectarios Benekos for offering the chance to get involved in the DQM business, by which I got a strong push when started working in ATLAS and developed good understanding of the muon spectrometer and the offline software thanks to his kind assistance in all the difficulties that an ATLAS newcomer has to face.

I thank my wonderful colleagues and, at the same time, dear friends, Vassiliki Kouskoura, Dimitris Iliadis, Dr. Andreas Petridis and Dr. Ilektra Christidi, for being the coolest I could have and for making bad days in the office a lot better. We have shared so much all these years, knowledge, code, fun and even the same roof, at times, with so many stories to tell.

I thank my dearest friend, Dr. Kostas Nikolopoulos, with which I share all of my good memories from my stay at CERN (with the 'requiem to Diafana Krina' being the highlight), for his constant support, hospitality and encouragement. Special thanks for organizing fun things in Geneva!

I must thank Dr. Christos Anastopoulos for installing linux on my TurboX laptop (not easy), for passing knowledge from his B^{+} studies for the ATLAS CSC book and for his wise words during the small hours.

All my friends from CERN, Dr. Eleni Mountricha, Dr. Christos Lazaridis, Dr. Fanouria+Theo Argyropoulos for being such a lovely company from the first day I

got there. Also Kostas Karakostas for the coffee breaks and music nights which would have been so lonely otherwise.

Lastly, I need to mention my better half, Mariela, and good friends from school and university who know how grateful I am for their help in many and different ways and their company, without which I would not have managed. I need to thank you for the respect you have been showing for my work, as well as for your tolerance of my inability to act like a normal person during the hard times. Your presence in my life is very important and this thesis is dedicated to you; and to my parents, also, for making all this possible by letting me choose my own goals in life.